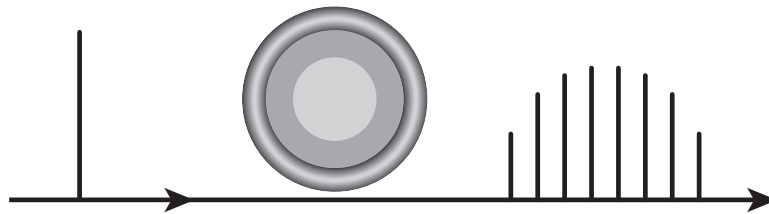# Optical Frequency Comb Generation in Monolithic Microresonators

Pascal Del'Haye

München 2011

Optical Frequency Comb Generation in Monolithic Microresonators

Pascal Del'Haye

Dissertation
an der Fakultät für Physik
der Ludwig–Maximilians–Universität
München

vorgelegt von
Pascal Del'Haye
aus München

München, den 23.02.2011

Meiner Familie und Mǎ Ruì gewidmet

Weil in der Stille des Tempelgartens das Quellwasser aus dem Munde eines bronzenen Drachen in ein Steinbecken fällt, gibt es die Zeit.

Toyotama Tsuno, M.H.

Contents

Zusammenfassung

Die optische Spektroskopie wurde 1814 mit Fraunhofers Entdeckung von dunklen Linien im Sonnenspektrum begründet und beschäftigt seitdem Generationen von Wissenschaftlern. Kirchhoff und Bunsen konnten schließlich 1859 das Phänomen als Lichtabsorption in Atomen und Molekülen erklären. Im letzten Jahrzehnt hat die Erfindung des optischen Frequenzkammes das Feld der Spektroskopie revolutioniert und Messungen mit vorher unerreichter Genauigkeit ermöglicht, was zur Ehrung mit dem Nobelpreis im Jahre 2005 geführt hat. Frequenzkämme haben sich erstaunlich schnell in vielen Forschungsfeldern verbreitet und werden mittlerweile für Präzisionsspektroskopie, optische Uhren, Gasanalytik, Abstandsmessungen und Kalibration von Spektrometern in Teleskopen genutzt.

Die vorliegende Dissertation zeigt ein neuartiges Konzept zur Erzeugung von Frequenzkämmen, das auf nichtlinearen optischen Effekten in Mikroresonatoren beruht. Der zugrunde liegende Prozess nutzt energieerhaltende Wechselwirkungen zwischen jeweils vier Photonen (Vierwellenmischen) und ist eine Folge von extrem hohen Lichtintensitäten, die durch verhältnismäßig lange Speicherung von Licht in sehr kleinen optischen Resonatoren erreicht werden. Die Arbeit ist in vier Kapitel unterteilt, in denen grundlegende Eigenschaften und praktische Anwendungen von mikroresonatorbasierten Frequenzkämmen diskutiert werden.

Das erste Kapitel bietet eine Einführung in Vierwellenmischen-induzierte optische Frequenzkammerzeugung und stellt verschiedene auf Mikroresonatoren basierende Kammgeneratoren vor, deren Entwicklung von dieser Dissertation beeinflusst wurde.

Der zweite Teil ist Messungen zur Äquidistanz der durch Vierwellenmischen erzeugten Moden in Mikroresonatoren gewidmet. Diese fundamentalen Messungen zeigen, dass optische Mikroresonatoren tatsächlich zur Frequenzkammerzeugung genutzt werden können.

Im dritten Kapitel wird demonstriert, dass es möglich ist die erzeugten Kammlinien auf beliebige optische Frequenzen einzustellen. Des Weiteren wird die Kontrolle des Abstandes der Kammmoden über einen schnellen thermischen Effekt gezeigt, der eine vollständige Stabilisierung des Kammspektrums ermöglicht.

Das vierte und letzte Kapitel beschäftigt sich mit der grundsätzlichen Frage, wieso Frequenzkammerzeugung in Mikroresonatoren stattfinden kann. Diese Frage ist eng verbunden mit Dispersioneigenschaften die bestimmen, ob ein Frequenzkamm in einen Mikroresonator "hineinpasst" oder nicht. Sowohl theoretische als auch experimentelle Untersuchungen geben Aufschluss über die maximal erzeugbare Bandbreite der Frequenzkämme.

Abstract

Optical spectroscopy has attracted attention of generations of scientists, starting with Fraunhofer's discovery of dark lines in the sun spectrum in 1814 followed by work of Kirchhoff and Bunsen in 1859, who explained these lines as absorption of light in atoms and molecules. Within the last decade, the invention of optical frequency combs has revolutionized the field of spectroscopy and paved the way for groundbreaking measurements at previously unattainable accuracy, which has been rewarded with the Nobel Prize in 2005. Meanwhile frequency combs have spread into a variety of research fields at fast pace and are used for precision spectroscopy, optical clocks, chemical sensing, distance measurements, astrophysical spectrometer calibration and many other applications.

This thesis presents an entirely novel approach for frequency comb generation based on nonlinear frequency conversion in micrometer sized optical resonators. Here, the comb generation process can be directly described in frequency domain as energy conserving interactions between four photons (four-photon mixing). This process is a result of extremely high light intensities that build up in microresonators with long photon storage times. The thesis is composed of four main parts that answer fundamental questions in the context of microresonator-based frequency comb generation as well as providing insights in the control and possible applications of this type of comb generators.

The first part is an introductory chapter about the novel frequency comb generation scheme and presents different microresonator- and four-photon-mixing-based comb generators that have emerged from the work of this thesis.

The second chapter is dedicated to measurements that show the equidistant nature of modes generated by four-photon mixing in microcavities, which is answering the question whether microresonators are suitable tools for optical frequency comb generation.

A third part demonstrates full control of the comb modes, allowing for positioning of comb lines at any desired frequency of choice. Moreover, variation of the comb spacing via fast thermal effects in the microresonator material is shown. This allows for full stabilization of microresonator-based frequency combs, which is an important precondition for many applications.

The fourth and last chapter focuses on the question why comb generation can occur in microresonators. This question is strongly related to the intrinsic dispersion of microcavity modes, which determines whether a frequency comb "fits" into a microresonator or not. Both theoretical and experimental considerations give an insight into the maximum achievable comb bandwidths.

Publications, Patents, Conferences, Awards

Publications

[1] A. Schliesser, P. Del'Haye, N. Nooshi, K. J. Vahala, and T. J. Kippenberg, "Radiation pressure cooling of a micromechanical oscillator using dynamical backaction," *Physical Review Letters* **97**, p. 243905, Dec. 2006.

[2] R. Ma, A. Schliesser, P. Del'Haye, A. Dabirian, G. Anetsberger, and T. J. Kippenberg, "Radiation-pressure-driven vibrational modes in ultrahigh-q silica microspheres," *Optics Letters* **32**, pp. 2200–2202, Aug. 2007.

[3] P. Del'Haye, A. Schliesser, O. Arcizet, T. Wilken, R. Holzwarth, and T. J. Kippenberg, "Optical frequency comb generation from a monolithic microresonator," *Nature* **450**, pp. 1214–1217, Dec. 2007.

[4] P. Del'Haye, O. Arcizet, A. Schliesser, R. Holzwarth, and T. J. Kippenberg, "Full stabilization of a microresonator-based optical frequency comb," *Physical Review Letters* **101**, p. 053903, Aug. 2008.

[5] P. Del'Haye, O. Arcizet, M. L. Gorodetsky, R. Holzwarth, and T. J. Kippenberg, "Frequency comb assisted diode laser spectroscopy for measurement of microcavity dispersion," *Nature Photonics* **3**, pp. 529–533, Sept. 2009.

[6] O. Arcizet, A. Schliesser, P. Del'Haye, R. Holzwarth, and T. J. Kippenberg, Bookchapter in: *Practical applications of microresonators*, ch. 11. Optical frequency comb generation in monolithic microresonators, pp. 483—506. CRC press, 2009.

[7] P. Del'Haye, T. Herr, E. Gavartin, R. Holzwarth, and T. J. Kippenberg, "Octave spanning frequency comb on a chip." arXiv:0912.4890.

Patents

[8] P. Del'Haye, T. J. Kippenberg, and A. Schliesser, "Method and apparatus for optical frequency comb generation using a monolithic microresonator. European (EP 07009067) and US (US 60.916045) patent applications," 2007.

[9] P. Del'Haye, O. Arcizet, and T. J. Kippenberg, "Method and apparatus for frequency comb assisted laser spectroscopy. (US 61/217,220, provisional patent application)," 2009.

Conferences and Seminars

[10] European Conference on Optical Communication (ECOC), Torino, Italy, P. Del'Haye, T. Herr, E. Gavartin, R. Holzwarth, and T. J. Kippenberg, "Octave-spanning tunable frequency combs on a chip" **(invited talk)**, 2010.

[11] Ringberg Seminar of the MPQ Laser spectroscopy Division, Rottach-Egern, Germany, P. Del'Haye, C. Wang, T. Herr, M. Gorodetsky, R. Holzwarth, and T. J. Kippenberg, "Frequency comb generation from microresonators", 2010.

[12] CLEO/IQEC, San Jose, USA, P. Del'Haye, T. Herr, E. Gavartin, R. Holzwarth, and T. J. Kippenberg, "Octave-spanning tunable frequency combs on a chip", 2010.

[13] National Institute of Standards and Technology, Boulder, USA, P. Del'Haye and T. J. Kippenberg, "Chip-based frequency combs - towards an optical octave" **(invited)**, 2009.

[14] CLEO Europe/EQEC, Munich, Germany, P. Del'Haye, O. Arcizet, R. Holzwarth, and T. J. Kippenberg, "Broadband precision spectroscopy using a scanning diode laser and a frequency comb", 2009.

[15] Conference on Lasers and Electro-Optics (CLEO), Baltimore, USA, P. Del'Haye, O. Arcizet, R. Holzwarth, and T. J. Kippenberg, "Precision spectroscopy with a scanning diode laser and measurement of microcavity dispersion", 2009.

[16] Deutsche Physikalische Gesellschaft Meeting, Hamburg, Germany, P. Del'Haye, O. Arcizet, R. Holzwarth, and T. J. Kippenberg, "Microcavity spectroscopy and chip-scale frequency combs", 2009.

[17] NPL Time and Frequency Division Seminar Series, Teddington, United Kingdom, P. Del'Haye and T. J. Kippenberg, "Frequency comb generation in whispering gallery mode resonators" **(invited)**, 2008.

[18] URSI General Assembly 2008, Chicago, USA, P. Del'Haye, A. Schliesser, O. Arcizet, T. Wilken, R. Holzwarth, and T. J. Kippenberg, "Optical frequency comb generation and stabilization in a monolithic microcavity", 2008.

[19] Ringberg Seminar of the MPQ Laser spectroscopy Division, Rottach-Egern, Germany, P. Del'Haye and T. J. Kippenberg, "Full stabilization of a microresonator-based optical frequency comb", 2008.

[20] CLEO/QELS, San Jose, USA, P. Del'Haye, A. Schliesser, O. Arcizet, T. Wilken, R. Holzwarth, and T. J. Kippenberg, "Full stabilization of a microcavity frequency comb" **(invited talk)**, 2008.

[21] NIM D Workshop, Munich, Germany, P. Del'Haye, A. Schliesser, O. Arcizet, T. Wilken, R. Holzwarth, and T. J. Kippenberg, "Optical frequency comb generation and stabilization", 2008.

[22] Frontiers in Optics, San Jose, USA, P. Del'Haye, A. Schliesser, T. Wilken, R. Holzwarth, and T. J. Kippenberg, "Optical frequency comb generation from a monolithic microresonator" **(invited talk)**, 2007.

[23] CLEO/IQEC Europe, Munich, Germany, P. Del'Haye, A. Schliesser, T. Wilken, R. Holzwarth, and T. J. Kippenberg, "Kerr nonlinearity induced optical frequency comb generation in microcavities", 2007.

[24] Seminar Series of the MPQ Laser Spectroscopy Division, Munich, Germany, P. Del'Haye and T. J. Kippenberg, "Optical frequency comb generation in monolithic microcavities", 2007.

[25] CQO9, Rochester, USA, P. Del'Haye, A. Schliesser, T. Wilken, R. Holzwarth, and T. J. Kippenberg, "Generation of an optical frequency comb from a monolithic microresonator via the kerr-nonlinearity" (poster), 2007.

[26] Conference on Lasers and Electro Optics (CLEO), P. Del'Haye, A. Schliesser, T. Wilken, R. Holzwarth, and T. J. Kippenberg, "Kerr nonlinearity induced optical frequency comb generation in microcavities", 2007.

Awards

May 2010 - Finalist of the **Theodore Maiman Student Award**, CLEO/IQEC, San Jose, USA. Student prize granted by HRL Laboratories, LLC, IEEE Photonics Society, APS and OSA. For the paper "*Octave-spanning tunable frequency combs on a chip*".

June 2009 - **Helmholtz-Prize for Metrology**. For the "*Developement of microresonator based frequency combs*".

June 2009 - Finalist of the **Theodore Maiman Student Award**, CLEO/IQEC, Baltimore, USA. Student prize granted by HRL Laboratories, LLC, IEEE Photonics Society, APS and OSA. For the paper "*Precision spectroscopy with a scanning diode laser and measurement of microcavity dispersion*".

September 2007 - **Best of Topicals Award**, Frontiers in Optics, San Jose USA. Awarded by the Optical Society of America for the conference submission "*Optical frequency comb generation from a monolithic micro-resonator via the Kerr nonlinearity*".

CHAPTER 1

Microresonator-based frequency comb generation
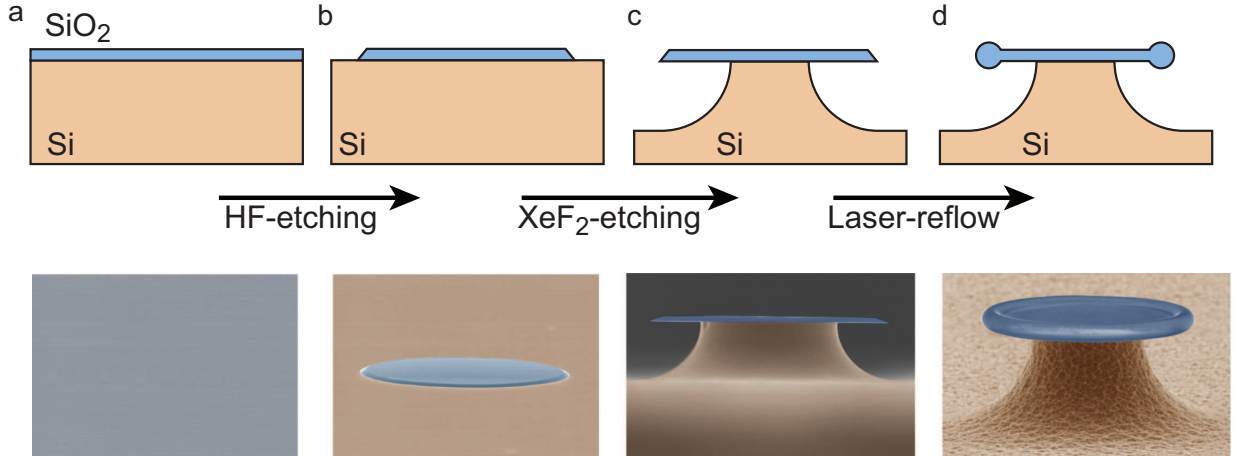
1.1   Whispering gallery mode resonators

This first chapter introduces the optical system that is used throughout the thesis as nonlinear optical device: *the whispering gallery mode microresonator*. Additionally, a detailed explanation of the nonlinear optical effect leading to frequency comb generation is given. The name "whispering gallery" originates from an acoustic phenomenon in the famous St. Paul's cathedral in London. Located inside the dome of the cathedral is a circular gallery with a diameter of 34 m, which is surrounded by a smooth stone wall (figure 1.1c,d). This gallery is well known for the interesting acoustical effect that a whispered word on one side of the dome can be easily heard by a person on the other side of the dome. Lord Rayleigh could explain this phenomenon by continuous reflection of sound waves at the inner wall of the dome in 1912 [10]. Similar whispering galleries exist at several other places for example on the Tiantan temple compound in Beijing (figure 1.1a,b). Solving wave equations with the periodic boundary condition of a whispering gallery leads to modes at discrete wavelengths. In a simple picture, a whispering gallery with a radius R can just support wavelengths λ_res which correspond to an integer fraction ℓ of the circumference of the gallery:

$$\lambda_\mathrm{res} \cdot \ell = 2\pi \cdot R \quad . \tag{1.1}$$

The wavelengths λ_res are the resonance wavelengths, which can be explained by constructive interference of the wave after a round trip in the whispering gallery. Richtmyer transfered the concept of whispering gallery resonators from the acoustical domain to electromagnetic microwaves already in 1939 [11]. Surprisingly, whispering gallery mode resonators at optical frequencies have been developed only twenty years ago. First high quality spherical resonators were introduced by the scientists Braginsky, Gorodetsky (who contributed to this work as visiting professor in our group) and Ilchenko in 1989 by melting optical fiber tips made of fused quartz [12]. Since then, optical microresonators [13–15] have opened a vast research field and have triggered numerous scientific developments, propelled by their ability to store huge amounts of light within tiny volumina. Meanwhile, microresonators are used for nonlinear optical effects [16–23], laser cavities [24–28], cavity quantum electrodynamics [29–31], molecular sensing [32], observation of radiation pressure induced effects of light [2, 33–37] as well as actively cooling micromechanical motion with light [1, 38–40]. Especially the strong light confinement in microresonators gives rise to nonlinear optical effects at very low optical power levels and enabled the observation of Raman lasing [18–20, 23, 41], parametric oscillations [22], four-wave mixing [16, 17] as well as frequency doubling [21] and tripling [42]. This thesis focuses on four-wave mixing in microresonators as the governing effect for optical frequency comb generation, which is discussed in detail in section 1.5. However, the high optical power levels that are required for the comb generation drive other optical nonlinearities as well. Comb generation in particular is strongly influenced by Raman scattering and thermal nonlinearities as well as radiation pressure induced instabilities. Before going into the details of comb generation, whispering gallery mode microresonators are introduced briefly.

Figure 1.1: Acoustic whispering galleries. Panel a and b show the "temple of heaven" compound in Beijing with a circular 200-m-diameter courtyard surrounded by a smooth stone wall, forming an acoustic whispering gallery. Panel c and d show the St. Paul's Cathedral in London with a 34-m-diameter whispering gallery in the dome. Lord Rayleigh explained the acoustic phenomenon of whispering gallery modes in St. Paul's cathedral for the first time in 1912.

Figure 1.2: Fabrication of microtoroidal whispering gallery mode resonators. Starting with an oxidized silicon wafer, photolithographical methods are used to generate circular disks from a photoresist layer that is spun onto the wafer. Etching with hydrofluoric acid transfers the photoresist pattern to the silicon dioxide (SiO_2, fused silica) layer as shown in panel b. The next step is a selective dry etching of the silicon in order to produce a free-standing SiO_2 disk on a silicon pillar (panel c). Subsequently, a CO_2 laser is used to melt the circumference of the disk (panel d) in order to reduce the surface roughness, which is required to obtain high optical quality factors. The lower row shows corresponding scanning electron microscope images (colored) of the respective fabrication steps.

1.2 Fused silica microtoroids

The main "workhorse" of this thesis is the fused silica microtoroid, a doughnut-shaped whispering gallery mode resonator. This type of microresonator has been developed in 2003 in the group of Kerry Vahala [43] and has the major advantage of extraordinary small mode volumes [44], which are leading to extremely low threshold powers for nonlinear optical effects [16, 20, 42].

Figure 1.2 illustrates the fabrication process of microtoroids. An oxidized silicon wafer serves as precursor for the process. The thickness of the oxide layer (amorphous SiO_2, fused silica) is in the order of 1 to 2 μm and influences the final size of the resonator. Two oxidation processes are commonly used, wet and dry oxidation. The corresponding chemical reactions take place at high temperatures of around 1000 °C and the molecular formulae are

$$Si_{(s)} + 2\,H_2O_{(g)} \rightleftharpoons SiO_{2\,(s)} + 2\,H_{2\,(g)} \tag{1.2}$$
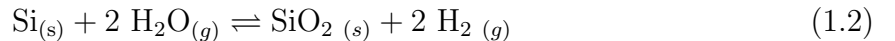
for wet oxidation and

$$Si_{(s)} + O_{2\,(g)} \rightleftharpoons SiO_{2\,(s)} \tag{1.3}$$

for dry oxidation. The presence of hydrogen in the wet oxidation processes is principally

unfavorable as it generates OH^- bonds within the SiO_2 with strong optical absorption lines in the infrared [45]. However, dry oxidation is a very slow process, and growing a 2 μm oxide layer can take several weeks [46]. The next fabrication step forms disk-shaped fused silica pads by UV-lithography and subsequent etching with buffered oxide etchant (BOE) containing hydrofluoric acid (HF) as shown in figure 1.2b. This chemical process removes the fused silica from the silicon wafer except a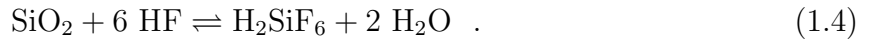t the position of the disks that are protected by a photoresist layer. The underlying chemical process leads to the generation of hydrofluosilicic acid and water [47]

$$SiO_2 + 6\ HF \rightleftharpoons H_2SiF_6 + 2\ H_2O\ \ . \tag{1.4}$$

In order to maintain a constant etch rate, the etchant is buffered with ammonium fluoride (NH_4F) that ensures a constant HF concentration via the reaction

$$NH_4F \rightleftharpoons NH_3 + HF\ \ . \tag{1.5}$$

The HF etching step produces fused silica disks on a silicon wafer. In order to use the SiO_2 pads as optical whispering gallery mode resonators it is required to fabricate free standing disks, otherwise the light would couple into the silicon which has a higher refractive index ($n \approx 3.5$) compared to fused silica ($n \approx 1.44$). Free standing disks are realized by underetching the fused silica pads with xenon difluoride gas. Xenon difluoride (XeF_2) is a crystalline powder with a high vapor pressure of 5 hPa [48] that can be sublimated with a vacuum pump for the etching process. An undercut of the fused silica disk is obtained as a result of the high selectivity of the XeF_2-etching, which is 1000:1 for etching of silicon compared to SiO_2. The chemical reaction with silicon leads to the formation of gaseous silicon fluoride SiF_4 which is removed from the etching chamber (cf. equation 1.6). A detailed description of the etching process is shown in [49] and [50].

$$2\ XeF_{2\ (g)} + Si_{(s)} \rightleftharpoons 2\ Xe_{(g)} + SiF_{4\ (g)}\ \ . \tag{1.6}$$

The etching process has to take place in a water-vapor-free environment. This is essential, because water would react with xenon difluoride to hydrofluoric acid [51] which attacks the silica disk.

$$2\ XeF_2 + 2\ H_2O \rightleftharpoons 2\ Xe + O_2 + 4\ HF \tag{1.7}$$
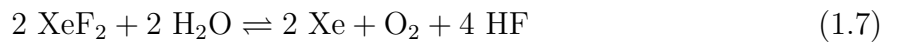
A water free environment is realized by purging the etching chamber with nitrogen prior to the XeF_2 etching process. A last fabrication step, shown in figure 1.2d is necessary to smoothen the whispering gallery surface, which has a roughness in the order of 100 nm induced by the etching steps [52].

Figure 1.3 shows a scanning electron microscope image of a 60-μm-diameter microtoroid in false colors. The light can travel around the circumference of these resonators typically for around 500 nanoseconds. This corresponds to an optical quality factor of $Q = 6 \times 10^8$ or more than 300,000 round-trips of a photon within the resonator.
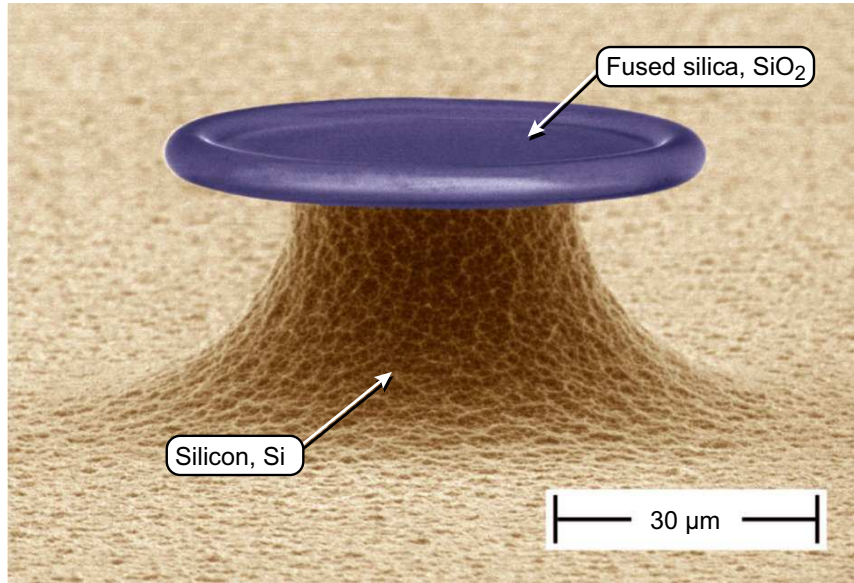
Figure 1.3: Scanning electron microscope image of a microtoroidal whispering gallery mode resonator (colored). The diameter of the toroid is ≈ 60 μm and the toroid cross-section has a diameter of ≈ 5 μm.

1.3   Experimental setup for comb generation

This section gives a brief description of the basic setup, which is used for optical frequency comb generation. An important part of this setup (shown in figure 1.4) is the laser source that has to be tunable in frequency in order to reach the resonance frequency of the employed microresonator. Typically (and most conveniently) the pump source is an external cavity diode laser system (eg. "New Focus Velocity" series), which can be tuned without mode-hops within bandwidths of > 5 THz. For applications that require low noise pump lasers it is possible to use titanium sapphire or fiber lasers, however the later ones typically have frequency tuning ranges of only a few tenths of gigahertz, making it difficult to find appropriate resonances in microresonators with significantly larger mode spacings. Another basic part of the coupling setup is a polarization controller that is used for matching the polarization of the laser light with the polarization of the resonator mode of interest. Equally important is the ability to control and optimize coupling between of the laser light to the resonator. The coupling method shown in figure 1.4 relies on tapered optical fibers with diameters of less than 1 micron at the thinnest part. Since the diameter of the fiber is in the order of the optical wavelength an evanescent part of the light field is outside of the fiber and can couple to a microresonator mode [53–60]. Coupling can be controlled by fine tuning the relative distance between resonator and optical fiber. This allows to change between regimes of undercoupling (intrinsic resonator losses > coupling losses), critical coupling (resonator losses = coupling losses) and overcoupling (resonator losses < coupling losses). In order to optimize the coupling to the microresonator, the laser source is swept
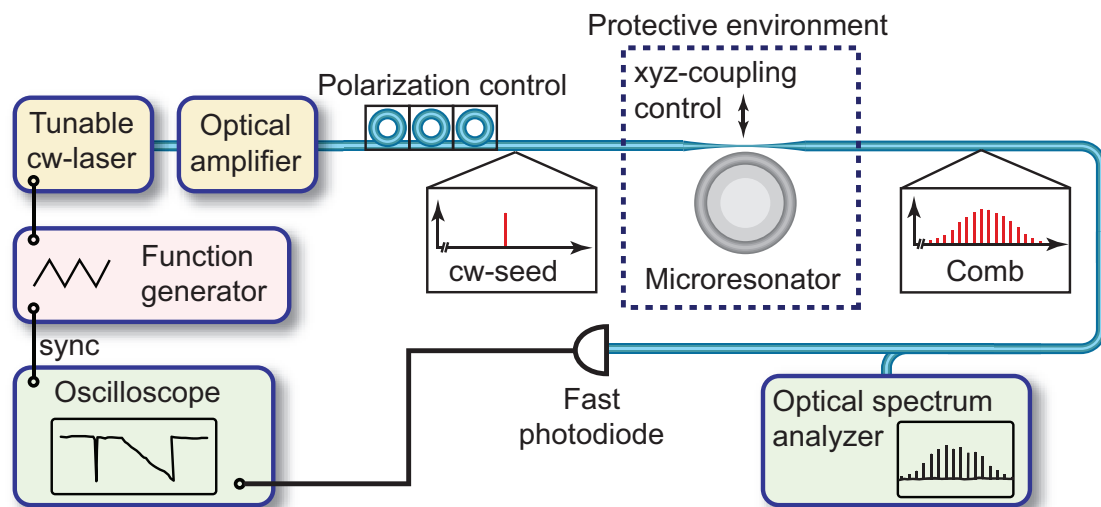
Figure 1.4: Basic experimental setup for optical frequency comb generation in microresonators. An amplified tunable diode laser is used as pump source and coupled to the microresonator via a tapered optical fiber. Periodic sweeping of the diode laser across a resonance frequency and simultaneous monitoring the transmission signal allows for optimization of both coupling gap between tapered fiber and resonator as well as matching the polarization of the laser with the resonator mode. The generated comb modes in the microresonator couple back to the optical fiber and can be monitored with an optical spectrum analyzer.

periodically across a cavity resonance while simultaneously monitoring the transmission signal of the tapered optical fiber. This allows to maximize the amount of light coupled to the resonator by adjusting both polarization and coupling distance. Additionally it is necessary to ensure phase matching between the resonator mode and the mode in the tapered fiber (as described by Knight et. al. [55]). This corresponds to matching the propagation constant of the field in the tapered optical fiber and the resonator mode and can be achieved by changing the fiber diameter at the coupling position (for instance by moving the tapered fiber in tangential direction with respect to the toroid). Once the coupling to the resonator is optimized, an optical spectrum analyzer is used to observe and optimize a generated frequency combs in the microresonator. The coupling between tapered optical fiber and microresonator is wavelength dependent with the consequence that fine tuning the tapered fiber position can improve the collection of light from the generated comb lines. Alternatively, wavelength independent coupling can be achieved by using a bent tapered fiber as shown in [61].

A photograph of the coupling setup is shown in figure 1.5. Rough alignment of the microresonator is achieved with a manual translation stage. The tapered optical fiber is mounted in a bracket that is sitting on a 3-axis piezo translation stage, which allows for fine positioning of the fiber.

1.4 Coupling of light into microresonators

1.4.1 Experimental techniques

The previous section briefly mentioned coupling to a microresonator with a tapered optical fiber. However, several other methods exist to transfer light into optical microcavities as show in figure 1.6. The first method used in 1989 to couple light into fused silica microspheres [12] is shown in figure 1.6d and utilizes a prism that is approached to the resonator. Laser light is focused onto a spot in the vicinity of the microresonator and undergoes total internal reflection within the prism. The right gap size between prism and resonator and proper mode matching between free space beam and the resonator mode allows for the evanescent tail of the light wave to couple into the resonator and vice versa. A similar method relies on angle cleaved fibers as shown in figure 1.6e. This method requires two fibers for coupling in and out of the resonator, which doubles the degrees of freedom for proper positioning of the fibers. Tapered optical fiber coupling has the huge advantage of high ideality (close to unity coupling efficiency as well as close to zero losses within the tapered fiber). Additionally, tapered fiber coupling allows variation of the coupling position with just one 3-axis-translation stage. Unlike prism coupling and cleaved fiber coupling it is moreover possible to couple microresonators from below or from top (which is useful for coupling microdisks and microtoroids). Panel a of figure 1.6 shows a photograph of the experimental setup being used for fabrication of tapered optical fibers. Conventional single mode fibers are clamped into movable brackets and then heated by the flame of a hydrogen torch. The used air-hydrogen flame has a temperature of approximately 2000 °C, which is
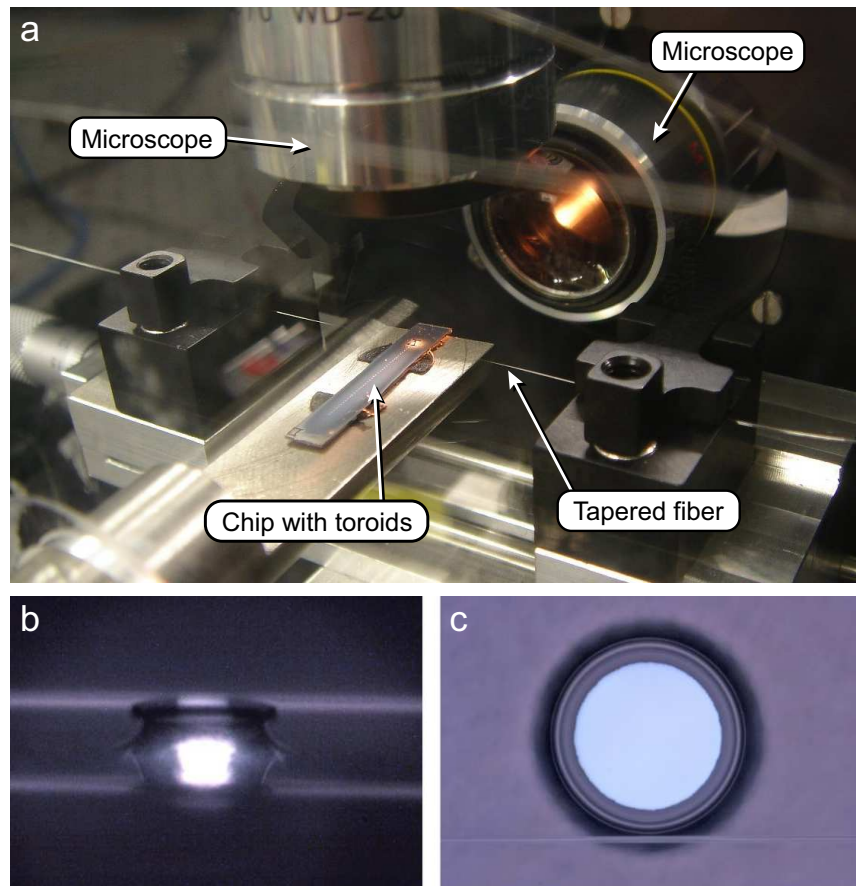
Figure 1.5: Photograph of the coupling setup. The tapered optical fiber is mounted on a 3-axis piezo translation stage in order to approach the microresonator and optimize coupling efficiency. Two camera-equipped microscopes from side and from the top are used to position the tapered fiber. Panel b and c show images of the two cameras (the lower part in panel b is a reflection of microtoroid and fiber on the silicon chip).
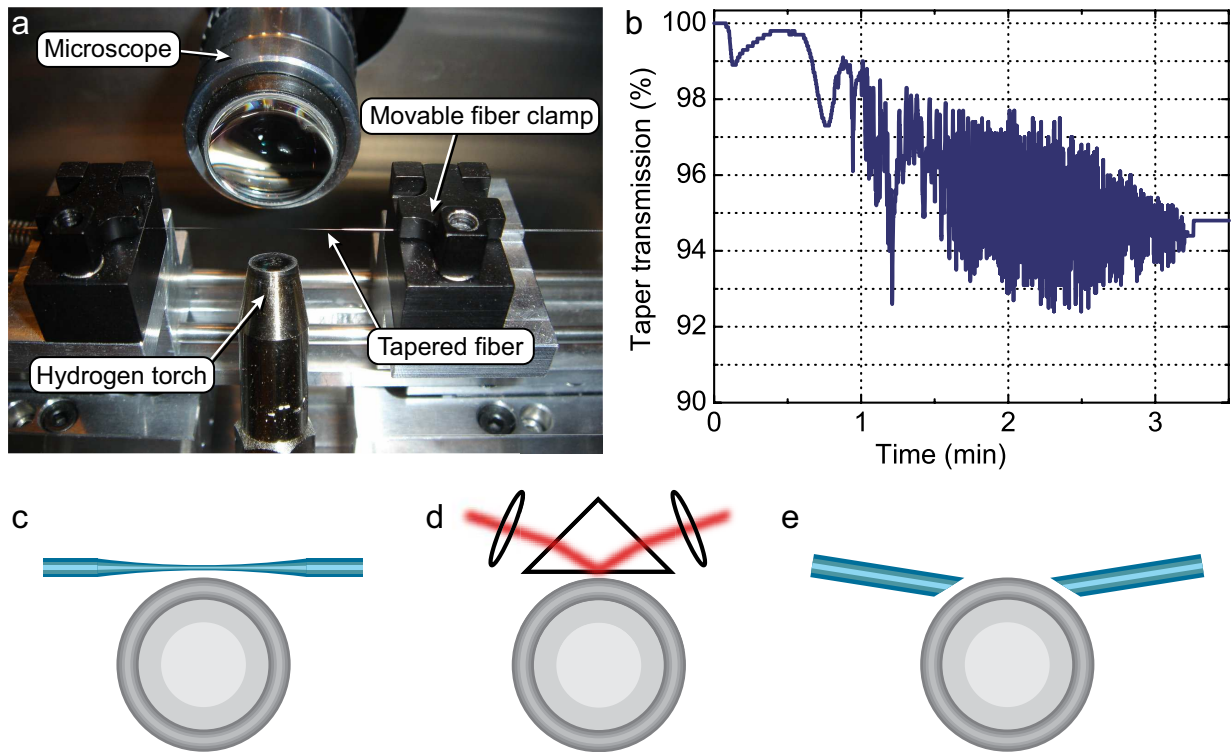
Figure 1.6: Setup for fabrication of tapered optical fibers and different coupling methods. Panel a shows the setup in which a single mode fiber is heated by a hydrogen flame while simultaneously stretching it slowly with a stepper motor. Panel b depicts a corresponding transmission curve of laser light at 1550 nm during the fiber pulling (tapering) process. The diameter of the fiber is decreased from initially 125 μm down to less than 1 μm diameter. Panel b shows the measured transmission through the fiber during the tapering process with a final loss of around 5%. The oscillations in the transmission signal arise from interference of the transmitted light as a result of mixing the 8-μm-diameter core and the 125-μm-diameter cladding of the fiber (which makes the fiber multimode). The tapering process is stopped when the oscillations stop, indicating that the tapered fiber is single mode again by guiding the light by the air-silica boundary. The lower row shows different coupling methods for microresonators. Panel c illustrates tapered fiber coupling [56], panel d prism coupling [12, 62] and panel e coupling with angle cleaved fibers [63].

higher than the softening point of fused silica at 1683 °C [64]. Even higher temperatures can be reached using an oxygen-hydrogen mixture with flame temperatures up to 2800 °C. A single mode fiber used for tapering typically consist of a 125-μm-diameter fused silica cladding and a doped core with slightly higher refractive index with a diameter of around 8 μm (eg. "Corning SMF28"). The light is guided by the refractive index contrast between core and cladding. Tapering the fiber leads to mixing of cladding and core material such that the light starts to be guided by the refractive index contrast between air and fused silica. As a result of the bigger diameter of the core/cladding mixture, the fiber starts to be multimode, which can be seen by oscillations in the fiber transmission resulting from interference effects. The tapering process is stopped when the oscillations in the transmission signal stop, which indicates that the fiber is single mode again within the air/fused silica boundary. Surprisingly, the optical light finds its way back into the core of the single mode fiber after the tapered region. Good fiber tapers can have losses of less than one percent, which can be achieved by an adiabatic transition between original single mode fiber and tapered region [65, 66].

1.4.2 Theoretical description of microresonator coupling

A detailed description of light coupling into resonators has been developed in the group of Hermann Haus [56]. This section briefly introduces some basic ideas of microresonator coupling [53–60] that are used throughout this thesis. Especially for nonlinear optics it is of interest to know the relationship between the launched optical power and the circulating power within the resonator. Two important parameters for optical microresonators are the *quality factor* and the *finesse*. The quality factor Q of an oscillator is defined as 2π times the ratio between the stored energy E_{cav} and the dissipated energy per oscillation cycle $E_{\mathrm{diss}} = P_{\mathrm{diss}}/\nu$ (with ν being the oscillators frequency). The ratio $E_{\mathrm{cav}}/P_{\mathrm{diss}}$ corresponds to the *cavity lifetime* τ.

$$Q = 2\pi \cdot \nu \cdot \frac{P_{\mathrm{diss}}}{E_{\mathrm{cav}}} = 2\pi \cdot \nu \cdot \tau \quad . \tag{1.8}$$

In the limit of a weakly damped oscillator the quality factor can be approximated as

$$Q = \frac{\nu}{\Delta\nu} \quad , \tag{1.9}$$

with the cavity linewidth $\Delta\nu$. The finesse of a resonator is defined as the ratio between free spectral range $\Delta\nu_{\mathrm{FSR}}$ and the linewidth

$$\mathcal{F} = \frac{\Delta\nu_{\mathrm{FSR}}}{\Delta\nu} \quad . \tag{1.10}$$

Optical quality factor and finesse are both determined by the photon loss rate τ^{-1} of the resonator. This loss rate has several contributions and can be split up into different terms (which are detailed in table 1.1)

$$\tau^{-1} = \tau_{\mathrm{mat}}^{-1} + \tau_{\mathrm{scatt}}^{-1} + \tau_{\mathrm{surf}}^{-1} + \tau_{\mathrm{WGM}}^{-1} + \tau_{\mathrm{ext}}^{-1} = \tau_0^{-1} + \tau_{\mathrm{ext}}^{-1} \quad . \tag{1.11}$$

Here we can distinguish between intrinsic losses of the cavity itself τ_0^{-1} and losses related

Loss rate	Description
τ_{mat}^{-1}	Losses by intrinsic material absorption
τ_{scatt}^{-1}	Scattering losses due to material imperfections
τ_{surf}^{-1}	Absorption at the resonator surface
τ_{WGM}^{-1}	Whispering gallery losses (tunneling losses)
τ_{ext}^{-1}	Coupling losses (eg. into tapered fiber)
τ_0^{-1}	Sum of the intrinsic cavity loss rates

Table 1.1: Different loss mechanisms in a microcavity

to coupling of the resonator to an external light field τ_{ext}^{-1} in a waveguide. The relative values of τ_0^{-1} and τ_{ext}^{-1} are important for power enhancement within the microresonator. To calculate the coupling from a waveguide to a resonator, we use the approach of H. Haus [53] with the following rate equation for the normalized amplitude of the mode within the cavity $a(t)$ (without taking the modes spatial profile into account)

$$\dot{a}(t) = \left(i \cdot \Delta - \frac{1}{2\tau} \right) a(t) + \frac{s_{\text{in}}}{\sqrt{\tau_{\text{ext}}}} \quad . \tag{1.12}$$

Here, $a(t)$ is normalized such that $|a(t)|^2$ corresponds to the stored energy within the resonator, $|s_{\text{in}}|^2 = P_{\text{in}}$ is the launched power in the waveguide and $\Delta = 2\pi(\nu_l - \nu_c)$ is the detuning between laser frequency ν_l and resonance frequency ν_c. In the steady state $\dot{a}(t) = 0$ we get

$$|a(t)|^2 = \frac{1}{\Delta^2 + \left(\frac{1}{2\tau} \right)^2} \cdot \frac{P_{\text{in}}}{\tau_{\text{ext}}} \quad . \tag{1.13}$$

The circulating power P_{cav} within the resonator is given by the stored energy divided by the cavity roundtrip time $\tau_{\text{rt}} = \frac{1}{\Delta\nu_{\text{FSR}}}$ (with $\Delta\nu_{\text{FSR}}$ being the free spectral range of the resonator).

$$P_{\text{cav}} = \Delta\nu_{\text{FSR}} \cdot |a(t)|^2 = \Delta\nu_{\text{FSR}} \cdot \frac{4\tau^2}{\tau_{\text{ext}}} \cdot \frac{1}{1 + 4\tau^2\Delta^2} \cdot \frac{P_{\text{in}}}{\tau_{\text{ext}}} \tag{1.14}$$

As a function of the cavity linewidth $\Delta\nu = 2\pi\tau$ and the finesse $\mathcal{F}$, the circulating power in the cavity equates to

$$P_{\text{cav}} = \frac{\mathcal{F}}{\pi} \cdot \frac{\tau_0}{\tau_0 + \tau_{\text{ext}}} \cdot \frac{1}{1 + 4\left(\frac{\nu_l - \nu_c}{\Delta\nu} \right)^2} \cdot P_{\text{in}} \quad . \tag{1.15}$$

The second term in equation 1.15 defines different coupling regimes depending on whether the intrinsic cavity loss rate is higher or lower compared to the outcoupling rate. The different regimes are generally referred to as

- **Undercoupled** ($\tau_{\text{ext}}^{-1} < \tau_0^{-1}$): In this regime the cavity coupling rate τ_{ext}^{-1} is smaller than the intrinsic cavity loss rate τ_0^{-1}. The field transmitted through the external waveguide is higher than the field coupled from the resonator to the waveguide. The phase shift of the field leaking out of the cavity is less than 180°. This regime can experimentally reached by increasing the coupling gap between waveguide and resonator.

- **Critically coupled** ($\tau_{\text{ext}}^{-1} = \tau_0^{-1}$): In the case of critical coupling, the coupling rate τ_{ext}^{-1} is equal to the the intrinsic cavity loss rate τ_0^{-1}. On resonance $\Delta\omega = 0$, the field that leaks out of the cavity and the field in the waveguide are 180° out of phase, leading to destructive interference.

- **Overcoupled** ($\tau_{\text{ext}}^{-1} > \tau_0^{-1}$): Here, the cavity coupling rate τ_{ext}^{-1} is larger than the intrinsic cavity loss rate τ_0^{-1}. Most of the power couples directly into the cavity, leading to a cavity leakage field that is higher than the field transmitted through the waveguide. The phase shift of the cavity leakage field is more than 180°. This regime can be experimentally reached by reducing the coupling gap between waveguide and resonator.

Experimentally, the coupling regime can be controlled by fine tuning of the position of the tapered optical fiber with respect to the microresonator. The ability to optimize the in- and outcoupling from and to the tapered optical fiber is an important precondition for broadband optical frequency comb generation. Note that the best coupling condition is not necessarily the critical coupling point for the seed laser, since the outcoupling of the comb modes back into the tapered fiber has to be optimized as well. In case of critical coupling ($\tau_{\text{ext}} = \tau_0$) and on resonance ($\nu_l = \nu_c$) the power enhancement of a resonator with optical finesse $\mathcal{F}$ is given as

$$P_{\text{cav}} = P_{\text{in}} \cdot \frac{\mathcal{F}}{2\pi} \quad . \tag{1.16}$$

1.5   Theoretical description of four-wave induced comb generation

Conventional frequency comb generators are typically based on mode locked lasers, which can be described in time domain. An excellent introduction to optical frequency comb generation has been written by Steven Cundiff and Jun Ye in reference [67]. This section focuses on a novel frequency comb generation scheme via nonlinear four-wave mixing and introduces the theoretical framework of this nonlinear optical effect in microresonators. First nonlinear optical effects have been studied already shortly after the construction of the first laser by Theodore Maiman in 1960 [68]. In classical optics light cannot directly interact with light and the frequency of a light wave is not influenced by other light beams. However, the interaction between a light wave and bound electrons in a nonlinear optical
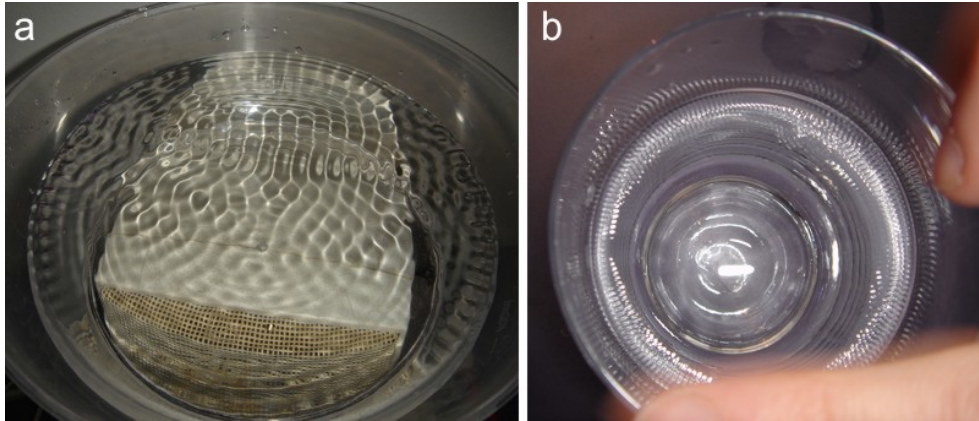
Figure 1.7: Standing "Faraday waves" in water. Panel a shows a standing wave pattern in a water bowl excited by a loudspeaker. The frequency of the standing waves corresponds to twice the frequency of the signal that is applied to the loudspeaker (60 Hz). Panel b shows the same phenomenon in a "singing" water glass, excited by a wet finger that is moved around the rim of the glass.

medium enables the generation of light at new frequencies. The first observed nonlinear optical effect was the generation of light at doubled frequency in a quartz plate, which has been observed by Franken and coworkers in 1961 [69]. Nonlinear optical effects can be subdivided in effects with energy transfer to the medium such as Raman scattering and effects without energy transfer to the nonlinear optical medium such as frequency doubling. The later ones can be referred to as pure frequency mixing effects and have in common that the total *optical* energy is conserved.

One class of nonlinear frequency conversion effects is strongly related to the so-called *parametric* oscillator, which is an harmonic oscillator with periodically changing parameters. A well known example for parametric oscillations is a child on a swing that periodically changes its center of gravity by moving the legs for and back. Scientifically, parametric oscillations have first been described by Michael Faraday in 1831 in an article called "On a Peculiar Class of Acoustical Figures; and on Certain Forms Assumed by Groups of Particles upon Vibrating Elastic Surfaces", where he explains the formation of ripple waves in a water that are excited by a periodic perturbation at twice the frequency (cf. figure 1.7). The optical analogon of parametric oscillations has been observed by Giordmaine and Miller in the Bell laboratories in 1965 for the first time [70]. These optic parametric oscillations (OPO) can be described as energy conserving annihilation and generation of photons obeying

$$\omega_p = \omega_s + \omega_i \quad . \tag{1.17}$$

Here, $\omega_{\{p,s,i\}}$ denote the angular frequencies of the interacting electromagnetic waves (the different waves are referred to as pump, signal and idler wave, indicated by the indices). While optical parametric oscillations typically refer to interaction of 3 waves (or photons), the interaction of 4 waves is referred to as hyperparametric oscillations [71] or four-wave

mixing. This effect has been first studied at high power in optical fibers in the pioneering work of Stolen and Bjorkholm [72–74]. The energy conserving nature of four-wave mixing leads to the following relation between the frequencies of the waves:

$$\omega_{p1} + \omega_{p2} = \omega_s + \omega_i \quad . \tag{1.18}$$

A special case is the degenerate four-wave mixing in which the two pump waves have equal frequencies $\omega_{p1} = \omega_{p2}$.

In general, nonlinear optical effects can be described by the response of the nonlinear medium to an electromagnetic wave, which can be expressed by the dielectric polarization $\vec{P}(\vec{E})$. The dielectric polarization can be expanded in a power series of the electrical field [75]

$$\vec{P}(\vec{E}) = \epsilon_0 \chi \vec{E} + \epsilon_0 \chi^{(2)} \vec{E}\vec{E} + \epsilon_0 \chi^{(3)} \vec{E}\vec{E}\vec{E} + ... \tag{1.19}$$

with the electric field vector $\vec{E}$, the vacuum permittivity ϵ_0 and the n-th order electrical susceptibility $\chi^{(n)}$ (being a tensor of rank $n + 1$ in the most general case). Because of inversion symmetry in silica, the second order nonlinearity term $\chi^{(2)}$ vanishes such that the dielectric polarization for four-wave mixing can be approximated as

$$\vec{P}(\vec{E}) = \epsilon_0 \chi \vec{E} + \epsilon_0 \chi^{(3)} \vec{E}\vec{E}\vec{E} \tag{1.20}$$

The last term on the right hand side of equation 1.20 can be defined as the nonlinear polarization $\vec{P}_{NL}$. Using Maxwell's equations we can derive the wave equation with the nonlinear polarization as driving term

$$\nabla^2 \vec{E} - \frac{n^2}{c_0^2}\frac{\partial^2}{\partial t^2}\vec{E} = -\mu_0 \frac{\partial^2}{\partial t^2}\vec{P}_{NL} \quad , \tag{1.21}$$

with the nonlinear part of the polarization $\vec{P}_{NL} = \epsilon_0 \chi^{(3)} \vec{E}\vec{E}\vec{E}$, the speed of light in vacuum c_0, the refractive index of the medium n and the permeability of free space μ_0. The electrical field can be split into four waves at frequencies ω_ℓ. For calculation of four-wave mixing in an axisymmetric microresonator it is moreover convenient to use a cylindrical coordinate system with the coordinates r, φ and z. Thus, the electrical field of *one* of the contributing waves is given as

$$E_\ell(r, \varphi, z, t) = \frac{1}{2}A_\ell(t) \cdot \tilde{E}_\ell(r, z) \cdot e^{i(\beta_r r + \beta_\varphi \varphi + \beta_z z - \omega_\ell t)} + c.c. \tag{1.22}$$

with $(\beta_r, \beta_\varphi, \beta_z)$ being the wave vector, $A_\ell(t)$ representing the time dependence of the electrical field amplitude and *c.c.* standing for the complex conjugated term. The periodic boundary condition of a microresonator $E(\varphi) = E(\varphi + 2\pi)$ leads to the constraint that β_φ has to be an integer number (this integer number corresponds to the angular mode number ℓ of the cavity mode). Moreover we assume that the modes of interest are fundamental whispering gallery modes with $\beta_r = \beta_z = 0$, which simplifies the electrical field to

$$E_\ell(r, \varphi, z, t) = \frac{1}{2} A_\ell(t) \cdot \tilde{E}_\ell(r, z) \cdot e^{i(\ell\varphi - \omega_\ell t)} + c.c. \tag{1.23}$$

Inserting the total electric field $E = \sum_\ell E_\ell$ into the wave equation 1.21 yields

$$-\mu_0 \frac{\partial^2 P_{NL}}{\partial t^2} = \sum_\ell A_\ell(t) \cdot \overbrace{\left(\nabla^2 - \frac{n^2}{c_0^2} \frac{\partial^2}{\partial t^2}\right) \tilde{E}_\ell(r, z) \cdot e^{i\ell\varphi - i\omega_\ell t}}^{=0}$$

$$- \sum_\ell \tilde{E}_\ell(r, z) \cdot e^{i\ell\varphi - i\omega_\ell t} \cdot \left(\frac{n^2}{c_0^2} \frac{\partial^2 A_\ell(t)}{\partial t^2} + 2i\omega_\ell \frac{n^2}{c_0^2} \frac{\partial A_\ell(t)}{\partial t}\right) \quad . \tag{1.24}$$

The first sum on the right hand side of the equation corresponds to the homogeneous part of the differential equation. This part of the equation vanishes since it is assumed that $\tilde{E}_\ell(r, z) \cdot e^{i\ell\varphi - i\omega_\ell t}$ are eigenmodes of the resonator. Moreover we can assume that the modal amplitudes evolve at much slower time scales than the period time of the carrier wave, which is commonly referred to as the "slowly varying envelope approximation":

$$\left|\frac{\partial^2 A_\ell(t)}{\partial t^2}\right| \ll \left|2i\omega_\ell \frac{\partial A_\ell(t)}{\partial t}\right| \quad . \tag{1.25}$$

With the slowly varying envelope approximation equation 1.24 can be written as

$$\sum_\ell \tilde{E}_\ell(r, z) e^{i\ell\varphi - i\omega_\ell t} \cdot \left(2i\omega_\ell \frac{n^2}{c_0^2} \frac{\partial A_\ell(t)}{\partial t}\right) = \mu_0 \frac{\partial^2 P_{NL}}{\partial t^2} \quad . \tag{1.26}$$

Now, we can express the nonlinear dielectric polarization P_{NL} as a function of the electric field of four modes with mode numbers $\ell_{1,2,3,4}$

$$P_{NL} = \epsilon_0 \chi^{(3)} E^3 = \epsilon_0 \chi^{(3)} \left(\sum_{\ell=\ell_1}^{\ell_4} E_\ell\right)^3 \quad . \tag{1.27}$$

This is cumbersome because P_{NL} consists of 120 terms describing all possible interactions between the different modes in a $\chi^{(3)}$-material. However, equation 1.26 contains the *combined* evolution of the modes and we can further simplify it by projection onto a single mode of interest (eg. the mode with $\ell = \ell_\alpha$). This can be done by multiplying equation 1.26 with $\tilde{E}_\alpha^*(r, z) \cdot e^{i\omega_\alpha t}$ and spatially integrating the equation (Hermitian inner product). Following this approach yields the coupled rate equations for the interacting modes [76] (here, the time dependent amplitude $A_\ell(t)$ has been normalized to $\mathcal{A}_\ell$ such that the photon number in the respective mode is given by $|\mathcal{A}_\ell|^2$):

$$\frac{\mathrm{d}}{\mathrm{d}t}\mathcal{A}_\alpha = -\eta_1 \cdot \mathcal{A}_\alpha - i \cdot \eta_2 \sum_{\beta,\gamma,\delta=1}^{4} \Lambda_\alpha^{\beta\gamma\delta} \cdot \mathcal{A}_\beta \mathcal{A}_\gamma^* \mathcal{A}_\delta \cdot \mathrm{e}^{-i\cdot\Delta\omega_1\cdot t}\mathrm{e}^{i\cdot\Delta\ell_1\cdot\varphi}$$

$$- i \cdot \eta_2 \sum_{\beta,\gamma,\delta=1}^{4} \Lambda_\alpha^{\beta\gamma\delta} \cdot \mathcal{A}_\beta \mathcal{A}_\gamma \mathcal{A}_\delta \cdot \mathrm{e}^{-i\cdot\Delta\omega_2\cdot t}\mathrm{e}^{i\cdot\Delta\ell_2\cdot\varphi} + \eta_3 \cdot P_{\mathrm{in}} \cdot \mathrm{e}^{-i(\Omega_0-\omega_\alpha)t} \quad (1.28)$$

The first term on the right hand side of equation 1.28 takes into account the intrinsic cavity losses as well as outcoupling losses, while the last term corresponds to the pump laser (power P_{in}) at a frequency of Ω_0 and can be neglected for other modes than the pump mode in a high-Q resonator (the constants η_1 and η_3 take into account the cavity loss rate and build-up factor respectively). Important for the nonlinear wave mixing are the second and third term in equation 1.28. The constant η_2 represents the gain coefficient for the parametric interaction [17, 76–79] and is given by

$$\eta_2 = \frac{n_2}{n_0^2} \cdot \frac{\hbar\Omega_0^2 \cdot c}{V_0} \qquad (1.29)$$

with the refractive index n_0, the nonlinear refractive index n_2 and the effective mode volume V_0. An additional constant $\Lambda_\alpha^{\beta\gamma\delta}$ describes the coupling between the different modes and depends on the geometric dispersion of the cavity (cf. chapter 4). The newly introduced variables $\Delta\omega_{1,2}$ and $\Delta\ell_{1,2}$ are defined as

$$\Delta\omega_1 = \omega_\beta - \omega_\gamma + \omega_\delta - \omega_\alpha \qquad (1.30)$$

$$\Delta\omega_2 = \omega_\beta + \omega_\gamma + \omega_\delta - \omega_\alpha \qquad (1.31)$$

$$\Delta\ell_1 = \ell_\beta - \ell_\gamma + \ell_\delta - \ell_\alpha \qquad (1.32)$$

$$\Delta\ell_2 = \ell_\beta + \ell_\gamma + \ell_\delta - \ell_\alpha \quad . \qquad (1.33)$$

An efficient nonlinear coupling between the different modes is just possible if either $\Delta\omega_1$ and $\Delta\ell_1$ are zero for the second term in equation 1.28 or $\Delta\omega_2$ and $\Delta\ell_2$ are zero for the third term, which can be interpreted as energy and momentum conservation. The third term in equation 1.28 corresponds to "third harmonic"-like four-wave mixing with a generated wave at a frequency $\omega_\alpha = \omega_\beta + \omega_\gamma + \omega_\delta$ (third harmonic generation is a special case with $\omega_\beta = \omega_\gamma = \omega_\delta$). Typically the "third harmonic"-like terms are neglected because the generated wave at ω_α is not resonant in the cavity. However, in fused silica microtoroids these kind of interactions can still be observed as shown in appendix A. Especially pumping in the infrared around 1550 nm leads to generation of colorful spectra in the visible in microtoroids (shown in figure A.6). However, the most important term for optical frequency comb generation in microresonators is the second term of equation 1.28. The sum in this term

$$\sum_{\beta,\gamma,\delta=1}^{4} \Lambda_\alpha^{\beta\gamma\delta} \cdot \mathcal{A}_\beta \mathcal{A}_\gamma^* \mathcal{A}_\delta \cdot \mathrm{e}^{-i\cdot\Delta\omega_1\cdot t}\mathrm{e}^{i\cdot\Delta\ell_1\cdot\varphi} \qquad (1.34)$$

can be subdivided in terms containing $|A_\alpha|^2 \cdot A_\alpha$ which are referred to as *self-phase modulation* and terms containing $|A_x|^2 \cdot A_\alpha$ (with $x \neq \alpha$), which correspond to *cross-phase modulation*. All other terms lead to the generation of new frequencies at $\omega_\alpha = \omega_\beta - \omega_\gamma + \omega_\delta$. Another distinction can be made between so called degenerate and non-degenerate four-wave mixing. Degenerate four-wave mixing is the case in which $\omega_\beta = \omega_\delta$ and the amplitude of the third wave is zero at a certain time t_0 ($\mathcal{A}_\gamma(t_0) = 0$). Quantum fluctuations of the modes at frequencies ω_α and ω_γ can then lead to the generation of symmetric sidebands around the mode at $\omega_\beta = \omega_\delta$ (typically referred to as pump mode). Non-degenerate four-wave mixing on the other hand is the more general case when $\omega_\alpha \neq \omega_\beta \neq \omega_\gamma \neq \omega_\delta$. Pumping a microresonator with one continuous wave laser initially leads to degenerate four-wave mixing as a result of the absence of waves at different frequencies. In a photon picture this corresponds to the energy conserving conversion of 2 pump photons ω_p into one signal ω_s and one idler ω_i photon:

$$2\omega_p = \omega_s + \omega_i \tag{1.35}$$

Typically, the generated photon with lower energy/frequency is called idler and the other one signal. Both signal and idler are equidistantly spaced with respect to the pump laser ($\omega_p - \omega_i = \omega_s - \omega_p$). Degenerate four-wave mixing and first evidence for non-degenerate four-wave mixing in microresonators has been observed in 2004 in the group of Kerry Vahala (microtoroids [16]) and the group of Lute Maleki (crystalline microresonators [17]). Once three optical waves are present in a microresonator non-degenerate four-wave mixing can occur.

Figure 1.8 shows all four-wave mixing process that take place in the presence of three optical modes with frequencies f_1, f_2 and f_3 (dashed lines in the figure). Moreover, it is assumed that the modal coupling parameter $\Lambda_\alpha^{\beta\gamma\delta}$ is constant for the interacting modes and that the resonator dispersion is negligible compared to the optical linewidth of the modes. The four-wave mixing process generates light at frequencies $f_{ijk} = f_i + f_j - f_k$ with ($i, j, k = 1..3$, $i, j \neq k$). Obviously, some frequencies can be generated in different ways, for example $f_{321} = f_{231}$. Strongly cascaded four-wave mixing with many interacting modes has been first observed in 2006 in microresonators with high quality factors and low dispersion [3].

The threshold for degenerate four-wave mixing can be determined from the simplified coupled wave equations for four-wave mixing with one pump wave and one pair of signal/idler sidebands. In the steady state with $\frac{\mathrm{d}A}{\mathrm{d}t} = 0$ the threshold power P_{thresh}^{4WM} can be derived by solving equation 1.28 (the detailed calculation is shown in appendix G) and yields [16, 80]:

$$P_{\text{thresh}}^{4WM} = \left[\frac{\Delta\omega^2}{4} + \left(\frac{\pi\nu_L}{Q} \right)^2 \right] \cdot \frac{4\pi^2 \cdot n_0^2 \cdot V_0}{\Delta\omega \cdot n_2 \cdot \eta_{\text{ext}} \cdot c \cdot Q} \tag{1.36}$$

Here, ν_L is the laser frequency, Q the resonators quality factor, $\Delta\omega = 2\omega_p - \omega_s - \omega_i$ corresponds to the cavity dispersion, V_0 is the effective mode volume, n_0 and n_2 are the linear and nonlinear refractive indices and η_{ext} takes into account the total coupling efficiency.
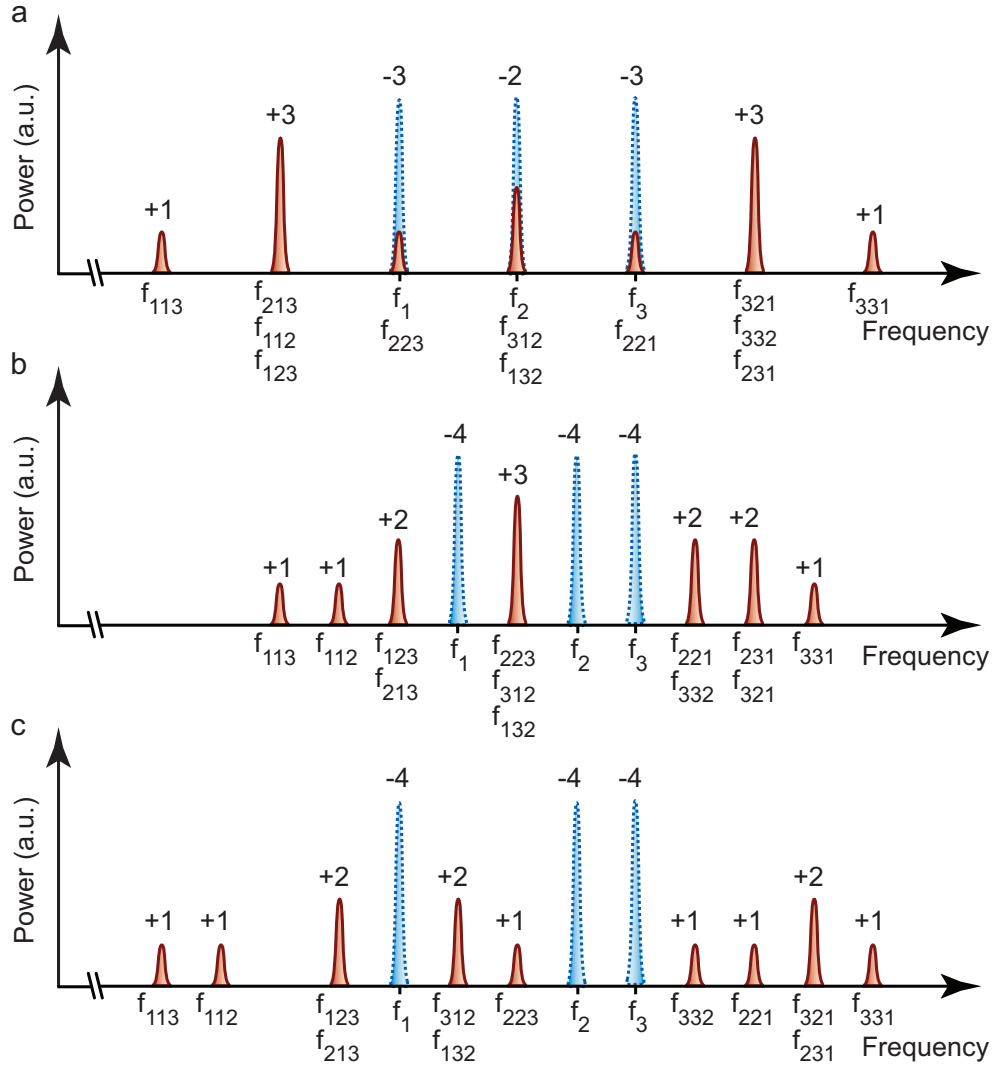
Figure 1.8: Generation of optical sidebands via four-wave mixing. The dashed lines depict the initial modes with three waves at frequencies of f_1, f_2 and f_3. The generated modes (solid lines) are located at frequencies $f_{ijk} = f_i + f_j - f_k$ with $(i, j \neq k)$. The cases of $i = k$ and $j = k$ can be neglected since the generated waves would be located at the same frequencies as the original waves. This leads to a total of 12 possible four-wave mixing processes. Panel a shows three primary waves with equal frequency spacing, leading to the generation of four new frequencies. Panel b and c show four-wave mixing of three modes with $f_2 - f_1 = 2 \cdot (f_3 - f_2)$ and $f_2 - f_1 = 3 \cdot (f_3 - f_2)$, which is leading to the generation of 7 and 9 modes respectively (with some modes at degenerate frequencies). The numbers above the respective modes in the figure correspond to the number of generated/annihilated photons assuming that all different four-wave mixing processes take place with the same probability.
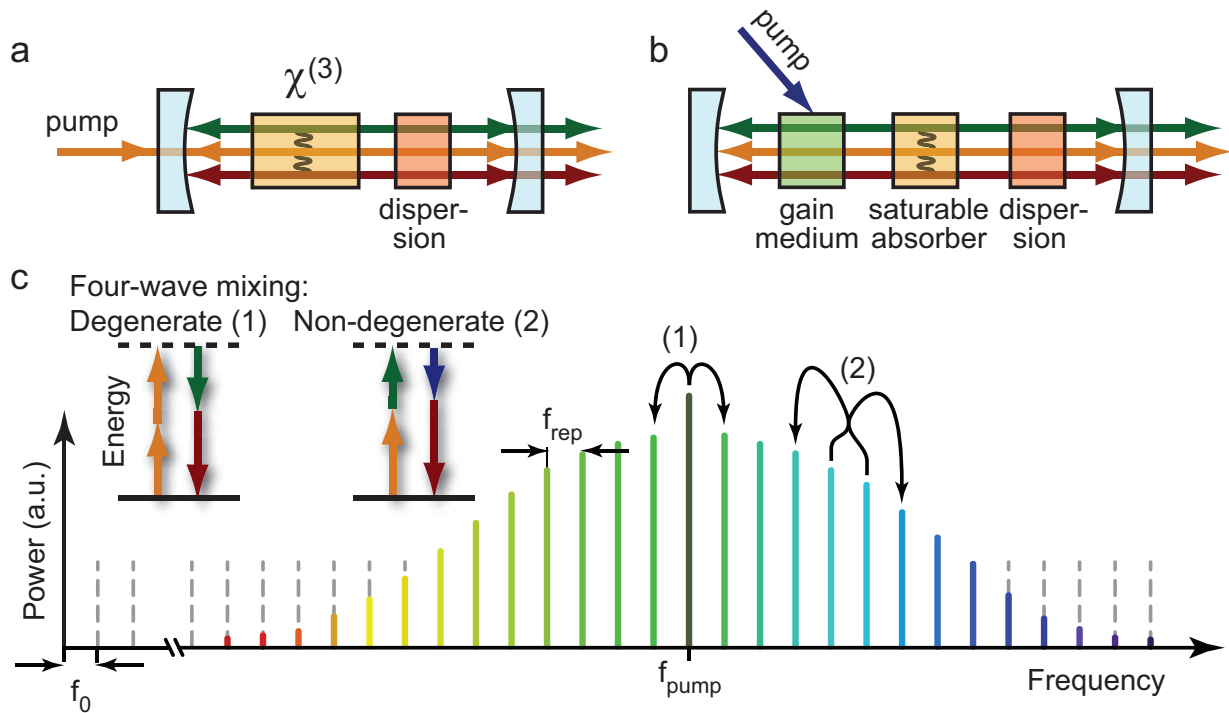
Figure 1.9: Comparison of conventional frequency comb generators and microresonator-based comb generation. Panel a illustrates frequency comb generation in a microresonator, which is governed by a nonlinear χ^3-medium and can be described in frequency domain. In contrast, conventional frequency comb generation in mode locked lasers requires a gain medium and a saturable absorber within the resonator as shown in panel b. A main difference between the comb generators is that the pump laser constitutes one of the comb modes in microresonators. Panel c depicts the principle of degenerate and non-degenerate four-wave mixing.

Figure 1.9 shows a comparison of conventional frequency comb generators and microresonators. The main difference is the absence of a gain medium in microresonator-based frequency comb generators. As a result of the four-wave mixing induced comb generation, the pump laser itself is part of the frequency comb in microresonators. This feature provides an additional possibility to *directly* control the comb spectra via the pump laser frequency as shown in chapter 3. In addition to the gain medium, conventional frequency comb generators require a saturable absorber in order to lock the phases of the oscillating modes. This (passive) mode-locking mechanism is mostly described in time domain and the saturable absorber ensures that weak signals are suppressed while signals with high power are amplified by the gain medium in the resonator [81–84]. Both comb generators have in common that the comb generation process is influenced by resonator dispersion as shown in figure 1.9a,b. Mode locked lasers can be described by the Hermann A. Haus master equation [83, 85, 86]. This equation determines the evolution of the complex amplitude $A(t)$ of a pulse within a resonator (with the time t being normalized such that a pulse passes the cavity once per $\Delta t = 1$).

$$\left(-(l + i \cdot x) + g\left(1 + \frac{1}{\Omega_g^2} \cdot \frac{\mathrm{d}}{\mathrm{d}t^2}\right) + i \cdot D\frac{\mathrm{d}}{\mathrm{d}t^2} + (\gamma - i\delta)|A(t)|^2\right) A(t) = 0 \qquad (1.37)$$

Here, l and x describe resonator losses and phase shift, g is the gain parameter with a parabolic gain bandwidths of Ω_g, D is the dispersion parameter, the term $\gamma \cdot |A(t)|^2 \cdot A(t)$ takes into account the saturable absorber and $-i\delta \cdot |A(t)|^2 \cdot A(t)$ represents the self-phase modulation. Up to now it is not clear whether the comb generation process in microresonators can be described in time domain by a mode-locking mechanism. One possibility of mode locking in microresonators could be a self-focusing and soliton generation effects in the resonator material that lead to the formation of pulses. Auto- and cross-correlation experiments shown in appendix E indicate that the comb lines in microresonators have a fixed phase relationship (which can be derived from cross-correlation traces, which are not changing within time scales of several minutes). However, according to Matsko et al. [80] there exist regimes for both phase and amplitude modulation for microresonator-based four-wave mixing processes. A detailed time domain description of frequency comb generation in microresonators is among the most interesting questions for future research.

1.6 Experimentally observed frequency combs

During the course of this thesis, different resonator geometries and materials have been tested for optical frequency comb generation. Figure 1.10 shows examples of recorded frequency comb spectra in fused silica microtoroids with different sizes and at different pump powers. The envelope of the generated combs is determined mainly by the resonator mode spectrum (dispersion) as well as interactions between different mode families as shown in chapter 4. However, also absorption bands of hydroxyl bonds (OH) in fused silica, which are located in the infrared around 1360 nm and beyond 2 μm [45] can influence the comb
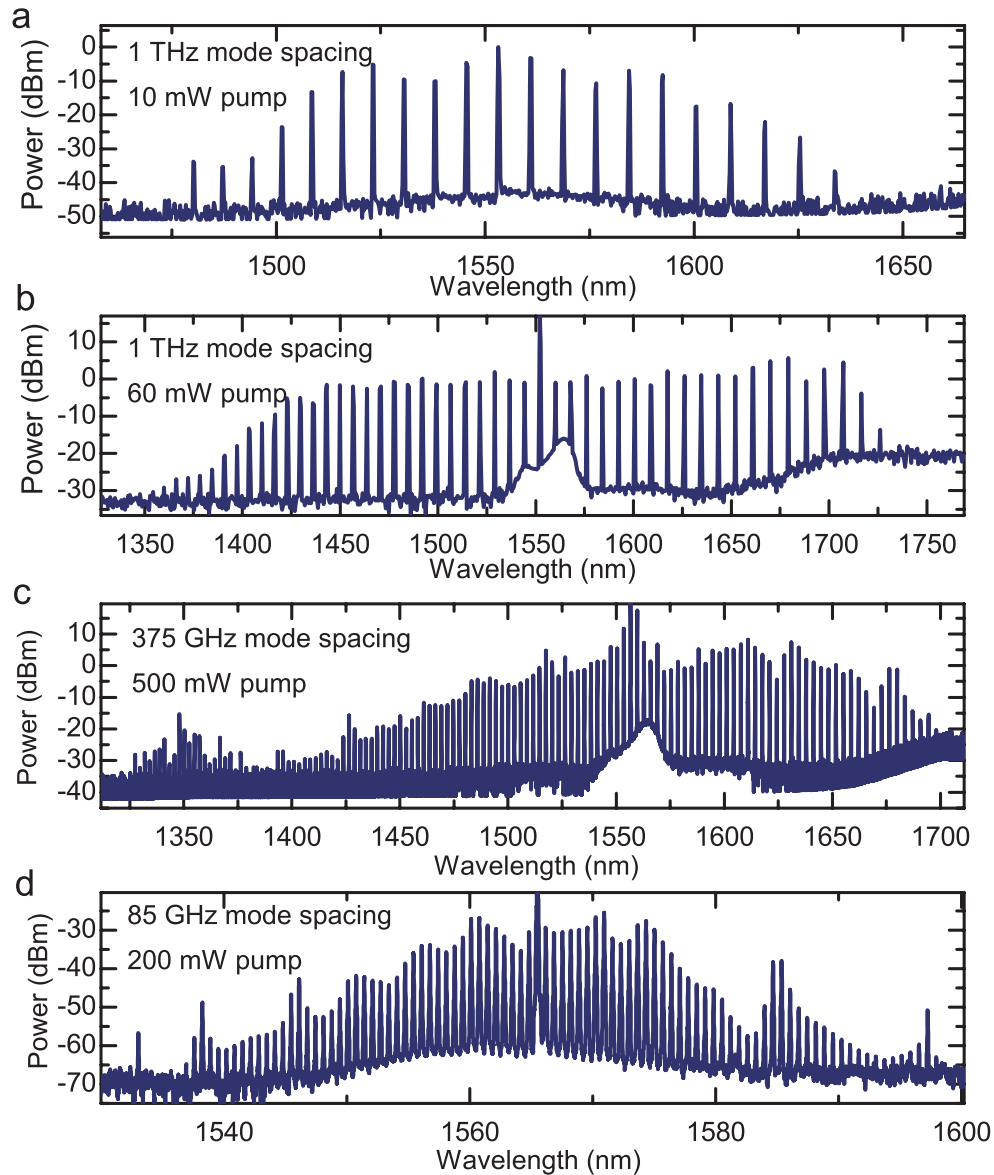
Figure 1.10: Frequency comb spectra generated in fused silica microtoroids. Panel a-d show different comb generation in resonators of different sizes with mode spacings between 1 THz and 85 GHz. The diameters of the employed resonators are 66 μm in panel a and b, 177 μm in panel c and 780 μm in panel d. The corresponding setup for the comb generation is shown in figure 1.4.
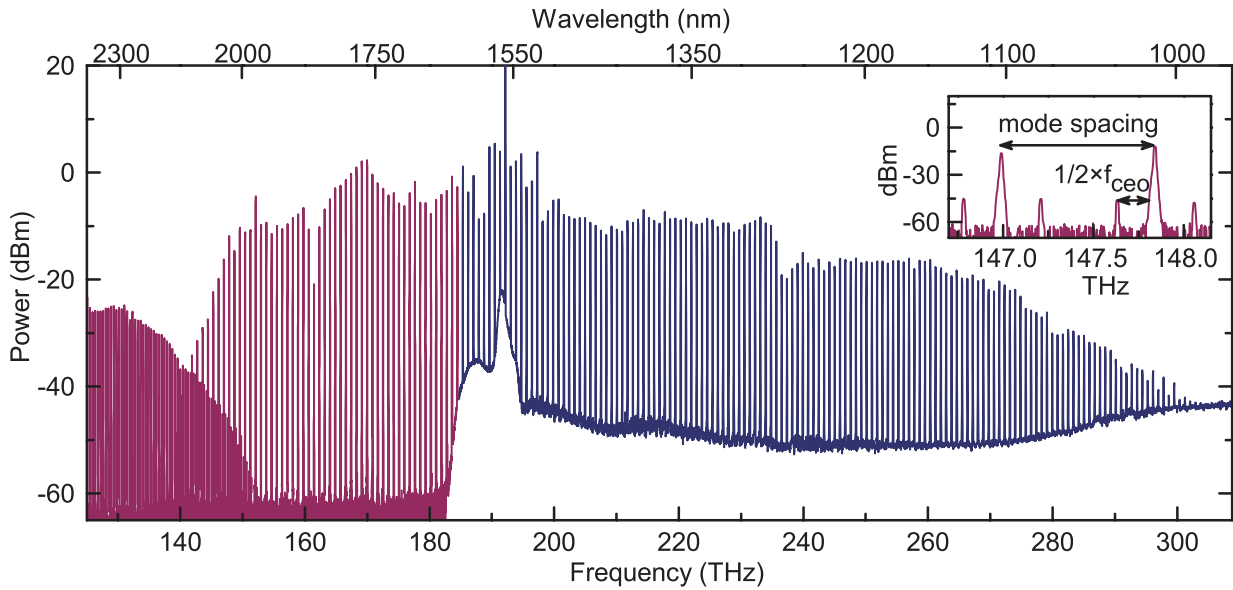
Figure 1.11: Octave spanning frequency comb generation in a 80-μm-diameter micro-toroid. The denser lines on the low frequency side are a replica of the high frequency end of the spectrum at half the frequency due to the grating spectrometer's second order diffraction. This artefact allows determining the approximate magnitude of the carrier envelope offset frequency directly from the optical spectrum as shown in the inset [7].

generation process by modifying the optical linewidth of microresonators modes. Another process that influences the comb structure is stimulated Raman scattering with a maximum gain at -12 THz (in fused silica) with respect to the pump laser [18–20, 23, 41, 52, 87].

Comb generation at even higher power levels in high-Q-resonators with optimized dispersion can even lead to generation of more than octave-spanning comb spectra show in figure 1.11. Octave spanning frequency combs are of special interest with regard to direct measurement and stabilization of the comb's offset frequency [67, 88]. As stated before, optical frequency combs generated via four-wave mixing obey momentum and energy conservation as well as *photon number* conservation (neglecting the "third-harmonic"-type four-wave mixing). The latter two conserved quantities can be interpreted as a conservation of the "centre of mass" of the measured comb spectra, which constantly stays at the pump laser frequency ω_p,

$$\sum_j \omega_j \cdot \frac{n_j}{N} = \omega_p \quad , \tag{1.38}$$

where ω_j and n_j are the frequencies and photon numbers in the jth comb mode, and N being the total number of photons in the cavity ($N = \sum_j n_j$). This conservation of the "centre of mass" is reflected in the envelope of the frequency comb in figure 1.11, showing an asymmetric comb around the pump laser, with higher power per comb mode but less lines on the low frequency side with respect to the pump laser. The "centre of mass" of
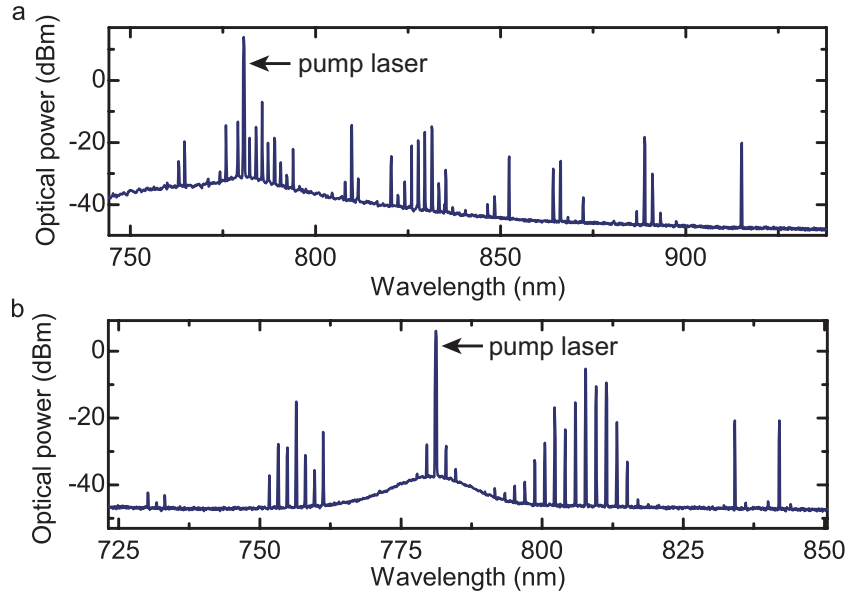
Figure 1.12: Nonlinear interactions in a fused silica microtoroid pumped with a 150 mW laser at 780 nm. The observed nonlinear processes are dominated by Raman with additional Stokes-anti-Stokes-coupling which can be seen in panel b. A few pure four-wave mixing sidebands can also be seen around the pump laser wavelength.

the measured spectrum is shifted by only 220 GHz from the pump laser towards lower frequencies, indicating that to a very good approximation the comb is generated in a pure four-wave mixing process, even though wavelength dependent losses, Raman scattering (which would amplify the red portion of the spectrum) and coupling to the tapered optical fiber have not been taken into account.

1.7   Nonlinear interactions in the normal dispersion regime

The previously shown frequency combs are generated in the anomalous dispersion regime or close to the zero dispersion point of fused silica microresonators (a detailed discussion about microresonator dispersion is presented in chapter 4). Frequency combs in microresonators could be explained in time domain by soliton formation in the anomalous dispersion regime. Thus, it is of interest to know whether combs can be generated by four-wave mixing in the normal dispersion regime as well. The zero dispersion point of fused silica microresonators can be shifted by varying the geometry of the resonator. However, the zero dispersion point can just be shifted towards higher wavelengths compared to the zero dispersion point in bulk fused silica ($\approx$ 1300 nm) as shown in chapter 4, figure 4.11.

Figure 1.12 shows nonlinear processes in a microtoroid pumped by a 780-nm-laser in the normal dispersion regime. In this regime Raman scattering dominated the nonlinear
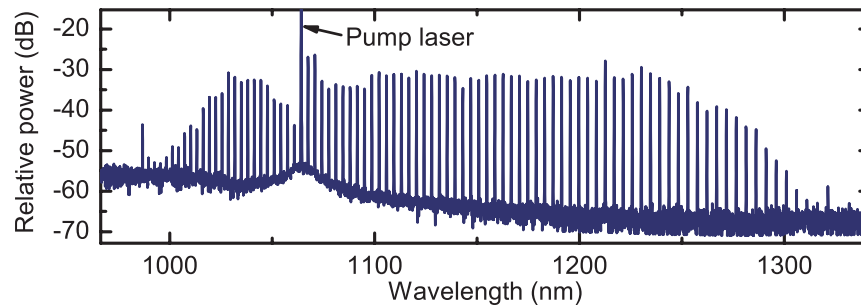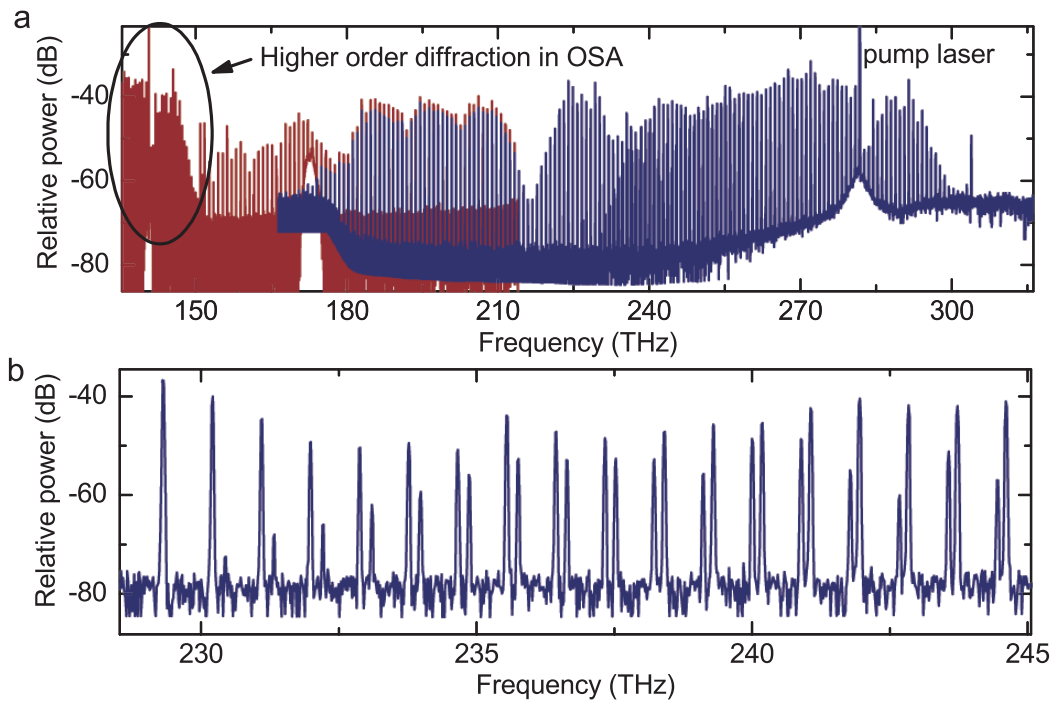
Figure 1.13: Comb generation in the normal dispersion regime with an Ytterbium fiber laser at a pump wavelength of 1064 nm and a launched power of ≈ 500 mW. The generated comb spans 300 nm and extends mostly to longer wavelengths. This indicates that stimulated Raman scattering is involved in the comb generation process.

interactions in conjunction with Stokes-anti-Stokes scattering induced by four-wave mixing. However, it has not been possible to generate continuous frequency combs in this wavelength regime, which indicates that some kind of soliton formation process is required for four-wave mixing based comb generation.

Additional experiments have been carried out with an Ytterbium fiber laser at a wavelength of 1064 nm. Here it has been possible to generate several hundred nanometer spanning combs as shown in figure 1.13 and 1.14. The pump wavelength is still in the normal dispersion regime and the generated frequency combs extend more to higher wavelengths than to shorter wavelength. This indicates that stimulated Raman scattering is involved in the comb generation process. The spectrum shown in figure 1.14 even spans more than an octave at a launched pump power of 700 mW. However, the zoom into the optical spectrum in panel b of this figure reveals, that two separate combs with different mode spacings are generated. This can be explained by strong Raman modes at lower frequencies, which can generate their "own" frequency comb. The different mode spacing can be attributed to the cavity dispersion leading to a different free spectral range around the Raman mode that is responsible for the second comb.

1.8 Four-wave mixing based comb generation in other systems

Microresonator-based frequency comb generation has been demonstrated in a variety of different materials and resonator types within the last three years. This section gives a brief overview and comparison of different frequency comb generators relying on four-wave mixing effects.

Figure 1.14: Comb generation in the normal dispersion regime with an Ytterbium fiber laser at a pump wavelength of 1064 nm and a launched power of ≈ 700 mW. The generated spectrum span more than an optical octave. The left hand side of the spectrum in panel a shows a copy of the high frequency end of the comb as a result of second order diffraction in the optical spectrum analyzer (OSA). Closer inspection of the spectrum in panel b reveals that it consists of two overlapping frequency combs with different mode spacing.
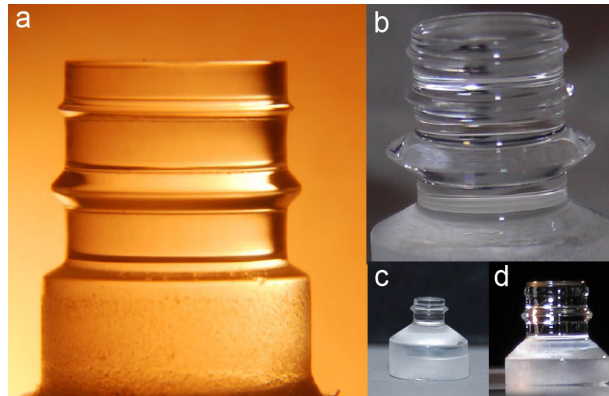
Figure 1.15: Polished calcium fluoride resonators for optical frequency comb generation. (from [91])

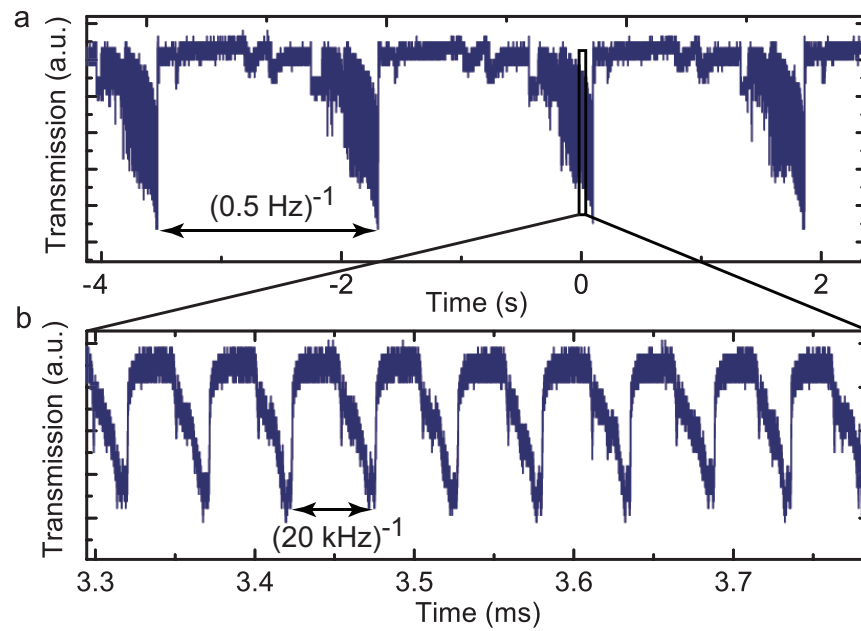### 1.8.1   Calcium fluoride resonators

Optical frequency comb generation in crystalline resonators has been demonstrated in 2008 for the first time in resonators made of calcium fluoride CaF_2 [89, 90]. These type of microresonators can be polished by hand from bulk CaF_2 rods using a turning lathe.

Figure 1.15 shows images of different calcium fluoride resonators. These resonators exhibit extraordinary high optical quality factors of $Q > 10^{10}$ [92, 93] as a result of the high transparency of the material. On the other hand, the mode volume and size of crystalline resonators is larger due to the turning process. Calcium fluoride is a brittle material and it is difficult to produce resonators with a diameter smaller than 1 mm. However, the larger mode volume can be compensated by the higher quality factor such that it is still possible to generate optical frequency comb via four-wave mixing.

A major drawback of calcium fluoride resonators for optical frequency comb generation are the thermal properties of the material. In general, resonance frequency shifts can be induced by three effects:

- Thermoelastic change of the resonator size

- Thermorefractive change of refractive index

- Kerr-nonlinearity induced change of the refractive index (at high intracavity power)

In case all these effects lead to a shift of the cavities resonance frequency in the same direction, this effect can be used to automatically lock the cavity mode to a pump laser. A detailed discussion of this phenomenon is given in chapter 3. Unfortunately the two thermal effects in calcium fluoride have opposite signs and in conjunction with the Kerr-nonlinearity this can lead to oscillatory instabilities of the resonance frequency [94, 95]. A measurement of these oscillations is shown in figure 1.16. Here, a calcium fluoride resonator is pumped with 500 mW at 1550 nm by a tapered optical fiber while simultaneously monitoring the transmission signal. Note that the pump laser frequency is *not* changed during the

Figure 1.16: Oscillatory instability of resonance frequencies in calcium fluoride. The vertical axis shows the transmission signal of a tapered fiber coupled calcium fluoride resonator pumped with 500 mW at 1550 nm (the pump laser frequency is not changed during the measurement). The graphs show that the cavity resonance is periodically sweeping across the pump laser frequency at characteristic oscillation frequencies of 0.5 Hz and 20 kHz. These oscillations in calcium fluoride originate from different signs of thermorefractive, thermoelastic and Kerr-nonlinearity induced resonance frequency shifts.
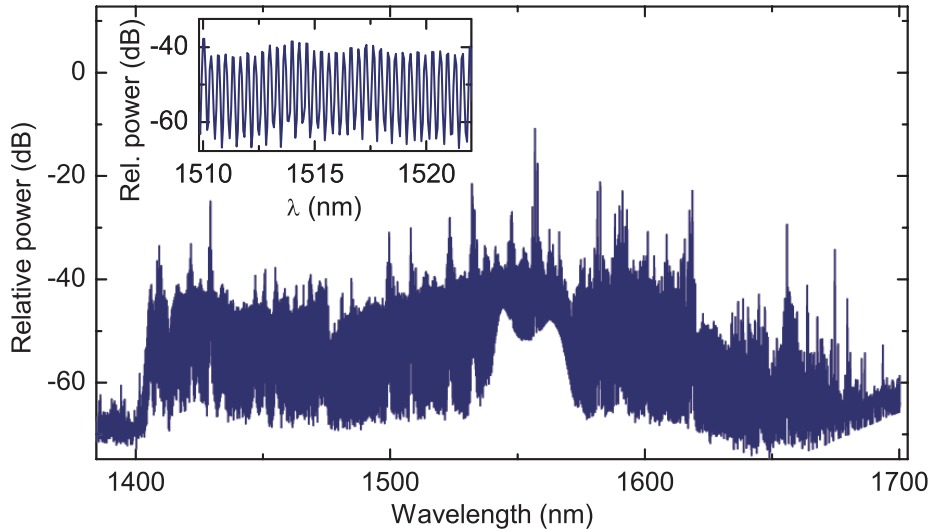
Figure 1.17: Spectrum of an optical frequency comb generated in a magnesium fluoride resonator. This comb is generated in a resonator with 43 GHz mode spacing, corresponding to a resonator diameter of 1.5 mm. It consists of more than 840 comb modes that can be resolved by zooming into the data, as shown in the inset. The launched pump power is in the order of 800 mW and the resonator's quality factor $Q \approx 2 \times 10^8$

measurement. However, the cavities resonance frequency is periodically sweeping through the pump laser frequency as a result of the oscillatory instability induced by the thermal effects and Kerr-nonlinearity. Two fundamental oscillation frequencies at 0.5 Hz and 20 kHz can be observed (The 20 kHz oscillations can be seen in panel b of figure 1.16, which is a zoom into the data shown in panel a). As a consequence of these oscillations it is difficult to generate stable frequency combs in calcium fluoride since an active locking scheme of the pump laser frequency to the cavity mode is required. Combs with bandwidths up to 35 THz around 1550 nm have been observed in CaF_2 resonators with mode spacings between 13 GHz and 200 GHz [89, 90, 96]. A spectrum of a calcium fluoride comb is show in figure 1.18.

1.8.2 Magnesium fluoride resonators

Crystalline resonators made of magnesium fluoride (MgF_2) can be produced similar to calcium fluoride resonators with a turning machine and manual polishing. MgF_2 is nearly as transparent as CaF_2 which allows for high optical quality factors. In addition, the thermoelastic and thermorefractive effect in magnesium fluoride has the same sign, enabling a thermal self-locking of the resonator mode to a pump laser, which is important for long-term stable comb generation. An corresponding optical comb spectrum is shown in figure 1.17. The comb is generated in a 1.5-mm-diameter resonator with a mode spacing of approximately 43 GHz and extends over nearly 300 nm.

	SiO_2 toroid	Si_3N_4	CaF_2	MgF_2	SiO_2 sphere
max. comb width (THz)	160	80	35	35	25
mode spacing (GHz)	80–1200	200–1200	13–200	43	265
refractive index n	1.44	1.98	1.43	1.37	1.44
n_2 (10^{-20} W/m^2)	2.2	25	1.9	0.9	2.2
Q factor	6×10^8	2×10^5	6×10^9	2×10^8	2×10^7
transparency (μm)	0.21–2.8	—	0.2–7.0	0.13–7.7	0.21–2.8
dL/dT (10^{-6}/K)	0.55	1.1, 2.1	18.9	9.4, 13.6	0.55
dn/dT (10^{-6}/K)	10.5	10	-11.5	1	10.5

Table 1.2: Comparison of different microresonator types for optical frequency comb generation. The first row shows the maximum reported comb width for the respective resonators. Other important parameters are the optical quality factor and the nonlinear refractive index n_2. The comparably small optical quality factor in silicon nitride (Si_3N_4) can be partly compensated by a one order of magnitude higher n_2 compared to other materials. Another interesting feature is the inverted thermorefractive constant dn/dT in CaF_2 compared to the thermal expansion coefficient dL/dT. The displayed values are compiled from different books and research articles [64, 89, 90, 99, 101, 102].
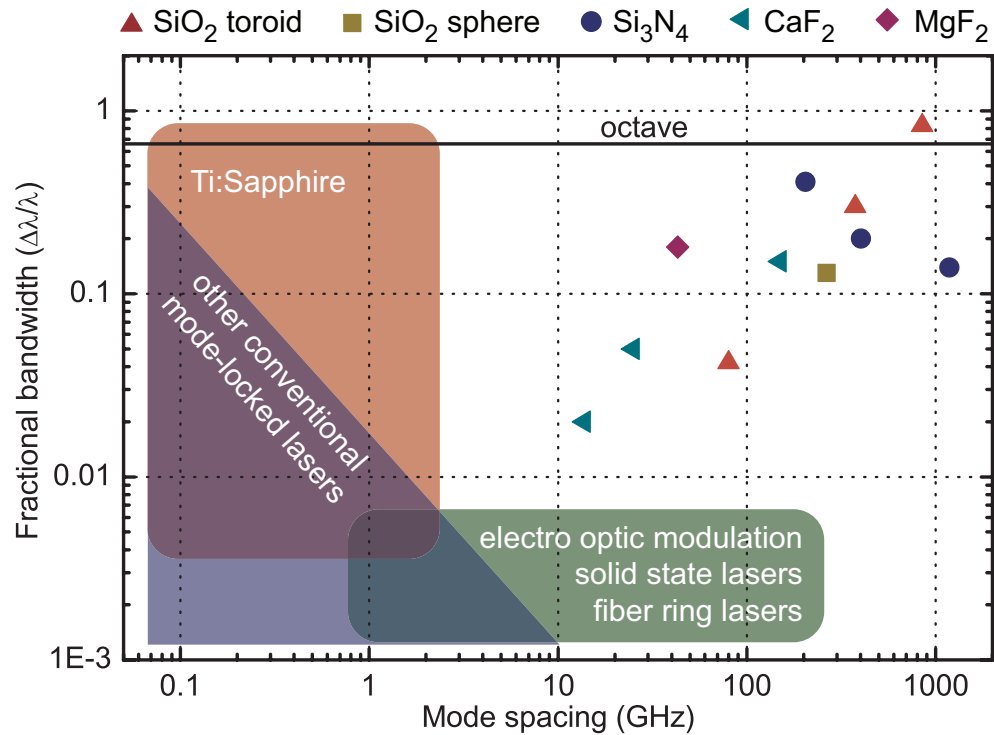
1.8.3   Comparison of different microresonator-based comb generators

Figure 1.18 shows an overview of different microresonator-based comb generators together with the generated comb spectra. The broadest frequency combs so far have been generated in fused silica microtoroids, however, recent results in silicon nitride are very promising and could potentially allow for octave spanning frequency comb generation in near future. Table 1.2 gives an overview of the properties of different comb generator systems along with a collection of relevant material constants. Interesting to note is the opposite sign of the thermorefractive effective effect with a negative dn/dT in calcium fluoride, which leads to regenerative oscillations in this material as shown in figure 1.16.

Figure 1.19 illustrates the fractional bandwidths and mode spacings of different optical frequency comb generators. The fractional bandwidth of a frequency comb is defined as the ratio of comb bandwidth and center wavelength $\Delta\lambda/\lambda$. With this definition, an octave spanning frequency comb has a fractional bandwidth of $\Delta\lambda/\lambda = 2/3$, illustrated by the horizontal line in the graph in figure 1.19. In addition, the graph shows rough operating ranges of other comb generators, for example mode locked titanium sapphire lasers that can directly emit octave spanning spectra with mode spacings up to more than 1 GHz [82, 103–111]. Other conventional frequency comb generators include erbium and ytterbium doped fiber lasers [112–116] with a mode locking mechanism based on nonlinear polarization rotation. A completely different approach for optical comb generation has been presented by Kourogi et. al. in 1993 and is based on intracavity phase modulation of laser light [117–119]. Using an electro optic phase modulator in a microwave cavity, this scheme allows for generation of equidistant comb spectra spanning more than 5 THz. Another class of comb
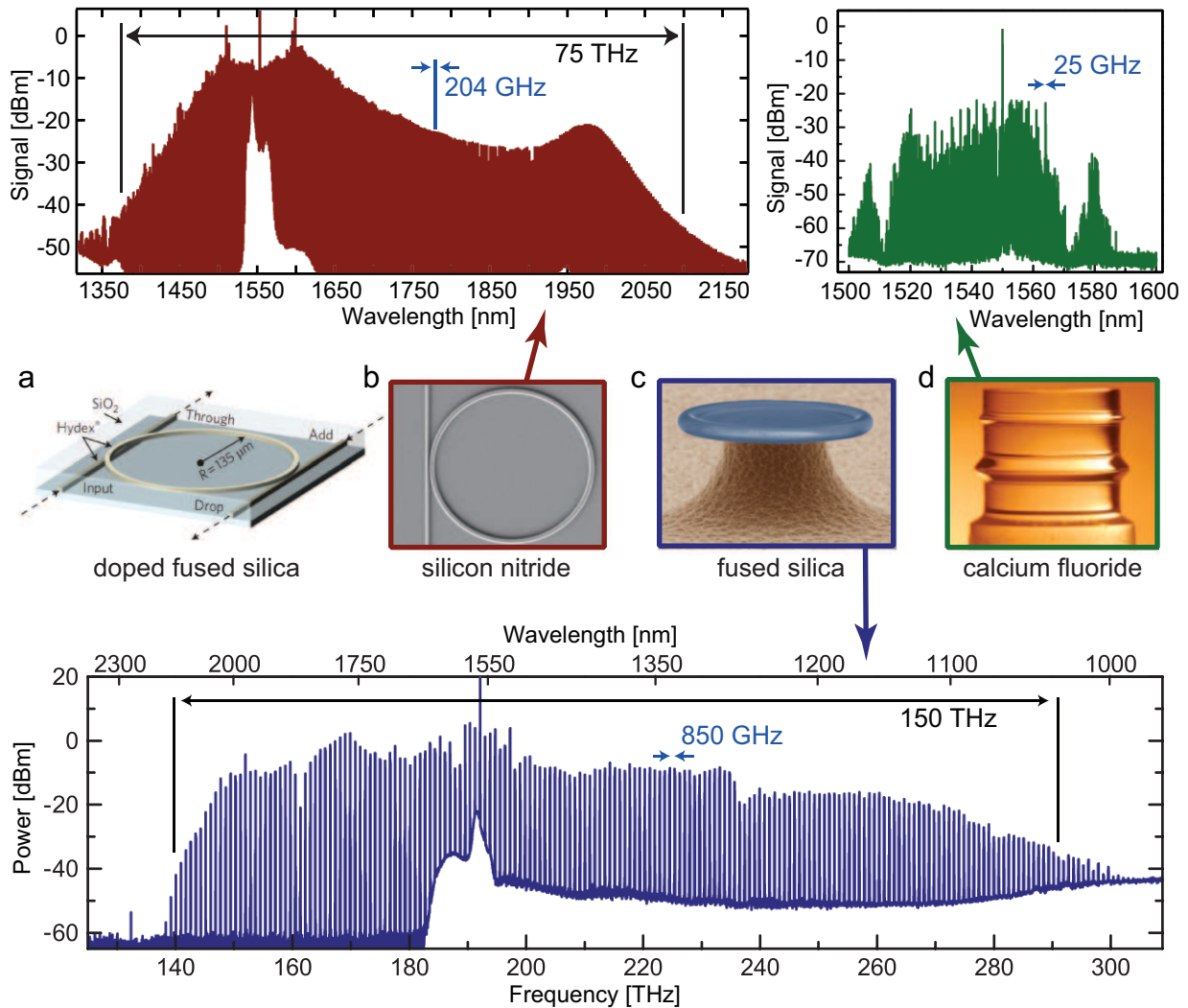
Figure 1.18: Overview of different microresonator-based comb generators with corresponding spectra (adapted from [97]). Panel a shows an integrated resonator made of doped fused silica for frequency comb generation as reported by Razzari et. al. [98]. Panel b depicts an integrated silicon nitride comb generator with corresponding spectrum presented by Levy et. al. [99, 100]. Panel c shows fused silica microtoroidal comb generator [7] and panel d shows a crystalline calcium fluoride resonator from Grudinin et. al. [90, 96].

Figure 1.19: Comparison of different optical frequency comb generators and four-wave mixing based microresonator frequency combs (modified from [97]). The fractional bandwidth on the vertical axis is defined as $\Delta\lambda/\lambda$ and a value of 2/3 corresponds to an optical octave as indicated by the horizontal line. The horizontal axis corresponds to the mode spacing of the respective frequency comb. Note that the shaded areas for non-microresonator-based frequency combs are just approximative values of typically reported bandwidths/mode spacings.

generators works with soliton generation and modulational instability in fiber ring lasers. In this case, an additional wavelength selection can be implemented for example by an etalon or a fiber Bragg grating within the resonator [120–131]. These lasers can emit comb-like spectra with high mode spacings of more than 100 GHz at the expense of a small bandwidth of only a few THz. The different kind of optical comb generators are shown in figure 1.20. A distinguishing attribute of frequency comb generation in microresonators is the large attainable mode spacing of more than 1 THz. Mode spacings of this order of magnitude are difficult to be generated in modelocked lasers as they require cavity lengths of less than 300 μm. A workaround to generate high repetition rate frequency combs with modelocked lasers is the use of filter cavities as proposed by Murphy et. al. and shown by Steinmetz et. al. [132, 133]. The attainable bandwidths in microresonators depends on many different parameters like the quality factor and the dispersion of the respective resonator. However, the data points in figure 1.19 shows a general trend of increasing comb width with higher mode spacing, which can be attributed to the higher mode volume/smaller finesse in larger resonators and a consequently higher threshold power for nonlinear four-wave mixing.
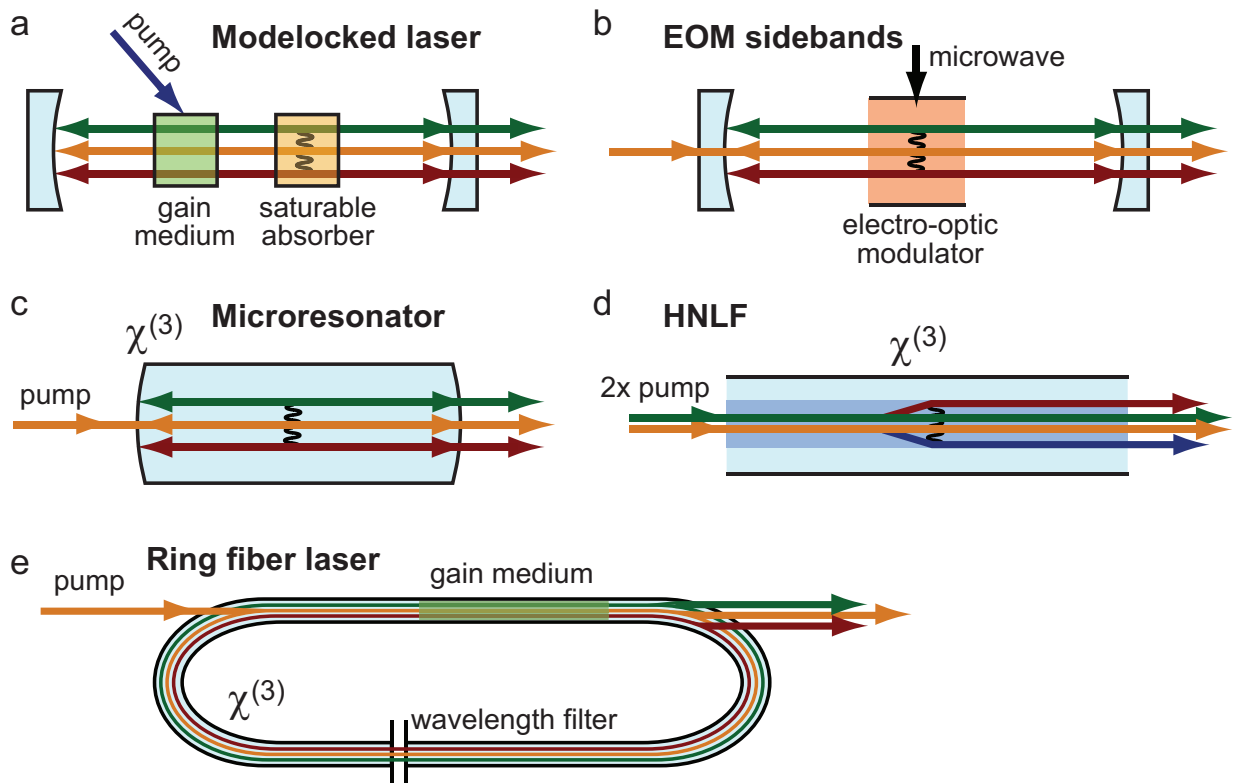
Figure 1.20: Different methods for generation of equidistant optical frequencies. Panel a shows a mode locked laser with gain medium and saturable absorber [82]. Panel b shows a comb generator based on intracavity electro-optic modulation with a microwave field [117–119]. Panel c shows comb generation by four-wave mixing in microresonators [3, 90, 99]. Panel d shows comb generation by a strong bi-chromatic pump in highly nonlinear fiber (HNLF) [134]. Panel e shows soliton generation in a fiber ring laser with an additional wavelength selective element (etalon, fiber Bragg grating) [120–131]

CHAPTER 2

## Equidistance of the generated comb modes

2.1   Motivation

One of the most evident questions raised from the generation of comb-like spectra in fused silica microresonators is whether the generated modes form an equidistant frequency comb? The pairwise generation of optical sidebands outside of Brillouin and Raman gain regions indicates that the underlying principle is based on four-wave mixing. However, it has to be experimentally verified whether the generated pairs of sidebands are indeed exactly equally spaced. Moreover, it has to be analyzed whether the modes in the cascaded regime have a uniform spacing, which does not necessarily follow from theoretical considerations. This chapter presents measurements showing that the generated mode spectra in a microresonator indeed constitute an equidistant frequency comb spectrum. Over a bandwidth of 50 nm it is shown that the mode spacing varies by less than 2×10^{-3} Hz, a value that is just limited by the total measurement time.

Degenerate four-wave mixing ($2f_\mathrm{p} = f_\mathrm{i} + f_\mathrm{s}$) in a microresonator is an energy conserving process and consequently, the generated sidebands at frequencies f_i and f_s are forced to be symmetric around the carrier frequency f_p. This process is shown in figure 2.1. The frequency difference between the pump laser f_p and the signal f_s and idler sidebands f_i is determined by the modal structure of the resonator and corresponds to the average free spectral range between the pump mode and the neighboring modes. Panel **b** in figure 2.1 shows non-degenerate four-wave mixing as a possible process for broadening the optical frequency comb (a more detailed compilation of all possible four-wave mixing processes is shown in figure 1.8).

Despite the combination of degenerate and non-degenerate four-wave mixing can lead to the generation of equidistant sidebands, there are conceivable processes that would generate non-equidistant modes. Examples of these processes, which are linked to the modal structure of the resonator are shown in figure 2.2. In case of a cavity dispersion with a changing mode spacing, it might be possible that eg. the signal sideband generates new symmetric sidebands with a different spacing than the initial spacing between pump laser and signal sideband (cf. figure 2.2a). This process might be possible in case the generated wave in the four-wave mixing process $f_\mathrm{s'} = 2f_\mathrm{s} - f_\mathrm{p}$ is not resonant with a microcavity mode anymore. Another process leading to a non-equidistant mode spectrum could take place by pumping the resonator close to zero dispersion (note that four-wave mixing is not possible in a perfectly dispersionless cavity [16]). In this case, the pump mode could generate two orders of sidebands that are both equidistantly spaced around the pump mode but not mutually equidistant. This chapter focuses on experimental measurements of the mode structure of microresonator-based cascaded four-wave mixing with the goal of answering the question whether microresonators can generate optical frequency combs.
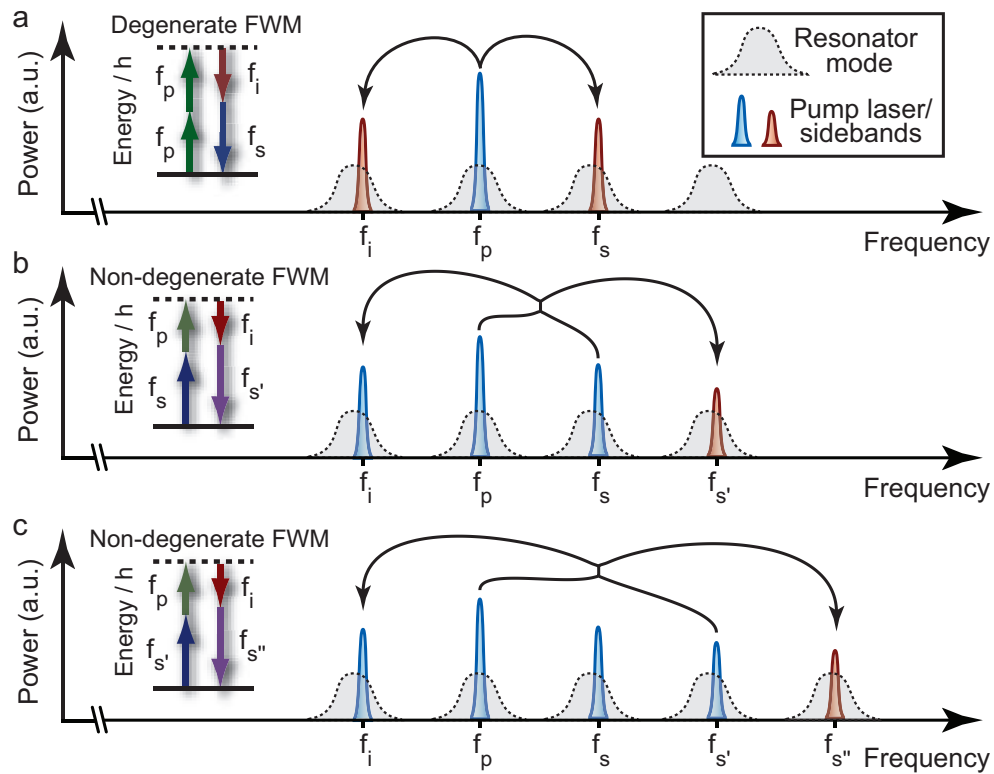
Figure 2.1: Degenerate and Non-degenerate four-wave mixing in a microresonator. Panel a depicts degenerate four-wave mixing ($2f_\mathrm{p} = f_\mathrm{i} + f_\mathrm{s}$) from the pump laser with frequency f_p to the idler f_i and signal f_s frequency. The mode spacing is determined by the position of the cavity modes (dashed lines). In case of cavity dispersion, the resulting mode spacing maximizes the overlap between sidebands and resonator modes. Panel b shows cascading of the generated sidebands via non-degenerate four-wave mixing ($f_\mathrm{p} + f_\mathrm{s} = f_\mathrm{i} + f_\mathrm{s'}$). Panel c depicts another possible four-wave mixing process for further cascaded sideband generation. The insets depict the corresponding energy diagrams for degenerate and non-degenerate four-wave mixing. For a complete set of possible four-wave mixing processes see figure 1.8
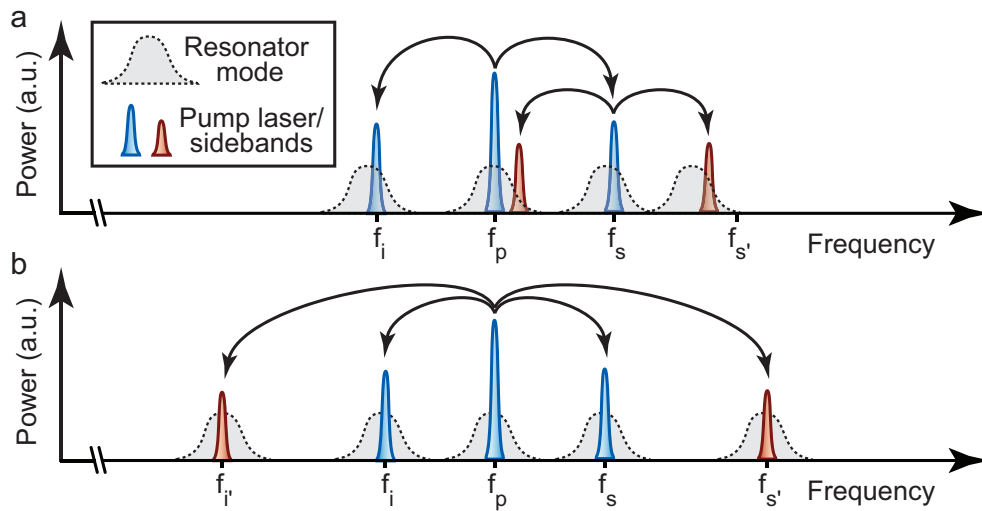
Figure 2.2: Processes leading to non-equidistant mode spectra. Panel a shows the case of a dispersive cavity in which the generated signal mode f_s could generate sidebands at a different spacing than the initial spacing between pump laser f_p and signal. This process is conceivable in case of a monotonic change of the resonator mode spacing in which the frequency $f_{s'} = 2f_s - f_p$ is not resonant with a cavity mode. Panel b shows another process leading to non-equidistant modes. Here, the pump laser itself generates two pairs of sidebands that are each symmetric around the pump frequency but leading to a spectrum in which the modes are not mutually equidistant.

2.2 Multiheterodyne equidistance measurement principle

An experimental approach for determination of the frequencies of the four-wave mixing modes in a microresonator is multiheterodyne spectroscopy with an additional frequency comb. In this experiment, several beat notes are generated between the modes from the microresonator and the modes of a stabilized frequency comb (termed reference comb). Since the modes of the reference comb are known to be equidistant, the generated beat notes between adjacent modes from microresonator and reference comb are expected to be equidistant as well in case of an equal spacing of the microresonator modes. Multiheterodyne spectroscopy has been first developed and used for gas sensing applications by superimposing two frequency combs at slightly different repetition rates and measurement of the radio frequency beat notes [135–137]. Another similar example of this principle is Fourier transform spectroscopy with only one frequency comb, in which a Michelson interferometer with a movable arm is used to increase or decrease the repetition rate of part of the frequency comb, which also enables the generation of low frequency beat notes between the frequency shifted modes and the original modes of the comb [138].

Multiheterodyne spectroscopy typically employs frequency combs with nearly the same repetition rate, such that the frequency difference of the generated beat notes is much smaller than the mode spacing. However, to prove the equidistance of a microresonator based comb with a fiber laser reference comb it has to be taken into account that the mode spacings are different by a factor of around 10,000 (with $\approx$1 THz mode spacing of the microresonator comb and $\approx$100 MHz mode spacing of the reference comb). To derive the most general case of beat note generation between two frequency combs, the modes of the two frequency combs f_{c1} and f_{c2} can be defined as

$$f_{c1} = f_{\text{ceo1}} + n \cdot f_{\text{rep1}} \tag{2.1}$$

$$f_{c2} = f_{\text{ceo2}} + m \cdot f_{\text{rep2}} \quad , \tag{2.2}$$

with f_{ceo1} and f_{ceo2} being the carrier envelope offset frequencies, f_{rep1} and f_{rep2} the repetition rates and $n, m \in \mathbb{N}$. Without loss of generality we assume $f_{\text{rep1}} \gg f_{\text{rep2}}$ and consequently we can derive the beat note f_{B0} of the nth mode of comb 1 with the nearest mode of comb 2 as

$$f_{\text{B0}} = |f_{\text{ceo2}} + m_0 \cdot f_{\text{rep2}} - f_{\text{ceo1}} - n \cdot f_{\text{rep1}}| \tag{2.3}$$

$$\text{with} \quad m_0 = \left\lceil \frac{f_{\text{ceo1}} + n \cdot f_{\text{rep1}} - f_{\text{ceo2}}}{f_{\text{rep2}}} \right\rfloor \quad , \tag{2.4}$$

where $\lceil x \rfloor$ denotes the rounded value of x (to the closest integer number).

The general principle of multiheterodyne beat note generation is depicted in figure 2.3. To determine the equidistance of one of the combs (eg. comb 1), it is necessary to generate
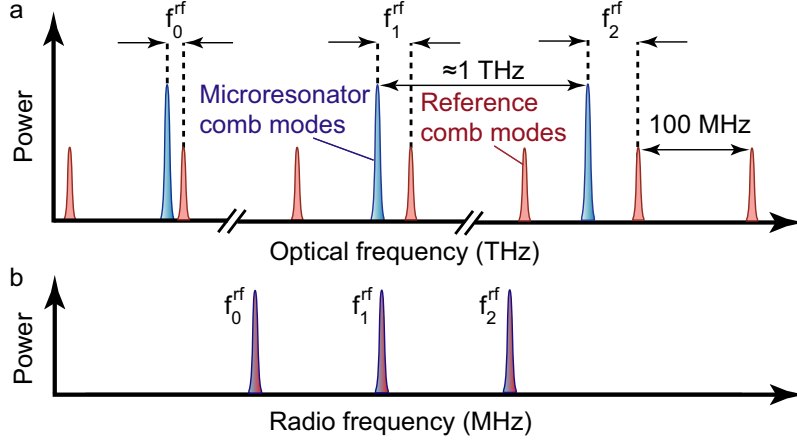
Figure 2.3: Principle of multiheterodyne beat note generation. Panel a. Superimposing two frequency combs with different repetition rates (in this case 1 THz and 100 MHz) leads to the generation of beat notes between the comb modes. The lowest frequency beat notes (Panel b) denoted f_0^{rf}, f_1^{rf} and f_2^{rf} can be measured with a fast photodiode. Note that the frequency axis in panel a is broken in order to display several beat notes simultaneously. Approximately 10,000 reference comb modes are in between two adjacent microresonator comb modes.

beat notes of at least three modes of comb 1 with adjacent modes of comb 2. Thus, the additional beat notes of the neighboring modes of comb 1 are defined as f_{Bk}:

$$f_{\mathrm{Bk}} = |f_{\mathrm{ceo2}} + m_k \cdot f_{\mathrm{rep2}} - f_{\mathrm{ceo1}} - (n+k) \cdot f_{\mathrm{rep1}}| \tag{2.5}$$

$$\text{with } \quad m_k = \left\lceil \frac{f_{\mathrm{ceo1}} + (n+k) \cdot f_{\mathrm{rep1}} - f_{\mathrm{ceo2}}}{f_{\mathrm{rep2}}} \right\rceil \quad . \tag{2.6}$$

Figure 2.4 shows the beat notes of four adjacent modes of comb 1 with the neighboring modes of comb 2. In this figure, the repetition rate of comb 1 is fixed at 110 Hz, while the repetition rate of comb 2 is varied. Obviously, the relative frequency of the beat notes depends on the repetition rate of the combs, with degenerate beat note frequencies in case of the repetition rate of comb 1 corresponds to an integer multiple of the repetition rate of comb 2. This also follows from equations 2.4 and 2.6. For beat notes at equal frequencies, it is necessary that $f_{\mathrm{Bk}} - f_{\mathrm{B0}} = 0 \; \forall \; k \in \mathbb{N}$. Without loss of generality we assume that the comb mode of comb 2 is at higher frequency than the neighboring mode of comb 1, which allows for neglecting the absolute value in f_{B0} and f_{Bk}. Consequently we obtain

$$0 \overset{!}{=} f_{\mathrm{Bk}} - f_{\mathrm{B0}} = (m_k - m_0) \cdot f_{\mathrm{rep2}} - k \cdot f_{\mathrm{rep1}}$$
$$= \left(\left\lceil \frac{f_{\mathrm{ceo1}} - f_{\mathrm{ceo2}} + (n+k) \cdot f_{\mathrm{rep1}}}{f_{\mathrm{rep2}}} \right\rceil - \left\lceil \frac{f_{\mathrm{ceo1}} - f_{\mathrm{ceo2}} + n \cdot f_{\mathrm{rep1}}}{f_{\mathrm{rep2}}} \right\rceil \right) \cdot f_{\mathrm{rep2}} - k \cdot f_{\mathrm{rep1}} \tag{2.7}$$
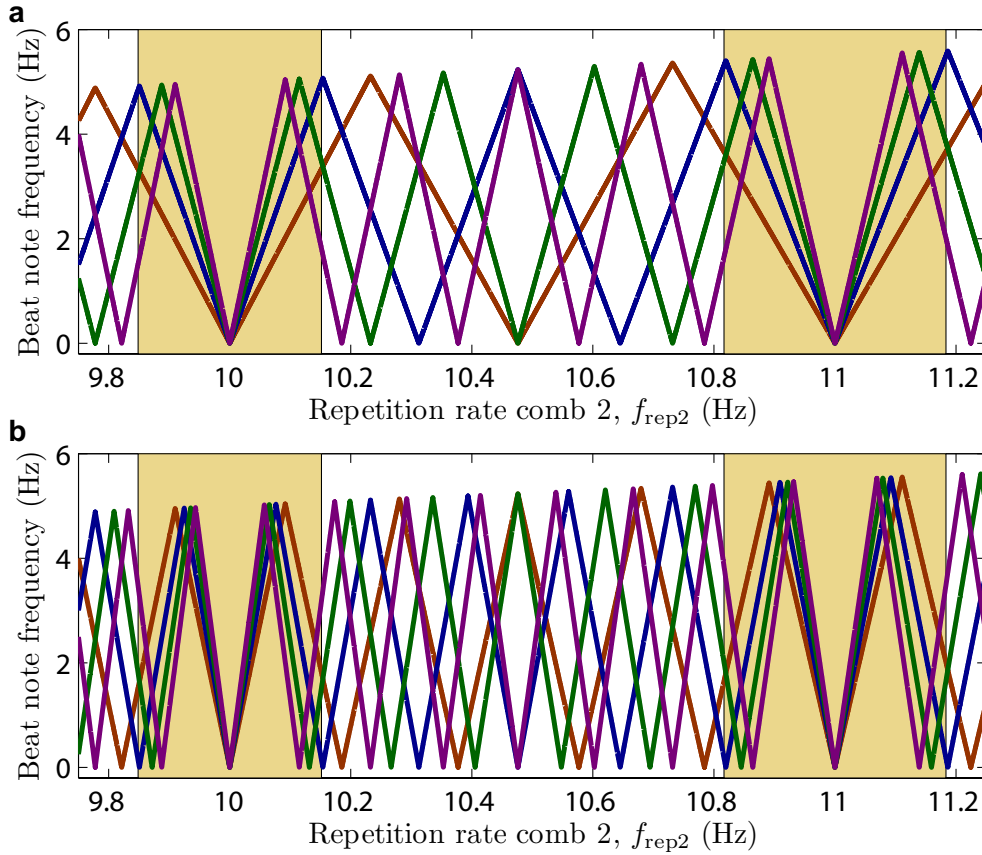
Figure 2.4: Multiheterodyne beat notes between two frequency combs with different repetition rate. The repetition rate of comb 1 is fixed at $f_{rep1} = 110$ Hz, while the repetition rate of comb 2 is varied (horizontal axis). For convenience, the carrier envelope frequency of both combs is set to zero. The vertical axes show beat notes of four adjacent modes of comb 1 with the nearest neighboring modes of comb 2. Panel a shows beat notes of modes $n = 2, 3, 4, 5$ of comb 1 with the respective modes of comb 2. Panel b shows beat notes at higher frequencies generated by the modes $n = 5, 6, 7, 8$ of comb 1. In case of the repetition rate of comb 1 being an integer multiple of the repetition rate of comb 2, the four beat notes are at the same frequency ($f_{rep1} = 110$ Hz is an integer multiple of $f_{rep2} = 10$ and $f_{rep2} = 11$). The shaded regions depict the repetition rate ranges in which equidistant beat notes can be observed. This is evident in the vicinity of $f_{rep2} = 10$ and $f_{rep2} = 11$. At the outer parts of the shaded region, the beat notes are not equidistant in this graph, but can still be changed to be equidistant by varying the carrier envelope offset frequency of one of the combs.

It is easy to show that equation 2.7 is satisfied in case $f_{\mathrm{rep1}} = \ell \cdot f_{\mathrm{rep2}}$ with ℓ being an integer value. In figure 2.4 this is the case for $f_{\mathrm{rep2}} = 10$ and $f_{\mathrm{rep2}} = 11$ and the four adjacent beat notes are equidistant in the vicinity of these repetition rates. An important value is the range in which equidistant beat notes can be observed. This corresponds to the range in which the difference between the beat note frequencies is smaller than half the repetition rate of the comb with smaller mode spacing. The difference between two beat notes Δf_{B} close to a degenerate point with $f_{\mathrm{rep1}} = \ell \cdot f_{\mathrm{rep2}}$ is given as

$$\Delta f_{\mathrm{B}} = (m_k - m_0) \cdot \Delta f_{\mathrm{rep2}} \overset{!}{<} \frac{f_{\mathrm{rep2}}}{2} \quad . \tag{2.8}$$

Inserting m_k and m_0, we obtain the maximum change Δf_{rep2} of the repetition rate f_{rep2} that still allows for observation of equidistant beat notes as

$$\Delta f_{\mathrm{rep2}} \overset{!}{<} \frac{f_{\mathrm{rep2}}^2}{2k \cdot f_{\mathrm{rep1}}} \tag{2.9}$$

with k being the number of simultaneously observed beat notes. Additionally we assume that one of the carrier envelope offset frequencies can be tuned by more than 50% of the smaller repetition rate and that $f_{\mathrm{rep2}} < f_{\mathrm{rep1}}$ as defined before. The shaded region in figure 2.4 depicts the repetition rate ranges in which equidistant beat notes can be observed according to equation 2.9.

Figure 2.5 shows four adjacent beat notes as they are expected between a microresonator based frequency comb with a mode spacing of $f_{\mathrm{rep1}} = 1$ THz and a reference comb with $f_{\mathrm{rep2}} = 100$ MHz. The four beat notes are originating from the 200th to the 203rd mode of the microresonator comb (which would experimentally correspond to a wavelength around 1500 nm). The lower panel shows the response of the beat note frequencies to a variation of the repetition rate of the reference comb. The plotting range on the horizontal axis corresponds to $f_{\mathrm{rep2}} = f_{\mathrm{rep1}}/\ell$ with $\ell = 10{,}000$ and $\ell = 9{,}999$. Consequently, the beat notes are at degenerate frequencies at the low and high frequency end of the plot. The upper panels show zooms into the data at different frequencies in between these degenerate points. Here, it can be seen that it is likely to not experimentally observe equidistant beat notes between the two frequency combs unless the repetition rate of the reference comb is adapted to an adequate value according to equation 2.9.

2.3 Equidistance measurements

Figure 2.6 shows the experimental setup used for generation and measurement of beat notes between the optical modes from the microresonator and a reference comb (a fiber laser based optical frequency comb [113]). First, light of an external cavity diode laser is coupled into a mode of a fused silica microresonator via a tapered optical fiber. The coupling gap between the fiber and the resonator can be controlled and optimized with a 3-axis piezo translation stage. Additionally, a fiber based polarization controller is used to match the polarization of the launched laser with the polarization of the high finesse mode
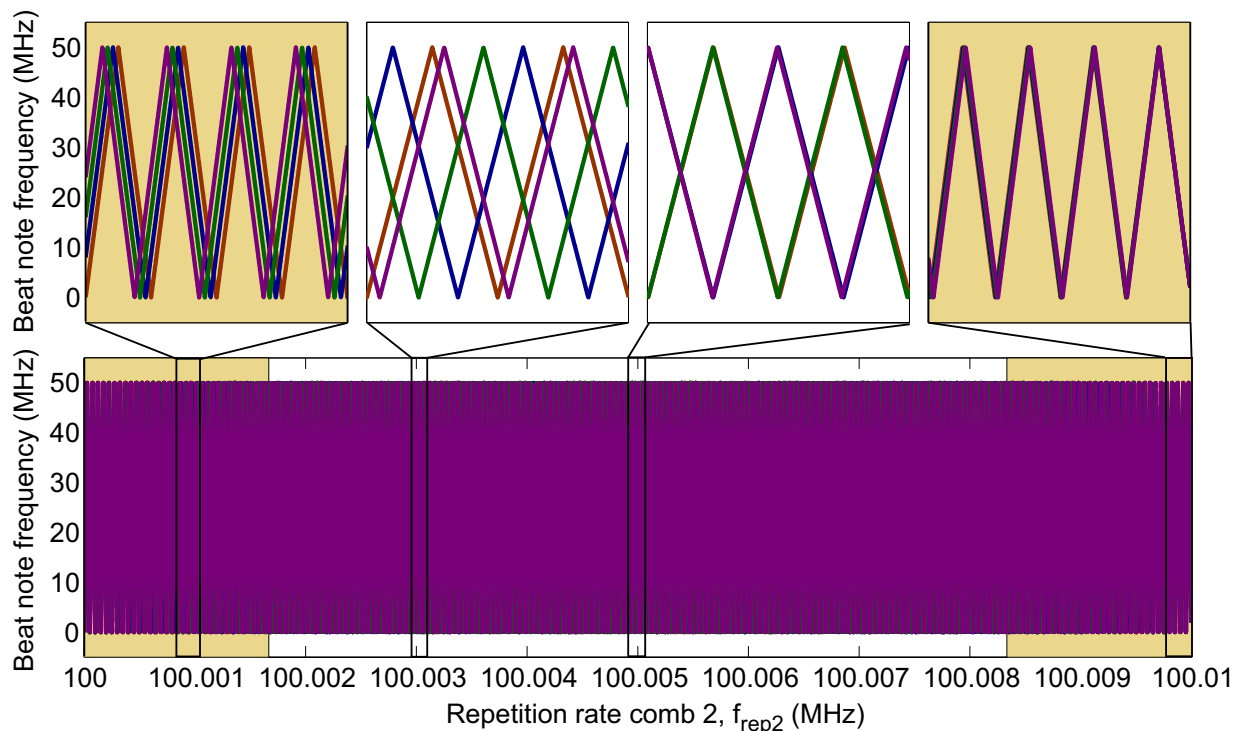
Figure 2.5: Calculation of four adjacent multiheterodyne beat notes between a microresonator comb with 1 THz mode spacing and a reference comb with around 100 MHz mode spacing. The low frequency end on the horizontal axis corresponds to $f_{\mathrm{rep1}} = 10,000 \cdot f_{\mathrm{rep2}}$ and the high frequency end to $f_{\mathrm{rep1}} = 9,999 \cdot f_{\mathrm{rep2}}$ (leading to degenerate beat note frequencies at these points). In between, a complex behavior of the beat note frequencies can be observed where it is not obvious that the two frequency combs are equidistant. The shaded regions depict the repetition rate range of the reference comb f_{rep2}, in which equidistant beat notes can be observed according to equation 2.9.
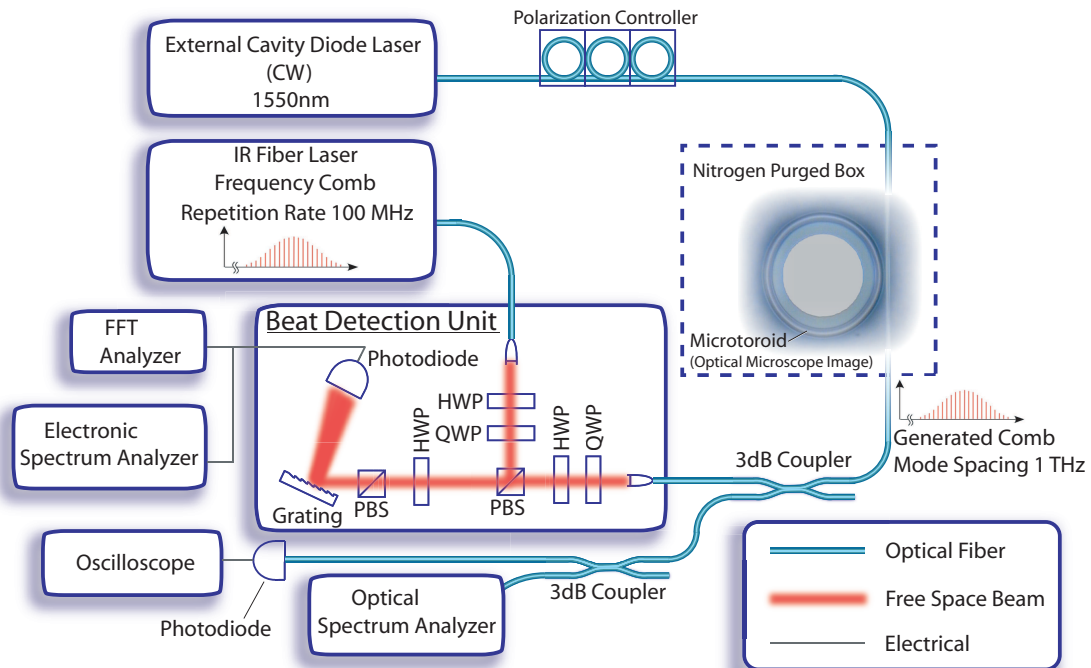
Figure 2.6: Setup for equidistance measurements with multiheterodyne beat notes. A tunable external cavity diode laser is used to generate a frequency comb in a microresonator. The generated frequency comb is superimposed spatially with a fiber laser based reference comb in the "beat detection unit". The polarization of the comb modes can be adjusted by means of half- and quarter wave plates in order to maximize the beat signal. Additionally, a grating is used to isolate the spectral region of interest (which increases the signal to noise ratio of the measured beat notes). The beat notes are analyzed with a fast Fourier transform analyzer and/or an electronic spectrum analyzer. The light emerging from the tapered optical fiber, which is used to send light to the microresonator is simultaneously analyzed with a fast photodiode and an optical spectrum analyzer in order to optimize the light coupling from the tapered fiber to the resonator. FFT - fast Fourier transform, HWP - half wave plate, QWP - quarter wave plate, PBS - polarizing beam splitter.
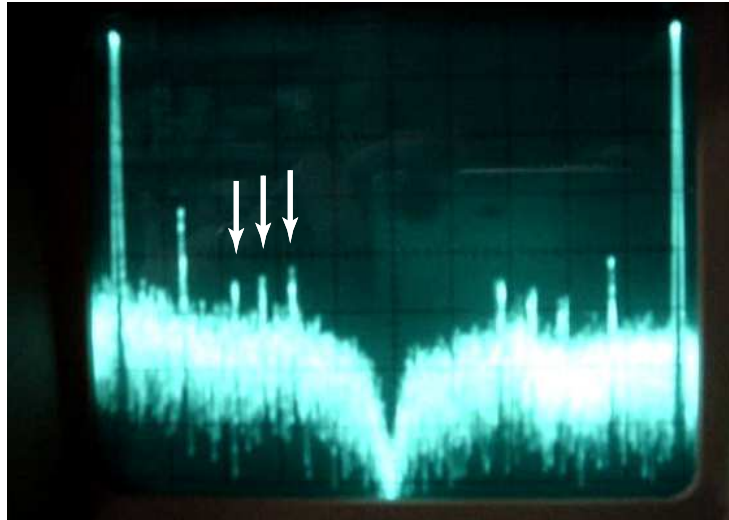
Figure 2.7: First observation of equidistant beat notes, recorded with an electronic spectrum analyzer. The figure shows a still image from a video [139] with three equidistant beat notes from three adjacent microresonator comb modes with a reference comb (beat notes are marked with arrows). The equidistance of these beat notes was the first evidence of four-wave mixing based frequency comb generation in microresonators. The line left of the marked beat notes is originating from a mechanical eigenmode of the resonator and stays at a constant frequency and is not changed by tuning the pump laser frequency (which can be seen in the full video [139])

of the microresonator. Part of the laser light emerging from the output of the tapered fiber is sent to a photodiode connected to an oscilloscope to monitor the coupling condition via the transmitted signal. Another part of the light from the tapered fiber is sent to an optical spectrum analyzer for analysis of the generated optical spectrum. The actual multiheterodyne equidistance measurement is done in a "beat detection unit" in which the light of the microresonator comb and the fiber laser reference comb is superimposed. A grating is used to suppress noise from parts of the optical spectrum that is not of interest for the multiheterodyne measurement. The generated beat note signal is subsequently analyzed with a "Fast Fourier Transform" (FFT) Analyzer and/or an electronic spectrum analyzer.

Figure 2.7 shows the first evidence for equidistant microresonator comb modes in a 70-μm-diameter toroid. The figure shows a single frame of a video [139] and depicts beat notes of the pump mode, first and second sideband with the fiber laser reference comb. Following this measurement, broader combs and beat notes between more remote modes (in the wings of the comb) and the reference comb are generated as shown in figure 2.8. The comb spectrum consists of more than 20 optical modes with a spacing of approximately 7.5 nm around 1550 nm, which corresponds to a mode spacing of ≈ 930 GHz. The pump laser source is a tunable external cavity diode laser with a power of 7 mW (without further amplification). Generated beat note frequencies of 9 adjacent modes with a fiber laser comb
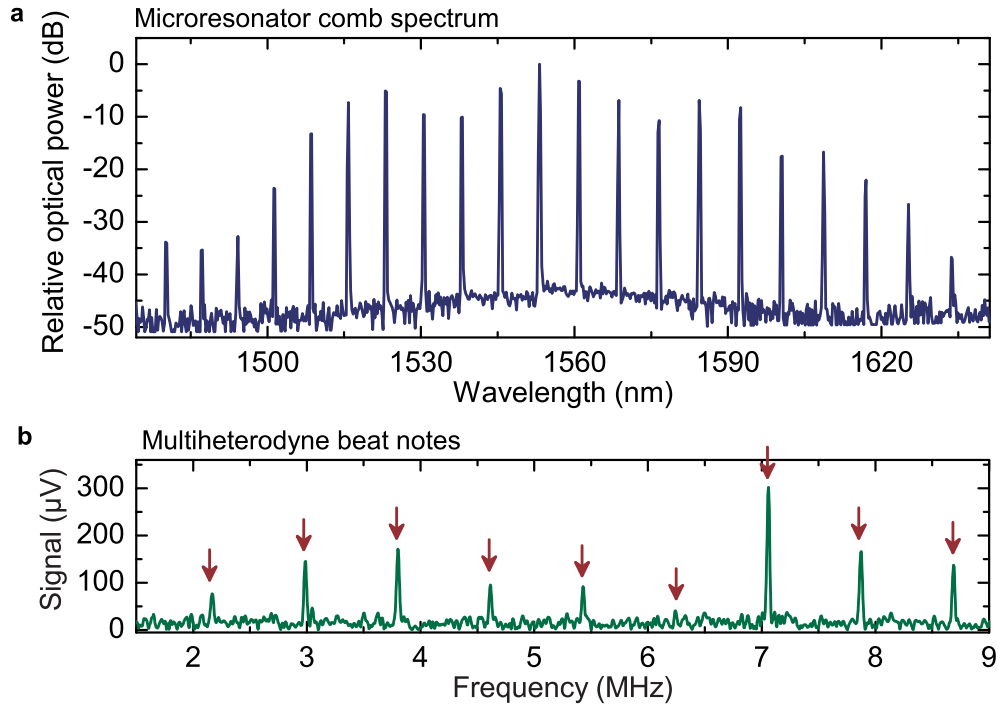
Figure 2.8: Optical comb spectrum and multiheterodyne beat notes of a microresonator frequency comb. Panel a shows a comb spectrum consisting of more than 20 modes covering a wavelength range of ≈ 150 nm. The pump laser is located around 1550 nm with a launched power of 7 mW (the vertical power scale is relative to the pump laser power). This comb is generated in a 70-μm-diameter microtoroid. Nine adjacent comb modes in the vicinity of the pump laser are used to generate multiheterodyne beat notes (panel b) with a reference comb. The variation in the beat note signal is a result of polarization rotation in optical fibers, such that it is not possible to match the polarization of all microresonator modes with the adjacent reference comb modes simultaneously.
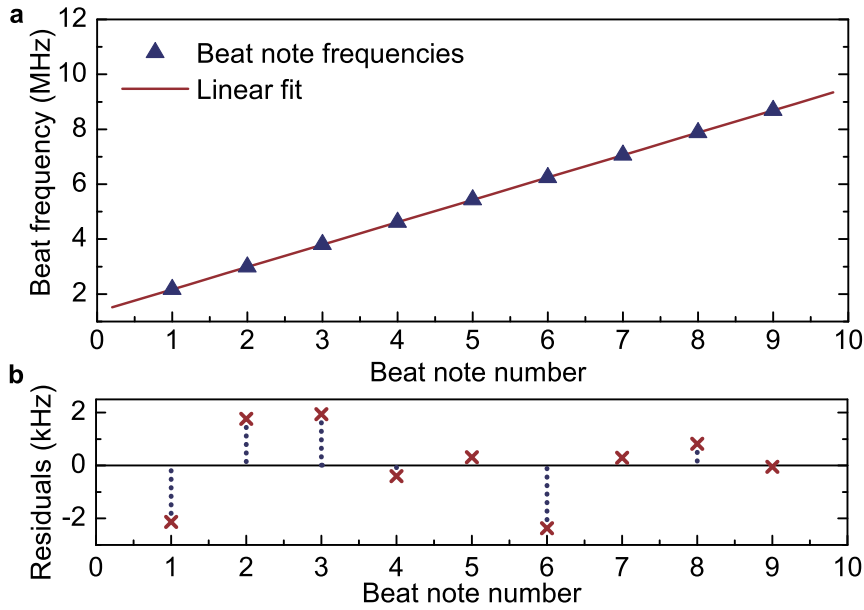
Figure 2.9: Multiheterodyne beat note frequencies. The plot in panel a shows the frequencies of 9 adjacent multiheterodyne beat notes from the frequency comb in figure 2.8. The horizontal axis corresponds to the beat note number and the linear fit indicates that the measured beat notes are nearly equidistantly spaced. Panel b shows the residuals of the linear fit in panel a with a deviation of the microresonator comb modes from equidistance in the order of 2 kHz, which is limited by the resolution bandwidth of the fast Fourier transform spectrum analyzer.

(repetition rate 100 MHz) are depicted in panel b of figure 2.8 and correspond to an optical frequency range of 8.4 THz ($\approx$ 70 nm in the 1550 nm region). It is shown that the beat notes can be frequency tuned in a uniform way by changing the pump laser frequency, which is an indication that the ratio of the mode spacings of microresonator comb and reference comb is in the vicinity of an integer value as shown in figure 2.5. The beat notes are recorded with an oscilloscope as "Fast-Fourier-Transform" (FFT) spectrum analyzer. Obviously, a strong power variation is present in the different beat notes and moreover they do not follow the power variation of the optical modes of the microresonator comb. This is a result of the wavelength dependent polarization rotation in the employed optical fibers (and tapered fiber), such that the polarization of microresonator comb and reference comb can just be matched locally but not over a wavelength range covering all nine beat notes. By adjusting the polarization controllers in the beat note generation setup, it is possible to maximize the power in each beat note to approximately the same level, however, for the measurement in figure 2.8b a polarization for simultaneous recording of all 9 beat notes has been chosen.

In figure 2.9, the frequency of the nine beat notes in figure 2.8 is displayed as a function of the beat note number. In case of equidistant frequency combs, the multiheterodyne beat notes are located on a line as indicated by the linear fit in figure 2.9a. Panel b in the same figure shows the residuals (deviation of the measured beat note frequencies from the linear fit) of the measurement with a deviation of less than 2 kHz from the expected value, limited only by the 10 kHz resolution bandwidth of the FFT-routine. The measurement has been performed with 9 adjacent microresonator comb modes spanning 8.4 THz and consequently, the generated comb is equidistant to a level better than ≈ 220 Hz/FSR or ≈ 240 Hz/THz (assuming a constant variation of the mode spacing $(f_{m+1} - f_m) - (f_m - f_{m-1}) = \text{const}$, with f_m being the mth comb mode). Since the microresonator comb is not stabilized the beat notes are slowly drifting. As a result, further reduction of the resolution bandwidth of the fast Fourier transform spectrum analyzer does not yield better results for the accuracy of the equidistance measurement due to an increased measurement time and mode drift.

2.4   Frequency counting

The measurements presented in the previous section already show strong evidence for optical frequency comb generation via four-wave mixing in microresonators. It has been demonstrated that the deviation of the generated comb lines from equidistant frequencies is less than 2 kHz. However, owing to a compensation of material and geometric dispersion (shown later in chapter 4), the microresonator modes itself are not expected to deviate much from equidistance. Consequently, there is still the possibility of the comb modes being non-equidistant with a frequency deviation of less than 2 kHz within the range of 9 free spectral ranges (corresponding to 8.4 THz in the respective resonator).

A more accurate measurement of the equidistance of microresonator combs can be performed by using radio frequency counters to determine the exact frequency of 3 or more comb modes simultaneously. Radio frequency counters can determine the frequency of an applied electronic signal by counting the number of zero crossings and comparing them to the number of zero crossings of a known reference signal (also termed time base). A more detailed description of a modern frequency counter's working principle is given in appendix C. In the presented experiments, the time base is a 10-MHz-signal from an in-house GPS-disciplined hydrogen maser. Figure 2.10 shows an experimental setup that is used to simultaneously measure 3 heterodyne beat notes between a microresonator comb and a reference comb. An external cavity diode laser is used as pump source to generate a frequency comb in a fused silica microtoroid. The generated comb is split into 3 parts which are sent to 3 separate "Beat Detection Units" (BDU) to generate beat notes with a fiber laser reference comb (cf. appendix B). Each BDU has a grating to select the spectral region of exactly one microresonator comb line and generate its beat note with the reference comb. The grating in the first BDU is adjusted to the pump laser wavelength and the corresponding rf beat note f_0^{rf} is used to stabilize the pump laser frequency to the 10-MHz-frequency-standard. Two more BDUs are used to measure beat note frequencies f_N^{rf} and f_M^{rf} of the Nth and M^{th} sideband of the microresonator comb, respectively. Note
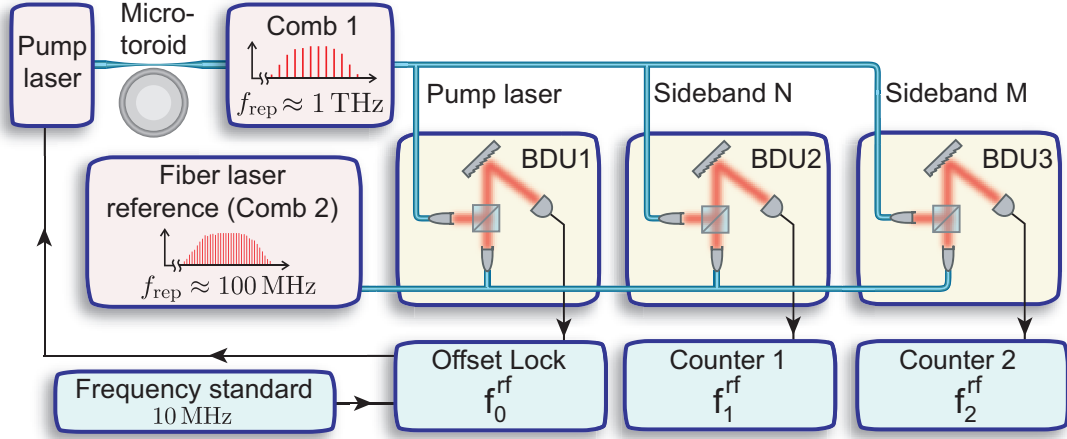
Figure 2.10: Experimental setup for multiheterodyne equidistance measurements with high-resolution frequency counters. Three beat notes between a microresonator frequency comb and a fiber laser reference comb are generated. The different beat notes are generated in "Beat Detection Units" (BDU) with an integrated grating to optically select a single microresonator comb mode. One beat note (f_0^{rf}, generated in BDU1) is used for locking of the pump laser frequency to a mode of the reference comb. The two beat notes from BDU2 and BDU3 (f_1^{rf} and f_2^{rf}) are generated by the Nth and M^{th} microresonator comb sideband respectively. The equidistance of the comb modes is verified by measuring f_1^{rf} and f_2^{rf} with radio frequency counters.

that the repetition rate of the reference frequency comb is adjusted in a trial-and-error approach in such a way that all the beat notes are nearly at the same frequency and "move" into the same direction when changing the pump frequency (according to the theoretical considerations shown in figure 2.5). Additionally, an approximately 1-MHz-wide radio frequency bandpass filter is used in each of the beat note detection units to improve the signal to noise ratio of the respective beats. By knowing the frequencies f_0^{rf}, which is set by the phase locked loop and the two frequencies f_N^{rf} and f_M^{rf} that are measured by frequency counters, it is possible to define the deviation from equidistant microresonator comb spacing as

$$\epsilon = \frac{f_M^{\mathrm{rf}} - f_N^{\mathrm{rf}}}{M - N} - \frac{f_N^{\mathrm{rf}} - f_0^{\mathrm{rf}}}{N} \quad . \tag{2.10}$$

Figure 2.11 shows a beat note measurement of symmetric sidebands around the pump laser. The vertical axis has been offset by the beat note frequency of the pump, such that the beat notes of the sidebands $N = 1$ and $M = -1$ are symmetric around zero. This measurement indicates that the optical sidebands are generated by an energy conserving four-wave mixing process. Calculating the sum of the two curves yields the mode spacing difference between the two sidebands with respect to the pump laser with a mean value of (-1.4 ± 11.2) Hz. However, with this measurement it is not possible to exclude the potential processes leading to non-equidistant sideband generation shown in figure 2.2.
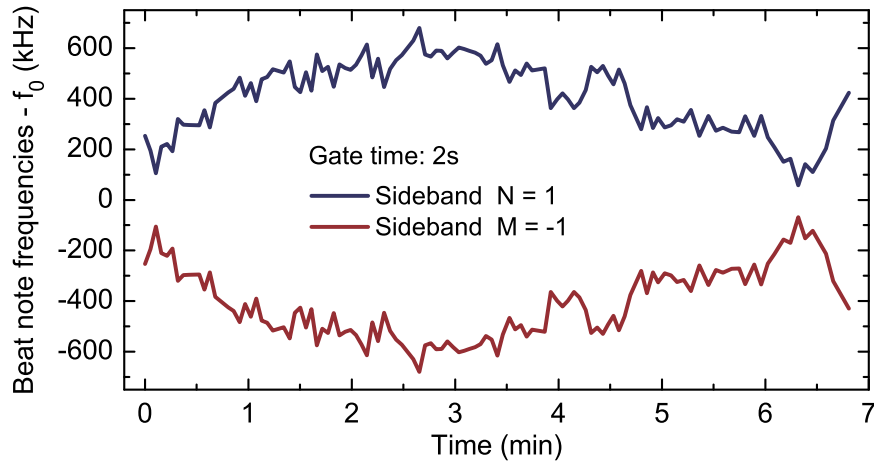
Figure 2.11: Multiheterodyne beat notes of symmetric sidebands around the pump laser. The graph shows beat notes between two microresonator comb modes ($N = 1$ and $M = -1$) and a fiber laser reference comb. The beat note frequencies are offset by the beat note frequency of the pump laser, which is stabilized to the reference comb with a phase locked loop. Obviously, the mode spacing is drifting by a few hundred kilohertz during the measurement but the distance between sidebands and pump laser remains constant.

Thus, it is required to perform measurements with comb modes that are separated by several free spectral ranges and compare the spacing between these modes. Such an optical microresonator comb spectrum is shown in figure 2.12.

The spectrum is recorded with the tapered optical fiber in contact with the microresonator, which allows for a significantly more stable coupling. Note that it is still possible to optimize the coupling gap between the tapered optical fiber and the resonator mode by changing the position where the fiber is in contact with the resonator (Another scheme for stabilization of the tapered fiber position is shown in appendix F). The spectrum in figure 2.12 is recorded in slightly overcoupled position, which can be seen from the rather flat power distribution of the comb modes (sidebands and pump laser are nearly at the same power level). As a result of the tapered fiber being in contact with the resonator it is possible to maintain stable frequency comb generation for more than 10 hours. This is especially important for long term measurements of the comb stability. The following equidistance measurements are done with the 5th and 7th sideband of the spectrum in figure 2.12. Two different methods to determine a quantitative values of the equidistance of comb modes are presented in the next sections.
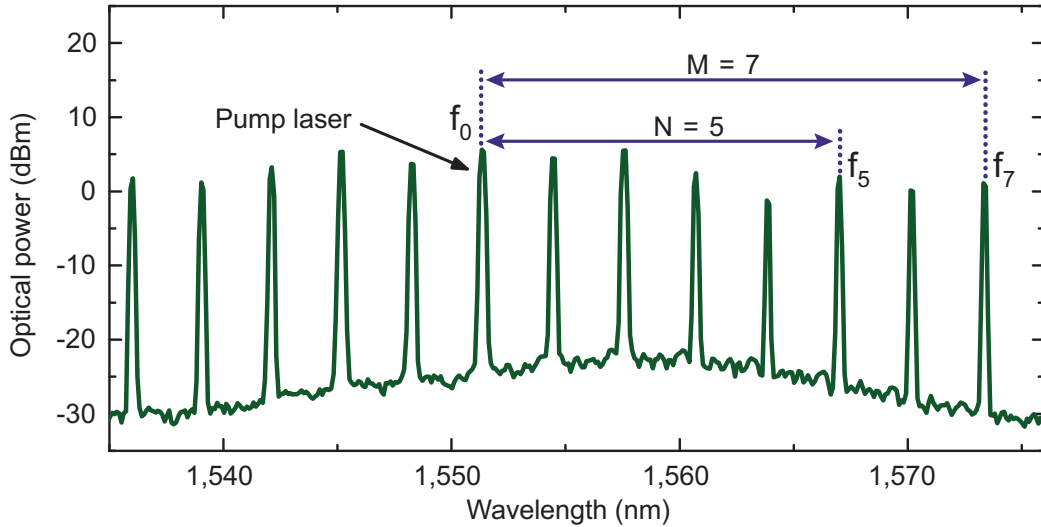
Figure 2.12: Optical microresonator comb spectrum for measurement of the equidistant mode spacing. The spacing of the comb modes is 386 GHz corresponding to a 172-μm-diameter resonator. Three heterodyne beat notes between the modes at f_0 (pump laser), f_5, f_7 and the respective modes of a fiber laser reference comb are generated. The pump laser beat note at f_0 is phase locked to a 10-MHz-reference signal. Subsequently, the equidistance of the comb modes is measured by frequency counting the beat notes of the sidebands at f_5 and f_7.

2.4.1   Equidistance measurement with two frequency counters

The probably most obvious method to obtain a measure for the equidistance of microresonator comb modes is the measurement of three different multiheterodyne beat notes between the microresonator comb and a reference comb. A variation of this principle is done by phase locking one of the comb modes (for simplicity the pump laser) to a known frequency and determine the frequency of two sidebands as shown in figure 2.10. In this case a quantitative value for the comb's equidistance follows from equation 2.10. At a first glance this methods appears to be the method of choice for equidistance measurements, however, it is required to measure the two sideband frequencies *at the same time.* This is essential as a result of the free-drifting mode spacing of the microresonator comb, which is subject to pump power and thermal perturbations as discussed in more detail in chapter 3. Unfortunately it is difficult to perform two frequency measurements at the same time using radio frequency counters. This is an intrinsic problem related to the working principle of high resolution frequency counters. The employed frequency counters (HP53131A) have an trigger input, however the actual counting period starts not with the trigger signal but with the next trigger signal of the applied time base. A detailed explanation of the working principle of high resolution frequency counters is given in appendix C. To improve the simultaneity of the frequency counting both the cable length for the counters trigger signal as well as the cable length for signal and 10-MHz-reference are matched. Assuming random mode spacing fluctuations, the measured values for the equidistance are expected
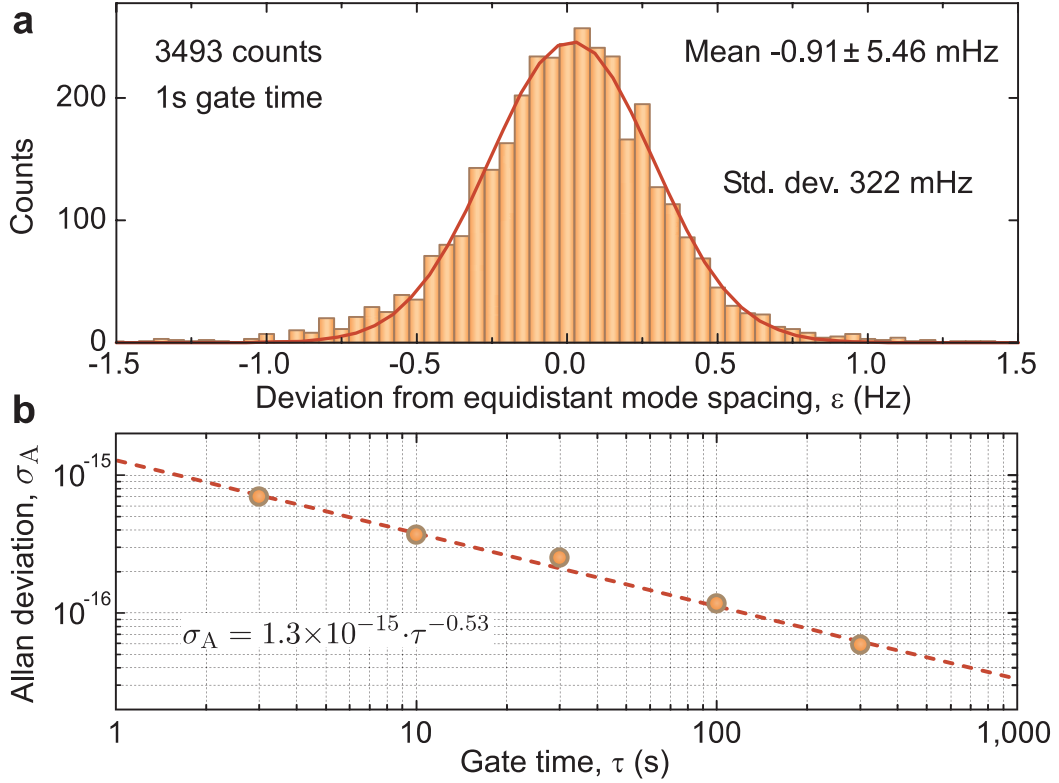
Figure 2.13: Measurement of the equidistance of a microresonator comb. The measurement is performed on the 5$^{\text{th}}$ and 7$^{\text{th}}$ sideband with a frequency locked pump laser (the corresponding optical spectrum is shown in figure 2.12). Panel a shows a bar plot of 3493 measured values of ϵ (according to equation 2.10) at a gate time of 1 second per measurement (total measurement time is approximately 1 hour). The mean value of ϵ is derived from a Gaussian fit and corresponds to $\bar{\epsilon} = (-0.91 \pm 5.46)$ mHz. The standard deviation of the distribution is 0.322 Hz. Panel b shows the modified Allan deviation [140] of ϵ at different gate times τ.

to show a larger scatter in case the frequency counters are not measuring simultaneously. Consequently longer measurement and more averaging is required with this equidistance measurement method to achieve a high accuracy.

Figure 2.13 shows an equidistance measurement with the microresonator comb spectrum in figure 2.12. Panel a depicts a bar plot of measured values for $\epsilon = \frac{f_7^{\text{rf}} - f_5^{\text{rf}}}{7-5} - \frac{f_5^{\text{rf}} - f_0^{\text{rf}}}{5}$. The measured values follow a Gaussian distribution with a standard deviation corresponding to $\sigma_{\text{std}} = 322$ mHz. In this measurement run a total of 3493 values for ϵ with a gate time of $\tau = 1$ s are recorded (corresponding to a total measurement time of approximately 1 hour). A Gaussian fit to the obtained ϵ-distribution confirms the equidistance of the generated microresonator comb down to a level of $\epsilon = (-0.91 \pm 5.46)$ Hz. Panel b of figure 2.13 shows a measurement of the modified Allan deviation σ_A [140] for gate times of up to 300 seconds. A fit reveals a behavior of $\sigma_A = 1.3 \times 10^{-15} \cdot \tau^{-0.53}$, which is expected for white frequency noise [140] as dominating noise source. The Allan deviation is determined

by

$$\sigma_A(\tau) = \frac{1}{2} \cdot \frac{1}{N-1} \cdot \frac{1}{f_0^2} \sum_{i=1}^{N} \left(\epsilon_{i+1} - \epsilon_i\right)^2 \quad . \tag{2.11}$$

with f_0 being the pump laser frequency and ϵ_i corresponding to the ith measurement of ϵ. Note that all the Allan deviations at a certain gate time τ are measured in separate runs and not stitched together from measurements at shorter gate times which would lead to wrong results [141]. The employed frequency counter is a lambda-type counter (HP53131A), such that the measured values correspond to the modified Allan deviation according to Dawkins et. al. [140]. Note that the counter dead times are significantly smaller than the gate time in all measurements, which is an important requirement for Allan deviation measurements.
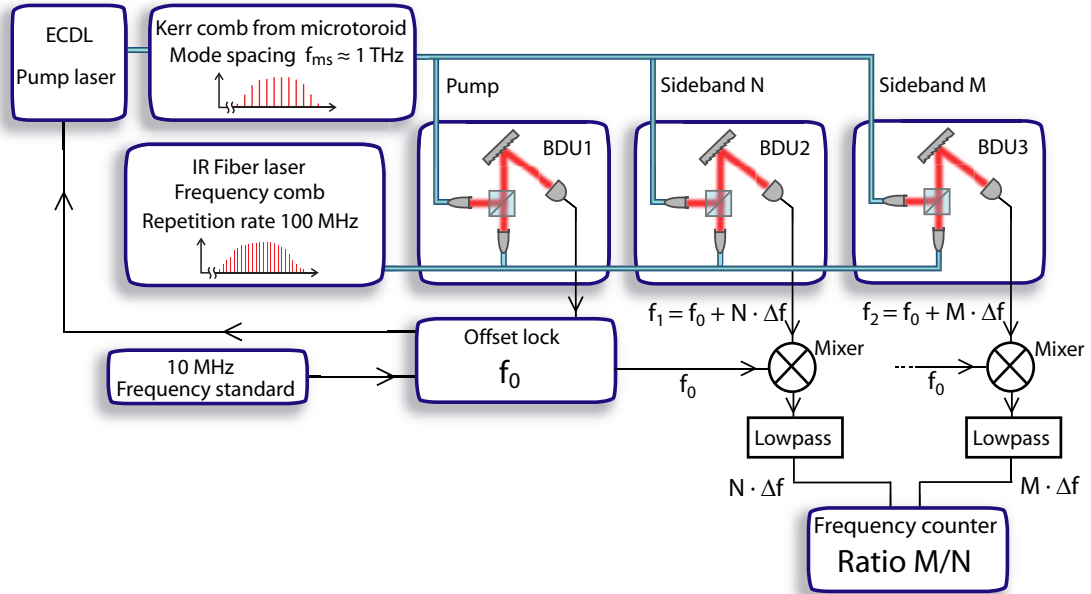
2.4.2   Beat note ratio measurements

High resolution frequency counters have inherent problems of measuring more than one frequency simultaneously (cf. appendix C). Thus, drifts in the beat note signals of measurements with two counters would influence the equidistance measurement in case the two beat notes are not measured at the same time. A method that can determine "equidistance" of the generated frequency comb with just one frequency counter might lead to a higher accuracy of the measurement. Many modern high-resolution frequency counters can measure frequency ratios of applied radio frequency signals. A simple explanation for this measurement scheme is the replacement of the normal 10-MHz-time-base by one of the signals, which allows to directly determine the ratio of the zero crossings of the two inputs. This feature of radio frequency counters can be used for direct determination of the ratio of two mode spacings of the microresonator comb. However, since the multiheterodyne beat notes are shifted by an "offset frequency" (eg. the beat note frequency of the pump laser), it is required to subtract this offset prior to the measurement that determines the ratio of two mode spacings. In general the ratio of the difference of two pairs of comb modes is given as

$$R = \frac{f_M^{\text{rf}} - f_0^{\text{rf}}}{f_N^{\text{rf}} - f_0^{\text{rf}}} = \frac{M}{N} \tag{2.12}$$

with f_0^{rf}, f_N^{rf} and f_M^{rf} being the radio frequency beat notes of the reference comb with the pump laser, the Nth and M^{th} sideband, respectively. Experimentally, the subtraction of the pump laser beat note frequency is realized by employing radio frequency mixers for nonlinear difference frequency generation and using the locking reference frequency for the pump laser stabilization and the respective sideband beat note frequency as input signals. In conjunction with a low pass filter it is possible to generate the frequencies $f_N^{\text{rf}} - f_0^{\text{rf}} = N \cdot \Delta f_{\text{rep\_rf}}$ and $f_M^{\text{rf}} - f_0^{\text{rf}} = M \cdot \Delta f_{\text{rep\_rf}}$ as shown in figure 2.14.

The deviation of the measured value for R from the expected value $\frac{M}{N}$ can be directly used as measure of the comb's equidistance. Figure 2.15 shows a measurement of the ratio $R = M/N = 7/5$ of the frequency differences between pump laser and the 7th and 5th

Figure 2.14: Experimental setup for direct measurement of the ratio of mode spacings in a microresonator-based frequency comb. The principle setup is similar to the one in figure 2.10. Three beat notes between a microresonator-based frequency comb and a fiber laser comb are generated. First, the beat note of the pump laser frequency f_0 is stabilized to a 10-MHz-frequency-standard. The beat notes of the Nth and M^{th} sideband at frequencies $f_1 = f_0 + N \cdot \Delta f$ and $f_2 = f_0 + M \cdot \Delta f$ are electronically processed with a radio frequency mixer and a lowpass filter. Mixing the sideband frequencies with the frequency f_0 (being used for pump laser frequency stabilization) leads to generation of the difference frequencies $N \cdot \Delta f$ and $M \cdot \Delta f$. The frequency ratio $\frac{M}{N}$ is a measure for the comb's equidistance and can be directly measured with a high-resolution frequency counter.
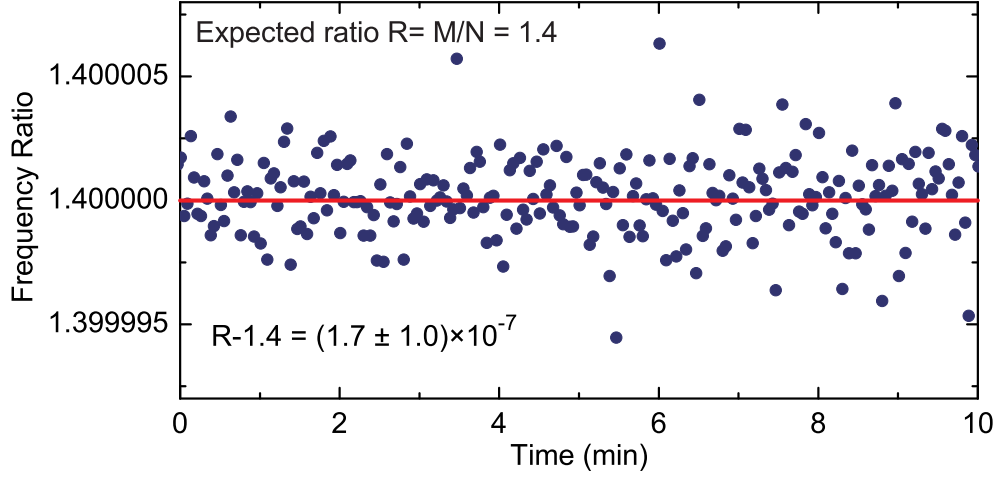
Figure 2.15: Ratio of the frequency offsets of the 7th and 5th sideband with respect to the pump laser in the microresonator-based frequency comb shown in figure 2.12. The ratio $R = 7/5 = 1.4$ is directly measured with the setup presented in figure 2.14 at a gate time of 1 second.

sideband. The measured value $R = 7/5 + (1.7 \pm 1.0) \times 10^{-7}$ is in good agreement with the expected value of $R = 7/5$.

2.5 Conclusion of equidistance measurements

Two methods for measurement of the equidistance of microresonator based frequency combs have been shown in the previous section. The first method is straight forward and determines a value for the equidistance of the comb's mode spacing by stabilizing the pump laser frequency and measuring the frequency of two other comb modes. In order to circumvent difficulties of simultaneous measurements with two frequency counters, the "ratio counting method" has been introduced. This method relies on direct measurement of the ratio of two frequency differences between comb modes, which should correspond to a rational number in case of an equidistant frequency comb. Finally, we have introduced the value ϵ (cf. equation 2.10) as a measure of the equidistance of a frequency comb. Equidistance values R measured with the "ratio counting method" according to the previous section can be converted to ϵ using

$$\epsilon = \frac{f_M^{\text{rf}} - f_N^{\text{rf}}}{M - N} - \frac{f_N^{\text{rf}} - f_0^{\text{rf}}}{N} = \frac{f_N^{\text{rf}} - f_0^{\text{rf}}}{M - N} \cdot R + \left(f_0^{\text{rf}} - f_N^{\text{rf}} \right) \cdot \frac{M}{(M - N) \cdot N} \quad , \tag{2.13}$$

with f_M^{rf}, f_N^{rf} and f_0^{rf} being the beat note of the Mth sideband, N^{th} sideband and the pump laser with the reference comb, respectively. Table 2.1 shows a summary of equidistance measurements at different gate times with the corresponding values for ϵ. These ϵ-values can be used to calculate a weighted mean that represents the stability of microresonator-based optical frequency combs. Using the standard error σ_ϵ of the values $\bar\epsilon$ as the weight, the weighted mean $\bar\epsilon_w$ is calculated as

$$\bar\epsilon_w = \frac{\sum \epsilon/\sigma_\epsilon^2}{\sum 1/\sigma_\epsilon^2} \tag{2.14}$$

and the corresponding error σ_{ϵ_w} of the weighted mean is derived from

$$\sigma_{\epsilon_w}^2 = \frac{1}{\sum 1/\sigma_\epsilon^2} \quad . \tag{2.15}$$

Taking all measurements from table 2.1 into account leads to a value of the comb equidistance of

$$\boxed{\bar\epsilon_w = (-0.8 \pm 1.4) \ \text{mHz}}$$

measured in a microresonator with a diameter of 172 μm and a corresponding mode spacing of 386 GHz. The value for $\bar\epsilon_w$ is measured over a bandwidth of 7 free spectral ranges of the resonator (2.7 THz bandwidth) and the accuracy of the comb's equidistance relative to the measurement bandwidth is

$$\boxed{\frac{\sigma_{\epsilon_w}}{2.7 \ \text{THz}} \approx 5.2 \times 10^{-16}}$$

Normalization to the optical carrier frequency of 193 THz ($\approx$ 1550 nm) yields a relative accuracy of the mode spacing equidistance in the order of 7.3×10^{-18}. This value describes the stability of sideband beat notes with an unknown light source assuming a stabilized pump laser with known frequency is used for the experiment. Note that 9 data points have been removed from the total of 8382 measurements that are used to determine the weighted mean of ϵ in table 2.1. These data points were more that 15 standard deviations off the mean value of the respective measurement and are expected to originate from the pump laser being out-of-lock.

Gate time (s)	Counts	$\bar{\epsilon} \pm \sigma_\epsilon$ (mHz)	StdDev of ϵ (Hz)	Method
0.03	217	-33 ± 556	8.2	ratio
0.1	223	-80 ± 181	2.7	ratio
0.3	293	2.4 ± 50.1	0.86	ratio
1	3493	-0.91 ± 5.46	0.32	2 counters
1	3499	3.9 ± 10.1	0.60	2 counters
1	98	-40.1 ± 27.4	0.27	ratio
1	179	8.0 ± 25.5	0.34	ratio
3	173	5.8 ± 12.6	0.17	ratio
10	22	-17.9 ± 15.0	0.070	ratio
30	39	1.65 ± 7.41	0.046	ratio
60	72	-1.88 ± 3.00	0.025	ratio
100	18	1.12 ± 5.98	0.024	ratio
100	42	-0.26 ± 2.69	0.017	ratio
300	14	-0.82 ± 2.83	0.011	ratio
Weighted Mean $\bar{\epsilon}_w$:		-0.8 mHz ± 1.4 mHz	-	-

Table 2.1: Measured mean values of ϵ at different gate times τ ($\epsilon \equiv 0$ is expected for a perfectly equidistant comb). Mean values $\bar{\epsilon}$ and standard error σ_ϵ are given in the third column. The second column shows the number of frequency counts for each measurement and the standard deviation of the corresponding ϵ distribution is given in the fourth column. The last column states the measurement method (either with two counters or direct measurement of the mode spacing ratio). The total measurement time sums up to 6 h 37 min.

CHAPTER 3

Stabilization and control of microresonator based frequency combs

3.1   Motivation

A light source emitting a large number of equidistantly spaced optical frequencies is an interesting tool for a variety of applications in both basic research and applied sciences. Several applications including channel generation for optical telecommunication or measurement of relative optical frequencies do not require a fully referenced and stabilized optical frequency comb and can solely rely on the intrinsic stability of the microresonator modes. However, highly accurate frequency measurements require referencing and stabilization to a primary frequency standard. This chapter shows that measurement and control of the offset frequency and the mode spacing of microresonator based frequency combs can be achieved by actuating on the power and frequency of the laser source that is used to pump the microcavity. The demonstration of frequency comb control goes along with an analysis of the intrinsic stability of microresonator based frequency combs, which is affected by intensity and frequency noise of the pump laser light in the microresonator as well as temperature and mechanical stability of the experimental setup. Two different schemes for the stabilization of microresonator based frequency combs are presented. In the first case, stabilization of a comb with a mode spacing exceeding 500 GHz is demonstrated by locking two different comb modes to neighboring comb lines of a conventional fiber laser based frequency comb. The second scheme demonstrates direct referencing of the mode spacing to a primary frequency standard by using millimeter size resonators with a mode spacing below 100 GHz, which is amenable to direct detection with a fast photodiode. The second degree of freedom in both schemes can be directly controlled and stabilized via the frequency of the pump laser, which is constituting one of the comb modes.

3.2   Basic principle of microresonator frequency comb stabilization

Active stabilization of a frequency comb requires control of mode spacing f_{rep} and offset frequency f_{ceo}, which define the position of each comb mode. The comb modes are located at the frequencies $f_n = f_{\text{ceo}} + n \cdot f_{\text{rep}}$ with n being an integer number. Microcavity-based frequency combs enable *direct access* to one of the comb lines via the pump laser frequency f_{p}, which is part of the frequency comb. Thus, it is convenient to rewrite the comb modes as

$$f_n = f_{\text{p}} \pm n \cdot f_{\text{rep}} \quad . \tag{3.1}$$

One degree of freedom of the microresonator comb can easily be controlled via the frequency of the pump laser f_{p}. However, control of the comb's mode spacing is more challenging, since a mechanical control of the resonator size is not a priori possible. In conventional mode locked lasers, the repetition rate can be controlled by changing the cavity length with piezo mounted mirrors. A similar approach was thought to be possible with chip based microresonators by slightly bending the whole chip with a piezo crystal to change

the geometry of the microresonator. This idea has been dismissed because it would require to bend the chip at a position that ensures that the rim of the microresonator does not move away from the coupling position relative to the tapered optical fiber. Thus, a simpler approach has been developed that uses the pump laser power as additional degree of freedom to gain full control of the combs mode spacing and offset frequency.

3.3 Thermal effects in monolithic microresonators for comb control

The two control parameters that are readily accessible during microresonator comb generation are the pump laser's frequency and power. To understand how to exploit these actuators to control a frequency comb, it is important to understand the impact on the microresonators modal structure due to variations of pump frequency and power.

3.3.1 Theoretical analysis of the thermal effect

The strongest effect on the resonance frequencies arises from the temperature dependence of the refractive index and the thermal expansion of the resonator material [94, 142, 143]. This allows us to use the heat equation for a toroid (equation 3.2) to determine the temporal and spatial temperature distribution $T(\vec{r}, t)$ of a toroid mode. This heat equation has a driving term proportional to the intracavity power distribution $P_{\mathrm{cav}}(\vec{r}, t)$ corresponding to the excited electromagnetic eigenmode of the resonator.

$$\frac{\partial}{\partial t} T(\vec{r}, t) - D \cdot \nabla^2 T(\vec{r}, t) = \frac{P_{\mathrm{cav}}(t) \cdot |\Psi(\vec{r})|^2 \cdot \eta_{\mathrm{abs}}}{V_{\mathrm{eff}} \cdot \rho \cdot c_p} \tag{3.2}$$

Here, D is the thermal diffusivity for fused silica, $|\Psi(\vec{r})|^2$ corresponds to the power distribution of the excited mode in the resonator (with $\int |\Psi(\vec{r})|^2 \, \mathrm{d}\vec{r} = 1$), η_{abs} is the absorption probability for a photon, V_{eff} is the effective mode volume of the resonator, ρ is the density of fused silica and c_p the specific heat capacity. Solving the heat equation requires knowledge of the intracavity power P_{cav}, which is not accessible a priori since it depends on the detuning of the laser with respect to the microresonator mode, which in turn is influenced by the light inside the cavity and the resonance line shape. In the steady state, the intracavity power is given by the following equation, assuming a Lorentzian line shape with a full width at half maximum of $\Delta\nu$ and a detuning $(\nu_L - \nu_c)$ between laser frequency ν_L and cavity mode ν_c:

$$P_{\mathrm{cav}} = \underbrace{P_{\mathrm{in}}}_{\substack{\text{launched} \\ \text{power}}} \cdot \underbrace{\eta_{\mathrm{ext}}}_{\substack{\text{coupling} \\ \text{efficiency}}} \cdot \underbrace{\frac{\mathcal{F}}{2\pi}}_{\substack{\text{cavity} \\ \text{enhancement}}} \cdot \underbrace{\frac{1}{1 + 4\left(\frac{\nu_L - \nu_c}{\Delta\nu}\right)^2}}_{\text{Lorentzian lineshape}} . \tag{3.3}$$

To solve the heat equation it is necessary to determine the connection between the cavity resonance frequency ν_c and the temperature. Assuming thermorefractive (refractive index n

changes with temperature) and thermoelastic (resonator size R changes with temperature) contributions we obtain

$$\nu_c = \frac{c_0}{2\pi R \cdot n} \cdot m \;\Rightarrow\; \frac{1}{\nu_c} \cdot \mathrm{d}\nu_c = \frac{1}{\nu_c} \cdot \left(\frac{\partial \nu_c}{\partial R} \cdot \mathrm{d}R + \frac{\partial \nu_c}{\partial n} \cdot \mathrm{d}n \right) = -\frac{1}{\nu_c} \cdot \left(\frac{\mathrm{d}R}{R} + \frac{\mathrm{d}n}{n} \right) \;, \quad (3.4)$$

with the vacuum speed of light c_0 and the angular optical mode number m of the resonance. Thus, the first order approximation for a resonance shift $\Delta\nu_c = \nu_c - \nu_{c0}$ with respect to the cold cavity mode ν_{c0} is given by

$$\Rightarrow\quad \frac{\Delta\nu_c}{\nu_{c0}} = -\left(\alpha + \frac{1}{n_0} \cdot \frac{\mathrm{d}n}{\mathrm{d}T} \right) \cdot \Delta T \;, \quad (3.5)$$

with the thermal expansion coefficient in fused silica $\alpha \approx 5.5 \cdot 10^{-7}\mathrm{K}^{-1}$ [64] and the temperature dependence of the refractive index with $\frac{\mathrm{d}n}{\mathrm{d}T} \approx 1 \cdot 10^{-5}\mathrm{K}^{-1}$ [64] and $n_0 \approx 1.44$. Using equation 3.5 and the heat equation 3.2 allows to calculate the temporal and spatial temperature distribution of a microresonator. However, experimentally more interesting values are the resonance shift and intracavity power as a function of power and frequency of the laser light being sent into the cavity. Assuming a linear dependence between the intracavity power P_{cav} and the effective resonator temperature, we can write the resonance frequency as

$$\nu_c = \nu_{c0} + \Gamma_p^* \cdot P_{\mathrm{cav}} \;. \quad (3.6)$$

Γ_p^* is a resonator specific constant and can be experimentally determined by measuring the maximum resonance shift $(\nu_c^{\mathrm{max}} - \nu_{c0})$ while slowly sweeping the laser frequency across a resonance. At the point of the maximum resonance frequency shift, the relation between launched power P_{in} and intracavity power is given by the cavity enhancement multiplied with the coupling efficiency $(\frac{\mathcal{F}}{2\pi} \cdot \eta_{\mathrm{ext}})$.

$$\nu_c^{\mathrm{max}} = \nu_{c0} + \Gamma_p^* \cdot P_{\mathrm{cav}}^{\mathrm{max}} = \nu_{c0} + \underbrace{\Gamma_p^* \cdot \frac{\mathcal{F}}{2\pi} \cdot \eta_{\mathrm{ext}}}_{=:\Gamma_p} \cdot P_{\mathrm{in}} \;. \quad (3.7)$$

Here, we have defined a parameter Γ_p for the resonance shift per launched power, which depends on the amount of absorbed power within the resonator material as well as the geometry of the resonator. Typical values are in the range of $-500\ \mathrm{MHz/mW} < \Gamma_p < -50\ \mathrm{MHz/mW}$ (cf. figures 3.6 and 3.7).

With knowledge of Γ_p^* we can rewrite equation 3.3 as

$$P_{\mathrm{cav}} = P_{\mathrm{in}} \cdot \eta_{\mathrm{ext}} \cdot \frac{\mathcal{F}}{2\pi} \cdot \frac{1}{1 + 4\left(\frac{\nu_L - \nu_{c0} - \Gamma_p^* \cdot P_{\mathrm{cav}}}{\Delta\nu} \right)^2} \;. \quad (3.8)$$

This equation can be solved for P_{cav} and enables to understand the connection between the cavity parameters (intracavity power P_{cav} and resonance frequency ν_c) and the external degrees of freedom (launched power P_{in} and laser frequency ν_L).
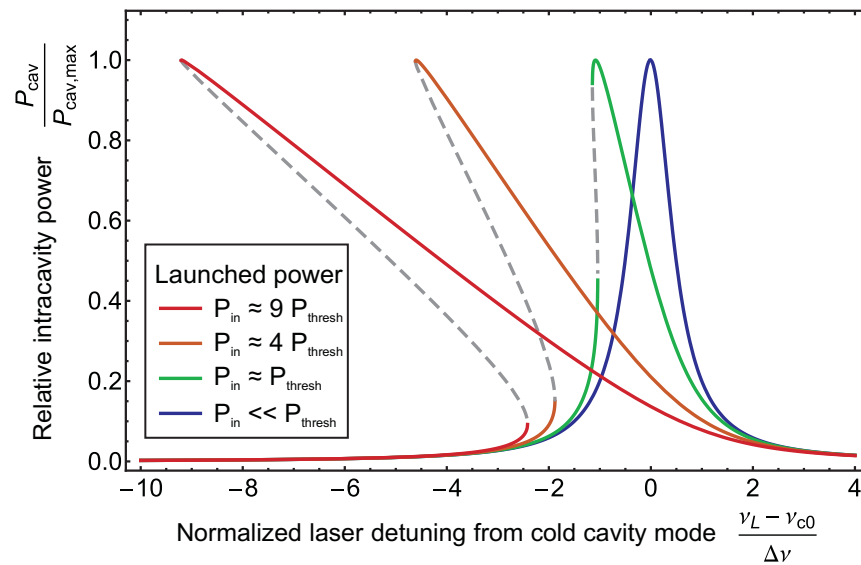
Figure 3.1: Intracavity power as a function of laser frequency. The horizontal axis corresponds to the frequency of the laser source coupled to a microresonator and is displayed in units of the cavity linewidth $\Delta\nu$ and shifted such that the cold resonance frequency is at zero detuning. For convenience, the vertical axis is normalized to the maximum intracavity power determined by the cavity's finesse. At low power levels below the threshold of the thermal effect, a Lorentzian line shape is observed (blue curve). Increasing the launched power leads to a bistability with the dashed lines being intrinsically unstable solutions of equation 3.8.
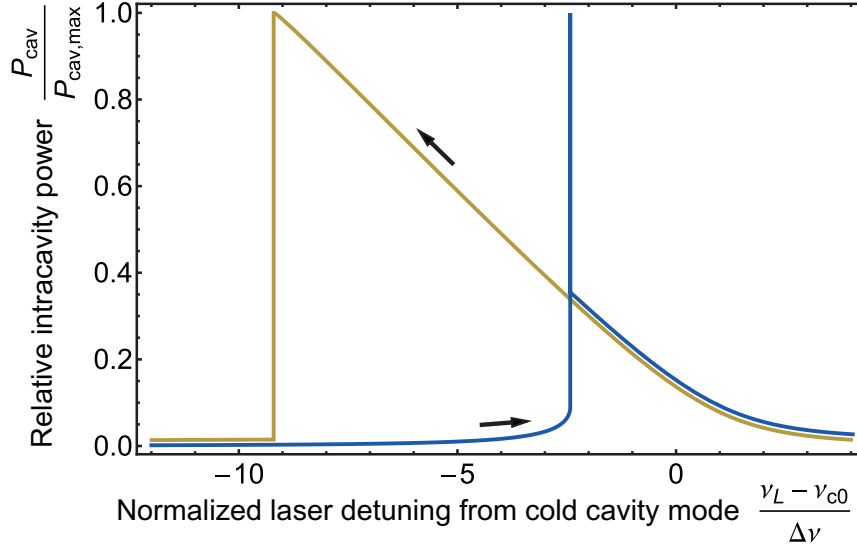
Figure 3.2: Distorted line shape of a fused silica microresonator measured with a scanning laser source. Coupling laser light into the resonator leads to heating and a resonance shift towards lower frequencies. As a result, scanning a laser source from high to low frequencies across a microresonator mode (yellow line) leads to an artificial broadening of the resonance while approaching the resonance from lower frequencies leads to observation of a narrowed resonance (blue line). The vertical "jumps" of the intracavity power correspond to a change of the detuning between laser frequency and resonance frequency at the transition to the dashed lines in figure 3.1. Note that this figure depicts the observed line shape for a laser source scanning slower than the thermal response time of the resonator.

Figure 3.1 depicts the optical power inside the resonator (normalized to the maximum intracavity power $P_{\text{cav}}^{\max} = P_{\text{in}} \cdot \eta_{\text{ext}} \cdot \frac{\mathcal{F}}{2\pi}$) as a function of the pump laser frequency. At low pump powers, the cavity mode is traced out by a sweeping laser revealing the natural Lorentzian lineshape. However, at a certain threshold power, the lineshape starts being deformed owing to heating of the microresonator. This threshold power can be approximated as the power that is required to generate a maximum shift of the cavity mode that corresponds to its optical linewidth $\Delta \nu$. With knowledge of the resonance shift per launched power Γ_p, this threshold is given by $P_{\text{thresh}} = \Delta \nu / \Gamma_p$ and is typically in the order of less than 1 μW of launched power. The curve at $P_{\text{thresh}} \approx P_{\text{in}}$ in figure 3.1 shows the cavity response close to the threshold. Since equation 3.8 is a cubic equation in P_{cav}, it has up to three real solutions (corresponding to the different segments in the graphs in figure 3.1). One of the solutions at higher pump powers is intrinsically unstable (dashed lines). Small perturbations in this regime are significantly increased and will change the intracavity power to one of the stable solutions (solid lines).

As a result, scanning a laser source with a power above the thermal threshold power leads to an observed cavity line shape that depends on the scanning direction of the laser source. Figure 3.2 shows a typical response of the intracavity power to a swept laser in a fused silica resonator. When slowly scanning the laser from lower to higher frequencies
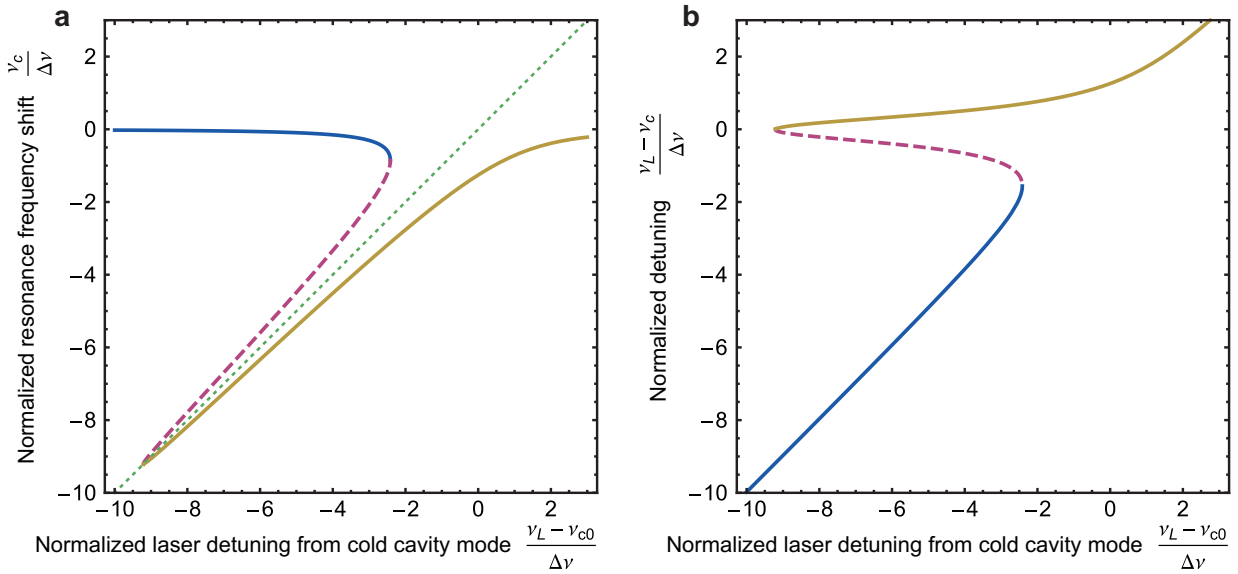
Figure 3.3: Microcavity resonance frequency response to the pump laser frequency. Panel **a** shows the shift of a microresonator resonance (normalized to the cavity linewidth $\Delta\nu$) with respect to the pump laser frequency ν_L. The laser frequency on the horizontal axis in both panels is offset by the cold cavity resonance frequency ν_{c0} and displayed in units of cavity linewidths $\Delta\nu$. Approaching the resonance frequency of a microresonator from the high frequency side (blue detuned) will shift the microcavity resonance to lower frequencies (yellow curve in panel **a**) while slowly decreasing the detuning between pump laser and cavity mode (yellow curve panel **b**). After reaching the maximum possible resonance shift $\nu_c^{\max}$ (cf. equation 3.7) the cavity resonance will jump back to the cold cavity's position on the blue curve. Approaching the resonance frequency from the red detuned side will just slightly shift the resonance frequency in the vicinity of the cold cavity mode (blue curves) and finally lead to an abrupt change of the sign of the detuning (corresponding to a "jump" back to the yellow curve). Dashed lines correspond to intrinsically unstable solutions and cannot be observed experimentally.

(blue curve), the intracavity power will increase when approaching the resonance and leads to a shift of the microresonator mode towards the laser, which in turn leads to a further increase in intracavity power. This eventually makes the resonance "jump" to the blue detuned side of the laser and as such, the experimentalist observes an artificially narrowed cavity mode. On the other hand, when approaching resonator mode from higher frequencies (blue detuned laser), the microresonator resonance frequency is shifted away from the laser frequency and leads to an artificially broadened resonance. This regime is especially interesting for using microresonators as frequency comb sources, as it allows for stable thermal locking of the resonator's resonance frequency to the employed laser source. At high pump powers this stable range can exceed 1 THz of optical frequencies (as shown in figure 3.8).

After knowing the relation between laser frequency and intracavity power, we can determine the microresonator resonance frequency ν_c as function of the laser frequency ν_L at

a fixed input power. This is shown in figure 3.3a as resonance frequency shift (in units of cavity linewidths) and as detuning between pump laser and resonance frequency in figure 3.3b (also in units of cavity linewidths). The horizontal axis in both panels corresponds to the laser frequency detuning with respect to the cold cavity mode position ν_{c0} (again in units of cavity linewidths). The color coding in figure 3.3 corresponds to the color coding in figure 3.2 and the dashed line shows again the unstable equilibrium that cannot be experimentally realized. The intrinsic instability of this regime can be explained by analyzing the laser/cavity detuning in this regime. It is obvious from figure 3.3b that the laser frequency ν_L is at a lower frequency than the cavity mode at ν_c (the laser is red detuned). In this case, a small power fluctuation in the cavity will be amplified by the changed detuning (eg. a small intracavity power increase will shift the resonance to lower frequencies as shown before and leads to a further increase of intracavity power). This lets the laser detuning jump to one of the stable curves. In case of a small increase of intracavity power, the microcavity resonance frequency will jump to the stable yellow line, while in case of a small intracavity power reduction a stable equilibrium on the blue curve will be reached.

Besides the pump laser frequency, the second accessible quantity that influences the intracavity power and resonance frequency is the optical power sent to the microresonator. Figure 3.4 shows the behavior of the intracavity power when the launched power is changed. The different rows in the figure correspond to different fixed detunings between laser frequency and cold cavity resonance position ($\nu_L - \nu_{c0}$). For positive and zero detunings, the intracavity power is slowly increasing with the launched power since the cavity heats up and the resonance frequency is shifted away from the pump laser. However, with a negative detuning, the cavity mode is first pulled towards the pump laser due to the heating, crossing it and finally being pushed away towards smaller frequencies (third row in figure 3.4). At negative detunings beyond one cavity linewidth, it is possible to observe a bistability with a hysteretic behavior of the intracavity power when changing the launched power. This is a result of the increased demand of launched power to attract the microresonator mode such that it directly "jumps" to the blue detuned side of the laser (yellow curve) at a certain threshold power.

Figure 3.5 depicts the normalized frequency detuning between laser and cavity resonance at different pump powers. This curve has been calculated with a fixed red detuned pump laser frequency at $\nu_L - \nu_{c0} = -1.8\Delta\nu$. It shows the same hysteretic behavior in the detuning as the the intracavity power in figure 3.4. This curve is of importance for the stabilization of a microresonator based frequency comb since it shows how the cavity mode spectrum can be controlled by the pump power at a fixed pump laser frequency.

3.3.2   Experimental measurement of the thermal effect

In the theoretical discussion it has been shown that the thermal nonlinearity of a microresonator can be fully described by the resonator constant Γ_p. Using equation 3.7 we obtain
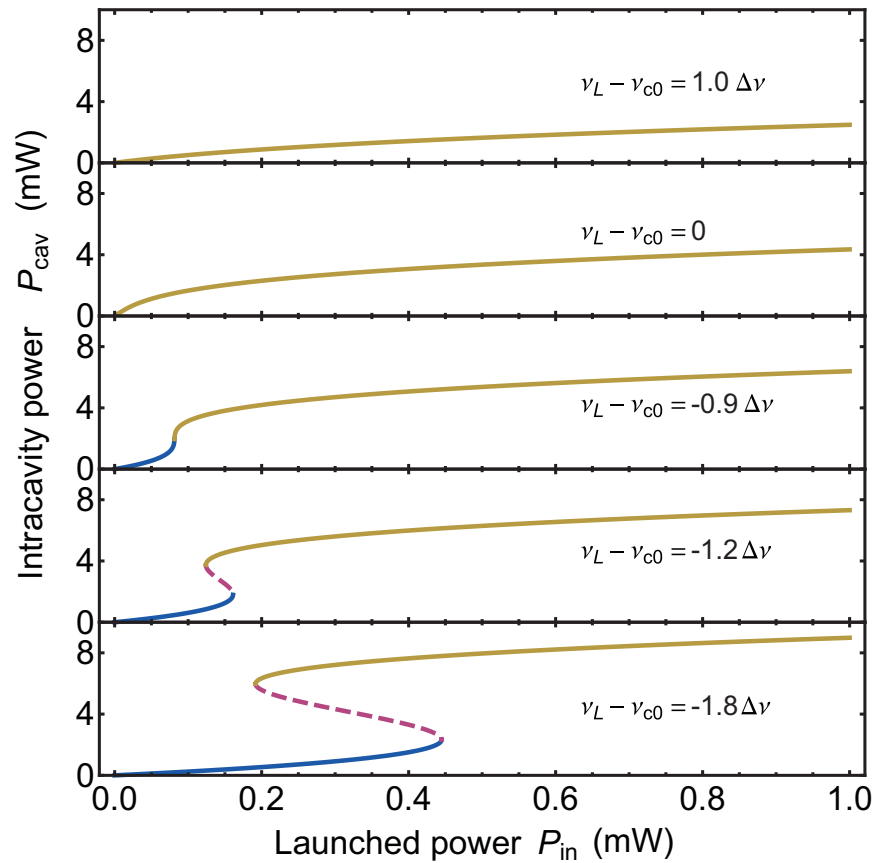
Figure 3.4: Intracavity power as a function of the launched power. The rows correspond to different fixed pump laser frequencies ν_L (displayed as detuning from the cold cavity mode ν_{c0} in units of cavity linewidths $\Delta\nu$). At a negative detuning smaller than $-\Delta\nu$ a hysteretic behavior of the intracavity power is observed. Dashed lines are intrinsically unstable and cannot be observed experimentally.
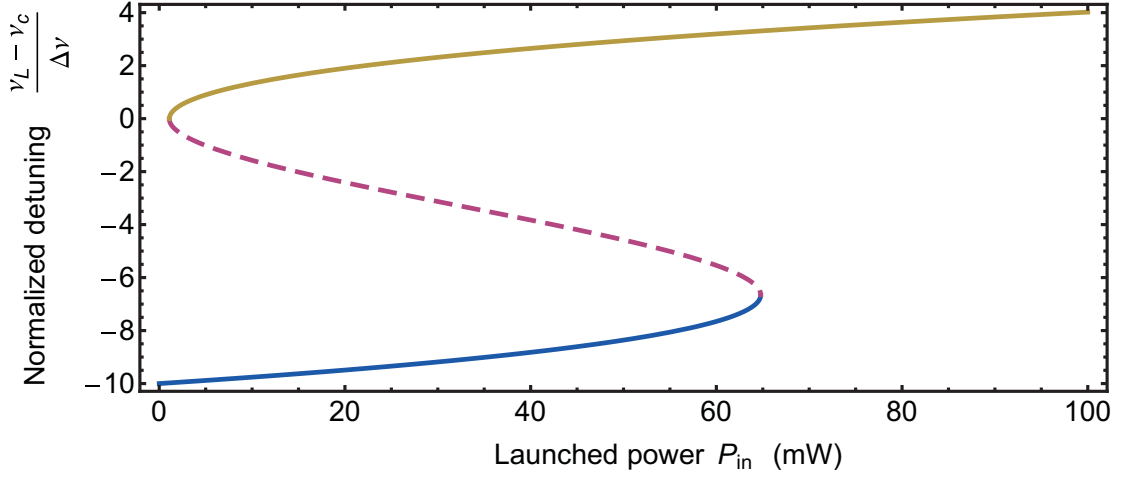
Figure 3.5: Normalized detuning between laser frequency and cavity resonance as function of the launched laser power P_{in}. The laser frequency is fixed with $\nu_L - \nu_{c0} = -1.8\Delta\nu$. The dashed line corresponds to an unstable regime and cannot be observed experimentally. The upper yellow part of the curve can be used for an active stabilization of the mode spectrum of a microresonator by controlling the launched power.

$$\Gamma_p = \frac{\mathrm{d}\nu_c^{\max}}{\mathrm{d}P_{\text{in}}} \quad , \qquad (3.9)$$

which allows to determine Γ_p by measuring the variation of the maximum resonance frequency shift in the thermally broadened resonance with the launched power. Figure 3.6b shows such a measurement with a 750-μm-diameter toroidal resonator. The data is offset such that the cold microresonator mode is located at zero. Scanning the laser from high to low frequencies yield the expected triangular shaped broadened resonance (cf. theoretical calculation in figure 3.2). Note that the transmitted power through the tapered optical fiber on the vertical axis is inverted compared to the power coupled into the resonator, similar to a Fabry-Pérot resonator with minimum transmission on resonance.

The data in figure 3.6b has been obtained by periodically sweeping a tunable diode laser across the resonance and by simultaneous stepwise variation of the launched power. The transmission of the tapered fiber is sent to a fast photodiode which is connected to an oscilloscope recording the transmission trace of the resonator. Calibration of the laser frequency is achieved by employing an electro optic phase modulator to generate calibration sidebands on the laser signal at a know frequency. It can be seen that the maximum resonance frequency shift is increasing at higher launched powers. Figure 3.6a shows the derived resonance frequency shift as function of the input power and a linear fit with a slope that corresponds to Γ_p in this respective cavity.

Figure 3.7 shows a laser sweep across a microresonator resonance and a measurement of Γ_p in a smaller fused silica microtoroid. The characteristic thermal broadening for a frequency sweep from high to low frequencies can be observed as well as the narrow resonance for a sweep from low to high frequencies. This effect has already been described
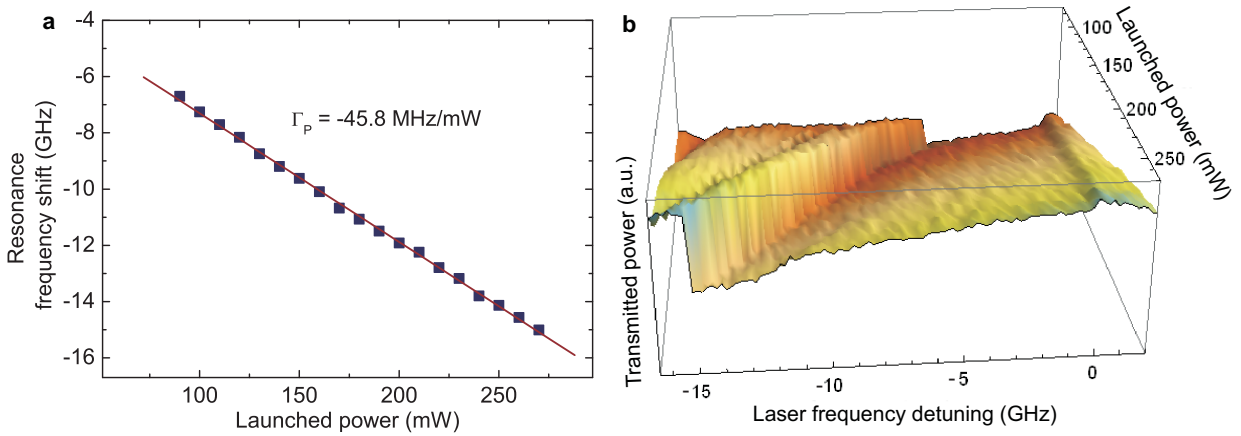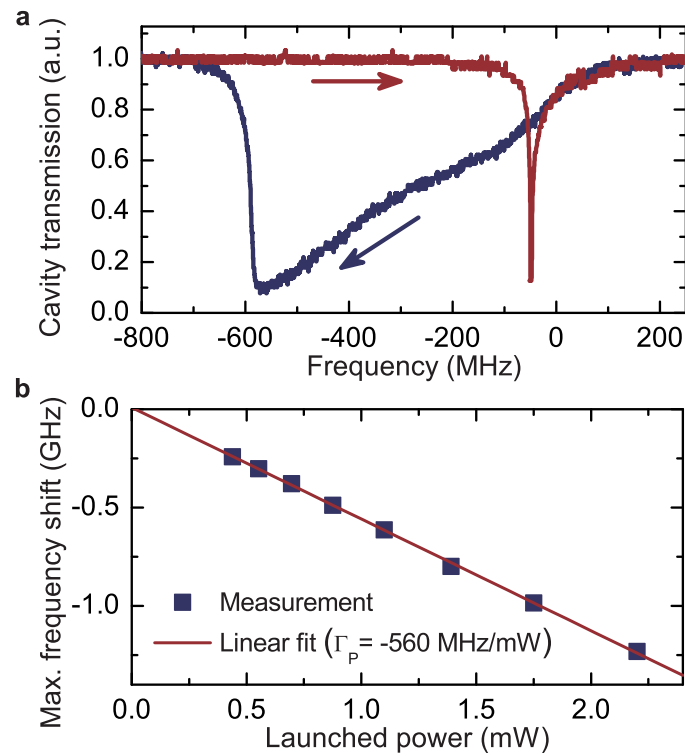
Figure 3.6: Thermal resonance frequency shift in a 750-μm-diameter microresonator with a free spectral range of ≈ 87 GHz. Panel **a** shows the maximum resonance frequency shift $\nu_c^{\max}$ as a function of the launched power. The data is taken from the measurement in panel **b**, showing a thermally broadened microresonator mode (probe laser is scanning from high to low frequencies) at different launched powers. The measured value for the cavities thermal response is $\Gamma_p \approx -46 \frac{\text{MHz}}{\text{mW}}$.

in the theoretical analysis (cf. figure 3.11). The diameter of the measured resonator is around 70 μm and the frequency shift with the launched power is one order of magnitude larger than the shift in the resonator in figure 3.6. The value of Γ_p depends on the amount of absorbed power within the resonator material as well as the heat dissipation, which in turn depends on the specific resonator geometry. Moreover, the parameter Γ_p is of interest for the tunability of a generated frequency comb. The value of $\Gamma_p \approx 500 \frac{\text{MHz}}{\text{mW}}$ for a resonator with 70 μm diameter (and a corresponding mode spacing of $\nu_{\text{FSR}} \approx 1$ THz) allows for shifting the resonator's resonance frequencies to arbitrary frequencies at pump powers as low as $P = \nu_{\text{FSR}}/\Gamma_p \approx 2$ W. The thermal response of the bigger resonator in figure 3.6 is smaller with $\Gamma_p \approx -50 \frac{\text{MHz}}{\text{mW}}$, however it also has a smaller mode spacing of ≈ 87 GHz so that a tuning over a full free spectral range requires roughly the same power level of around 1.7 W.

Figures 3.8 and 3.9 show actual measurements proving that it is indeed possible to tune microresonator based frequency combs over more than one free spectral range! This remarkable result allows to position comb modes at every desired frequency within the comb bandwidth. Figures 3.8 and 3.9 depict the color coded optical comb spectrum at different pump frequencies (vertical axis). The thermal effect allows the microresonator modes to follow the pump laser frequency in a tuning range exceeding 1 THz, while an octave spanning frequency comb from 140 THz to 280 THz is maintained over nearly 500 GHz tuning range in figure 3.8. Continuous tuning of f_{ceo} via pump frequency tuning is a distinguishing feature of the microresonator based combs and has so far not been achieved with optical frequency combs based on mode locked lasers. The inset of figure 3.8 is a zoom into a part of the spectrum, showing a shift of the comb modes of more than one free spectral range of the microresonator. The microresonator resonance pumped by

Figure 3.7: Thermal resonance frequency shift in a 70-μm-diameter microresonator. Panel **a** shows the measured transmission signal of a microresonator mode for a laser sweep in different directions. The scan from high frequencies to low frequencies results in a thermally broadened lineshape, while the sweep in opposite direction shows a narrowed lineshape as predicted in the theoretical discussion (cf. figure 3.2). The launched power in this measurement is around 1 mW. Panel **b** depicts the the maximum resonance shift of a series of laser sweeps at different laser powers and yields the resonator parameter Γ_p, which is in the order of -500 MHz/mW.
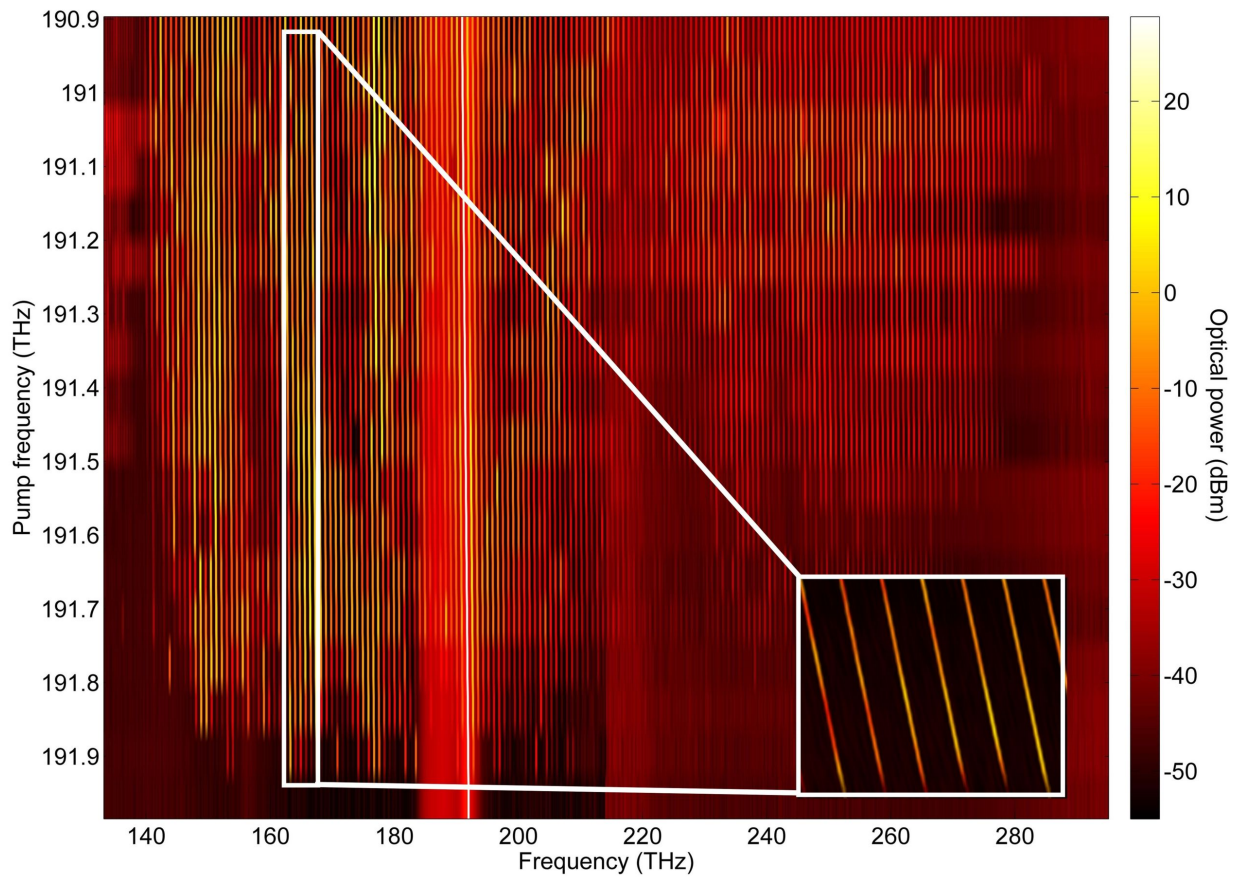
Figure 3.8: Tunable octave spanning microresonator based frequency comb. The horizontal axis shows the measured frequency comb at different pump laser frequencies (vertical axis). The brightest line corresponds to the pump laser (with a power of 1 W in this measurement). It can be seen that the whole frequency comb is uniformly shifted by more than one mode spacing as the pump frequency is detuned (inset).
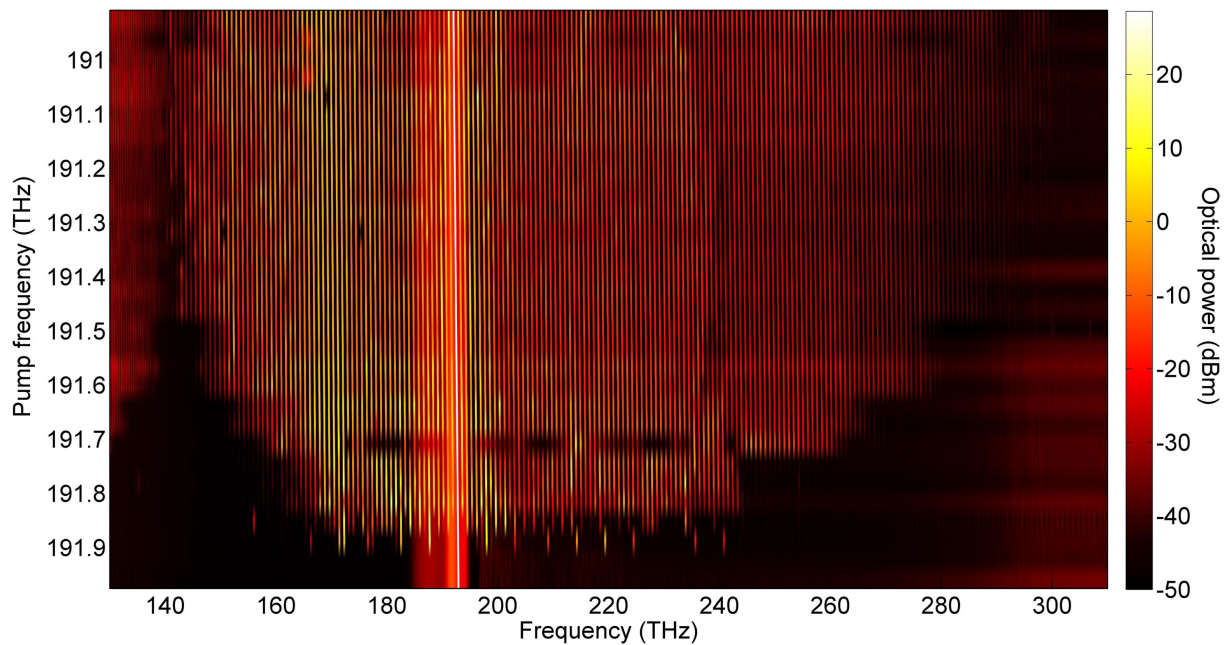
Figure 3.9: Pump frequency tuning range and impact on the comb spectrum. This measurement shows the comb spectrum evolution of a frequency comb with smoother amplitude variations but slightly smaller bandwidths compared to the comb in figure 3.8. At high pump laser frequencies corresponding to large detuning from the cavity resonance the spectrum shows combs with mode spacings of 6 times and 2 times the cavity free spectral range.

the tunable diode laser is shifted from 1561.8 nm to 1570.2 nm, equating to a continuous frequency shift of 1 THz. Since this frequency shift only depends on material properties of the microresonator, namely the thermal expansion, thermally induced refractive index change and the optical Kerr effect, it is possible to derive the temperature change of the resonator material. For this calculation the contribution of the Kerr effect is subtracted first, being responsible for a substantial resonance shift of $\Delta\nu_{\text{Kerr}} \approx 100$ GHz, which can be derived from equation 3.10 using the parameters for a 80-μm-diameter microresonator with a measured optical quality factor of $Q \approx 2 \times 10^8$, a mode cross section of $A_{\text{eff}} \approx 4\ \mu\text{m}^2$ and a launched power of $P_{\text{in}} \approx 1$ W:

$$\Delta\nu_{\text{Kerr}} \approx \frac{n_2}{n_0^2} \cdot \frac{c}{4\pi^2 \cdot R \cdot A_{\text{eff}}} \cdot P_{\text{in}} \cdot Q \tag{3.10}$$

The remaining parameters are the linear ($n = 1.44$) and nonlinear ($n_2 = 2.2 \times 10^{-20}\ \frac{\text{m}^2}{\text{W}}$) refractive index of fused silica and the speed of light in vacuum c. Subtracting the Kerr contribution leads to a mode shift of 900 GHz that is thermally induced. This thermal shift $\Delta\nu_{\text{therm}}$ can be described by

$$\frac{\Delta\nu_{\text{therm}}}{\nu} = a \cdot \Delta T \quad , \tag{3.11}$$

where $a = 6 \times 10^{-6}$ K^{-1} is a combined constant describing both the thermal expansion and thermally induced refractive index change of fused silica. Inserting the frequency of the pump laser $\nu = 192$ THz this equates to a remarkably high temperature change of $\Delta T \approx 800$ K. However, this temperature is still well below the annealing point at 1215 °C and the softening point at 1683 °C of fused silica [64]. This thereby demonstrates the stability of the approach which even under such strong heating allows stable and long term optical frequency comb generation.

On first notice, the data in figures 3.8 and 3.9 implies that the whole comb is shifted uniformly, which would correspond to a pure carrier envelope offset frequency change. However, a closer inspection of the comb modes reveals that the mode spacing is also affected by the pump laser frequency variation. The reason for this is the change in intracavity power due to the varying detuning between pump laser and microcavity mode [4]. Making use of the high number of comb modes, the comb spacing can statistically be determined much more precisely than expected from the resolution bandwidth of the optical spectrum analyzers, which was set to 25 GHz. Figure 3.10b and 3.10c show the variation of the mode spacing and the carrier envelope offset frequency as a function of the pump laser frequency (all the data has been derived from the optical spectra of the frequency combs). It can be seen that the influence of the pump laser detuning on the mode spacing is rather small with 4.83 GHz/THz compared to the impact on the carrier envelope offset frequency which equates to 153 GHz/THz. Figure 3.10a depicts the measured shift of the $\pm 25^{\text{th}}$ and $\pm 50^{\text{th}}$ comb modes as a function of the pump frequency and is displayed together with the calculated shift of the carrier envelope offset frequency. The zero position of the frequency shifts is set to the position of the cold microresonator mode that is used for comb generation.
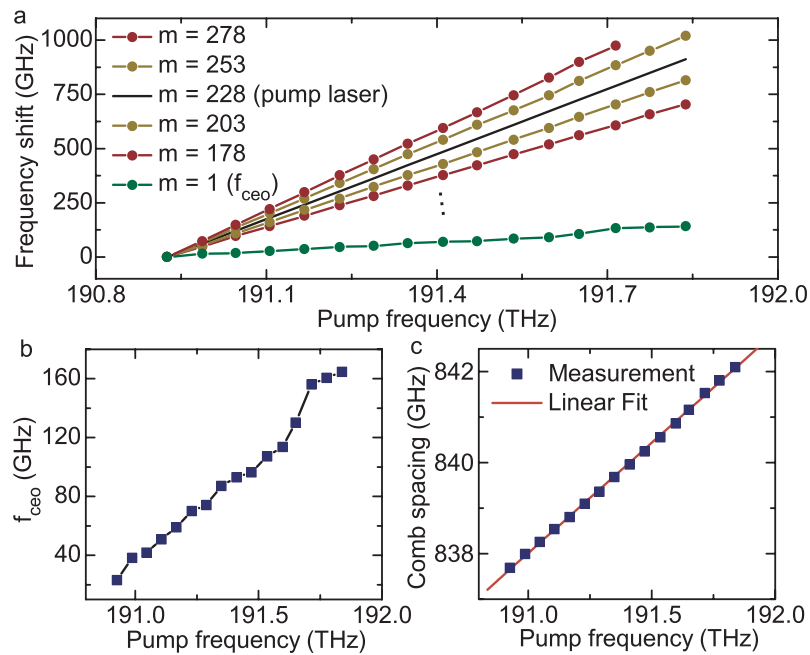
Figure 3.10: Microresonator based frequency comb tuning parameters. Panel a shows the measured frequency shift of the $\pm 25^{\text{th}}$ and $\pm 50^{\text{th}}$ sideband with respect to the pump laser at different pump laser detuning. The black line has a slope of 1 and depicts the shift of the pump laser itself. The green line shows the shift of the carrier envelope offset frequency f_{ceo}. Panel b and c show the effect of the pump frequency detuning on the carrier envelope offset frequency f_{ceo} and the comb spacing.
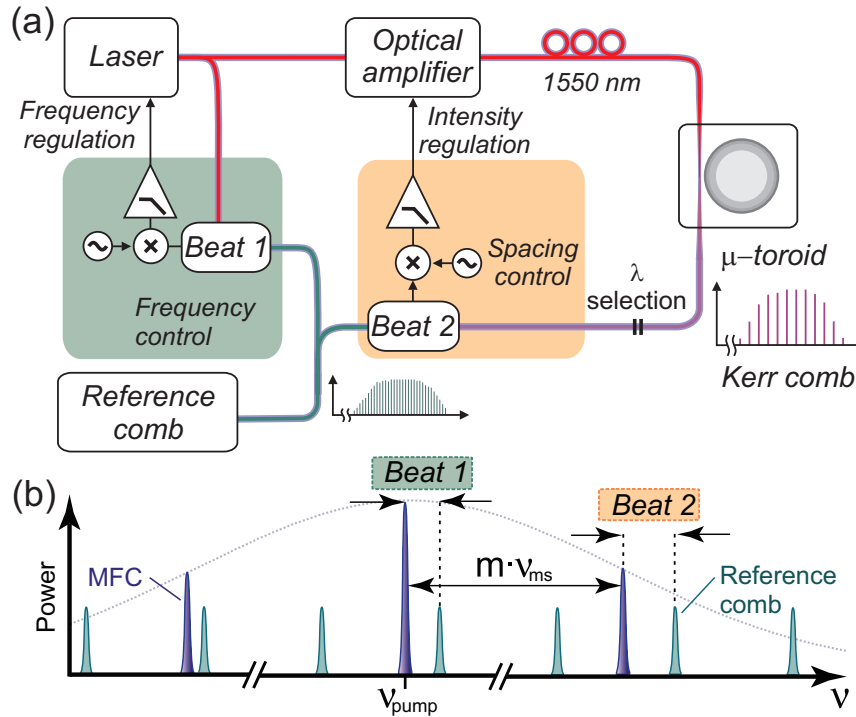
Figure 3.11: Frequency comb stabilization. (a) Scheme of the experimental setup used for stabilizing a microcavity frequency comb. An external cavity diode laser is tuned into a microcavity resonance and phase locked to a fully stabilized reference frequency comb ("Beat 1"). Simultaneously, one sideband of the microcavity comb (selected by a grating) generates a second beat note ("Beat 2") that is utilized to stabilize the mode spacing via the pump power. (b) Illustration of the corresponding beat notes between the microcavity comb and the reference comb. The modes labeled with "MFC" correspond to the microresonator frequency comb modes with a mode spacing of ν_{ms} and m being the number of the sideband (counting from the pump mode) used for stabilization.

3.4 Stabilization of high repetition rate combs

In the case of microresonators with a mode spacing beyond 100 GHz it is challenging to directly measure the mode spacing of the frequency comb and stabilize it to a reference frequency. However, a workaround to stabilize frequency combs at high repetition rates is the stabilization via locking of the comb modes to a reference comb with smaller repetition rate. Having just two degrees of freedom, it is possible to fully stabilize a frequency comb by locking two of its modes to neighboring modes of a reference comb.

The experimental setup and basic principle of such a stabilization scheme is depicted in figure 3.11. This setup is used to both control and stabilize the optical spectrum of the microresonator based frequency comb. One degree of freedom of the optical frequency comb can be stabilized via the pump laser frequency. This is achieved by generating beat notes between the pump laser and the modes of the reference frequency comb. A

fiber laser based frequency comb with a repetition rate of 100 MHz [113] is used for the measurements. First the pump laser is offset locked to a neighboring comb mode with a beat note frequency of 20 MHz ("Beat 1" in figure 3.11b). This beat note is stabilized using a digital phase locked loop (for details see appendix B) that can track up to 16π phase difference between the beat note and the employed local oscillator. The local oscillator signal used for the stabilization is obtained from a frequency synthesizer that is referenced to an in-house GPS-disciplined hydrogen maser. The same signal is used for stabilization of the reference frequency comb, however, for the presented measurements it is only important that both reference comb and beat notes with the microresonator-based frequency comb are stabilized with the same reference signal. The 20-MHz-beat-note signal is filtered with a narrowband RF-filter in order to improve the signal to noise ratio prior to sending it to a digital comparator and a "**P**roportional–**I**ntegral–**D**erivative"-controller (PID). The generated correction signal from the PID-controller is sent to the tunable diode laser current control input (having a bandwidth of 1 MHz in the employed "Velocity" laser system from "New Focus"). Using this static setup it is possible to lock the pump laser frequency at frequencies in steps of the 100-MHz-repetition rate of the reference laser, which is a sufficient frequency resolution since the thermal effect of the microresonator allows the microresonator mode to follow the pump laser more than 50 GHz at power levels of 100 mW. Note that the stabilization of the pump laser can be realized already before sending it to the microresonator as depicted in figure 3.11a. The stabilized pump laser signal is subsequently amplified with a home-made erbium doped fiber amplifier (EDFA) operated in saturation. It is important to operate the EDFA in saturation to eliminate the pump power fluctuations arising from the frequency stabilization of "Beat 1" via the diode laser power. Additionally, the amplifier has a fast current modulation input that can be used to control the output power with a modulation bandwidth of up to 50 kHz (via a "Pro 8000" system laser diode controller with a "LDC8010" current controller). The maximum pump power in this setup is in the order of 300 mW at 1550 nm wavelength and is directly sent to the microresonator for frequency comb generation. The output of the tapered optical fiber that used for light coupling into the microresonator is sent to a 3-nm-wide tunable optical filter to select a microcavity frequency comb sideband for generation of "Beat 2" in figure 3.11b. This beat note signal is then sent through a narrowband RF filter ($\approx$ 2 MHz bandwidth) and to a digital phase locked loop generating a correction signal that is fed to the current modulation input of the EDFA for mode spacing control and stabilization of "Beat 2" to the reference frequency applied to the digital phase locked loop. The mode spacing change due to the pump power variation can be explained by the resonance shift due to the thermal effect in the microresonator and is shown in detail in section 3.3 and in figure 3.5. Note that the pump laser frequency and correspondingly the central comb line is not affected by changing the launched power via the EDFA, such that this actuator just controls the mode spacing of the comb lines.

In addition to the stabilization of the frequency comb, the signals from "Beat 1" and "Beat 2" are simultaneously recorded with radio frequency counters (HP 53131A) in order to determine the stability of the comb. Figure 3.12 shows the measured stability of the comb generated from a fused silica toroid with a diameter of 165 μm and a corresponding
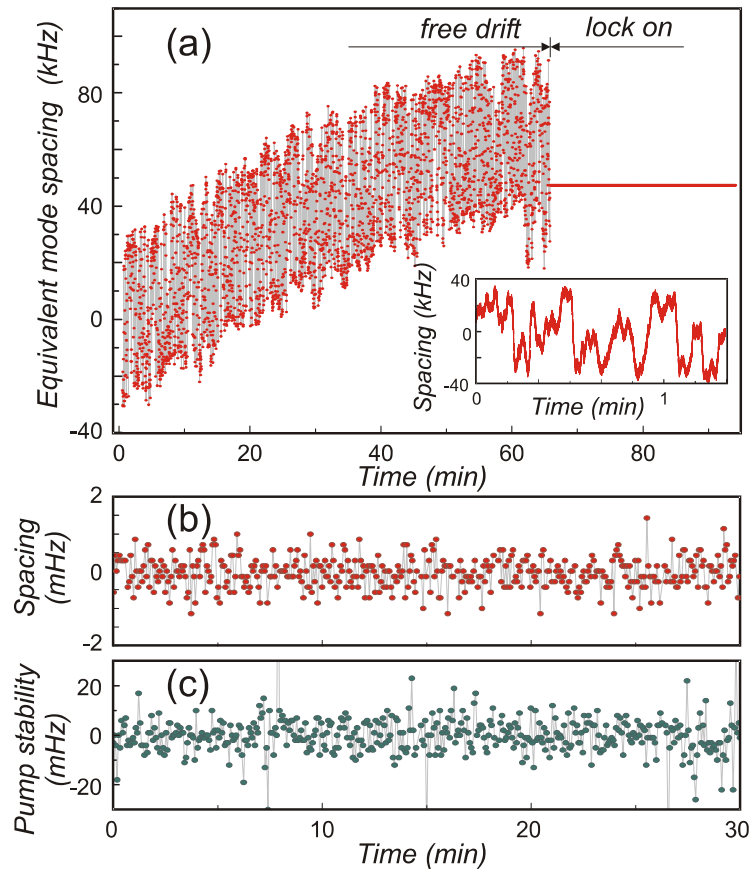
Figure 3.12: Locked and unlocked state of a microcavity frequency comb with 400 GHz mode spacing. Panel **a** displays a more than 90-minute measurement of the mode spacing of a microresonator comb (gate time 1 second). The first part of the data shows a free drift of the unstabilized mode spacing, while the thin line in the right part of the graph has been measured after enabling the stabilization loop of the comb. Mode spacing and pump laser frequency of the stabilized microcavity comb are depicted in panel **b** and **c** for a gate time of 1 s. The standard deviations for the measured data are 400 μHz (limited by the counter gate time) for the mode spacing lock in panel **b** and 5.7 mHz for the phase lock of the pump laser in panel **c**.

mode spacing of 400 GHz. In this experiment, the pump frequency remains phase locked to a reference comb mode while the beat note fluctuations of the 7th sideband ("Beat 2" with $m = 7$ in figure 3.11a) are recorded and then divided by 7 to investigate the relative mode spacing drifts. The result of this measurement is shown in figure 3.12a as a function of time. The first part of the data corresponds to the situation where the active feedback to the pump power is switched off. A slow mode spacing drift of approximately 60 kHz/hour has been observed, which can be attributed to temperature drifts of the environment during the measurement. Additionally, the unlocked comb exhibits faster mode spacing fluctuations with a time constant of several seconds (inset in figure 3.12a) which probably originates from pump power fluctuations of the EDFA and coupling fluctuations. The arrows denote the point at which the lock of the microresonator comb sideband to the reference comb has been enabled, resulting in a strong decrease of the observed fluctuations, as evident in the right part of the data in figure 3.12a. Closer inspection of the recorded beat note of the stabilized mode spacing data (figure 3.12b) reveals counter gate time limited fluctuations of less than 1 mHz for the stability of the combs mode spacing, corresponding to a more than 50 million times higher stability compared to the unlocked state. Figure 3.12c shows the stability of the pump laser frequency ("Beat 1" in figure 3.11b), phase locked to a reference comb mode.

Note that the measurements in figure 3.12 have been realized "in-loop", which means that the signal measured with the frequency counters is originating from the same photo diode used for recording the respective beat note. An "out-of-loop"-measurement using a completely independent comb line that is not part of the comb stabilization loops is shown in figure 3.13b. The used microresonator and generated comb spectrum is the same used in section 2.4 and is shown in figure 3.13a. In this measurement, the pump laser frequency ν_0 and the seventh sideband (at frequency ν_2) of the microresonator comb are stabilized via beat notes "Beat 1" and "Beat 2" with the reference frequency comb (cf. figure 3.11). The "out-of-loop"-measurement is realized by generating another beat note between the fifth sideband of the microresonator comb and the reference comb. For convenience, the repetition rate of the reference comb is adjusted to a value such that an integer multiple of the repetition rate corresponds to the mode spacing of the microresonator comb, which ensures that the respective radio frequency beat notes reproduce a frequency comb in the radio frequency domain (cf. chapter 2.2). In this regime, the radio frequency comb consists of the frequencies $f_Z^{\mathrm{rf}} = f_{0\_\mathrm{rf}} + Z \cdot \Delta f_{\mathrm{rep\_rf}}$ with $Z \in \mathbb{Z}$ being an integer corresponding to the sideband number with respect to the pump laser. Correspondingly, in the measurement in figure 3.13, the beat notes with $Z = 0$ and $Z = 7$ are stabilized while recording the beat note with $Z = 5$ for "out-of-loop"-analysis. The expected frequency or the "out-of-loop" beat note is given as $f_5^{\mathrm{rf}} = \frac{5}{7} \cdot (f_7^{\mathrm{rf}} - f_0^{\mathrm{rf}})$. Figure 3.13b shows the deviation of the measured value from the expected value for f_5^{rf} with a mean of 4 mHz $\pm$ 9.1 mHz and a standard deviation of 194 mHz. The data set consist of 455 measurement points with a gate time for a single measurement of 1 second. A more detailed "out-of-loop" beat note analysis is shown in figure 3.22 in section 3.5 for a larger microresonator with direct stabilization of the mode spacing.

In a next step it is of interest to understand the tuning range of the mode spacing and
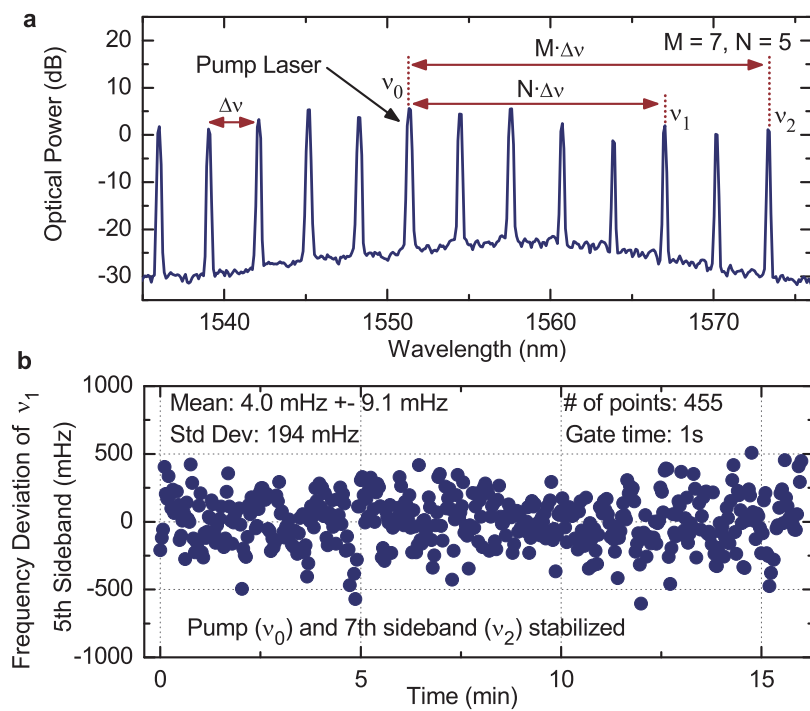
Figure 3.13: Out-of-loop measurement of a microresonator based frequency comb with $\Delta\nu \approx 400$ GHz repetition rate. Panel **a** shows the measured comb spectrum. Pump laser (frequency ν_0) and the 7th sideband (ν_2) are stabilized to a reference comb with the scheme presented in figure 3.11. Simultaneously the beat note of the 5th sideband with the reference laser is recorded. Panel **b** shows the deviation of the measured beat note frequency of the 5th sideband from the expected frequency. The data shows that the sideband is located at the expected position with a mean deviation of 4 mHz $\pm$ 9.1 mHz.
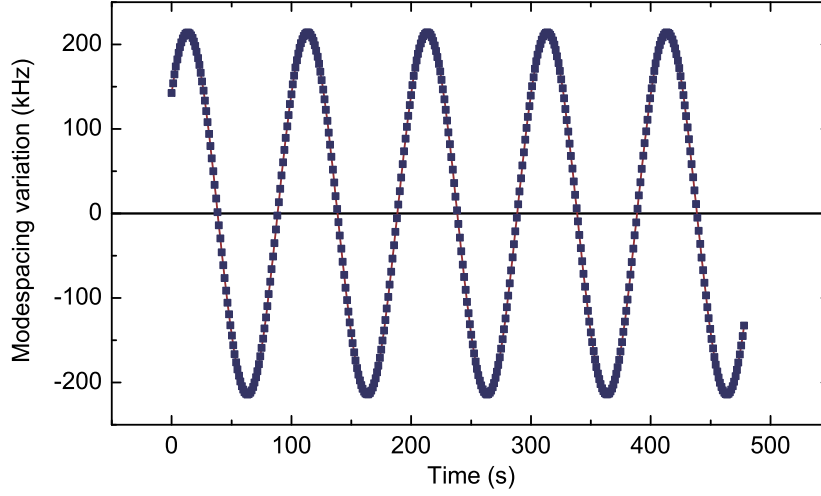
Figure 3.14: Proof of principle for the mode spacing control of a microresonator based frequency comb. The local oscillator of the stabilized "Beat 2" in figure 3.11 is slowly varied with a sine function by ± 1.5 MHz. The pump laser frequency ("Beat 1") is locked to a fixed frequency. Thus, the mode spacing of the comb is changed by ±1.5/7 MHz

center frequency of microresonator based frequency combs. Figure 3.14 shows a proof of principle measurement for the control of the comb's mode spacing. Here, the mode spacing is changed by ±200 kHz around the resonator intrinsic mode spacing of ≈400 GHz with a sinoidal function. As we have seen in the measurement in figure 3.12, the fluctuations and drifts in the mode spacing are in the order of 40 kHz/hour, such that this tuning range is already sufficient to maintain stable locking of the mode spacing over several hours.

Figure 3.15 shows more detailed measurements of the control parameters of a microresonator based frequency comb. In particular, it is of interest, whether the thermal effect discussed in section 3.3 is also responsible for the mode spacing change of the frequency comb via the pump power. For comparison with the thermal resonance frequency shift we define a new cavity parameter γ_p describing the mode spacing change with the launched power

$$\Delta f_{\mathrm{ms}} = \gamma_p \cdot \Delta P_{\mathrm{in}} \quad . \tag{3.12}$$

The relation with the thermal tuning constant Γ_p (cf. section 3.3) is given via the resonator's resonance frequency condition $\nu_m \approx m \cdot \nu_{\mathrm{ms}}$ with ν_m being the mth mode of a resonator with mode spacing ν_{ms}. Consequently, the variation of the mode spacing should be m-times smaller than the change of the cavity's resonance frequency. Note that it is assumed that the microresonator mode spacing equals the mode spacing of the generated frequency comb, which is a good approximation for high-Q microresonators with a narrow optical linewidth compared to the mode spacing. Thus, we expect that the ratio between
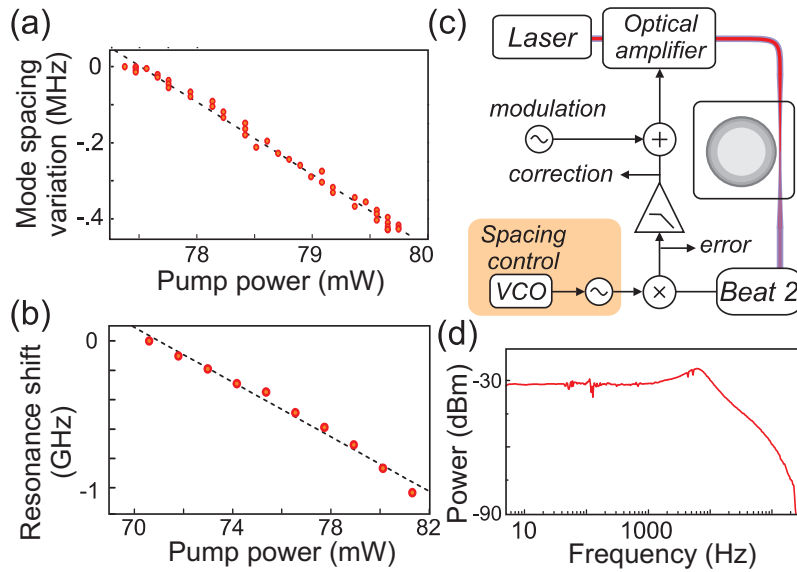
Figure 3.15: Microresonator response measurements with a 165-μm-diameter microtoroid ($\approx$ 400 GHz mode spacing). Panel **a** shows the linear dependence between pump power and mode spacing variation of the microcavity with a slope of $\gamma_p = -196 \, \frac{\text{kHz}}{\text{mW}}$. **b**. Pump power induced shift of the cavity's resonance frequency. The thermal response of this resonator is $\Gamma_p \approx -93 \, \frac{\text{MHz}}{\text{mW}}$. Panel **c** shows the experimental setup for a response measurement of the mode spacing control. A network analyzer is used to add a modulation to the mode spacing of the microresonator. Simultaneously, the correction signal of the stabilization loop is monitored to determine the maximum modulation frequency that can still be followed by the microresonator. Panel **d** shows the response of the correction signal to the modulation applied to the microresonator mode spacing. The cut-off frequency is around 10 kHz.

resonance shift Γ_p and the mode spacing tuning parameter γ_p equals the mode number of the cavity resonance:

$$\frac{\Gamma_p}{\gamma_p} = m \quad . \tag{3.13}$$

Panel **a** in figure 3.15 depicts the mode spacing change with variation of the launched pump power. This data has been obtained from the measurement shown in figure 3.14 by simultaneously measuring the launched power into the microresonator. The parameter γ_p can be obtained from a linear fit of the data in figure 3.15a and has a measured value of $\gamma_p = -196 \ \frac{\text{kHz}}{\text{mW}}$. On the other hand the thermal resonance shift in the same resonator is measured and yields $\Gamma_p = -93 \ \frac{\text{MHz}}{\text{mW}}$. Correspondingly, the microresonator mode number equates to $m = \Gamma_p/\gamma_p \approx 475$, which is in good agreement mode number determined by the pump laser frequency f_p and the comb spacing f_ms, equating to a mode number of $f_\text{p}/f_\text{ms} = \frac{193 \ \text{THz}}{400 \ \text{GHz}} \approx 484$. This measurement indicates that the same thermal effect leading to a broadening of the microresonator's resonance frequencies is the origin of the mode spacing tunability via the pump power sent to the resonator.

Another interesting parameter for the stabilization of a microresonator based frequency comb is the maximum attainable locking bandwidth. Since the mode spacing is controlled by the thermal effect of the resonator, one could expect a rather slow response of the resonator's modal structure to a change in launched power. However, the thermal effect takes place in a tiny mode volume with a cross-section of less than $2 \ \mu\text{m}^2$. This allows for an extremely fast thermalization with the surrounding silica and air, respectively. The fact that the comb stabilization is working very reliable (cf. figure 3.12) without being influenced by acoustic or other perturbations is an indicator that the stabilization loop is reasonably fast. A more precise measurement of the lower limit of the bandwidth of the mode spacing stabilization loop is performed with the experimental setup depicted in figure 3.15c. In this setup, an artificial perturbation is applied to the signal that controls the microresonators mode spacing. This perturbation is superimposed on the correction signal from the PID-loop with an electronic adder and is generated by a network analyzer. The network analyzer is then used to monitor the correction signal of the PID-loop to determine whether the microresonator is still able to follow the frequency modulation or not. Panel **d** in figure 3.15 shows the result of this response measurement with a sharp cut-off frequency around 10 kHz. The cut-off frequency is in good agreement with theoretical consideration following from the thermal diffusivity D and the toroidal cross-section (being just slightly bigger than the mode volume) with radius r. The cut-off frequency f_max can be estimated by [144]

$$f_\text{max} \approx \frac{D}{2\pi \cdot r^2} \approx 16 \ \text{kHz} \quad , \tag{3.14}$$

with $D = 9 \times 10^{-7} \ \frac{\text{m}^2}{\text{s}}$ for fused silica and $r \approx 3 \ \mu\text{m}$.
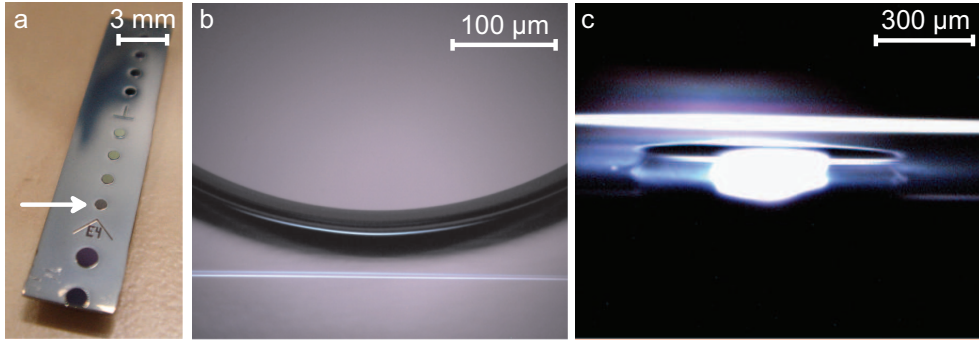
Figure 3.16: Photographs of larger toroidal resonators with electronically accessible mode spacing. Panel a shows a photo of a chip with several resonators with a diameter of 750 μm. The lower two resonators have a diameter of 1.4 mm. Panel b and c are microscope images of the toroid marked with the white arrow in panel a in top view and side view, respectively. The toroidal rim is formed by moving the focus of a CO_2 laser around the circumference of the resonator. The measured optical quality factor is $Q = 2 \times 10^7$.

3.5 Direct measurement and stabilization of microresonator mode spacings

In section 3.4 we have seen a viable frequency comb control and stabilization scheme for microresonators with mode spacings beyond electronically accessible frequencies. However, a major drawback in this case is the requirement of an additional stabilized reference frequency comb with a smaller repetition rate. To overcome this issue, larger resonators have been developed as shown in figure 3.16. Since the resonator's mode spacing ν_{ms} is inversely proportional to its radius, it is possible to determine the required resonator size for an electronically accessible mode spacing via equation 3.15.

$$\nu_{ms} = \frac{c_0}{2\pi \cdot R \cdot n_0} \tag{3.15}$$

Here, c_0 is the vacuum speed of light, R the resonator radius and n_0 the refractive index of the resonator material. At the time of these experiments in 2008, fast photodiodes that were commercially available ranged up to a 3 dB bandwidth of 50 GHz (eg. from u²t-photonics). Consequently, a fused silica resonator with a refractive index of 1.45 requires a diameter of $\approx$1.3 mm for a mode spacing matching this bandwidth. Meanwhile even photodiodes with bandwidths of 100 GHz are commercially available. However, the main challenge is not the detection of high frequencies with fast photodetectors but rather the subsequent processing of the microwave frequency signals. The equipment at hand for this experiment is a photodiode with a 3-dB-bandwidth of 50 GHz. A trial-and-error approach reveals that the photodiode still allows for detection of beat note frequencies up to 90 GHz with a sufficient signal-to-noise ratio for a phase locked loop.

Figure 3.17a is showing a simplified sketch of the setup used for direct modespacing
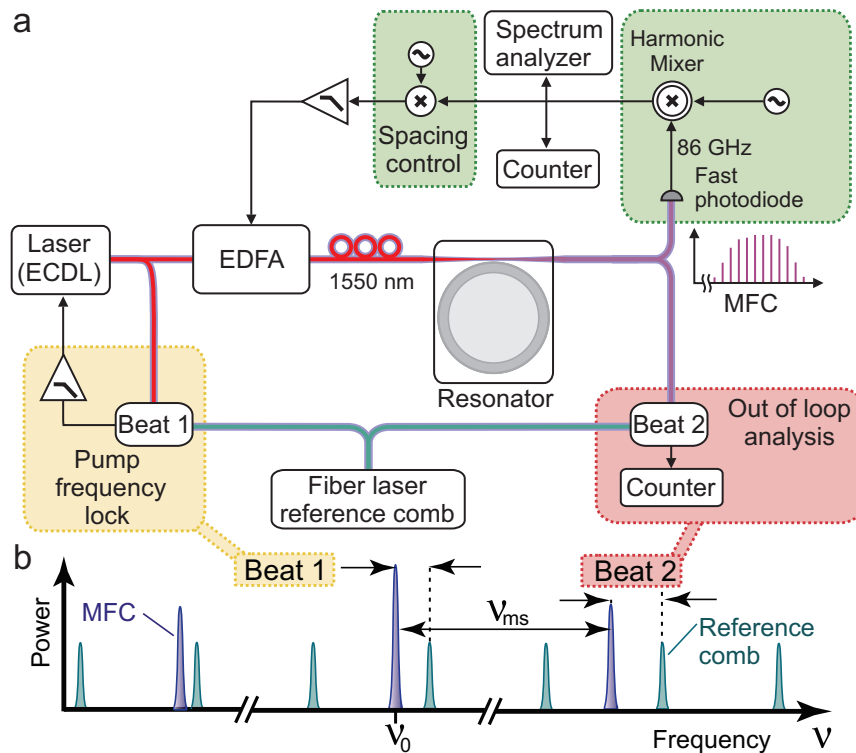
Figure 3.17: Experimental setup and scheme for "low"-repetition rate microresonator frequency comb control and stabilization. Here, the mode spacing of the microresonator is directly accessible with a fast photodiode and is stabilized using the launched pump power as actuator. The second degree of freedom of the optical frequency comb is stabilized via the pump laser frequency, which is locked to a mode of a reference comb (via "Beat 1"). An additional beat note with another frequency comb line is generated for out-of-loop analysis of the frequency comb ("Beat 2"). Panel **b** shows a sketch of the frequency spectrum with modes from the microcavity frequency comb (MFC) and the reference comb. Note the discontinuous frequency axis, since the mode spacing of the reference comb is about 860 times smaller than the microresonators mode spacing in this experiment.

stabilization of a microresonator-based frequency comb. An external cavity diode laser is phase locked to a reference comb mode ("Beat 1" in figure 3.17b), similar to the setup presented in figure 3.11 in section 3.4. Additionally, this diode laser is amplified with an erbium doped fiber amplifier and sent to the optical resonator via a tapered optical fiber. The employed toroidal resonator has a diameter of $\approx 765~\mu$m and generates and optical frequency comb with a mode spacing of 86 GHz. The output of the tapered fiber containing the frequency comb is split up with fiber based optical couplers and part of the light is sent to the 50-GHz-photodiode. The high-frequency microwave signal from this photodiode is sent to a harmonic mixer (cf. appendix B.1) via a microwave waveguide and mixed down with the 6th harmonic of a ≈ 14.3 GHz microwave signal. The mixed-down signal is then further analyzed with an electronic spectrum analyzer and/or an electronic frequency counter and additionally used for stabilization of the mode spacing to a reference frequency provided by a local oscillator (in this case a 10-MHz-signal from a GPS-disciplined hydrogen maser). The principle of the mode spacing control is the same already used for the high repetition rate resonators and relies on the fast thermal effect of the optical resonator to stabilize the roundtrip time of the photons in the cavity. Another part of the tapered fiber output light containing the frequency comb is used for an out-of-loop analysis of the frequency comb stability. A "beat detection unit" (similar to the one shown in figure 2.6) is used to generate a beat note ("Beat 2" in figure 3.17b) between the stabilized reference comb and the stabilized microresonator based comb. In the experiment, a specific microresonator frequency comb mode is selected with a diffraction grating, which additionally reduces the signal to noise ratio of the measurement by removing spectral regions of the reference comb that are not of interest for the beat note detection (a detailed description of the beat note generation is shown in appendix B).

The setup in figure 3.17 can also be used for analysis of the unstabilized mode spacing of the generated frequency comb (and the mode spacing of the microresonator respectively). For this experiment, the phase locked loop for the mode spacing stabilization is switched off and the output of the fast photo diode with subsequent harmonic mixer is connected to an electronic spectrum analyzer and a radio frequency counter. Figure 3.18 shows a simplified setup for the measurement of mode spacing beat notes of a frequency comb generated in a 765-μm-diameter resonator. Note that the beat note $f_{\mathrm{ms}}^{\mathrm{rf}}$ is measured at a frequency of a few 10th of megahertz; the data in the figure is converted back to the original mode spacing frequency by adding 6 times the local oscillator frequency $\nu_{\mathrm{lo}} \approx 14.3$ GHz. The ambiguity whether the actual mode spacing frequency corresponds to $f_{\mathrm{ms}} = 6 \cdot \nu_{\mathrm{lo}} + f_{\mathrm{ms}}^{\mathrm{rf}}$ or $f_{\mathrm{ms}} = 6 \cdot \nu_{\mathrm{lo}} - f_{\mathrm{ms}}^{\mathrm{rf}}$ can be solved by changing the local oscillator frequency and monitor the direction of the radio frequency beat note change. With applied correction of the local oscillator signal, the derived mode spacing has a frequency of 85.6572 GHz and is in good agreement with the expected mode spacing given by the approximate size of the resonator. This size is given by the 800-μm-diameter disk with a typical decrease of $\approx 40~\mu$m due to the reflow process leading to an expected mode spacing value of around 86 GHz. The measured beat note in figure 3.18 has a short term linewidth of a few kHz. The complete Allan deviation for the unstabilized mode spacing is shown in figure 3.20.

Figure 3.19 shows the temporal evolution of the unstabilized mode spacing frequency.
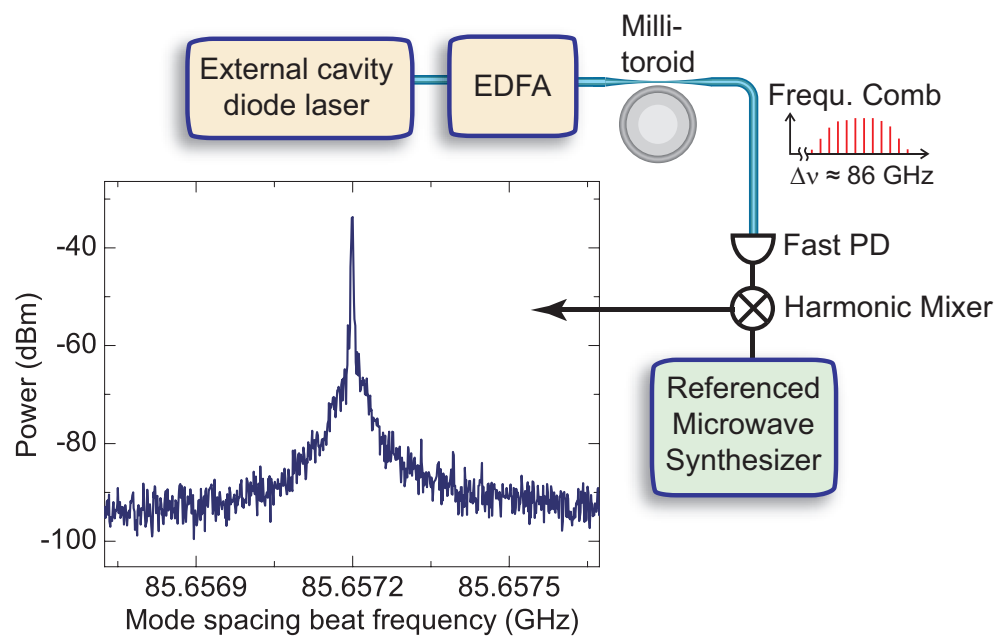
Figure 3.18: Setup and measurement of the unstabilized mode spacing beat note of a microresonator comb. The mode spacing frequency is around 86 GHz, which is in good agreement with the expected mode spacing in the 765-μm-diameter resonator. The measurement is conducted with a 3-GHz-electronic spectrum analyzer at a resolution bandwidth of 1 kHz. Note that the frequency axis of the data is already corrected for the down mixing of the harmonic mixer. The applied local oscillator signal from the employed microwave synthesizer has a frequency of ≈ 14.3 GHz and the 6th harmonic of this signal is used to down-convert the microresonator mode spacing frequency to radio frequency domain.
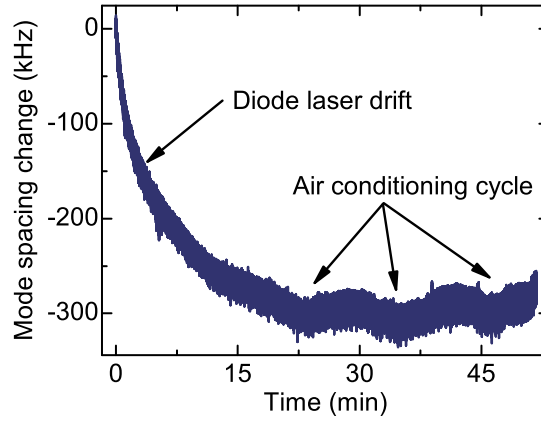
Figure 3.19: Temporal evolution of the unstabilized mode spacing of a fused silica microtoroid. The strong drift in the first 15 minutes can be attributed to the frequency drift of the employed external cavity diode laser (which usually drifts by a few hundred Megahertz after a wavelength change). At a later time an oscillation with a period of ≈ 12 minutes is present in the mode spacing beat note, corresponding to the cooling cycle of the air conditioning system in the laboratory.

The strong drift in the beginning of the measurement can be attributed to the drift of the pump laser frequency (cf. dependence of the mode spacing on the pump frequency in figure 3.23; the measured mode spacing change corresponds to a pump laser frequency drift of ≈ 460 MHz). After 15 minutes, the pump laser stops drifting and it is possible to observe an oscillation in the mode spacing with a period of approximately 12 minutes, which coincides with the cooling cycle of the air conditioning system in the laboratory. The slow mode spacing oscillations can be suppressed by turning off the air conditioning, at the expense of a larger long term drift in the beat note signal.

Figure 3.20 shows the modified Allan deviation $\sigma_A(\tau)$ (measured with a λ-type frequency counter) of the stabilized and unstabilized mode spacing as well as the counter limit, which has been determined by measuring the output of a referenced frequency synthesizer at the same frequency as the the down-mixed mode spacing beat note. The Allan deviation [145, 146] is a measure for the attainable frequency accuracy of an oscillator at a given gate time τ. It is proportional to the mean value of the squared frequency deviation of two consecutive measurement values normalized to their carrier frequency ν_0:

$$\sigma_A(\tau) = \frac{1}{2} \cdot \frac{1}{N-1} \cdot \frac{1}{\nu_0^2} \sum_{i=1}^{N} \left(\nu_{i+1} - \nu_i \right)^2 \quad . \tag{3.16}$$

Here, N denotes the total number of measurements and ν_i corresponds to the ith frequency measurement. The data in figure 3.20 has been measured with a "Fluke PM6681" frequency
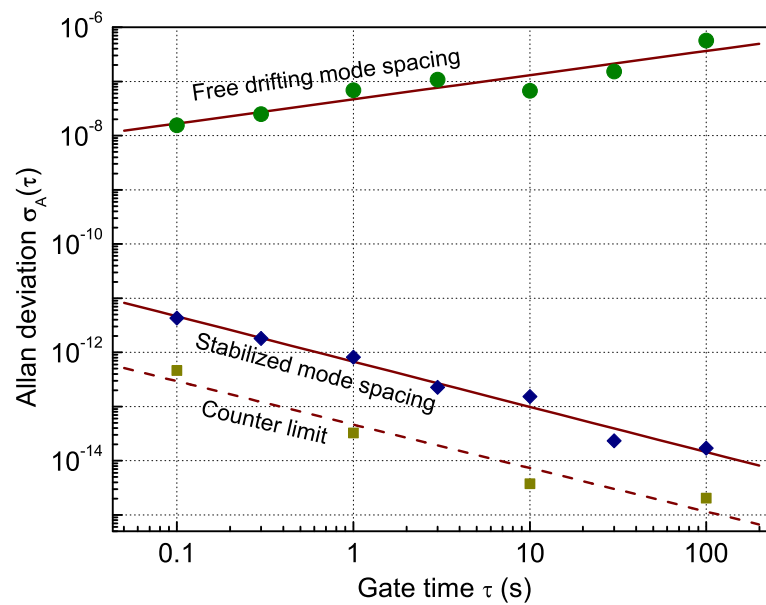
Figure 3.20: Modified Allan deviations of a microresonator comb's mode spacing. The upper trace is a measurement of the unstabilized Allan deviation showing thermal mode spacing drifts in the order of 10^{-7} relative to the carrier frequency of ≈ 86 GHz at gate times of 10 seconds. This corresponds to frequency variations in the order of 10 kHz. The stabilized mode spacing shows a dramatically decreased Allan deviation with relative stabilities around 10^{-12} at a 1-second gate time.

counter. Unfortunately Fluke does not provide the exact function principle of the employed frequency counter. However, most likely it is an overlapping λ-type counter (cf. [140]), which means that the measured data is the modified Allan deviation [140]. The upper graph in figure 3.20 corresponds to the free drifting mode spacing without stabilization. In this case, the modified Allan deviation is proportional to $\tau^{1/2}$ and consequently we obtain $\sigma_A^2 \propto \tau$ for the modified Allan variance. Following the work from Dawkins et.al. [140], the underlying noise process is a frequency modulated random walk noise, which is most probably a result of thermal drifts of the resonator resonance frequency induced by pump power fluctuations and temperature changes in the laboratory. The middle curve in figure 3.20 shows the modified Allan deviation for the stabilized mode spacing as function of the gate time. The slope of the curve corresponds to $\sigma_A \propto \tau^{-1}$ which yields a modified Allan variance of $\sigma_A^2 \propto \tau^{-2}$. This behavior is expected for flicker phase noise (so-called pink noise or $1/f$-noise). In general, flicker noise is an inherent feature of electronic circuits providing a direct current (DC) signal and might be converted to mode spacing fluctuations of the resonator via the pump laser. Note that the modified Allan deviation of the counter limit measurement shows approximately the same slope as the stabilized beat note at a ten times lower level.

The impact of the gain of the phase locked loop on the stability of the mode spacing beat note is shown in figure 3.21. Panel (1) to (6) show the stabilized 86-GHz beat note signal from low to high gain. The gain in the first two panels is too low, showing a slightly broadened beat note (this can be hardly seen in the data because of the limited resolution bandwidth of the spectrum analyzer; the broadening of the beat note has been obvious by measurements with a radio frequency counter). The optimum gain regime is reached in a region between the second and the third panel. Further increase of the gain leads to more and more pronounced oscillation sidebands symmetric around the beat frequency that are originating from the phase locked loop. At even higher gain, the phase locked loop starts to drive chaotic oscillations in the mode spacing, leading to a significantly broadened beat note shown in panel (6).

The previous presented stabilization data of the 86-GHz-resonator has been measured "in-loop" with the same electronic beat note signal being used for measurement and stabilization of the comb modes. These results can be potentially misleading since the stabilization loop itself might imprint electronic excess noise onto the frequency comb modes, such that the actual comb stability is lower than linewidth determined by the "in-loop" beat notes. To obtain a more precise values for the actual comb stability an "out-of-loop" beat note of a completely independent microresonator comb line with the reference comb is measured. The result of this measurement is shown in figure 3.22 and corresponds to a measurement of "Beat 2" in figure 3.17. Panel **a** shows the electronic spectrum of the "out-of-loop" beat note along with a more than one hour measurement of the frequency of the respective comb line in panel **b** and **c**. The zero frequency in this graph corresponds to the expected frequency of the beat note that has been determined from the values of the pump laser frequency (which is stabilized to the reference comb) and the measured mode spacing beat note. The measurement proves the uniform nature of the frequency comb with a deviation of the "out-of-loop" comb mode from its expected position of (-11 $\pm$ 20)
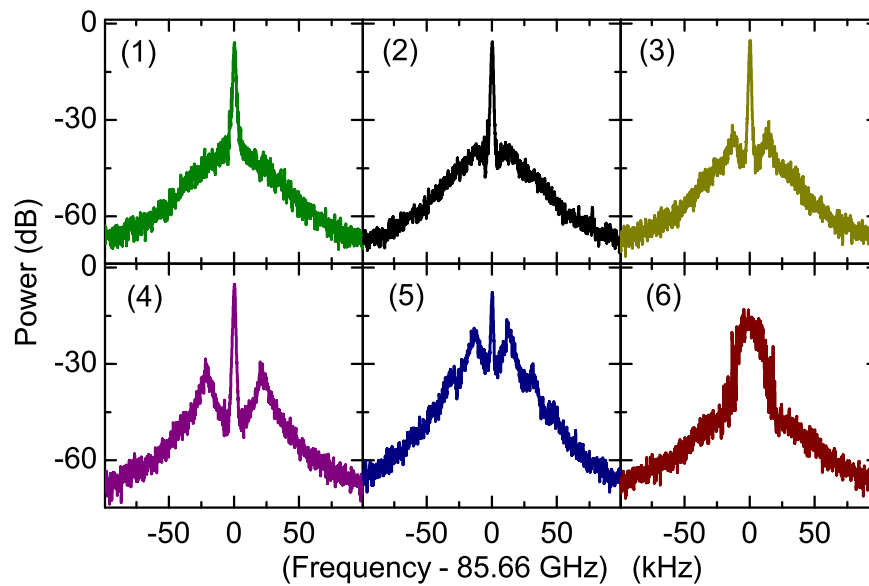
Figure 3.21: Beat note of a stabilized microresonator mode spacing at different gain parameters of the phase locked loop. The gain is increased stepwise from panel (1) to panel (6). A low gain shown in panel (1) leads to a broader lineshape while increasing the gain leads to an oscillatory behavior of the phase locked loop, which can be seen from sidebands that appear in panel (3). Further increase of the gain generates higher order sidebands in panel (5) and finally changes to a chaotic regime in panel (6), where the mode spacing beat note is fluctuating over several tenth of kilohertz. The best stabilization is achieved at a gain corresponding to panel (2)-(3). The resolution bandwidth of the measurements is 1 kHz.
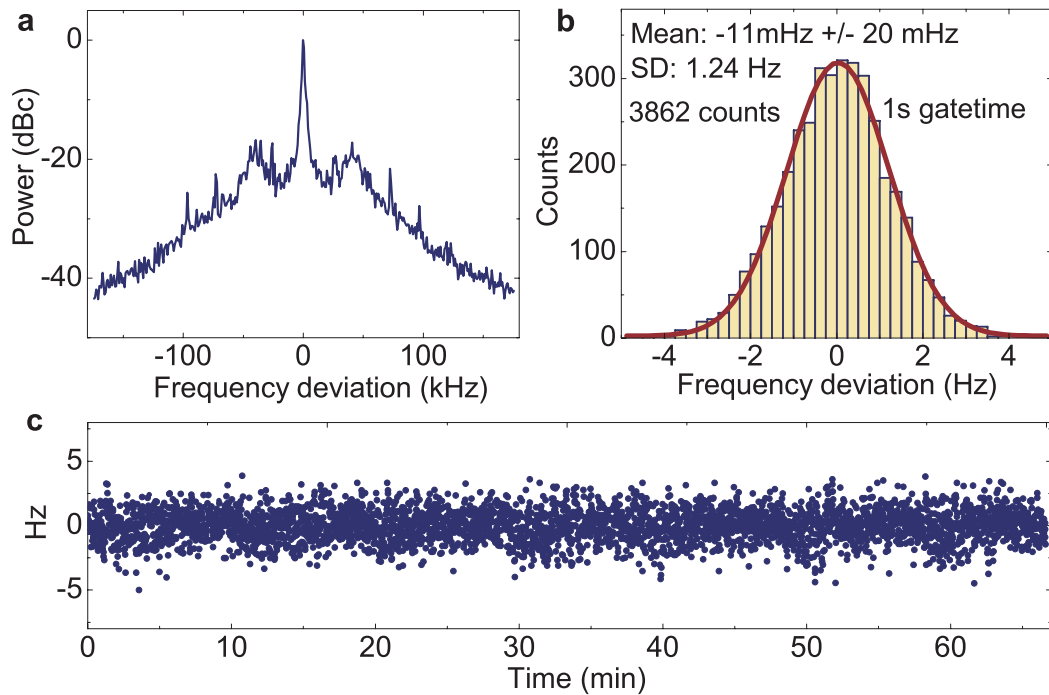
Figure 3.22: Out-of-loop stability of a microresonator based frequency comb. Panel **a** shows the beat note of a comb mode that is independent of the frequency stabilization loops ("Beat 2" in figure 3.17), measured at a resolution bandwidth of 100 Hz. More than 3800 frequency counter measurements of this beat note are shown in panel **b** and **c**. The gate time is 1 second in each measurement, summing up to a total measurement time of more than one hour. The measured frequency position of this "out of loop" comb line is (-11 ± 20) mHz with respect to the expected position that is determined by the stabilized pump laser and mode spacing frequency. The standard deviation of the measurement is 1.24 Hz.
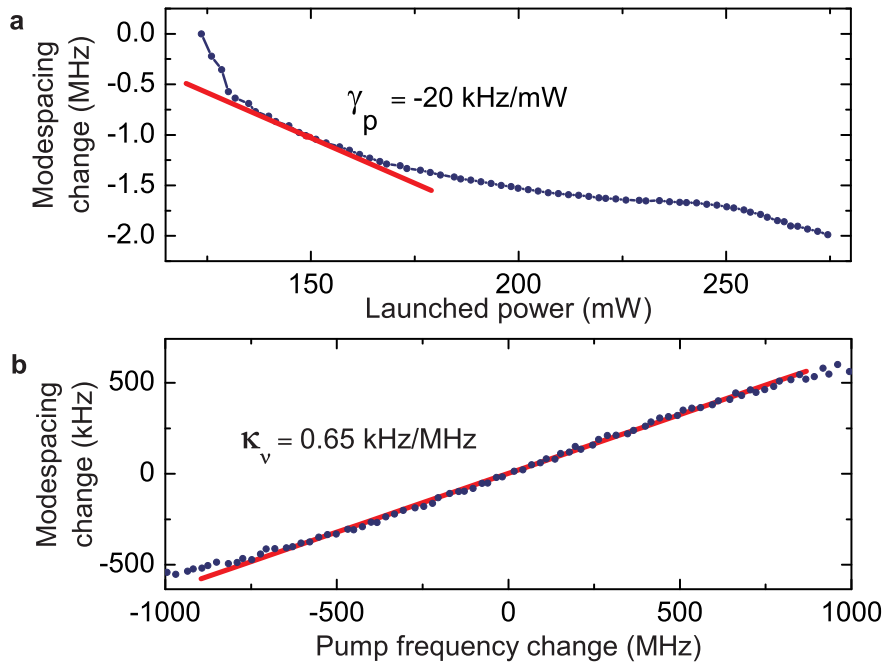
Figure 3.23: Impact of pump power and pump frequency variations on the mode spacing of a comb generated in a 765-μm-diameter resonator ($\approx$86 GHz mode spacing). Panel a shows the variation of the comb's mode spacing with the launched power, with a slope in the order of -20 kHz/mW. This effect corresponds to the cavity resonance shift (detuning shift) shown in figure 3.5, assuming that the comb mode spacing variation Δf_{ms} is directly linked to the resonance frequency shift $\Delta\nu_c$ via the optical mode number ($m\cdot\Delta f_{\mathrm{ms}} = \Delta\nu_c$). The variation of the comb spacing with the pump frequency is shown in panel b, exhibiting a mode spacing change of 0.65 kHz per MHz pump frequency shift. This data corresponds to the calculation of the resonance frequency shift as a function of the laser frequency shown in figure 3.3a.

mHz, which is derived from the mean value of more than 3800 frequency measurements at a gate time of 1 second.

After it has been shown that mode spacing and offset frequency of a microresonator comb with smaller mode spacing can be readily stabilized, it is of interest to analyze the control actuators in more detail. One degree of freedom of the frequency comb depends directly on the frequency of the pump laser, as already shown in the case of smaller microresonators in section 3.4. On the other hand, the influence of the pump power and pump frequency on the second degree of freedom (the comb's mode spacing) is of interest to determine the amount of noise and mode spacing drifts that can be compensated for. Figure 3.23 shows measurements of the mode spacing vs. pump power (panel a) and pump frequency (panel b). The mode spacing change with pump power can be explained by
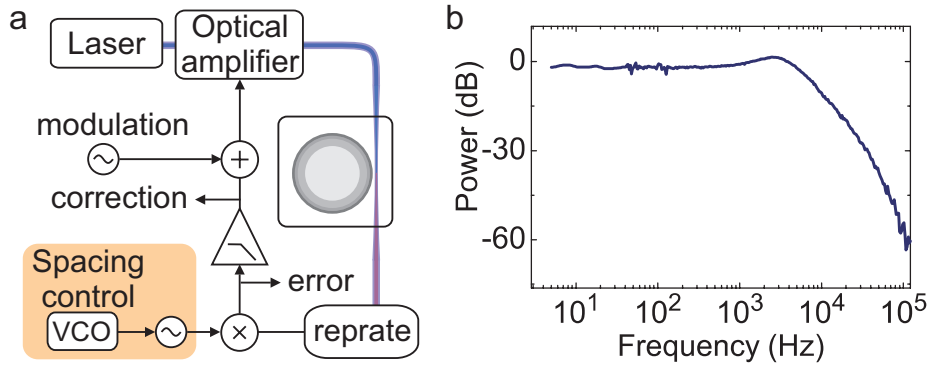
Figure 3.24: Response measurement for characterization of the mode spacing control in a 750-μm-diameter resonator. Panel a shows the experimental setup to determine the locking bandwidth of the mode spacing control. A network analyzer is used to apply an artificial modulation to the mode spacing control via the pump power. Simultaneously, the correction signal of the employed phase locked loop is measured with the network analyzer to determine whether it is able to follow the modulation. Panel b shows the correction signal as a function of the modulation frequency. A cut-off at around 10 kHz can be observed, similar to the measurement in smaller resonators shown in figure 3.15.

the thermal effect of the microresonator as shown before. This mode spacing change is a result of the resonator mode being pushed away from the (fixed) pump laser towards lower frequencies at higher powers (cf. theoretical analysis in figure 3.5).

The measured variation of the mode spacing with the pump power is on the order of $\gamma_{\mathrm{p}} = -20$ kHz/mW in the measured 750-μm-diameter-resonator. Note that the amount of absorbed power additionally depends on the wavelength of the oscillating modes within the cavity, such that nonlinear optical frequency conversion can change the magnitude of the thermal effect. As a result, a more complex curve is observed for the pump power dependence of the mode spacing in figure 3.23a. The value of $\gamma_{\mathrm{p}} = -20$ kHz/mW is smaller than the value measured in the 165-μm-diameter-resonator of $\gamma_{\mathrm{p}} = -196$ kHz/mW. The difference is a result of different ratio of scattering and absorption losses in the resonator material as well as a difference in the heat distribution due to the different resonator size. Panel b in figure 3.23 shows the measured change of the mode spacing with the frequency of the pump laser. This effect has been theoretically discussed before and is a result of the variation of the detuning between pump laser and microresonator mode shown in figure 3.3a. The measured mode spacing variation due to this effect is $\kappa_{\nu} = 0.65$ kHz/MHz and is small compared to the pump power induced shift (assuming a pump laser with a frequency stability of a few megahertz). In conclusion it is possible to fully describe the microresonator comb (with mode spacing f_{ms} and center frequency f_{p}) as a function of the accessible control parameters (pump power P_{in} and pump frequency f_{p}):

$$\begin{pmatrix} f_{\mathrm{p}} \\ \Delta f_{\mathrm{ms}} \end{pmatrix} = \begin{pmatrix} 1 & 0 \\ \kappa_{\nu} & \gamma_{\mathrm{p}} \end{pmatrix} \cdot \begin{pmatrix} f_{\mathrm{p}} \\ P_{\mathrm{in}} \end{pmatrix} \quad , \tag{3.17}$$

Figure 3.24 shows a response measurement of the mode spacing control for a 750-μm-

diameter microresonator comb. Similar to the experiment shown in figure 3.15, the mode spacing control signal (via the launched power) is modulated with a network analyzer while simultaneously monitoring the correction signal of the phase locked loop. However, in this experiment the mode spacing beat note is directly measured in contrast to the earlier experiment in which the mode spacing has been derived from two separate beat notes with a fiber laser reference comb. The measured cut-off frequency of the mode spacing control is at around 10 kHz (cf. figure 3.24b) and is in good agreement with the previous measurement shown in figure 3.15.

CHAPTER 4

Dispersion in whispering gallery mode resonators

4.1   Mathematical description of dispersion

Dispersion plays an important role in the generation of optical frequency combs as it is crucial for the maximum achievable comb bandwidth. In conventional mode locked lasers huge efforts are made to control and minimize dispersion of the resonator. This reduction of the dispersion is most commonly achieved by using prism pairs, grating pairs or chirped mirrors. Dispersion control in microresonators is more difficult since it is not possible to add additional optical elements for dispersion compensation. Thus it is required to fabricate a resonator with an intrinsically low dispersion. There are many different ways to express dispersion and different scientific communities have adopted different conventions to specify dispersive properties. This leads to a lot of confusion when terms like "positive", "negative", "normal" and "anomalous" dispersion are used, which have different meanings in the ultrafast laser community, fiber optics community and in the field of nonlinear optics. Dispersion is most commonly defined by the the frequency dependence of the propagation constant β of light in a dielectric medium. Using a Taylor expansion with respect to the angular optical frequency ω, the propagation constant β can be written as [75]:

$$\beta(\omega) = \frac{2\pi}{\lambda_0} \cdot n(\omega) = \frac{\omega}{c} \cdot n(\omega) = \sum_{m \in \mathbb{N}_0} \left(\frac{1}{m!} \left. \frac{\mathrm{d}^m \beta}{\mathrm{d}\omega^m} \right|_{\omega = \omega_0} \cdot (\omega - \omega_0)^m \right) \quad . \tag{4.1}$$

Here, λ_0 defines the vacuum wavelength of the light wave, c is the speed of light in vacuum and $n(\omega)$ is the frequency dependent refractive index of the medium. The coefficients in the Taylor expansion are referred to as different dispersion orders and correspond to the derivatives of β with respect to the angular frequency ω:

$$\beta_m := \left. \frac{\mathrm{d}^m \beta}{\mathrm{d}\omega^m} \right|_{\omega = \omega_0} \quad . \tag{4.2}$$

The integer number m is referred to as the order of the dispersion. Small contributions of higher order dispersion (β_m with $m \geq 3$) are usually neglected unless studying optical properties close to a zero dispersion point. Thus, β can be written as

$$\beta(\omega) \approx \beta_0 + \beta_1 \cdot (\omega - \omega_0) + \beta_2 \cdot (\omega - \omega_0)^2 \quad , \tag{4.3}$$

The zeroth order dispersion β_0 corresponds to a constant phase shift $\phi = \beta \cdot L$, for a dielectric material with length L. First order dispersion, which is described by $\beta_1 = \frac{\mathrm{d}\beta}{\mathrm{d}\omega} = \frac{1}{v_g}$ is inversely proportional to the group velocity v_g of the input signal and induces a constant group delay $T_g = \frac{\mathrm{d}\phi}{\mathrm{d}\omega} = L \cdot \frac{\mathrm{d}\beta}{\mathrm{d}\omega}$. Note that this additional time delay depends on the center wavelength ω_0 of the applied signal such that pulses with different center wavelengths propagate at different velocities in a material with first order dispersion. The shape of an optical pulse is not influenced by β_1. The most commonly used values that describe dispersion in a material are related to the second order dispersion (group velocity dispersion)

$$\beta_2 \equiv \text{GVD} = \frac{\mathrm{d}^2\beta}{\mathrm{d}\omega^2} \tag{4.4}$$

The parameter β_2 corresponds to the change of the inverse group velocity with the angular optical frequency and is given in units of $\left[\frac{\mathrm{s}^2}{\mathrm{m}}\right]$ or in $\left[\frac{\mathrm{fs}^2}{\mathrm{mm}}\right]$. In the ultrafast optics community it is more common to specify the dispersion of the group delay, which is directly related to β_2. The group delay T_G can be interpreted as the time delay of an optical pulse that passes through an optical element. It is defined by the change of the phase with respect to the angular frequency, $T_G = \frac{\mathrm{d}\phi}{\mathrm{d}\omega}$. The dispersion of the group delay is given as the derivative of the group delay with respect to the angular frequency and referred to as GDD:

$$\text{GDD} = \frac{\mathrm{d}^2\phi}{\mathrm{d}\omega^2} \quad . \tag{4.5}$$

The group delay dispersion has units of $[s^2]$ and can be used to calculate the temporal separation of two pulses at different wavelength after passing through an optical element. This separation of the pulses is given by the GDD multiplied by the spectral separation of the pulses center frequencies. The connection between group delay dispersion and group velocity dispersion can be seen by replacing the phase $\phi = \beta \cdot L$ in equation 4.5 by the propagation constant multiplied with the length of the optical element L. In other words, the group velocity dispersion corresponds to the group delay dispersion per unit length.

$$\text{GVD} = \beta_2 = \frac{\text{GDD}}{L} \tag{4.6}$$

The fiber optics community on the other hand defines dispersion as the so called group velocity dispersion parameter D. This parameter is defined as the variation of the first order dispersion parameter β_1 with the wavelength λ.

$$D = \frac{\mathrm{d}\beta_1}{\mathrm{d}\lambda} = \frac{\mathrm{d}^2\beta}{\mathrm{d}\lambda \, \mathrm{d}\omega} \tag{4.7}$$

A more physical interpretation of D is the change of the group delay T_G per unit length with the wavelength, which follows from equation 4.7 with $\frac{\mathrm{d}\beta}{\mathrm{d}\omega} = \frac{1}{L} \cdot \frac{\mathrm{d}\phi}{\mathrm{d}\omega} = \frac{T_G}{L}$, yielding

$$D = \frac{1}{L}\frac{\mathrm{d}T_G}{\mathrm{d}\lambda} \quad . \tag{4.8}$$

The group velocity dispersion parameter D in optical fibers is usually given in units of $\left[\frac{\mathrm{ps}}{\mathrm{nm \cdot km}}\right]$ and can be used to calculate the group delay difference of two optical pulses with different center wavelengths after propagating in an optical fiber with length L. As a result of the frequency dependent group velocity, second order dispersion is also responsible for broadening of optical pulses. However, the amount of pulse broadening strongly depends on the shape (or corresponding frequency spectrum) of the pulse. The relationship between the group velocity dispersion parameter D and the group velocity dispersion $\text{GVD} = \beta_2$ can be derived using

$$\frac{\partial}{\partial\lambda} = \frac{\mathrm{d}\omega}{\mathrm{d}\lambda} \cdot \frac{\partial}{\partial\omega} = -\frac{2\pi c}{\lambda^2}\frac{\partial}{\partial\omega} \ , \ \text{with} \ \ \omega = \frac{2\pi \cdot \nu}{c} \quad . \tag{4.9}$$

Combining equation 4.9 with equation 4.7 yields

$$D = -\frac{2\pi c}{\lambda^2} \cdot \mathrm{GVD} \quad . \tag{4.10}$$

Note that the value of D has the opposite sign compared to the values for GVD and GDD. Thus it might be confusing to use terms like negative or positive dispersion since it depends on the parameter that is used to describe the dispersion of a dielectric material. This ambiguity can be avoided by referring to normal dispersion (GDD> 0, GVD> 0 and $D < 0$) and anomalous dispersion (GDD< 0, GVD< 0 and $D > 0$) [75]. However, even the terms "normal" and "anomalous" dispersion are not used consistently. Frequently they are used to describe the variation of the refractive index with the wavelength $\frac{\mathrm{d}n}{\mathrm{d}\lambda}$ [147], which is related to the first order dispersion β_1 (the relation between refractive index n and D is derived later in equation 4.24). In this thesis the terms "normal" and "anomalous" dispersion are used to refer to the second order dispersion (given by GDD, GVD and D).

4.2 Dispersion in optical microresonators

In the previous sections it has been shown that dispersion originates from a the wavelength (frequency) dependence of the refractive index of a dielectric material. The physical background of dispersion is a result of characteristic resonance frequencies at which a dielectric medium interacts with an electromagnetic wave. This kind of dispersion is referred to as material dispersion. However, when using optical waveguides, different effects contribute to the total dispersion of an optical element. In general, dispersion in optical waveguides can be categorized in three categories

(a) Material dispersion

(b) Geometric dispersion (waveguide dispersion)

(c) Modal dispersion

(d) Polarization mode dispersion

Figure 4.1 shows examples for the different types of dispersion in an optical waveguide (or resonator containing an optical waveguide). All kinds of dispersion lead to different optical pathlength that electromagnetic waves experience depending on their frequencies. In the case of material dispersion the optical pathlength is directly determined by the frequency (wavelength) dependent refractive index of the material. Geometric dispersion originates from different optical paths that are taken by waves of different frequencies and depends on the geometry of the waveguide. In a dielectric waveguide (eg. an optical fiber) having a core with higher refractive index n_2 than the refractive index of the cladding n_1, an
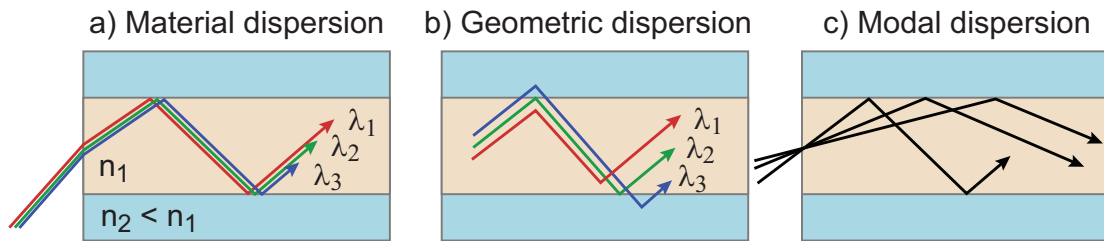
Figure 4.1: Dispersion contributions in a waveguide/microresonator with total internal reflection. Panel a) shows material dispersion in which electromagnetic waves of different frequencies propagate at different velocities. Panel b) depicts geometric dispersion in which the optical path depends on the position at which the electromagnetic wave is scattered due to the refractive index boundary ($n_1 > n_2$). Typically, longer wavelength experience a shorter optical pathlength. Panel c) sketches modal dispersion in which different spatial or polarization modes experience a different optical path within the waveguide.

electromagnetic wave with higher frequency is reflected closer to the boundary than a wave with lower frequency as depicted in figure 4.1b. Another type of dispersion is the modal dispersion, which is a result of different optical paths that are taken by light in different spatial modes within the waveguide (cf. figure 4.1c). Another source for dispersion is the so-called polarization mode dispersion, which leads to a variation of the propagation velocity of an electromagnetic wave depending on its polarization. Polarization mode dispersion plays a minor role in frequency comb generation in microresonators as just one mode family of the resonator is required for the four-wave mixing process. However, it will be shown later that interactions between different mode families can occur and influence the comb generation process as a result of modal dispersion.

The dispersion properties and values described in the previous section can be used to quantify dispersive properties of eg. optical fibers and other reflective or transmissive optical elements. Several methods exists that enable precise measurements of dispersion:

- Inserting the dispersive element into one arm of an interferometer to determine the phase shifts (eg. for laser mirrors and transmissive optical components)

- Measuring the group delay of optical pulses that are centered at different wavelength (eg. in optical fibers [148])

- Measurement of the repetition rate of mode locked lasers at different center wavelengths to determine dispersion of laser cavities

Measurement of the dispersion of an optical resonator is more difficult and none of the aforementioned methods can be applied. The only directly accessible parameter of a passive optical resonator is the mode spectrum. Thus, it is required to associate the position of the resonance frequencies to the dispersion parameters that have been introduced before. The resonance frequencies of a whispering gallery mode resonator are defined by
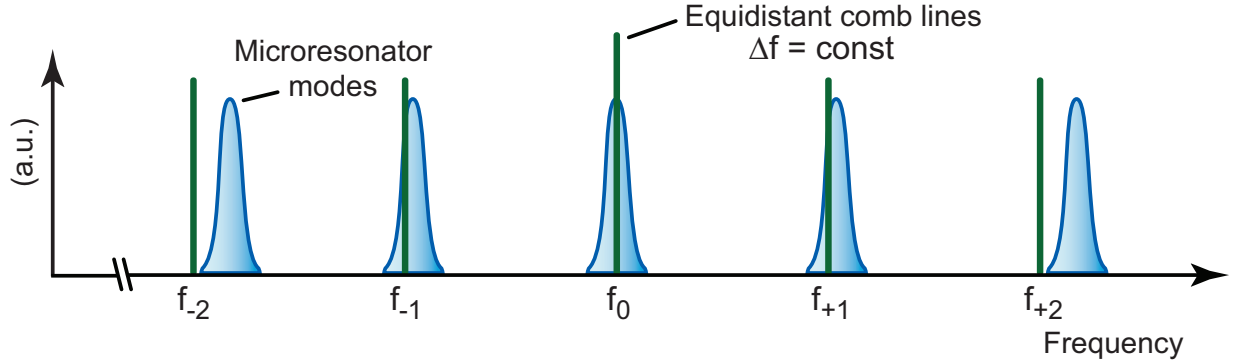
Figure 4.2: Frequency comb generation in a dispersive resonator. The mismatch between equidistant frequency comb lines and the non-equidistant resonator modes hinders broadband frequency comb generation in a microresonator.

$$\nu_\ell = \frac{\ell \cdot c}{2\pi \cdot R \cdot n} \tag{4.11}$$

with the integer (angular-)mode number ℓ, the speed of light in vacuum c, the resonator radius R and the refractive index n. Note that for simplicity R is assumed to be constant without influence of geometric dispersion. The contributions of geometric dispersion are included into the refractive index, such that n corresponds to an effective refractive index in the following discussion. It can be directly seen from equation 4.11 that the modes of the microresonator are perfectly equidistantly spaced in case n is frequency independent (no dispersion). If the refractive index is frequency dependent ($n = n(\omega)$), the mode spacing $\Delta\nu_\ell$ is not equidistantly spaced, with the consequence that the variation of the mode spacing $\Delta(\Delta\nu_\ell)$ has a non-zero value. This non-equidistant microresonator mode spacing hinders the generation of broadband optical frequency combs as a result of the mismatch between resonator modes and equidistant comb lines. In a resonator in which every m^{th} resonance frequency of the same mode family is known we can use

$$\Delta\nu_\ell = \frac{(\nu_{\ell+m} - \nu_\ell) + (\nu_\ell - \nu_{\ell-m})}{2m} = \frac{\nu_{\ell+m} - \nu_{\ell-m}}{2m} \tag{4.12}$$

$$\Delta(\Delta\nu_\ell) = \frac{(\nu_{\ell+m} - \nu_\ell) - (\nu_\ell - \nu_{\ell-m})}{m^2} = \frac{\nu_{\ell+m} - 2\nu_\ell + \nu_{\ell-m}}{m^2} \tag{4.13}$$

Note the m^2 in the denominator of equation 4.13 as a result of the subtracted mode spacings being again separated by m resonator modes. The resonance frequencies are connected to the group delay dispersion GDD $= \frac{\mathrm{d}^2\phi}{\mathrm{d}\omega^2}$ via the group delay that is experienced by an electromagnetic wave for one round-trip within the resonator. This group delay T_G is given by

$$T_G = \frac{\mathrm{d}\phi}{\mathrm{d}\omega} = \frac{L(\omega)}{c} \,, \tag{4.14}$$

with $L(\omega)$ being the frequency dependent optical pathlength for one round-trip and c the speed of light in vacuum. On the other hand $\frac{L(\omega)}{c}$ corresponds to the inverse mode spacing of the resonator $\Delta\nu_\ell^{-1}$. Thus, the GDD of the resonator can be derived as

$$\mathrm{GDD} \;=\; \frac{\mathrm{d}^2\phi}{\mathrm{d}\omega^2} = \frac{\mathrm{d}}{\mathrm{d}\omega}\frac{1}{\Delta\nu_\ell} \tag{4.15}$$

$$=\; -\frac{1}{2\pi}\cdot\frac{1}{(\Delta\nu_\ell)^2}\cdot\frac{\mathrm{d}}{\mathrm{d}\nu_\ell}\Delta\nu_\ell \tag{4.16}$$

$$=\; -\frac{1}{2\pi}\cdot\frac{\Delta(\Delta\nu_\ell)}{(\Delta\nu_\ell)^3} \;, \tag{4.17}$$

where the last step takes the discrete nature of the cavity resonances into account. With equation 4.6 and equation 4.10 the group velocity dispersion parameter in an optical resonator yields

$$D = \frac{\nu_\ell^2}{2\pi\cdot R\cdot c}\cdot\frac{\Delta(\Delta\nu_\ell)}{(\Delta\nu_\ell)^3} \;. \tag{4.18}$$

Another approach to derive the group velocity dispersion in an optical microresonator is to take into account the (angular-) momentum conservation of the light in the resonator. This momentum conservation leads to a propagation constant $\beta = 2\pi\cdot n/\lambda$ that is only proportional to the angular mode number ℓ, which follows directly from the resonator resonance condition $\ell\cdot\lambda = 2\pi\cdot R\cdot n$.

$$\beta = \frac{\ell}{R} \quad\Rightarrow\quad \frac{\Delta\beta}{\Delta\ell} = \frac{1}{R} \tag{4.19}$$

Note that R defines the actual radius of the resonator; all geometric dispersion contributions are included in the effective refractive index n. The first order dispersion in a resonator is inversely proportional to the free spectral range and is given by

$$\beta_1 = \frac{\mathrm{d}\beta}{\mathrm{d}\omega} = \frac{1}{2\pi\cdot R}\cdot\frac{1}{\Delta\nu_\ell} \;. \tag{4.20}$$

Now it is possible to derive the group velocity dispersion β_2 in a resonator with discrete modes as

$$\beta_2 = \frac{\mathrm{d}^2\beta}{\mathrm{d}\omega^2} = \frac{\mathrm{d}}{\mathrm{d}\omega}\frac{1}{2\pi\cdot\Delta\nu_\ell\cdot R} \tag{4.21}$$

with $\omega = 2\pi\cdot\nu_\ell$. Applying the chain rule to differentiate the equation yields

$$\beta_2 = -\frac{1}{4\pi^2\cdot R}\cdot\frac{1}{(\Delta\nu_\ell)^2}\cdot\frac{\mathrm{d}}{\mathrm{d}\nu_\ell}\Delta\nu_\ell = -\frac{1}{4\pi^2\cdot R}\cdot\frac{\Delta(\Delta\nu_\ell)}{(\Delta\nu_\ell)^3} \tag{4.22}$$

With $\mathrm{GDD} = L\cdot\beta_2$ it can be shown that this result matches the dispersion that has been calculated via the group delay of an electromagnetic wave in the resonator in equation 4.17.

4.2.1   Material dispersion in optical resonators

For most dielectric optical materials, dispersion can be derived from the wavelengths (or frequency) dependence of the refractive index of the material. The (vacuum-)wavelength dependence of the refractive index n can be approximated by equation 4.23 that has been developed by W. Sellmeier in 1871 [149].

$$n^2 = 1 + \sum_i \frac{A_i \cdot \lambda^2}{\lambda^2 - B_i^2} \quad . \tag{4.23}$$

Each term in the Sellmeier equation corresponds to an absorption line in the dielectric material. For most optical materials it is sufficient to specify the three leading terms for a decent accuracy of n. The Sellmeier coefficients A_i and B_i are usually given for wavelength λ in units of μm and the leading terms in fused silica for the wavelength range 0.21 μm $< \lambda <$ 3.71 μm are $A_1 = 0.6961663$, $A_2 = 0.4079426$, $A_3 = 0.8974794$, $B_1 = 0.0684043$, $B_2 = 0.1162414$ and $B_3 = 9.896161$. These values and Sellmeier coefficients for other materials can be found in handbooks for optical constants [64]. To derive the group velocity dispersion parameter from a Sellmeier equation it is required to express D as a function of the refractive index and the vacuum wavelength λ. For this we replace the propagation constant $\beta = \frac{2\pi \cdot n}{\lambda}$ in equation 4.7 and use $\frac{d}{d\omega} = -\frac{\lambda^2}{2\pi \cdot c}\frac{d}{d\lambda}$. With these substitutions, the group velocity dispersion parameter D as a function of the refractive index is given as

$$
\begin{aligned}
D & = \frac{d}{d\lambda}\frac{d\beta}{d\omega} = \frac{d}{d\lambda}\left(-\frac{\lambda^2}{2\pi \cdot c}\right)\frac{d}{d\lambda}\frac{2\pi \cdot n}{\lambda} \\
& = \frac{d}{d\lambda}\left(\frac{n}{c} - \frac{\lambda}{c}\cdot\frac{dn}{d\lambda}\right) \\
& = -\frac{\lambda}{c}\cdot\frac{d^2 n}{d\lambda^2}
\end{aligned}
\tag{4.24}
$$

The dispersion parameter for material dispersion of a microresonator can be calculated using equation 4.24 and the Sellmeier equation 4.23. Figure 4.3 illustrates dispersion in fused silica with negligible geometric dispersion. Depicted is the wavelength dependence of the refractive index, the second derivative of the refractive index with respect to the wavelength as well as the group velocity dispersion parameter D and the group delay dispersion GDD of a 100-μm-diameter whispering gallery mode resonator (here, just the GDD depends on the size of the resonator). The dispersive properties of fused silica change from normal to anomalous around 1276 nm, which can be seen by the zero crossings of D, $\frac{d^2 n}{d\lambda^2}$ and the GDD.

Figure 4.4 shows the wavelength dependence of the variation of the free spectral range $\Delta(\Delta\nu_\ell)$ (equation 4.13) in a 100-μm-diameter fused silica microresonator. The graph is calculated from the Sellmeier refractive index of the material without including the geometric contribution to the dispersion. As a consequence, the free spectral range of the
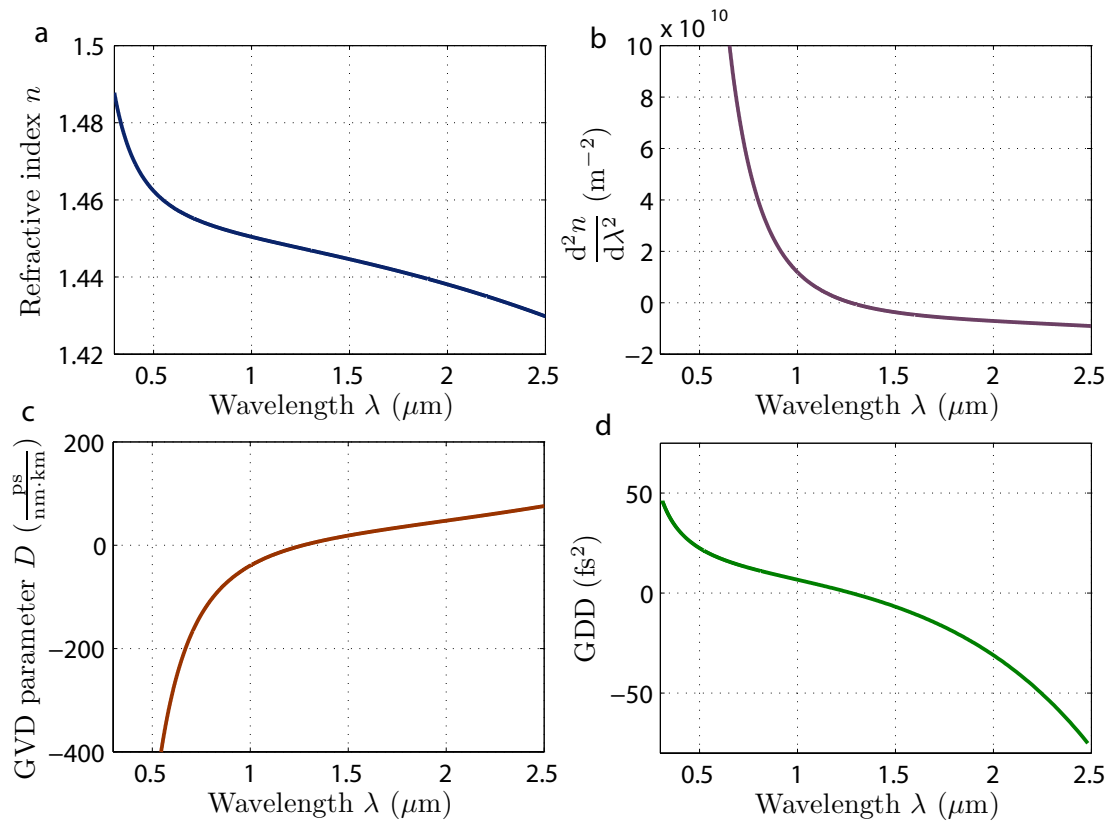
Figure 4.3: Material dispersion in fused silica. Panel a and b show the refractive index as a function of wavelength and its second derivative, respectively. Panel c depicts the group velocity dispersion parameter D. Panel d shows the group delay dispersion GDD in a 100-μm diameter microresonator without contributions of geometric dispersion. The zero dispersion point of fused silica is at 1276 nm.
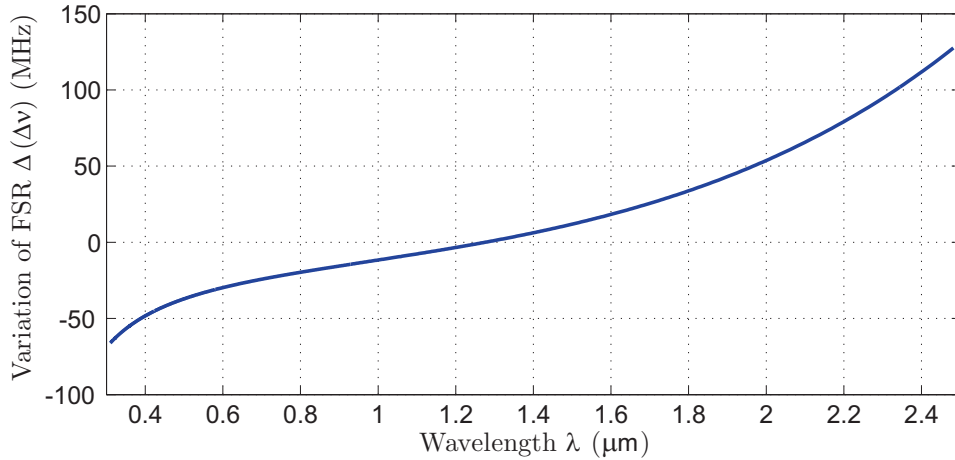
Figure 4.4: Sellmeier dispersion of microresonator modes. The graph shows the wavelength dependence of the variation of the free spectral range $\Delta(\Delta\nu_\ell)$ as a function of the wavelength in a 100-μm-diameter microresonator without geometric dispersion contributions. Values for the resonator dispersion are derived from the wavelength dependence of the refractive index given by the Sellmeier equation for fused silica. The free spectral range is nearly constant around the zero dispersion wavelength at 1276 nm.

resonator does not change at the zero dispersion wavelength of fused silica at around 1300 nm. Note that $\Delta(\Delta\nu_\ell)$ depends on the size of the resonator. A resonator size independent parameter (in the case of negligible geometric dispersion) is the group velocity dispersion GVD= β_2. From equation 4.22 and using $R \propto (\Delta\nu_\ell \cdot n)^{-1}$ follows that the variation of the free spectral range normalized to the squared free spectral range $(\Delta(\Delta\nu_\ell)/(\Delta\nu_\ell)^2)$ is independent of the resonator size for $\Delta n/n \ll 1$.

4.2.2   Geometric dispersion in optical resonators

This section presents a numerical approach that allows for precise calculations of the contribution of the resonator geometry to the total dispersion. It is well known that the geometry of an optical waveguides can strongly influence the propagation of electromagnetic waves. In standard single mode optical fiber for telecommunication, this effect leads to a shift of the zero dispersion wavelength from to 1310 nm compared to 1276 nm in bulk fused silica. As shown in the previous section, it is possible to derive the dispersion of a resonator from its resonance frequencies. For several standard geometries like spheres [150] and spheroids [151, 152] exist analytical formulae that enable determination of the resonance frequencies in optical resonators directly from Maxwell's equations. The main focus of this thesis is on toroidal shaped microresonators, which can be approximated to some extend by a spheroid (or ellipsoid). However, especially for frequency comb generation in resonators with very small mode volumes these approximations do not hold. In order to enhance the optical
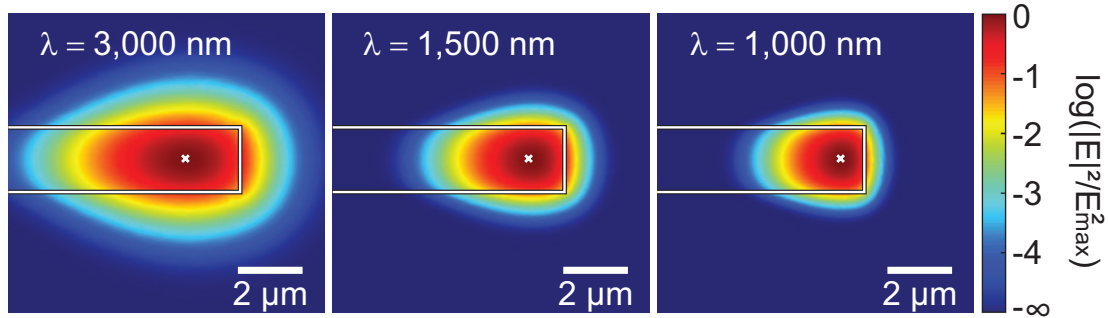
Figure 4.5: Electrical field distribution in the cross section of a 2-μm-thick fused silica disk with a major diameter of 100 μm. A meshing with 75,000 degrees of freedom is used for the simulation. The geometric dispersion is evident from the maximum of the electromagnetic field, which is approaching the resonator rim at decreasing wavelength.

nonlinearity it is required that the diameter of the toroid cross section is on the order of the wavelength of the optical light, with the consequence that not only the outer boundary of the resonator material but also the inner boundary influences the electromagnetic wave. Due to the lack of analytical methods to evaluate dispersion in microresonators, a numerical approach is used to solve the partial differential equations for the optical eigenmodes. The simulations are carried out with a finite-element solver (COMSOL Multiphysics). As the software does not natively support the calculation of electromagnetic eigenmodes in axial-symmetric structures, it is required to manually provide the weak form of the partial differential equations following the approach of M. Oxborrow [153, 154]. These simulations allow for accurate determination of the resonance frequencies and modal distributions in axial symmetric whispering gallery mode resonators. As a proof of concept, numerical simulations of the dispersion in a microsphere have been carried out and it is shown that the results are in excellent agreement with analytic calculations.

Figure 4.5 shows the electrical field distribution in a microdisk with a diameter of 100 μm and a thickness of 2 μm. The simulation directly reveals the first order geometric dispersion, which is leading to a shorter optical pathlength for higher wavelengths. Second order geometric dispersion on the other hand is proportional to the second derivative of the mode radius with respect to the wavelength as shown in equation 4.24 (the variation of the mode radius is included in the effective refractive index n).

Figure 4.6 shows finite element simulations of optical modes in a microtoroid. All modes belong to the same fundamental mode family of the resonator at different wavelengths and exhibit a reduced mode radius at longer wavelengths (here, mode radius refers to the mode position with respect to the symmetry axis of the toroid and not the size of the modal cross-section). The geometric dispersion can be derived from the curvature of the wavelength dependence of the mode radius, which is shown in panel b of figure 4.6. An important conclusion is that the curvature and thus the geometric dispersion has the same sign in whispering gallery mode resonators. This dispersion corresponds to "normal" dispersion and can compensate for "anomalous" material dispersion in fused
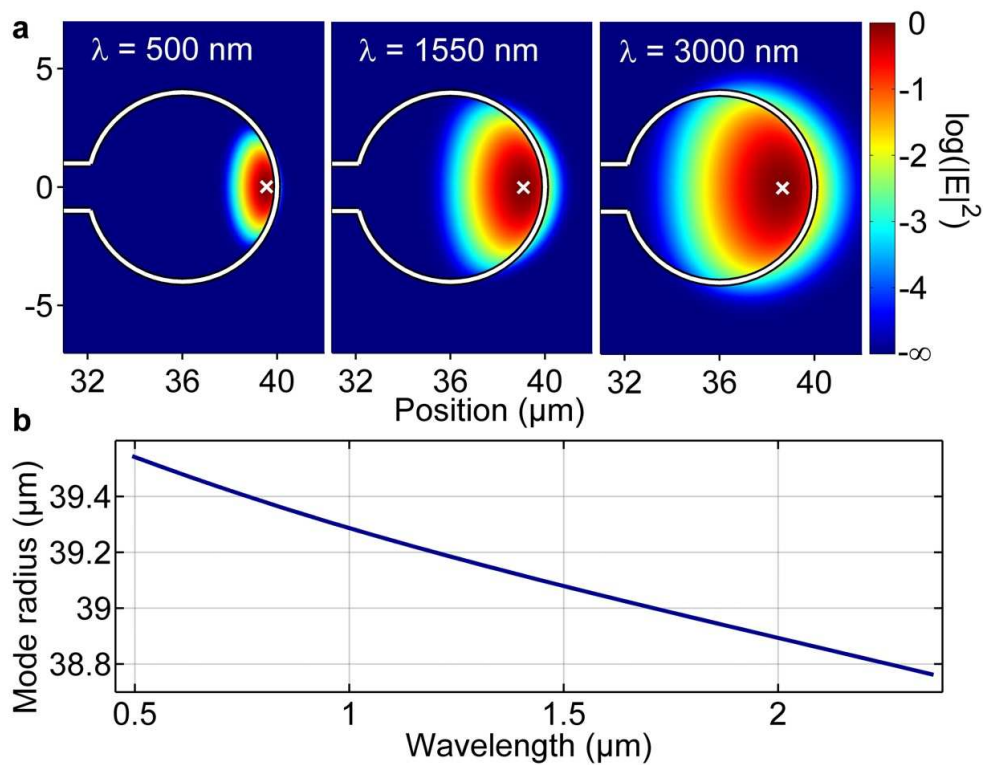
Figure 4.6: Fundamental optical modes in a 40-μm-radius microtoroid. The depicted modes are quasi transverse electric modes (TEM) and illustrate the geometric dispersion in the resonator. Panel b shows the mode radius as a function of the wavelength. Geometric contributions of the second order dispersion are determined by the curvature (second derivative) of the graph in panel b.
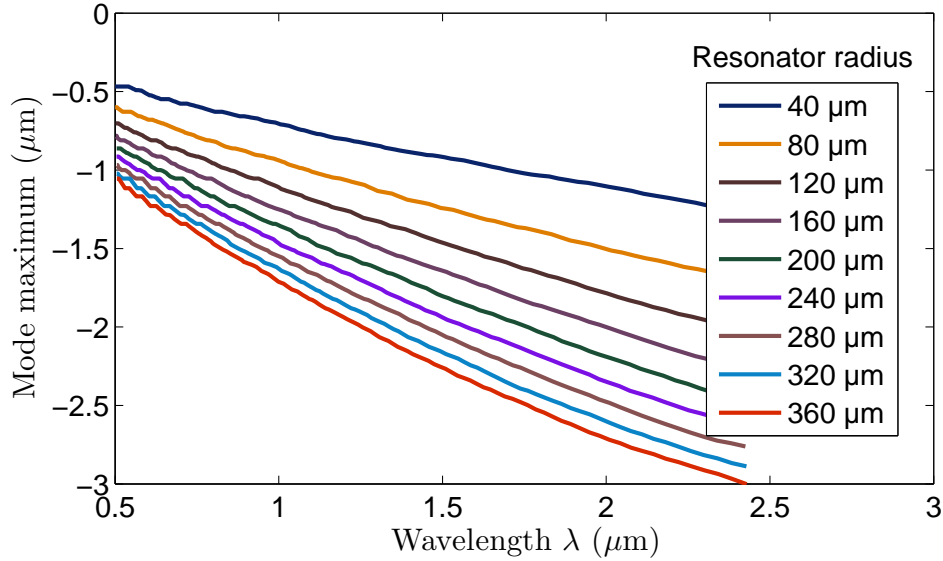
Figure 4.7: Finite element simulations of microresonator mode positions at different wavelengths. The graph shows the position of fundamental modes in a microtoroid (4 μm minor toroid radius) with respect to the rim of the resonator (located at zero on the vertical axis). Different curves correspond to resonators with different major radii. The position of the optical modes depends both on the wavelength and on the curvature of the resonator. Note that the mode maximum fluctuations at short wavelengths are numerical artifacts from the meshing of the finite element simulation.

silica resonators at wavelength beyond 1276 nm (cf. figure 4.3).

The amount of geometric dispersion in a microresonator is expected to depends on its size and the corresponding curvature of the waveguide. This effect is shown in figure 4.7, depicting the position of fundamental optical modes with respect to the outer rim of the resonator at different wavelength. It is evident that the optical modes are closer to the resonator surface in smaller resonators and at smaller wavelengths. A major difference between microtoroids and other whispering gallery mode resonators like microspheres or cylindrical resonators is the stronger confinement of the optical mode. Especially in case the minor diameter of the toroid cross-section approaches the optical wavelength, the dispersion of the resonator is influenced by the inner boundary of the toroid.

The impact of the inner boundary on the geometric dispersion in a microtoroid can be seen in figure 4.8. A comparison with the dispersion in a microsphere (illustrated as the variation of the free spectral range $\Delta(\Delta\nu)$) reveals an overall smaller geometric dispersion in a toroid compared to a sphere with the same fundamental diameter. An even further reduced geometric dispersion is observed at higher wavelengths with values that are close to the minor diameter of the simulated toroid. Note that the simulation in figure 4.8 are conducted with a fixed refractive index of the material and do not take into account material dispersion. Geometric dispersion in a microspheres can be approximated with an expansion from Schiller [150]. This expansion gives the following values for whispering
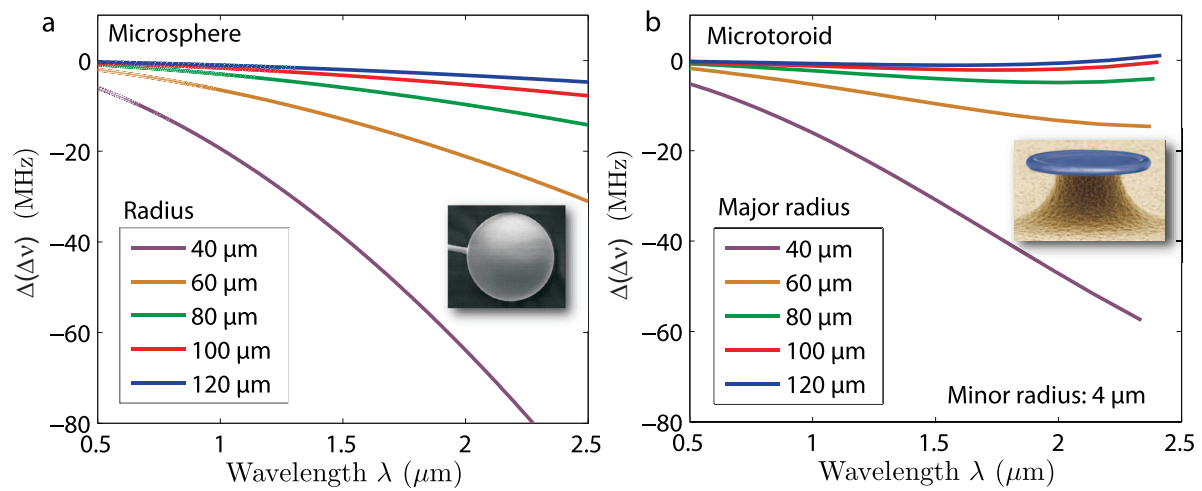
Figure 4.8: Comparison of the geometric dispersion in a microsphere and a microtoroid. Panel a shows the variation of the free spectral range $\Delta(\Delta\nu)$ in fused silica microspheres of different radii. The dispersion data for the microsphere is obtained from analytical calculations based on the expansion of optical modes in microspheres from Schiller [150]. Panel b shows finite element simulations of $\Delta(\Delta\nu)$ for microtoroids with a cross-section radius of 4 μm and different major radii corresponding to the values of the sphere in panel a. Note that the geometric dispersion in a microtoroid can change its sign at longer wavelengths as a result of the inner boundary of the toroid.

gallery mode resonance frequencies ν_{sph} (for fundamental modes with a radial mode number $n_{\text{rad}} = 1$):

$$\nu_{\text{sph}}(\ell) = \frac{c}{2\pi \cdot R \cdot n_a} \left[\frac{\ell + 1/2}{n_{\text{rel}}} - \frac{\zeta_1}{n_{\text{rel}}} \left(\frac{\ell + 1/2}{2} \right)^{\frac{1}{3}} + \sum_{k=0}^{k_{\text{max}}} \frac{d_k(n_{\text{rel}})}{(\ell + 1/2)^{\frac{k}{3}} (n_{\text{rel}}^2 - 1)^{\frac{k+1}{2}}} \right] \,.$$

(4.25)

Here, ℓ is the angular mode number; $\zeta_1 \approx -2.34$ is the first zero of the Airy function; $n_{\text{rel}} = \frac{n_s}{n_a}$ is the relative refractive index of sphere n_s and surrounding medium n_a; R is the radius of the microsphere and c is the speed of light in vacuum. Moreover, the coefficients d_k are given by (for $k_{\text{max}} = 2$)

$$d_0 = -p \tag{4.26}$$

$$d_1 = 2^{1/3} \cdot 3(n_{\text{rel}}^2 - 1)\frac{\zeta_1^2}{20 n_{\text{rel}}} \tag{4.27}$$

$$d_2 = -2^{2/3} n_{\text{rel}}^2 p(2p^2 - 3)\frac{\zeta_1}{6} \tag{4.28}$$

4.2.3 Combined material and geometric dispersion in microresonators

Both material and geometric dispersion have been analyzed separately in the previous sections. Now we want to try to combine both contributions to the total dispersion in whispering gallery mode resonators. A simple approximation for the total dispersion can be done by separating the wavelength dependent effective refractive index into two parts for the geometric and material dispersion $n(\lambda) = n_{\text{mat}}(\lambda) + n_{\text{geom}}(\lambda)$. The group velocity dispersion is proportional to the second derivative of $n(\lambda)$ and consequently one could just add the dispersion contributions. However, this requires that the material and geometric dispersion are mutually independent, which is not the case in whispering gallery mode resonators. One obvious problem is the evanescent field of the electromagnetic modes (cf. figure 4.6), which influences the net material dispersion via the spatial position of the mode. On the other hand, it is difficult to implement material dispersion into the finite element simulations as it would significantly raise the complexity of the partial differential equations that have to be solved. Thus, another approach is chosen to determine the combined dispersion in microresonators in which the Sellmeier material dispersion is added iteratively to the finite element simulations, assuming just small corrections to the refractive index. The finite element solver is used to first calculate the resonance frequency of a mode with given angular mode number ℓ using an approximate Sellmeier value for the refractive index given by the coarse position of the resonance wavelength λ_0 (which is approximated by $\lambda_0 = \frac{2\pi \cdot R \cdot n_0}{\ell}$ for a resonator with radius R and n_0 is the Sellmeier refractive index at the pump laser wavelength). In each additional iteration, the simulated resonance frequency is used to calculate a new value for the refractive index with the Sellmeier equation. Because
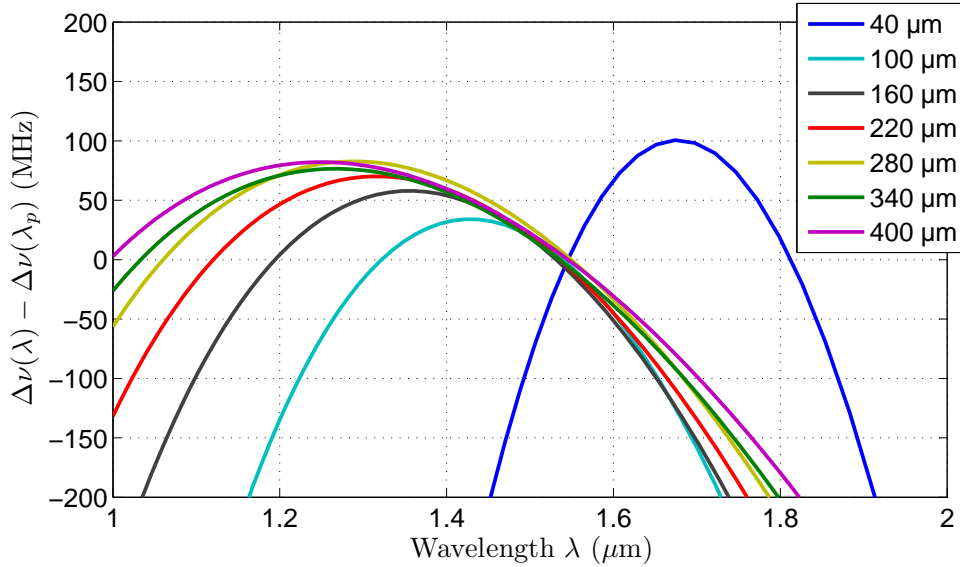
Figure 4.9: Finite element simulation of the free spectral range in a microtoroid including both material- and geometric dispersion. Different lines correspond to resonators with different major radii between 40 μm and 400 μm. The minor radius of the toroid cross-section is fixed at 4 μm. Dispersion of the resonator is proportional to $(\Delta\nu)^{-2} \cdot \frac{\mathrm{d}}{\mathrm{d}\nu} \cdot \Delta\nu$ such that the maxima of the curves correspond to the zero dispersion wavelengths. Curves in the figure are offset by the free spectral range at $\lambda_p = 1550$ nm to enable direct comparison of the various resonator sizes.

of the small variations of the refractive index, this method converges very fast and usually 4 to 5 iterations are sufficient to determine the total dispersion in a microresonator.

Figure 4.9 shows the simulated free spectral ranges $\Delta\nu(\lambda)$ for microtoroids with different major radii ranging from 40 μm to 400 μm. The plotted data is offset by the free spectral range at $\lambda_p = 1550$ nm in order to combine the different curves into one graph. Knowing that the derivative of the free spectral range with respect to the wavelength is related to the dispersion (cf. equation 4.22), we can infer the zero dispersion wavelength in the different resonators from the extrema of the curves. The free spectral range in fused silica has a *maximum* at the zero dispersion wavelength. Moreover it is evident that the dispersion (slope of the curve) changes its sign for small resonators at a wavelength around 1550 nm, corresponding to a working point in the normal dispersion regime. The values for the wavelength dependent free spectral ranges are calculated from finite element simulations of 200 resonance frequencies for each resonator size. Since the simulated resonance frequencies are not consecutive, equation 4.12 is used to calculate the average free spectral range for each simulation point.

Each finite element simulation is run using a meshing with 27,000 degrees of freedom and takes approximately 5 minutes for the calculation of one resonance frequency on a desktop computer system with a dual core 1.8 GHz processor. The total computation time for the

graphs in figure 4.9 and the following figures is around 5 days. An additional obstacle in the finite element simulation is the numerical instability of some solutions in certain resonator geometries (especially with small toroid cross-section). Thus it is required to provide a rather accurate starting value for the resonance frequency simulation to prevent the simulation of spurious higher order modes. The starting value for the resonance frequency is automatically adjusted by a Matlab script in order to find the fundamental modes of the respective microresonator using the following criteria for a successful simulation:

- Maximum electric field intensity close to the toroid axis for fundamental modes

- Strong decay of the electrical field intensity outside of the toroid (to avoid spurious "air"-modes)

- Direction of the electrical field vector at the mode maximum (to differentiate between quasi TE and TM modes)

In case of a failed simulation, the starting value is varied until a fundamental mode with the desired polarization is found. Figure 4.10 shows dispersion values of microtoroids based on these simulations.
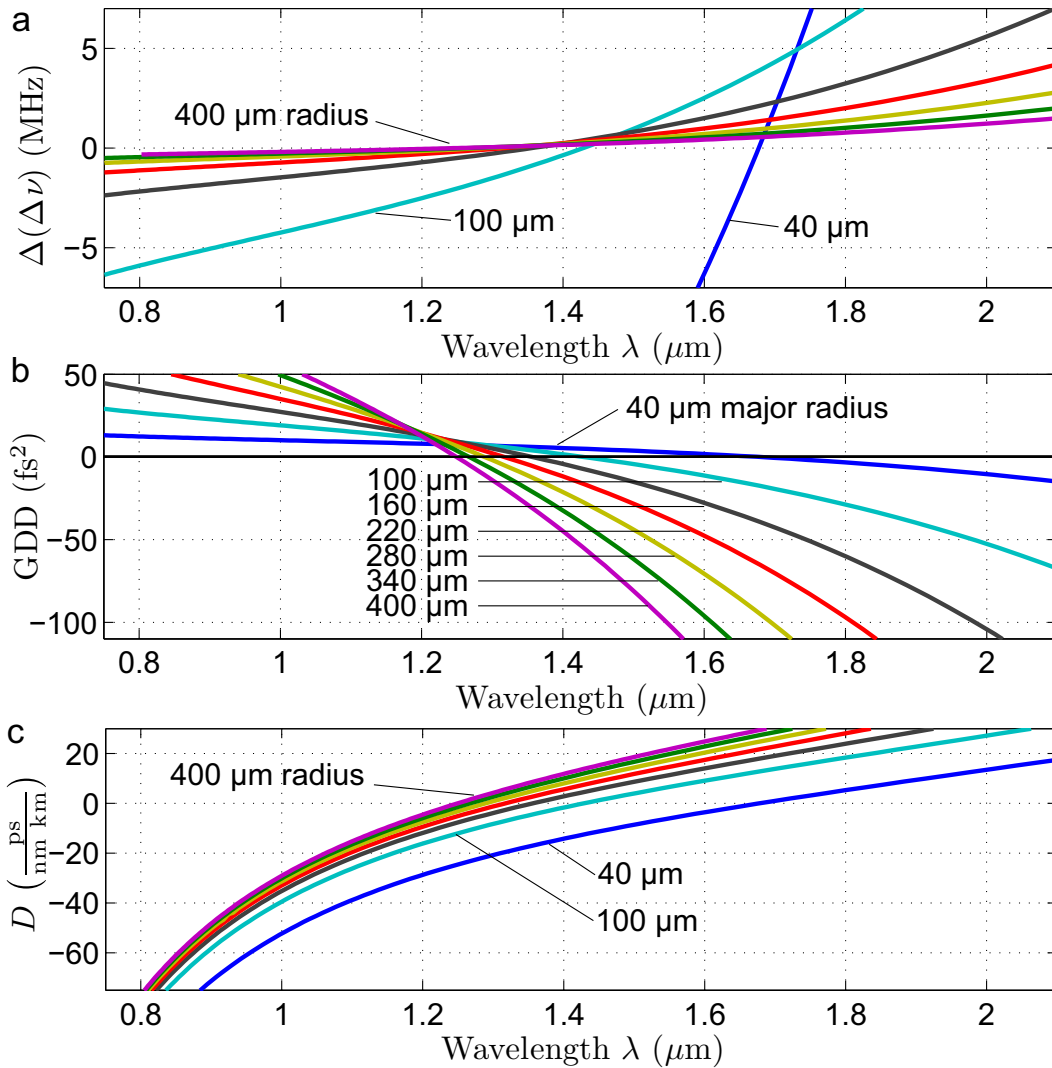
The variation of the free spectral range $\Delta(\Delta\nu)$ is calculated according to equation 4.13. The values for $\Delta(\Delta\nu)$ are generally higher in smaller resonators, however this effect is compensated by a fundamentally higher mode spacing. This is evident in the simulated values for the group delay dispersion GDD (equation 4.17) in panel b of figure 4.10. The zero dispersion wavelength is strongly shifted towards higher wavelengths in smaller resonators. In larger resonators on the other hand, the zero dispersion wavelength approaches the value for bulk fused silica as a result of the decreased influence of the geometric dispersion.

A more detailed analysis of the zero dispersion wavelength in microtoroids of different sizes is shown in figure 4.11. Interestingly, the zero dispersion wavelength in larger resonators can be even slightly smaller than the zero dispersion wavelength of bulk fused silica (1276 nm).

So far we have learned that microresonator dispersion is influenced by the geometry of the optical waveguide and that the zero dispersion wavelength is shifted towards higher wavelengths in smaller resonators. The crucial question for frequency comb generation, however, is the maximum achievable bandwidth in which the four-wave mixing process can take place. This bandwidth strongly depends on the mismatch $\Delta\nu_{\mathrm{mm}}$ between equidistant comb modes and the non-equidistant resonator modes. Figure 4.12a shows a sketch of the cold resonator modes and equidistant frequency comb modes. Assuming that the pump laser frequency coincides with a resonance frequency, this leads to a zero mismatch at the pump laser comb mode. In the following discussion $\Delta\nu_{\mathrm{mm}}$ is defined as

$$\Delta\nu_{\mathrm{mm}} = \nu_{\mathrm{comb}} - \nu_{\mathrm{cavity}} \quad . \tag{4.29}$$

Panel b of figure 4.12 shows the simulated mismatch between comb modes and cavity modes for a pump laser at 1550 nm. The mode spacing of the generated frequency comb

Figure 4.10: Finite element simulations of dispersion in a microtoroid with different diameters. Panel a shows the variation of the free spectral range $\Delta(\Delta\nu)$ according to equation 4.13. Panel b depicts the group delay dispersion (equation 4.17) and panel c the group velocity dispersion parameter (equation eqn:gvdparaminreson) as a function of the wavelength.
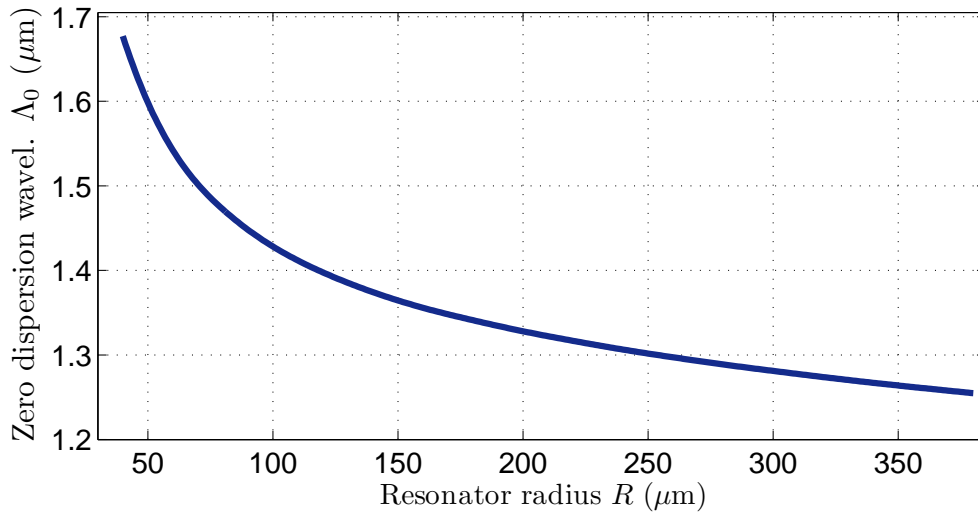
Figure 4.11: Zero dispersion wavelength Λ_0 as a function of the microresonator size. The horizontal axis represents the major radius of a microtoroid with a fixed toroid cross-section radius of 4 μm. Small resonator geometries can shift the zero dispersion wavelength in fused silica to more than 1600 nm.

is chosen as the resonator mode spacing around the pump mode. It is interesting to note that the absolute value of the frequency mismatch first increases with increasing distance to the pump mode. However, for a pump mode in the anomalous dispersion regime the mismatch shrinks again at lower wavelength and even returning to a zero mismatch (100 μm to 340 μm resonator radius in figure 4.12b). The situation for a pump laser in the normal dispersion regime (40 μm radius in Fig. 4.12b) is inverted such that the mismatch first increases and then decreases towards higher wavelengths. The mismatch depends strongly on the resonator geometry and for certain resonator sizes a mismatch close to zero can be maintained for a broad bandwidth. Figure 4.13 shows simulations of the dispersion induced comb-mode cavity mode-mismatch $\Delta\nu_{\mathrm{mm}}$ for pump wavelengths of 1000 nm and 1300 nm.

However, based on these simulations it is surprising that broadband optical frequency combs can be generated in microresonators, since the cavity linewidth is typically in the order of just 1 MHz. Consequently comb generation should be impossible already for a mismatch in the same order of magnitude. Thus there must be an additional effect that influences the position of the resonator modes. Note that the calculated mismatch is based on the dispersion simulation of the position of the cold cavity modes without frequency comb. In a pumped resonator on the other hand, the cavity modes are strongly affected by the high light intensities circulating within the cavity. A strong distortion of the mode spectrum arises from the third order Kerr effect in fused silica as the lowest order optical nonlinearity (resulting from the macroscopic inversion symmetry in amorphous SiO_2). This leads to cross-phase and self-phase modulation in the resonator that could potentially "pull" the resonator modes equidistant. To get an idea of the frequency pulling
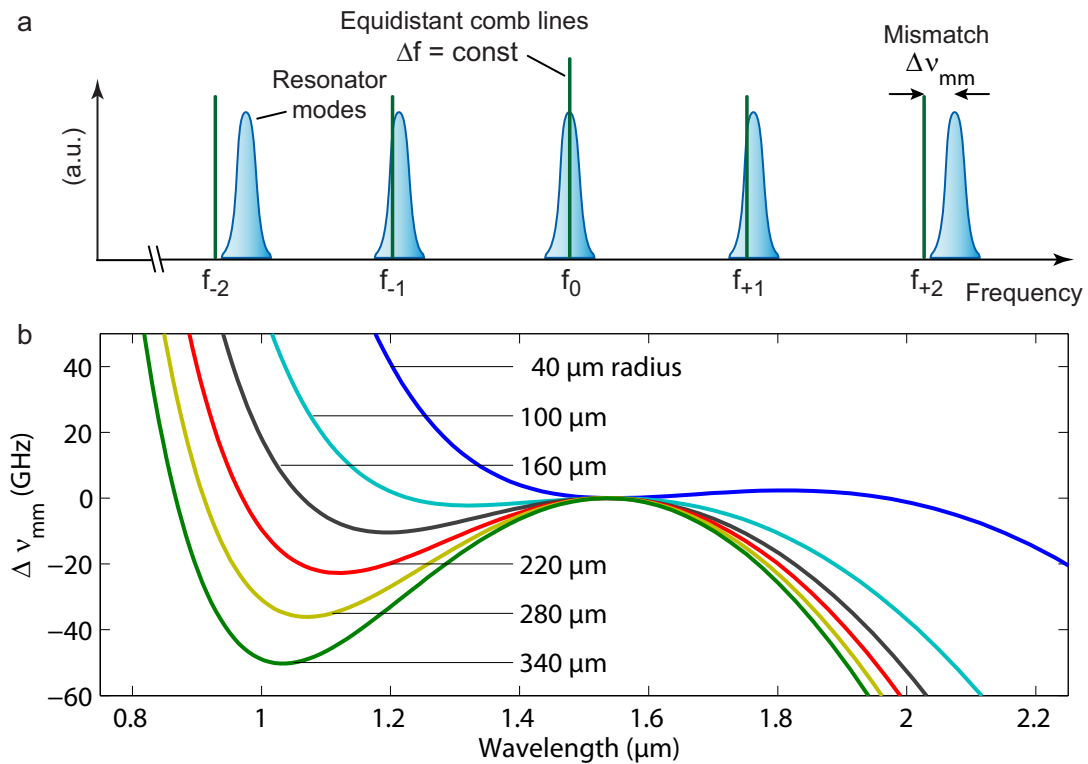
Figure 4.12: Mismatch between equidistant comb modes and cold cavity modes in toroidal microresonators (toroid cross-section radius 4 μm). Panel a shows a sketch of the increasing mismatch between comb modes and resonator modes in the vicinity of the pump laser (which is exactly resonant with a cavity mode). Panel b shows the mismatch $\Delta\nu_{mm}$ for different resonator sizes based on finite element simulations. Note that mismatch is first increasing but decreases again after passing the zero dispersion wavelength of the respective resonator.
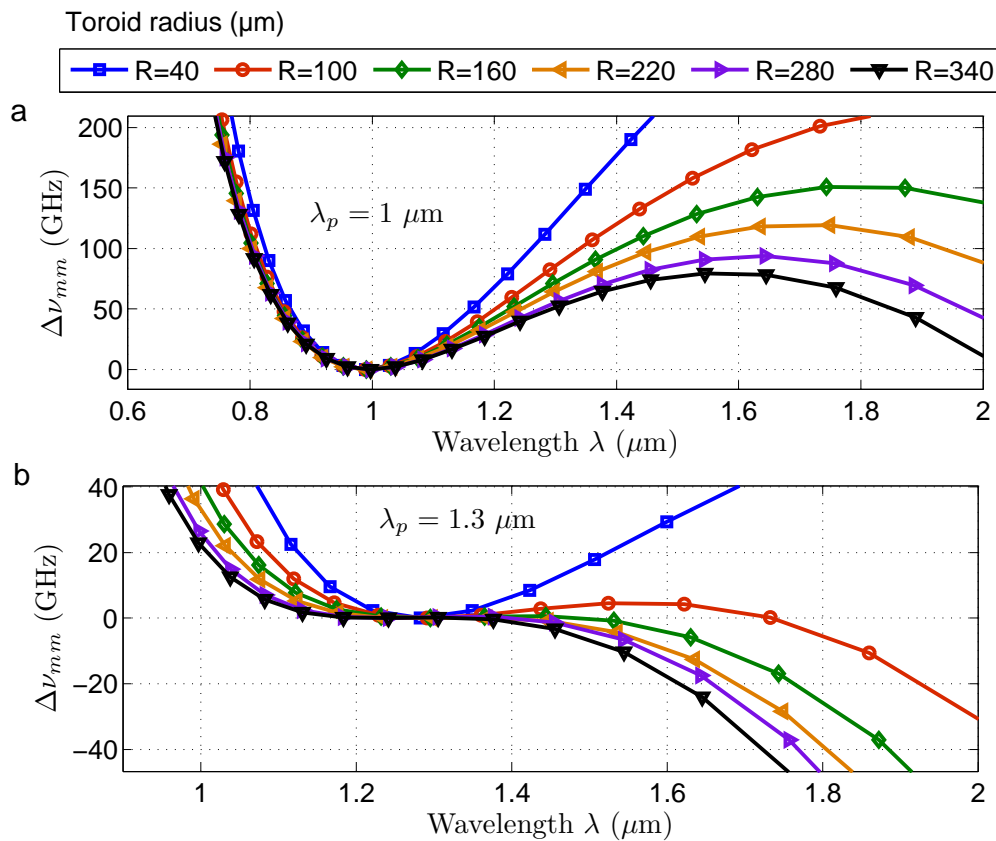
Figure 4.13: Dispersion displayed as mismatch between comb-/ and cavity modes for pump wavelengths (zero mismatch) of 1000 nm (panel a) and 1300 nm (panel b). The graph is based on finite element simulations of microtoroids with 4 μm toroid cross-section radius.

of resonator modes, we can derive the resonance frequency shift $\Delta\nu_{\mathrm{res}}$ based on the Kerr nonlinearity induced refractive index change Δn. From $\nu_{\mathrm{res}} \propto 1/n$ follows

$$\Delta\nu_{\mathrm{res}} \approx -\nu_{\mathrm{res}} \cdot \frac{\Delta n}{n} \quad . \tag{4.30}$$

The Kerr effect induced refractive index change is given as $\Delta n = n_2 \cdot I_{\mathrm{res}}$ (with the nonlinear refractive index $n_2 = 2.2 \times 10^{-20}$ m^2 W^{-1} and I_{res} being the circulating intensity in the resonator). Replacing the intracavity intensity by the launched power P_{in} yields

$$\Delta\nu_{\mathrm{res}} \approx -\nu_{\mathrm{res}} \cdot \frac{n_2}{n^2} \cdot \frac{c}{4\pi^2 \cdot R \cdot A_{\mathrm{eff}}} \cdot \frac{N}{\kappa} \cdot P_{\mathrm{in}} \quad , \tag{4.31}$$

with $n = 1.44$ being the refractive index of fused silica in a microresonator with radius R and effective mode area A_{eff}. Moreover κ corresponds to the linewidth of the resonator modes and N is an additional peak power enhancement or pulse enhancement due to the interference of the generated comb modes. The nonlinear mode shift $\Delta\nu_{\mathrm{res}}$ is inversely proportional to the resonator radius R as a result of the reduced nonlinear optical effect in a larger mode volume. Nonlinear mode shifts in microresonators can exceed several tenths of gigahertz due to the high circulating power. In a 100-μm-diameter resonator with an effective mode volume $A_{\mathrm{eff}} = 2$ μm^2, a linewidth of $\kappa = 2$ MHz, a pulse enhancement of $N = 10$ and a launched power $P_{\mathrm{in}} = 100$ mW the nonlinear mode shift equates to $\Delta\nu_{\mathrm{res}} \approx 80$ GHz. This effect has the potential to significantly lower the dispersion in a "hot" microresonator. Note however, that it requires a wavelength dependent variation of the spatial position of the modes (geometric dispersion) in order to achieve different mode shifts in different spectral regions for an overall flat dispersion.

Figure 4.14 shows the mismatch between comb- and cavity modes normalized to the absolute value of the nonlinear mode shift $|\Delta\nu_{\mathrm{res}}|$ in different toroidal resonators with a fixed minor radius of 4 μm. The sign of the nonlinear mode shift is always negative in fused silica, leading to a resonance shift towards lower frequencies at higher powers. We have defined the mismatch between comb modes and cavity modes as $\Delta\nu_{\mathrm{mm}} = \nu_{\mathrm{comb}} - \nu_{\mathrm{cavity}}$ and consequently it is only possible to compensate a negative mismatch $\Delta\nu_{\mathrm{mm}} < 0$ by nonlinear mode pulling. The shaded region in figure 4.14 illustrates the range in which the nonlinear mode shift can be larger than the mismatch between comb- and cavity modes ($\Delta\nu_{\mathrm{res}} \geq \Delta\nu_{\mathrm{mm}}$) corresponding to the region of possible comb generation. Especially, this graph shows that the nonlinear mode pulling has the potential to enable even *octave spanning* frequency comb generation for certain resonator sizes. In the case of a toroid cross section radius of 4 μm, the optimum major radius for broadband comb generation is in the order 200 μm.

The previously shown dispersion curves were simulated for toroidal microresonators with a fixed minor radius of 4 μm. However, as we have seen before, dispersion strongly depends on the waveguide geometry, which is influenced by the toroid cross section diameter as well. Figure 4.15 shows finite element simulations of modes in microresonators with different toroid cross sections and it is evident that the shape of the mode depends on the curvature of the toroid. Especially small toroid cross sections lead to a stronger confinement
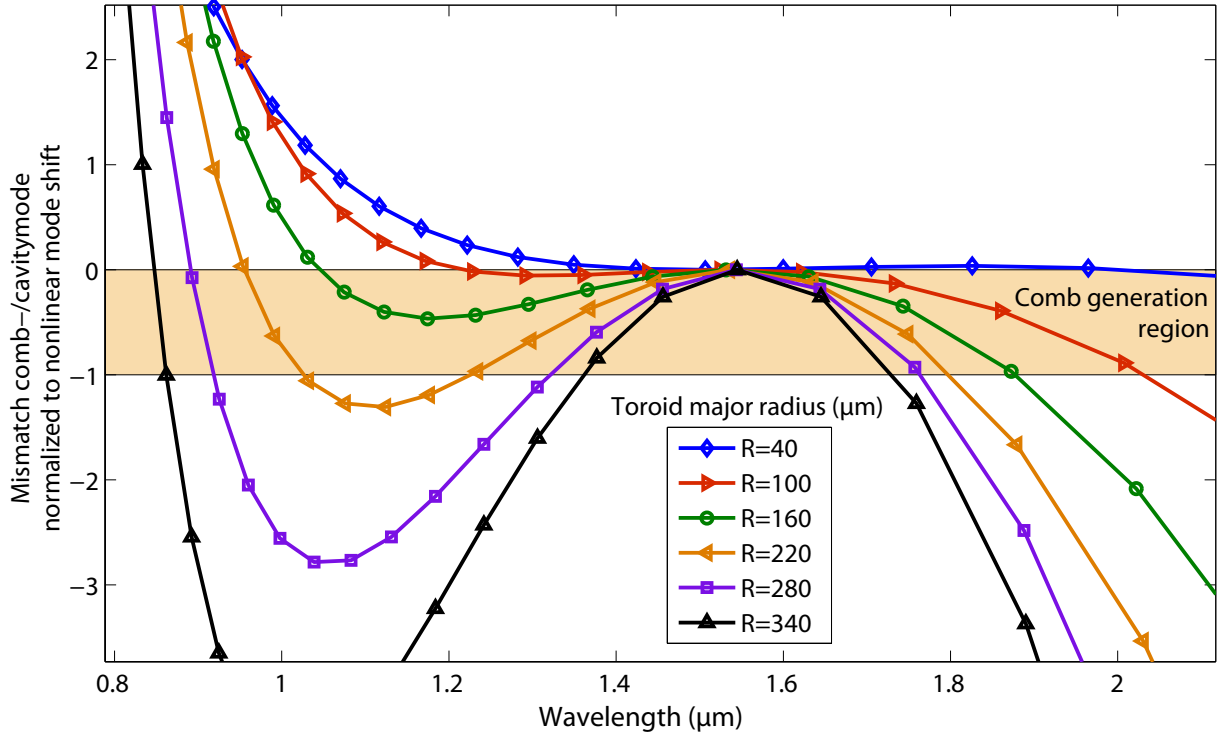
Figure 4.14: Comb generation bandwidths in different microresonator sizes. The plot shows the mismatch between comb- and microresonator modes normalized to the maximum nonlinear mode pulling in the respective resonator ($\Delta\nu_{\mathrm{mm}}/|\Delta\nu_{\mathrm{res}}|$). Different curves correspond to resonators with different major radii; the minor radius of the toroid cross-section is fixed at 4 μm. The shaded region depicts the wavelength range in which the nonlinear mode shift can be larger than the mismatch between comb- and cavity mode. Based on these finite element simulations, a resonator radius between 150 μm and 200 μm is expected to generate the broadest frequency combs in toroids with 4 μm cross-section radius.
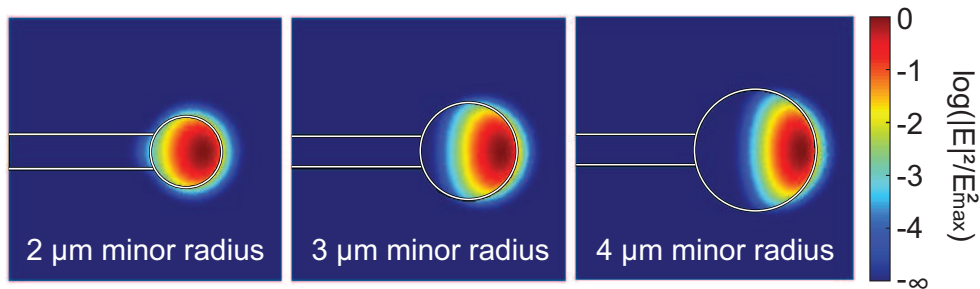
Figure 4.15: Finite element simulations of optical modes in a microtoroid. The major resonator radius is fixed at 40 μm, while the minor radius (toroid cross-section) is varied from 2 μm to 4 μm. The inner boundary of the toroid influences the shape of the optical mode in smaller resonators, which affects the geometric dispersion.
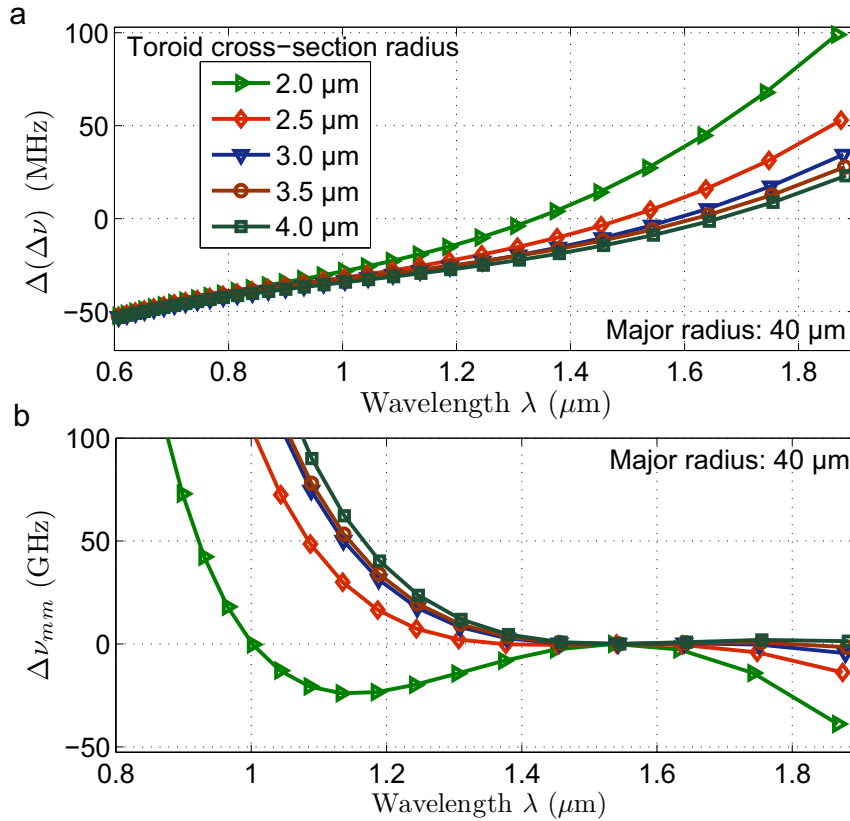
Figure 4.16: Microresonator dispersion control via cross-section variation. The graphs show dispersion in a 40-μm-radius microtoroid with different toroid cross-section radii. Panel a depicts the dispersion as the variation of the free spectral range $\Delta(\Delta\nu)$ and panel b as the mismatch between comb modes and cavity modes $\Delta\nu_{\mathrm{mm}}$ for a pump laser at 1550 nm. The graph in panel a shows that the zero dispersion wavelength is shifted towards shorter wavelengths in toroids with smaller cross-sections, providing an additional handle for microresonator dispersion control.

of the optical modes and the inner boundary of the resonator starts influencing the position of the mode. Comparison with figure 4.6 of modes at different wavelengths suggests that the effect of longer wavelength on the modal position is similar to the effect of a smaller minor diameter of the toroid cross section.

The impact of the inner boundary on the cavity dispersion in resonators with smaller cross-section can be seen in figure 4.16. It leads to a zero dispersion point that is pushed back to the zero dispersion wavelength of bulk fused silica since the spatial position of the optical mode cannot be pushed further towards the center of the toroid at higher wavelengths. Consequently, the minor diameter of a microtoroid can be used as additional handle to shift the zero dispersion wavelength of a resonator with a given major radius (and a fixed mode spacing) to a wavelength that supports broadband comb generation. This can be seen in figure 4.16b showing the mismatch between comb- and cavity mode.

We have learned before that this mismatch can be compensated by nonlinear mode pulling only when the mismatch is smaller than zero. Thus, a resonator with a major radius of 40 μm and a minor radius of 4 μm is expected to be unable to generate broad frequency combs. However, after reducing the cross-section radius to around 2 μm the dispersion changes sign in the vicinity of a pump laser at 1550 nm and enables the generation of broadband frequency combs. This is in good agreement with experimental observations in which smaller toroid cross-sections have shown broader combs in resonators with smaller major diameters, while larger resonators require a larger toroid cross-section.

4.3 Frequency comb assisted diode laser spectroscopy

Dispersion measurements of an optical microresonator can be realized by precise analysis of its mode spectrum, as we have learned in the previous section. These measurements are difficult because it is required to measure the resonator spectrum over a large bandwidth and at the same time with high precision. Additionally, the measurement needs to be performed very fast since the resonator modes are influenced by thermal drifts, which are in the order of several GHz per Kelvin as we have seen in chapter 3. The challenge to quantify dispersion in a microtoroid with a radius of 400 μm require the following measurement parameters:

- High resolution (cavity linewidth $<$ 5 MHz)

- High precision (difference between two adjacent FSR $<$ 500 kHz)

- Large bandwidth (large resonator FSR requires bandwidth $>$ 4 THz)

- Fast measurement (thermal drifts of the resonator modes in the order of 100 kHz/s)

The required bandwidth is higher than the actual mode spacing of the resonator in order to increase the statistical significance of the measurement. This is necessary as a result of interactions between different mode families that can locally shift certain modes to new positions and will be discussed later in this chapter (the smallest possible bandwidth for a dispersion measurement corresponds to twice the mode spacing and would lead to a single dispersion value). Optical frequency combs can easily provide the required precision, however, there is a drawback with the required resolution that needs to be smaller than 5 MHz in order to resolve the cavity resonances. Thus, using frequency combs with a typical mode spacing around 100 MHz, it would be necessary to change the position of the frequency comb modes via offset frequency and/or repetition rate in order to trace out the full microresonator mode spectrum. Direct frequency comb spectroscopy is typically used for gas sensing, in which broad spectral features with linewidths exceeding the comb spacing need to be resolved [155, 156] and features smaller than the comb spacing cannot be resolved without changing the comb parameters. The same difficulties apply to methods like multi-heterodyne or Fourier transform spectroscopy in which the beat notes between

the modes of two combs at slightly different repetition rates are used for spectroscopy [135–138, 157, 158].

To our knowledge there was no existing method to determine the dispersion of microresonators that can meet all the requirements in the list shown at the beginning of the section. However, since the dispersive properties of microresonators are crucial for optical frequency comb generation, a novel method is developed, combining the continuous resolution of a tunable external cavity diode laser with the accuracy of an optical frequency comb [5]. This spectroscopy method works by tracing out the mode spectrum with a tunable diode laser, which is simultaneously referenced to an optical frequency comb.

Figure 4.17 shows a principal sketch of the experimental setup for this experiment. A continuously tunable diode laser (New Focus velocity, short term linewidth 300 kHz) is scanned across the wavelengths region of interest to record a transmission or reflection spectrum of a device of interest (in this case a microtoroid). Another part of the diode laser light is combined with the emission spectrum of an optical frequency comb (Menlo Systems, fiber laser based comb, 250 MHz repetition rate) and generates beat notes with the different comb lines on a fast photodiode. As the diode laser is continuously changing its frequency during a scan, the heterodyne beat notes are changing their frequency as well. Panel c in figure 4.17 shows the beat note frequency between the scanning diode laser and the closest frequency comb line as a function of the diode laser frequency. The maximum beat note frequency corresponds to half the repetition rate ($f_{\mathrm{rep}}/2$) of the comb. In case of a linear diode laser sweep, this leads to a triangular shape of the beat note function with a frequency range from zero to $f_{\mathrm{rep}}/2$. The beat note frequency could be continuously recorded for a precise spectroscopic measurement to determine the diode laser frequency at every time. However, this would require a slowly scanning diode laser to determine the instantaneous beat frequency. The whole measurement of microresonator dispersion on the other hand should not last more than a few seconds to avoid measurement errors from thermal resonance frequency drifts. Thus, a we aim for a laser scanning speed of around 1 THz/s, which is to fast for direct beat note frequency counting. However, the amount of recorded data can be drastically decreased by just recording periodic "trigger" (calibration) signals at certain well-known frequency spacings to determine the diode laser frequency. These trigger signals can be generated by passing the beat note frequency through electronic bandpass filters as depicted in figure 4.17b and recording the output with a fast oscilloscope. Every time the beat note frequency falls within the the frequency of one of the bandpass filters, a trigger signal is recorded on the oscilloscope. The frequency combs repetition rate f_{rep} and carrier envelope offset frequency f_{ceo} is fully stabilized so that the comb modes are located at frequencies of $f_c = f_{\mathrm{ceo}} + n \cdot f_{\mathrm{rep}}$ ($n \in \mathbb{N}$). Consequently, trigger signals f_T are recorded at frequencies of

$$f_T = f_{\mathrm{ceo}} + n \cdot f_{\mathrm{rep}} \pm f_{\mathrm{BP}} \quad , \tag{4.32}$$

with f_{BP} being the frequency of the bandpass filter. Subsequently, the instantaneous diode laser frequency can be reconstructed by an interpolation of the trigger signals (eg. by assuming a linear laser sweep at times between trigger signals). Combining the frequency
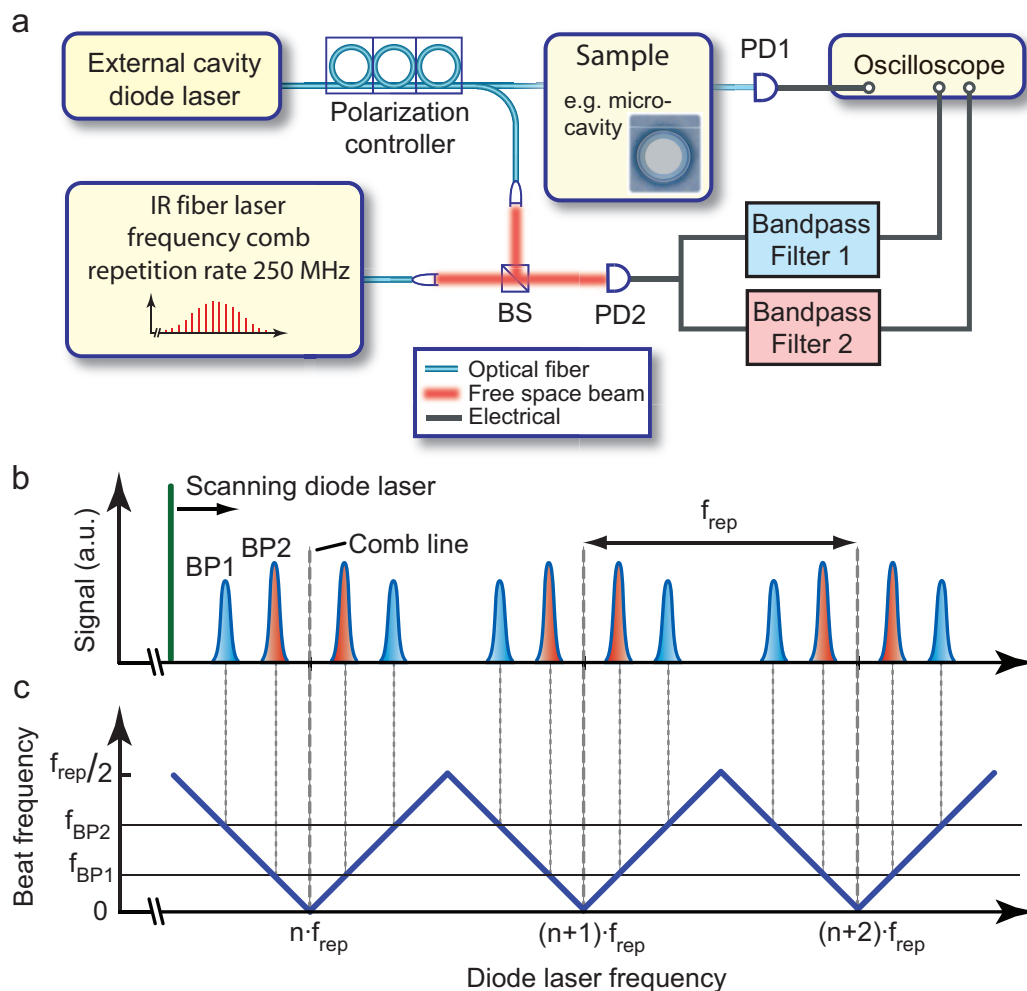
Figure 4.17: Frequency comb assisted diode laser spectroscopy principle and setup. Panel a shows the experimental setup with a mode hop free tunable external cavity diode laser that is used to record the transmission spectrum of a sample. Part of the diode laser signal is simultaneously used to generate a beat note with a fully stabilized frequency comb, resulting in a "running" beat notes while scanning. Panel c shows the lowest frequency beat note frequency as a function of the diode laser frequency. By filtering the "running" beat notes with two bandpass filters at frequencies f_{BP1} and f_{BP2} calibration four calibration markers are generated in each interval of the frequency comb's repetition rate, which can be used to calibrate the optical spectrum recorded by the sweeping diode laser. PD = photodiode.

calibration with the simultaneously measured transmission or reflection signal of the device under investigation (eg. microtoroid) enables reconstruction of the spectral response of the measured sample. The actual experiments are performed using two bandpass filters with center frequencies of 30 MHz and 75 MHz, leading to calibration peaks signals at $\pm$ 30 MHz and $\pm$ 75 MHz with respect to the frequency comb lines (which has a repetition rate of 250 MHz). The employed electronic bandpass filters are manually tunable filters from "K&L" (tuning range 30 MHz to 75 MHz, passband $\approx$ 1 MHz). Note that the adjusted center frequency of the bandpass filters can be determined by the measurement itself (by knowing the spacing of the comb modes) and is not required to be known a priori. The center frequencies of the bandpass filters could also be adjusted to frequencies that result in equally spaced calibration markers. However, the unequally spaced calibration signals are advantageous by providing a direct error correction in case some calibration peaks are not measured.

Figure 4.18 shows a measurement of a microtoroid transmission spectrum together with calibration markers generated by two different bandpass filters. The horizontal time axis is already converted to a frequency axis using the known position of the calibration markers. Note that the measurement is intended to quantify microresonator dispersion and thus it is sufficient to measure relative frequencies to determine the mode spacing change. An absolute frequency measurement requires (as usual for frequency comb measurements) an additional measurement with an accuracy better than the frequency comb's repetition rate. Alternatively the measurement can be repeated at a different repetition rate in order to obtain an absolute frequency calibration. The total bandwidth of the measurement in figure 4.18a is 2.5 THz at a wavelength of 1550 nm. Panels b,c show a zoom into the same data with 125x and 5000x magnification at the position of a microtoroid resonance frequency with a linewidth of approximately 15 MHz. Radius and mode spacing of the measured resonator are 400 μm and 83 GHz respectively. Note that the signal to noise ratio of the calibration peaks varies with the diode laser frequency, which is a result of wavelength dependent nonlinear polarization rotation of the frequency comb modes, leading to a not perfectly matched polarization of comb and diode laser over the full span. The measurement is recorded with an oscilloscope with 10 million data points per channel (two channels are used for the calibration peaks and a third channel for the measured spectrum). With a measurement bandwidth of 2.5 THz this leads to a resolution of 370 kHz per data point. Another crucial measurement parameter is the time resolution of the oscilloscope. Since the diode laser is frequency swept at a velocity of $v_{\mathrm{DL}} = 1$ THz/s the total measurement takes around 2.5 seconds. Consequently, the oscilloscope records 1 data point every 250 nanoseconds which is much slower than the $\approx$ 13 ns cycle length of the filtered beat note signal at 75 MHz. This undersampling makes it difficult to record reliable calibration markers with a normal sampling mode of an oscilloscope. A solution to this problem is the use of the "peak detect" mode which is available in most modern oscilloscopes. The "peak detect" modes allows the oscilloscope to obtain the maximum/minimum value of a signal faster than the sampling rate by running the analog to digital converter at the maximum sampling frequency and just storing the extremal value in each sampling interval. Note that the calibration markers in figure 4.18 are obtained from the squared signal recorded
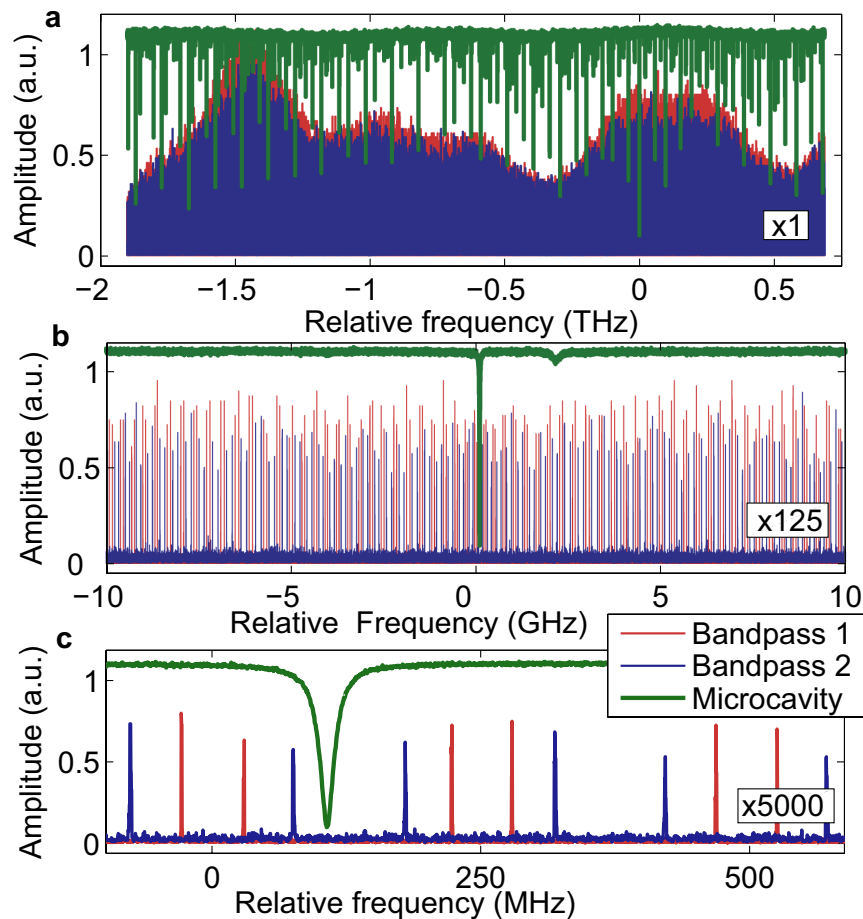
Figure 4.18: Measurement of the transmission spectrum of a 800-μm-diameter microtoroid. Panel a shows the full measurement with a scanning range of 2.5 THz. The resonator mode spectrum can be seen in the upper trace containing several different mode families. The fundamental mode family has a mode spacing of 83 GHz. Panel b and c shows zooms into the data in the vicinity of a 15-MHz-wide resonator mode. Frequency axis of the graphs are calibrated by the calibration peaks at 30 MHz and 75 MHz with respect to the comb modes with a spacing of 250 MHz.

in "peak detect" mode, since the oscilloscope alternates between recording maximum and minimum value of the AC beat note signal in each sample interval.

After solving the undersampling problem for the data recording of calibration markers we can quantify the maximum useful diode laser scanning speed. The employed "New Focus Velocity" tunable diode laser is specified for a maximum wavelength tuning speed of 20 nm/s around 1550 nm, corresponding to approximately 2.5 THz/s. However, another limitation for the scanning speed is the response time of the radio frequency bandpass filter that is used to generate the calibration markers. The time the beat note overlaps with the filter bandwidth is given as Γ/v_{DL} with Γ being the width of the passband and v_{DL} the diode laser scanning speed in units of Hz/s. Since the response time of a bandpass filter is approximately its inverse bandwidth, we can derive the maximum useful scanning speed v_{max} as

$$\Gamma/v_{\mathrm{max}} = \frac{1}{\Gamma} \quad \Rightarrow \quad v_{\mathrm{max}} = \Gamma^2 \quad . \tag{4.33}$$

The employed bandpass filter with a bandwidth of $\Gamma = 1$ MHz leads to a maximum scanning speed of 1 THz/s. Equation 4.33 shows the trade of between measurement speed and the achievable accuracy of this spectroscopy method.

The discussion before and the whole spectroscopy scheme is relying on a linearly, mode-hop-free scanning diode laser. More precisely, the laser is expected to scan linearly between two subsequent calibration markers for a reasonable interpolation of the laser frequency in this frequency range. Thus, a closer inspection of the diode laser scanning behavior is undertaken. Figure 4.19 contains measurement data of a 4-THz-wide diode laser sweep within 10 seconds. Panel a shows the determined diode laser frequency as function of the measurement time and looks nicely linear. The diode laser frequency is determined by the analysis of 64,000 calibration markers that are recorded with two different bandpass filters as shown in figure 4.17. A closer inspection of the data is done by applying a linear fit to the laser frequency position data and calculate the residuals between the linear fit and the measured diode laser frequency. These residuals are shown in panel b-d of figure 4.19 and reveal the deviation from a perfectly linear laser sweep. The maximum excursions of the diode laser frequency from the linear fit are in the order of 10 GHz within the whole scanning range of 4 THz. On shorter time scales of around 100 ms, the diode laser shows fluctuations in the order of 5 GHz, which can be seen in figure 4.19c. It is important to note that these fluctuations do not deteriorate the measurement as they are much slower than the rate at which calibration markers are recorded. An even closer zoom into the data reveals the position of the calibration peaks which corresponds to the data points in figure 4.19d. Two subsequent data points correspond to an exactly 250 MHz frequency shift of the diode laser, defined by the repetition rate of the employed frequency comb. Note that the 250-MHz-spacing is obtained for simplicity in this graph by averaging over 4 calibration markers that are recorded per 250-MHz-interval. Thus, the actual number of calibration markers is even 4 times higher. Important for the performance of the spectroscopy method are diode laser excursions at time scales shorter than the time between two calibration peaks. However, the smooth curve shape indicates the presence of only small frequency
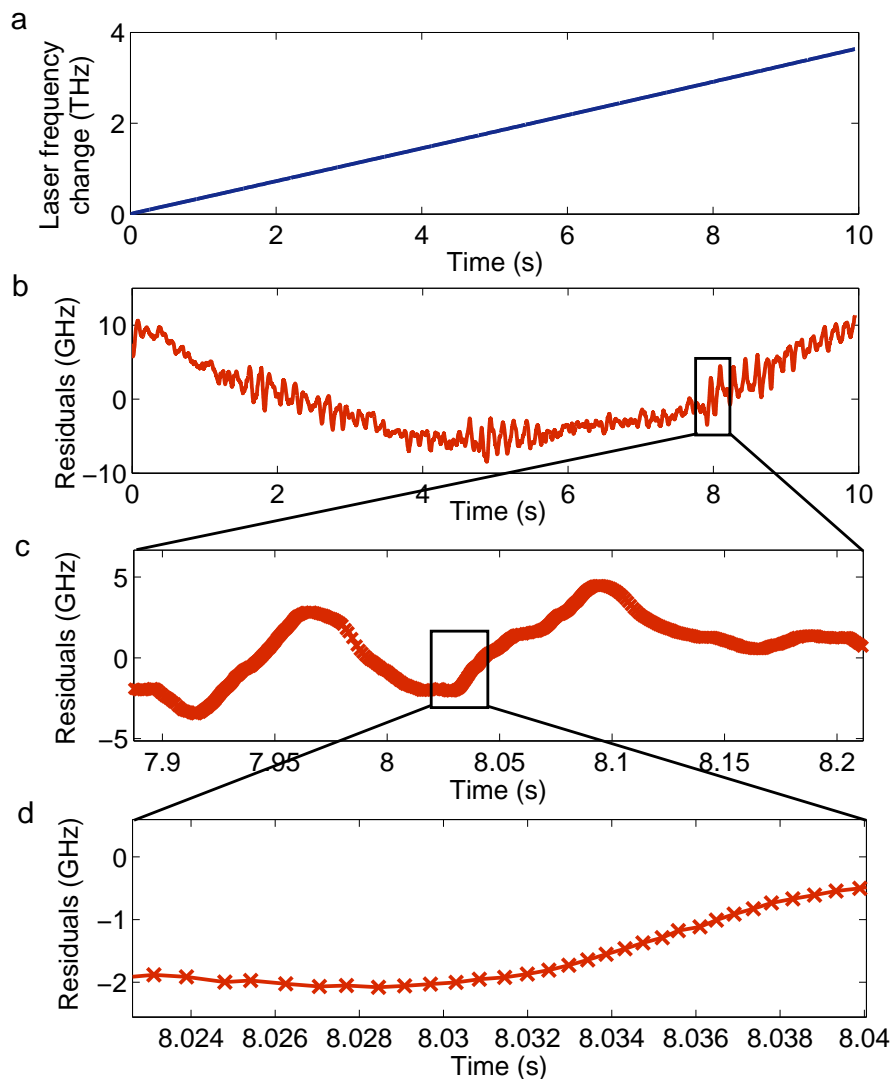
Figure 4.19: Diode laser frequency as a function of measurement time. Panel a shows a frequency comb calibrated diode laser sweep over 4 THz within 10 seconds. It is calibrated using 64,000 calibration markers generated from two bandpass filters as described in figure 4.17. At first sight the laser sweep looks linear. Panel b shows the difference of the data in panel a with respect to a linear fit of the same data, revealing the excursions of the diode laser frequency from a perfectly linear sweep. Panels c and d show magnified areas of the data residuals in panel b with diode laser frequency fluctuations on time scales of 100 milliseconds. Panel c and d show additionally the position of the calibration markers as data points. The diode laser frequency evolution looks sufficiently smooth at time scales between two calibration markers such that a linear or spline interpolation of the diode laser frequency at times between calibration markers can be applied.

fluctuations on these time scales. This allows for interpolation of the diode laser frequency at times between the calibration peaks. The most simple interpolation would be a linear approximation of the laser frequency between the calibration markers. Slightly better results can be obtained by using a spline interpolation which is done by local polynomial fits of a certain number of neighboring data points (using a polynomial of the same order as the number of data points). All the presented spectra in this chapter are calibrated with spline interpolations of groups of 5 calibration markers.

4.4 Microresonator spectroscopy and dispersion measurement

This section will focus on the measurement of microresonator mode spectra and their dispersion using the frequency comb assisted diode laser spectroscopy scheme that is described before. The tested microresonator sample is a 400-μm-radius microtoroid with a mode spacing of around 83 GHz. Figure 4.20 shows a picture of the frequency calibrated modal spectrum of this resonator over a bandwidth of 4 THz in the 1550-nm-wavelength region. Calibration of the frequency axis is achieved with a script that automatically determines the position of 64,000 calibration markers and generates a spline interpolation for the diode laser frequency at times in between calibration markers. Typically the employed external cavity diode laser is able to sweep 4 THz without mode hops. Occurring mode hops can be easily detected by a distorted calibration peak pattern (that does not correspond to the pattern defined by the radio frequency bandpass filters). In this case the measurement has to be repeated as the calibration relies on a continuously tuned diode laser. The spectrum in figure 4.20 shows a measurement with a mode hop free diode laser sweep. Coupling to the microresonator is optimized for a fundamental mode of the microtoroid (by adjusting the polarization and tapered fiber position). Fundamental modes can be distinguished from higher order modes since they just have one coupling maximum when moving the tapered fiber in horizontal and vertical direction across the toroid. However, several higher order mode families can still be seen in the optical spectrum as well. The measurement comprises 44 free spectral ranges of the toroid and the fundamental modes are fitted with a Lorentzian lineshape to determine optical linewidth and center frequency with high precision. A script is used for automatic fitting of the cavity modes of one family by providing the approximate frequency of two adjacent modes. The script searches for other modes of the same family based on the spacing of the two given mode frequencies. In figure 4.20b the free spectral range of the resonator is evident and different mode families can be distinguished. However, under some coupling conditions it is extremely difficult to track a certain mode family because of wavelength dependent coupling changes and a changing mode pattern as a result of different mode spacings in different mode families. This effect is already visible in figure 4.20b by comparing the free spectral ranges between the modes 16-17 and 22-23 (note that this numbering is not related to the optical mode number of the respective modes). Panel d shows one of the microresonator modes at a
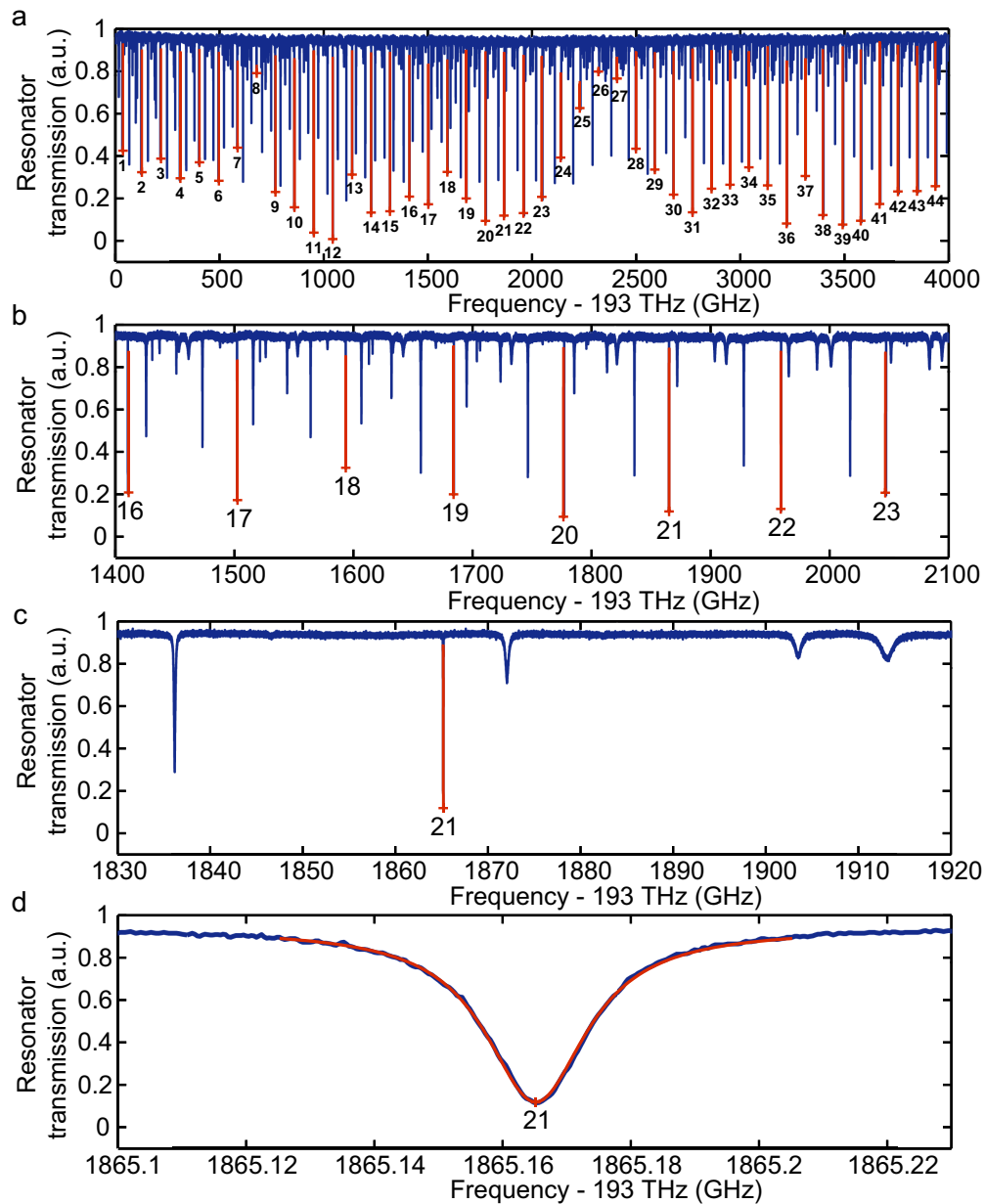
Figure 4.20: Frequency comb assisted diode laser spectroscopy of the transmission spectrum of a 800-μm diameter microtoroid (mode spacing $\approx$ 83 GHz). Panel a shows the full 4-THz-scanning-range comprising 44 free spectral ranges. Panel b-d show parts of the same spectrum at different magnifications. Red lines correspond to Lorentzian fits of the fundamental mode family in this resonator. Spectrum calibration and Lorentzian fits are done by an automated script that uses 64,000 calibration markers and a spline interpolation to determine the precise frequency of the microresonator modes.

30,000 time magnification compared to panel a, revealing an optical linewidth of 20 MHz.

Another interesting feature of the mode spectrum in figure 4.20a is the obviously smaller transmission dip of the mode number 8 and 25,26,27. This effect is caused by a modal crossing [159] between the fundamental modes and a modes from a higher order mode family. Figure 4.21 shows the crossing with a close up image of the modes 24 to 29. The coupling between the different mode families strongly deteriorates the optical linewidth (and thus the quality factor) of the fundamental mode. Frequency comb generation is strongly influenced by these mode crossings as it generates an additional loss channel once the comb extends to a deteriorated mode. This effect has a big impact on the overall envelope of microresonator based frequency combs and explains weaker and missing comb lines that are occasionally observed. However, a bad-quality mode does not necessarily cease comb generation since four-wave mixing based comb generation can skip several modes as shown in figure 1.8.

The frequency-calibrated spectrum from figure 4.20 allows to precisely determine linewidth and more importantly the mode spacing of microcavity modes within a broad frequency range. Figure 4.22a shows the evolution of the linewidth of the cavity modes. As already indicated before, mode crossings between different mode families lead to a reduced linewidths at the cavity modes 8 and 25-27. Moreover, a decrease of the linewidth towards modes at higher frequencies is observed from approximately 25 MHz down to 15 MHz in the 4-THz-scanning range, which can be explained by a wavelength dependence of coupling and intrinsic losses. Panel b of figure 4.22 shows a graph of the evolution of the free spectral ranges that are determined from the same resonator spectrum. A linear fit of the data quantifies an average mode spacing increase of $\Delta(\Delta\nu) = (780 \pm 280)$ kHz per free spectral range.

With a diode laser scanning speed of 1 THz per second it takes around 4 seconds to obtain the previously shown spectra. At these time scales, thermal drifts and coupling changes could potentially lead to drifting microresonator resonances and thus influence the measurement of the cavity mode spacing. However, these drifts would be unidirectional and consequently induce a mode spacing change that depends on the scanning direction. This has been excluded by measuring microresonator spectra with diode laser sweeps in different directions, which show the same mode spacing variations. Figure 4.23 shows several independent measurements of the mode spacing evolution in the same microresonator. The different measurements show mode spacing fluctuations in the order of 10 MHz and a combined mode spacing evolution shows yields a slope of $\Delta(\Delta\nu) = (770 \pm 110)$ kHz with a slightly smaller error compared to the single measurement in figure 4.22. Part of the deviation of the measured free spectral ranges from the linear fit is reproducible in different measurements and is assumed to originate from actual wavelength dependent dispersion fluctuations in the microresonator. Such a deviation from a smooth dispersion curve could be induced by imperfections of the resonator geometry.

The previous dispersion measurements just focused on fundamental microtoroid modes with the highest optical quality factors, which are suitable for frequency comb generation. Figure 4.24 depicts the measured mode spacing evolution not only of the a fundamental mode family but also of two other mode families. The measurement shows much higher
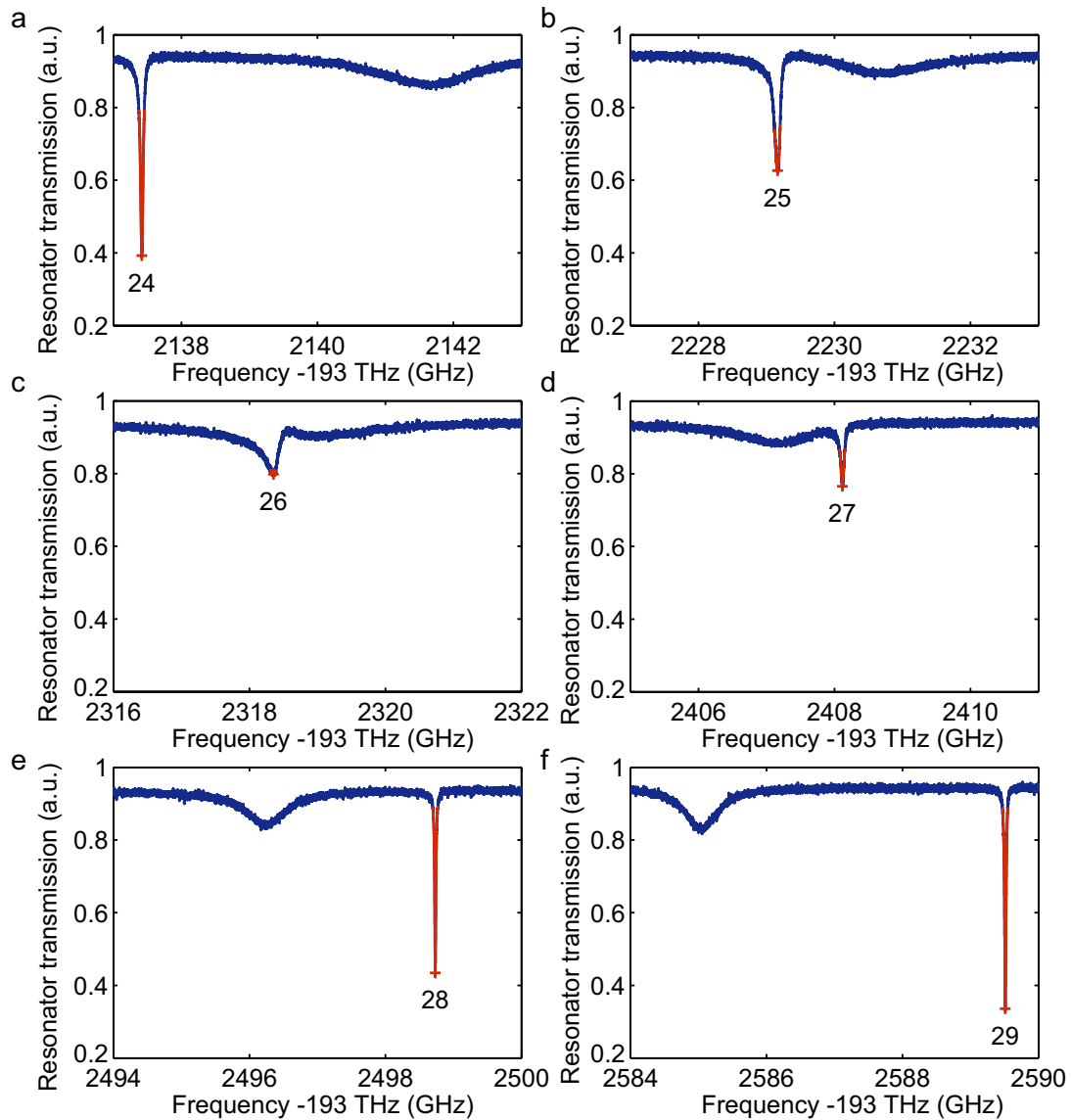
Figure 4.21: Mode crossings in an optical microresonator. The graphs show the modes 24 to 29 from figure 4.20. Panel a to f show that the frequency difference between modes of fundamental mode family and a low-quality factor mode family approach varies as a result of different mode spacings of the mode families. Modes from both families overlap in the graph in panel c, which deteriorates the quality factor of the fundamental mode. Two free spectral ranges further, both modes are separated again and the initial linewidth of the fundamental mode is recovered. These mode crossings strongly affect optical frequency comb generation in microresonators.
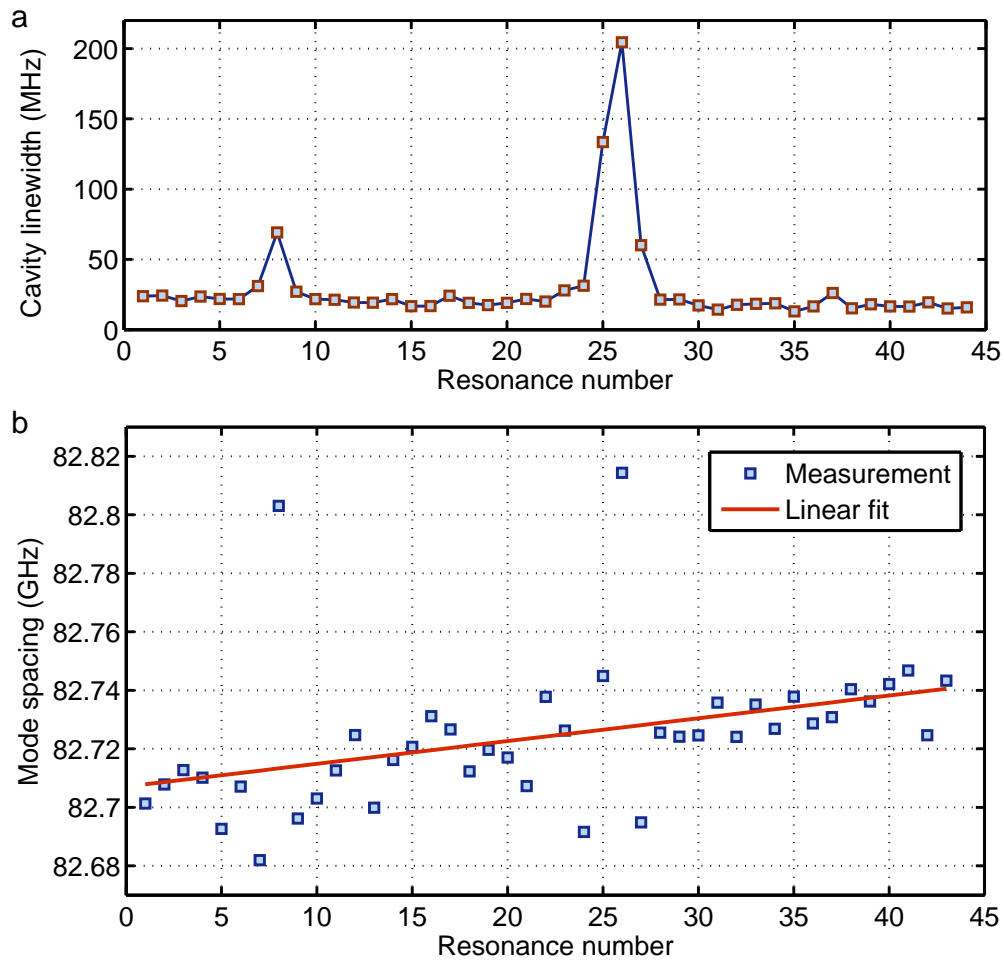
Figure 4.22: Cavity linewidth and mode spacing evolution in a 800-μm-microtoroid. Panel a shows the evolution of the cavity linewidth of a fundamental mode family shown in figure 4.20. The 8th and 25th, 26th and 27th resonator modes are significantly broadened due to mode crossings. Panel b shows the evolution of the cavity mode spacing in the same resonator with a slope of $\Delta(\Delta\nu) = (780 \pm 280)$ kHz.
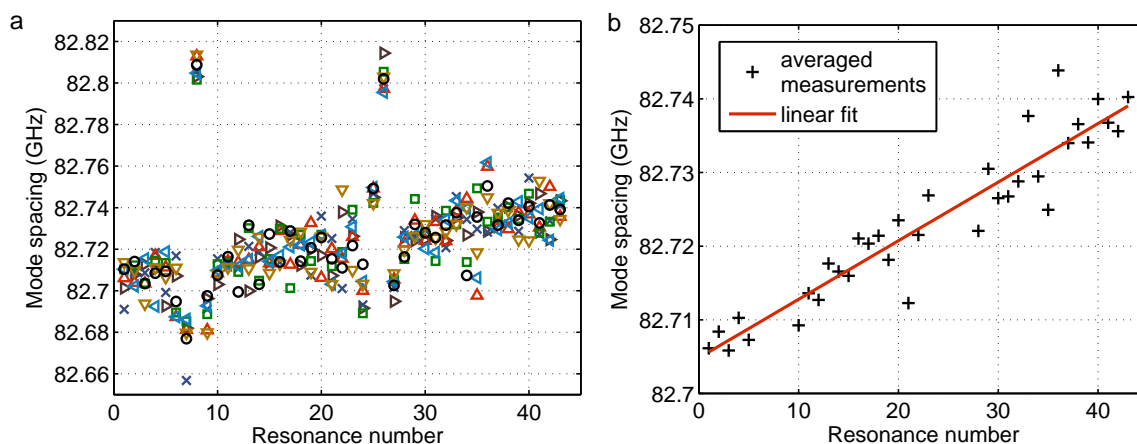
Figure 4.23: Dispersion measurement in a 400-μm-radius microtoroid. Panel a shows seven independent measurements of the evolution of the free spectral. Part of the measurements is performed in opposite scanning direction of the diode laser in order to exclude mode spacing drifts within the measurement time. Panel b shows the averaged variation of the free spectral range with a slope of $\Delta(\Delta\nu) = (770 \pm 110)$ kHz.
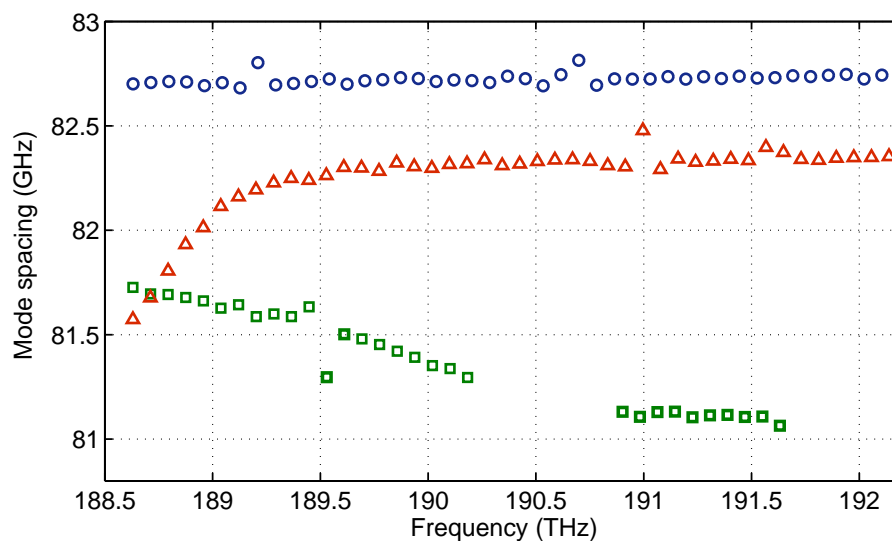
Figure 4.24: Measured mode spacing evolution of different mode families in a microresonator as a function of the optical frequency. The upper trace corresponds to a high-Q fundamental mode family while the lower traces show the dispersion of higher order azimuthal modes with lower optical quality factors. The large mode spacing variations in the lower traces result from coupling with other mode families which can can occur over wide wavelength ranges due to the larger optical linewidths.
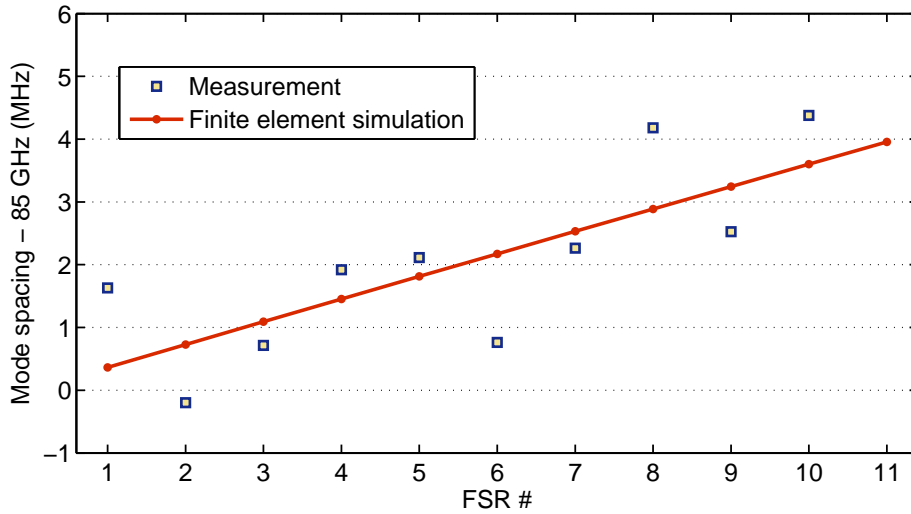
Figure 4.25: Measured microtoroid dispersion and finite element simulation. The solid line shows the result of a finite element simulation in a microresonator with the same geometry. The numerical simulation yielding a dispersion of $\Delta(\Delta\nu) = 350$ kHz is in good agreement with the measurement of $\Delta(\Delta\nu) = (370 \pm 110)$ kHz.

dispersion in higher order modes compared to the fundamental modes as a result of broader linewidths that lead to an extended coupling region to other mode families. Moreover it is evident that the fundamental mode has a higher mode spacing and consequently a shorter optical pathlength in the resonator, which is in agreement with theoretical considerations leading to a longer optical pathlength for higher order azimuthal modes.

Figure 4.25 shows a dispersion measurement of another microtoroid with a diameter around 800 μm and a toroid cross-section radius of 4 μm. The average dispersion in this resonator is $\Delta(\Delta\nu) = (370\pm110)kHz$ corresponding to a GDD of -104 fs^2. A finite element simulation for a resonator with the same geometry yields a dispersion of $\Delta(\Delta\nu) = 350$ kHz, which is in excellent agreement with the measurement.

CHAPTER 5

Summary and Outlook

This chapter summarizes the work presented in this thesis and gives a brief outlook towards future research related to four-wave mixing induced frequency comb generation. The following list gives an overview of the main topics that have been discussed in the preceding chapters.

- First, it is shown that the Kerr-nonlinearity in ultra-high-Q microresonators gives rise to nonlinear frequency conversions spanning more than a full optical octave. The comb generation process is explained by four-wave mixing as a result of the χ^3-nonlinearity of the resonator material. This comb generation process has the unique feature that the pump laser itself constitutes one of the comb modes.

- The equidistance of the microresonator comb modes has been verified down to a level of 1 mHz (5.2×10^{-16} relative to the measurement bandwidth) by comparison with a conventional frequency comb.

- Full control and stabilization of microresonator-based frequency combs is realized by fast thermal effects in the microresonator that allow for mode spacing control via the launched power. The second degree of freedom of the comb is controlled by the pump laser frequency.

- Resonator dispersion plays an important role in mode locked lasers as well as for microresonator comb generation. The dispersive properties of microresonators are analyzed both experimentally and theoretically. The experimental dispersion measurements rely on a newly developed frequency comb assisted diode laser spectroscopy scheme that enables continuous spectral measurements with sub-MHz resolution over bandwidths exceeding 4 THz within a few seconds. Theoretical predictions of microresonator dispersion are made by numerical finite element simulations and show that geometric- and material-dispersion can compensate each other. It has been shown that Optimized resonator geometries can lead to sufficiently small dispersion for octave-spanning comb generation.

Due to the novelty of direct comb generation via four-wave mixing and resulting from the variety of different comb generator systems, there are still many open questions regarding the comb generation process. One of the most striking challenges is related to the time domain picture of the comb generation with the central question whether optical solitons are generated. Ongoing experiments in magnesium fluoride resonators could provide new insights by analysis of combs with smaller repetition rates that might allow for auto- and cross-correlation measurements with well-separated pulses. Another central question is related to the noise properties of microresonator combs. The high power levels and strong confinement of light in microresonators lead to many different interacting nonlinearities and preliminary experiments have shown chaotic interaction regimes in which the comb lines can be significantly broadened. A detailed analysis of noise processes including Kerr-nonlinearity, radiation pressure, thermorefractive and thermoelastic effects could allow for further optimization of the comb generation process.

Microresonator based frequency combs have great potential for many applications in photonic technologies, especially for applications that require a wide mode spacing. Telecommunication would benefit from a cost-effective comb source for multi-channel data transfer. Here, the high mode spacing would be ideal for wavelength division multiplexing in order to separate different channels. Moreover, chip-scale frequency combs could replace many different laser sources by the ability to convert a single continuous wave laser to optical wavelengths ranging from the visible to the mid infrared. Another potential application for microresonator based combs is the generation of arbitrary optical waveforms [160], which requires a comb with large frequency spacing for spatial separation of the modes in order to modulate their phase and amplitude (for example with liquid crystal spatial light modulator [160]). In basic research, microresonator based-frequency combs could be ideal tools for astrophysical spectrometer calibration [132, 133], which also requires mode spacings of more than 20 GHz in order to resolve single comb modes on the spectrometer. At present, these high mode spacings are generated by optical filtering of conventional frequency combs with Fabry Pérot filter cavities. However, one limitation of this calibration scheme is the presence of side-modes that are not sufficiently suppressed by the filter cavities. Microresonator combs are side-mode-free as a result of their fundamentally high mode spacing and could be useful tools for spectrometer calibration. An additional consequence of the larger mode spacing are high power levels per comb line. Microresonator combs can cover a wavelength range of more than 140 THz with more than 100 μW per comb line (cf. figure 1.11). This is an additional advantage for telecommunication systems and also for applications like direct gas spectroscopy [135, 155, 161]. The intriguing ability to generate full octave spanning frequency combs within a monolithic, low cost microresonator is a great step towards direct integration of optical frequency standards into compact microphotonic devices. This may permit to bring a radio-frequency to optical link into a chip scale format, enabling entirely novel on-chip photonic functionality and unifying the fields of optical frequency metrology and nanophotonics.
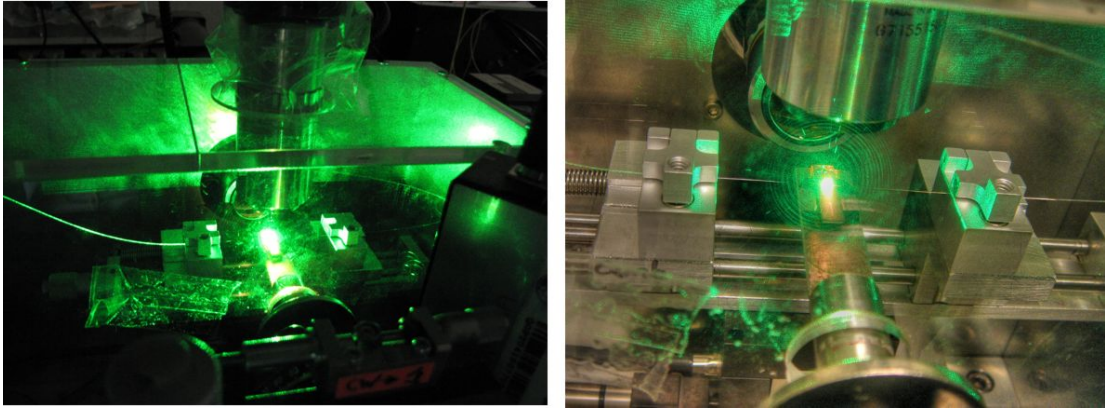
APPENDIX A

## Third harmonic generation and related four-wave mixing effects

Figure A.1: Photos of third harmonic generation in a fused silica microdisk pumped with 2 W power at 1550 nm. A video of the third harmonic generation while scanning across a microresonator resonance can be seen in reference [162].

Third harmonic generation can occur at high pump powers in microresonators [42]. Typically, a mixture of different nonlinear effects consisting of four-wave mixing, stimulated Raman scattering and third harmonic generation can be observed simultaneously at pump powers in the range of 100 mW in fused silica microtoroids with quality factors of $Q \approx 10^8$. As a consequence, not only pure third harmonic generation but also other wave mixing processes of the form (cf. chapter 1, section 1.5)

$$\omega_4 = \omega_1 + \omega_2 + \omega_3 \qquad \text{(A.1)}$$

can be observed. Typically the generated frequency ω_4 is not resonant in the resonator as result of dispersion. However, in the presence of four-wave mixing sidebands and Raman lines, the frequencies $\omega_{1,2,3}$ can be composed of many different combinations of modes and it is likely that one combination leads to an ω_4, which is resonant.

Figure A.1 shows a photograph of third harmonic light generated in a fused silica microresonator from a 2 W pump laser at 1550 nm. An example of cascaded nonlinear interactions is shown in figure A.2. The infrared spectrum in the upper panel is directly recorded from the tapered optical fiber output and shows some four-wave mixing sidebands around the pump laser. Simultaneously, a free space spectrometer for visible light (Ocean Optics USB4000) is used to record a spectrum from the stray light of the resonator. A direct observation of the visible light through the tapered optical fiber is not possible since the mode in the tapered fiber is phase matched with the 1550-nm-pump-mode, which leads to a insufficient coupling efficiency in the visible. However, another possibility to collect light from the visible spectrum would be a wavelength independent coupler as presented in reference [61]. The visible spectrum in figure A.2 shows several different oscillating modes that are most likely generated by third harmonic type interactions ($\omega_4 = \omega_1 + \omega_2 + \omega_3$) with different contributions from the modes at 1550 nm. However, another explanation for the visible spectrum could be that only one 1550-nm-mode is converted to the visible by third harmonic generation and subsequent four-wave mixing in the visible. In this case the
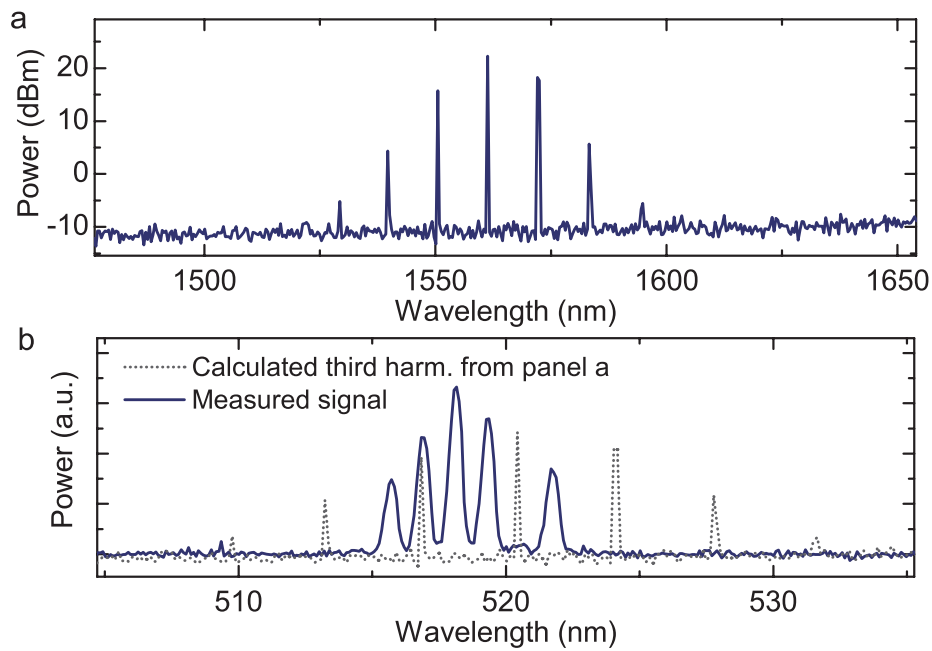
Figure A.2: Third harmonic generation in a microtoroid. Panel a shows the optical spectrum around the pump laser at 1550 nm (launched power $P_{in} \approx 250$ mW). Panel b is the measured spectrum around the tripled pump frequency. The dotted lines show the calculated spectrum for a pure third harmonic generation process (simply calculated by tripling the frequencies of the spectrum in panel a). Obviously, the measured third harmonic spectrum does not match the tripled spectrum from panel a, which indicates that the modes are generated by other interactions $\omega_4 = \omega_1 + \omega_2 + \omega_3$ with contributions from different modes around 1550 nm. Another explanation would be a cascaded process with four-wave mixing in the visible.
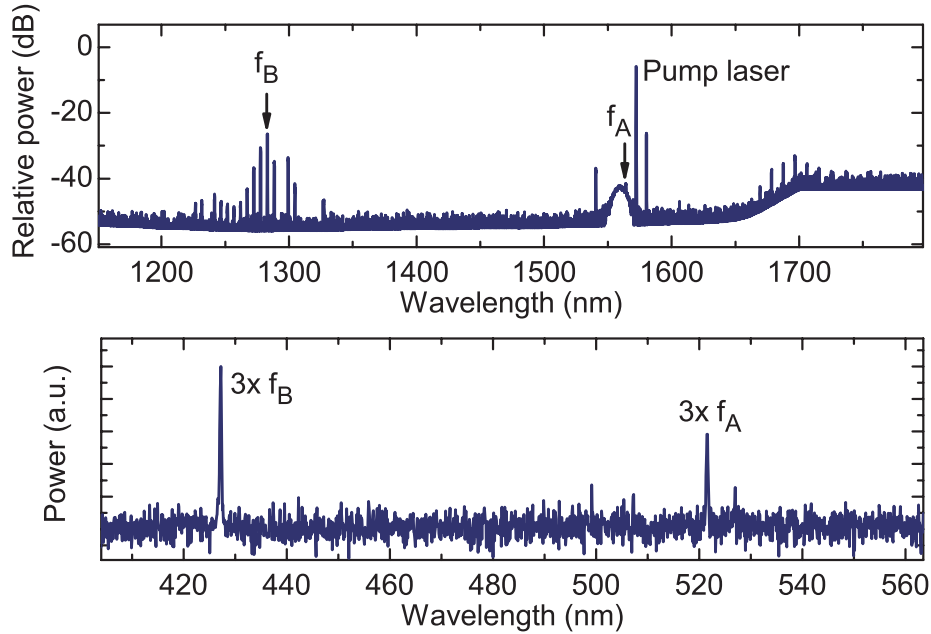
Figure A.3: Cascaded nonlinear interactions in a microtoroid with a single pump laser at 1550 nm. The infrared spectrum shows some modes at 1280 nm that are probably generated by Raman scattering and Stokes-anti-Stokes coupling via four-wave mixing. The visible spectrum (panel b) shows oscillating modes at 430 nm and 520 nm which can be attributed to third harmonics of modes from panel a. Interestingly, not the pump laser but the one sidebands next to the pump laser generates the light at 520 nm.

mode spacing in the visible could be slightly different than in the infrared due to cavity dispersion. However, in the case of direct third harmonic type conversion from the infrared to the visible, the generated visible comb has *exactly* the same mode spacing as the infrared comb, which could be potentially used to generated visible frequency combs directly from a 1550-nm-pump-source in a monolithic microresonator. Note that in this case the offset frequency f_{ceo} of the visible comb corresponds to the tripled offset frequency of the infrared comb. Consequently, the combs could be combined into one continuous comb in case of a zero offset frequency $f_{\text{ceo}} = 0$ or $3 \cdot f_{\text{ceo}} = f_{\text{rep}}$.

Figures A.3 and A.4 show different cascaded nonlinear interactions in a fused silica microtoroid pumped by a single 1550-nm continuous wave laser. The infrared spectrum in these figures shows a bunch of modes at around 1300 nm that are probably generated by a mixture of Raman scattering and four-wave mixing. Subsequent third harmonic generation of the 1300-nm-light as well as mixing of the 1300-nm-light with the pump laser leads to generation of blue visible light down to 430 nm.

As stated before, third harmonic type nonlinear interaction can just occur when the sum of three infrared waves is resonant with a resonator mode in the visible. With many oscillating modes in the infrared, it is possible to excite different visible modes by changing the pump laser frequency (shifting the infrared modes) until the sum frequency of three infrared waves is resonant with a resonator mode in the visible. Figure A.5 shows different
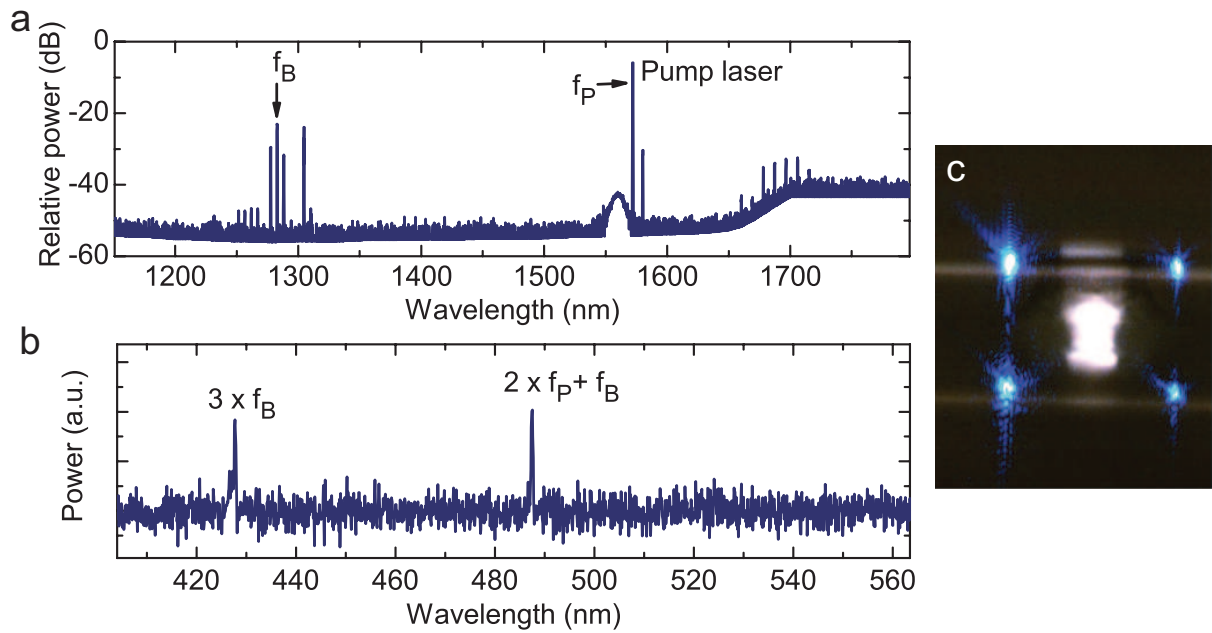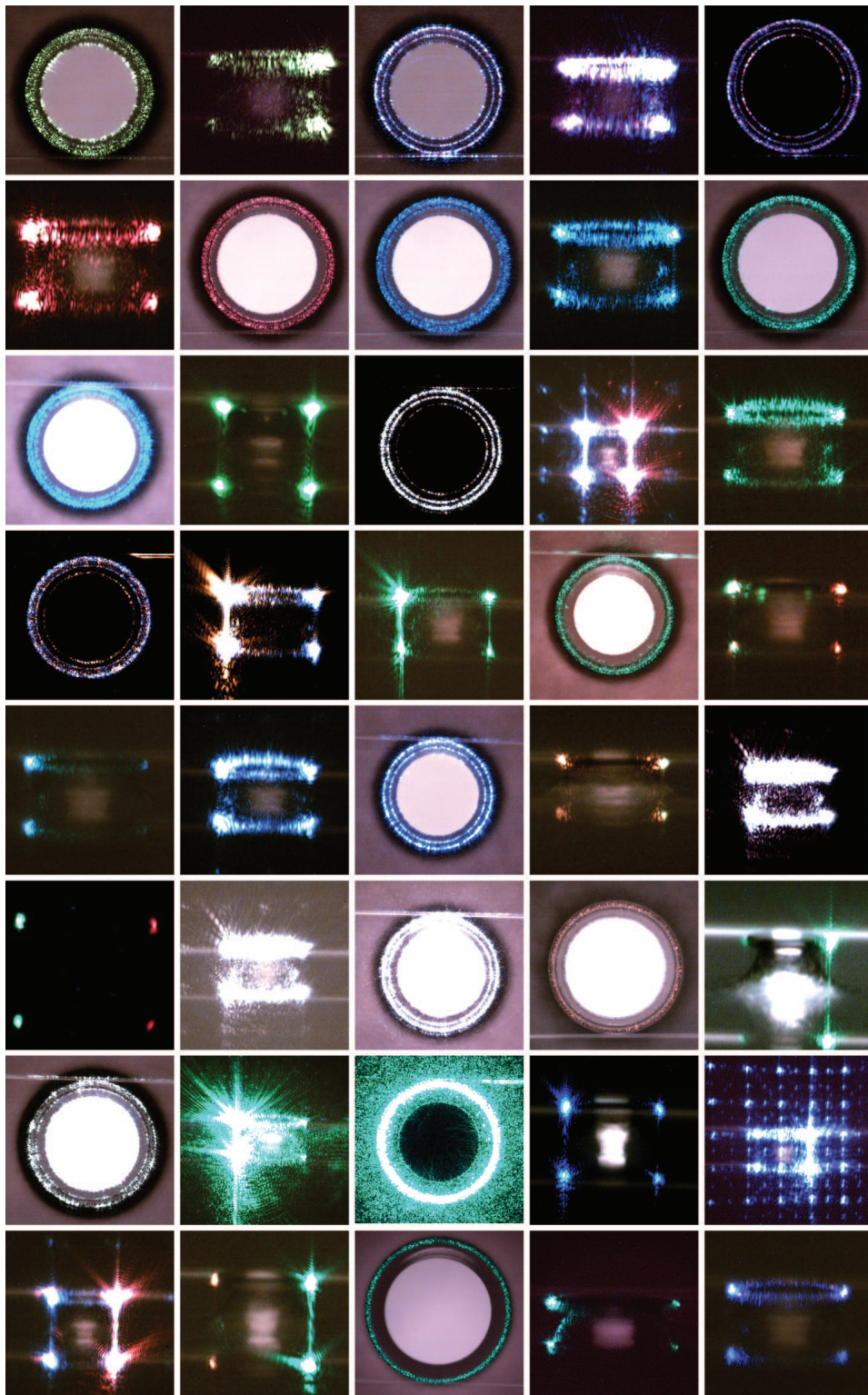
Figure A.4: Cascaded nonlinear effects in a microtoroid. This spectrum is recorded using the same resonator as in figure A.3. In this case the visible spectrum in panel b shows a mode at 490 nm that is generated by two photons from the pump laser (frequency f_P) and one photon from the light at 1280 nm (frequency f_B).
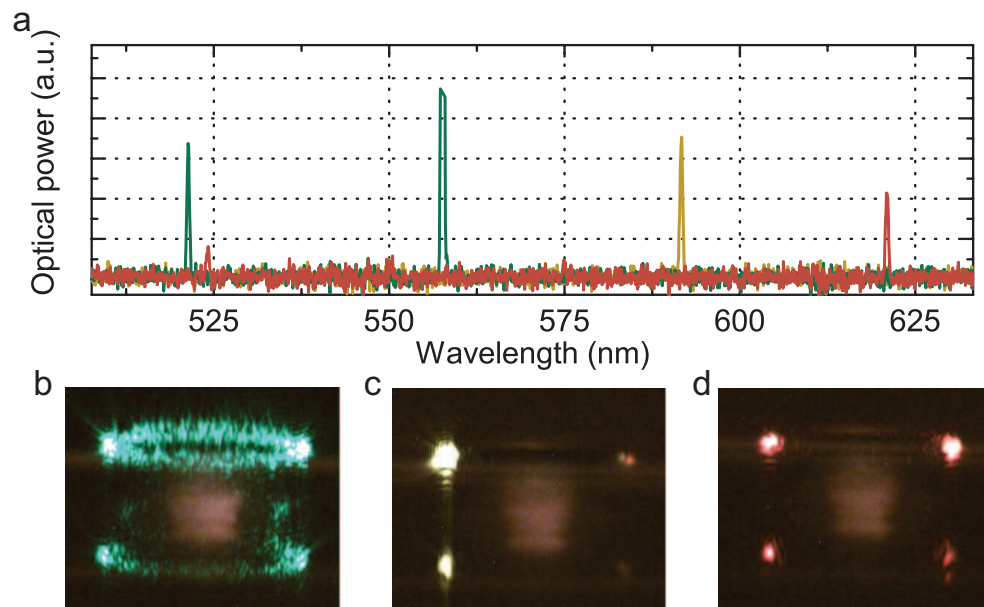

Figure A.5: Cascaded nonlinear interactions in microtoroids. The different colors in the visible are excited by varying the frequency of the pump laser.

excited visible frequencies and corresponding microscope photos of the same toroid showing emission of green, yellow and red light. Figure A.6 shows a gallery of third harmonic type frequency conversion in different fused silica microtoroids, covering the whole visible spectrum. The gallery shows pictures of toroids in side view and top view. Note that the lower part of the pictures of toroids in side view is a reflection of the toroid on the silicon chip. A corresponding video of different cascaded frequency conversions in a fused silica microtoroid is shown in reference [163]. Another effect that can be seen from the generated visible light is coupling of clockwise and counter-clockwise propagating modes in microtoroids [164] (a video of this effect is shown in reference [165]). This coupling of modes can be explained by slight asymmetries in the resonator geometry that lead to split modes.

Third harmonic generation is also observed in high-Q fused silica microspheres as shown in figure A.7. Another interesting effect in the context of third harmonic generation in fused silica microdisks is the observation of standing wave patterns in fused silica microdisks as shown in figure A.8. An exact explanation of this phenomenon is subject to future research.

Figure A.6: Third harmonic-type frequency conversion in fused silica microtoroids. The colors are generated by cascaded nonlinear interactions from a 1550 nm pump laser.
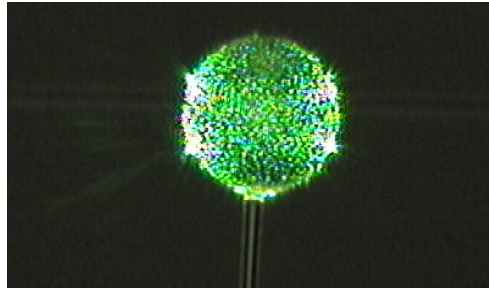
Figure A.7: Third harmonic generation in a microsphere with 30 mW launched power at 1550 nm. A video of the third harmonic generation for different pump laser frequency detunings is shown here [166].
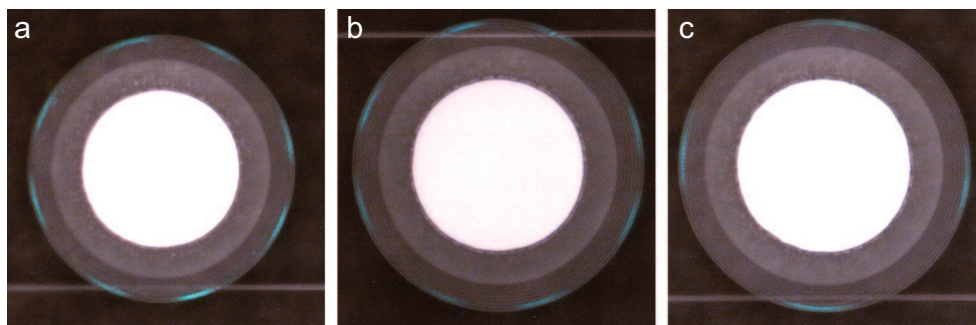
Figure A.8: Standing wave patterns of third harmonic light excited by a 2 W pump laser at 1550 nm in a fused silica microdisk. In panel a and b the pump laser is exciting the same mode leading to a standing wave pattern with 8-fold symmetry. The standing wave pattern does not depend on the coupling position of the tapered fiber which is changed in panel a and b. Panel c shows a standing wave pattern excited by a different pump mode and exhibits a 4-fold symmetry. Note that a closer inspection of the standing wave patterns reveals additional interference fringes at smaller scales.

APPENDIX B

Beat note measurement, stabilization and frequency mixing

This appendix gives a brief introduction into detection and stabilization of beat notes between different laser signals. These laser signals can be individual comb modes of two different frequency combs (cf. chapter 2 for multiheterodyne beat note measurements) or beat notes between a continuous wave laser with a neighboring mode of a frequency comb (as used in chapter 3 for stabilization of the pump laser frequency).

Figure B.1 shows a basic setup for beat note measurements and stabilization similar to the setup presented in reference [167]. We assume that the two lasers emit signals at two different frequencies ω_1 and ω_2 with electrical field components E_1 and E_2.

$$\mathcal{E}_1 = E_1 \cdot \mathrm{e}^{-i \cdot \omega_1 t} \tag{B.1}$$

$$\mathcal{E}_2 = E_2 \cdot \mathrm{e}^{-i \cdot (\omega_2 t + \phi)} \tag{B.2}$$

These two waves are spatially combined in a polarizing beam splitter and we assume that the polarization of the beams is adjusted such that the beam of laser 1 is completely reflected and the beam of laser 2 transmitted. A subsequent polarizer is used to adjust the relative power levels of the two signals (which is important in order to maximize the beat note signal). In case both lasers emit the same power, the polarizer is set in 45° direction with respect to the polarization of both beams. For a linear polarized input field E_{in} the transmitted field is given by $E_{\mathrm{out}} = E_{\mathrm{in}} \cdot \cos\Theta$, with Θ being the angle between electrical field and polarizer axis. Consequently, the total field in the setup in figure B.1 after the polarizer is given as

$$\mathcal{E} = \mathcal{E}_1 + \mathcal{E}_2 = E_1 \cdot \mathrm{e}^{-i \cdot \omega_1 t} \cdot \cos\Theta + E_2 \cdot \mathrm{e}^{-i \cdot (\omega_2 t + \phi)} \cdot \cos(\Theta - \pi/2) \tag{B.3}$$

The beat note is measured with a photodetector which is generating a voltage $V_{\mathrm{PD}} \propto |\mathcal{E}|^2$ proportional to the incident optical power

$$V_{\mathrm{PD}} \propto E_1^2 \cdot \cos^2\Theta + E_2^2 \cdot \sin^2\Theta + 2 \iint E_1 E_2 \, \mathrm{d}A \cdot \cos\Theta \sin\Theta \cdot \cos((\omega_2 - \omega_1)t + \phi) \, . \tag{B.4}$$

Here, the integral in the last term takes into account the modal overlap between the two laser fields. For a perfect overlap of the signals, it is expected to measure an amplitude of the AC voltage V_{AC} from the combined lasers corresponding to

$$V_{\mathrm{AC}} = 2\sqrt{V_1} \cdot \sqrt{V_2} \, , \tag{B.5}$$

with V_1 and V_2 being the DC voltages measured with only one of the respective laser signals. The DC parts of the photodiode signal can be removed by a bandpass filter and subsequently the beat note signal V_{beat} can be measured with an electronic frequency counter or an electronic spectrum analyzer (assuming a perfect spatial overlap of the modes)

$$V_{\mathrm{beat}} \propto 2E_1 \cdot E_2 \cdot \cos\Theta \sin\Theta \cdot \cos((\omega_2 - \omega_1)t + \phi) \, . \tag{B.6}$$

Additionally, the beat note signal can be stabilized to an external reference frequency. For the stabilization it is required to obtain an error signal that depends on the phase
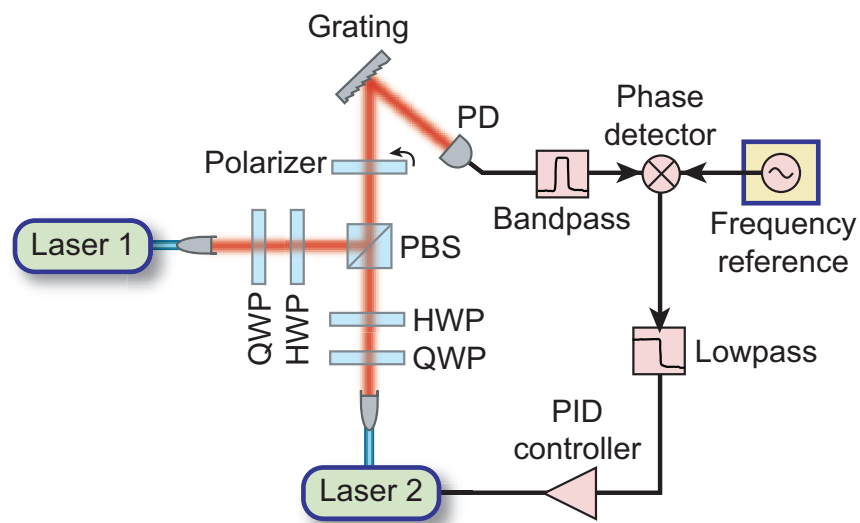
Figure B.1: Experimental setup for beat note generation and stabilization. Two laser signals are spatially superimposed in a polarizing beam splitter cube (PBS) and a subsequent polarizer allows for adjustment of the relative power of the two signals in order to maximize the beat signal. A grating is used to filter out spectral parts of the light field that do not contribute to the beat note of interest for an improved the signal-to-noise ratio. The beat note is observed with a fast photodiode (PD) and filtered with an electronic bandpass filter for further noise reduction. Subsequently, a phase detector (eg. radio frequency mixer) is used to generate an error signal that is proportional to the frequency mismatch between beat note and a reference frequency. This error signal is converted by an "proportional-integral-derivative"-controller (PID) into a correction signal that actuates on one of the laser frequencies in order to stabilize the beat note frequency to the reference frequency. QWP = quarter-wave plate, HWP = half-wave plate.

mismatch between beat note and reference. This can be achieved by using a radio frequency mixer as phase detector [168]. The radio frequency mixer generates a signal at the difference frequency between beat note and reference frequency (cf. section B.1). With a frequency reference oscillating at a frequency ω_{LO} (and with a phase ϕ_{LO}), the generated error signal V_{err} is proportional to

$$V_{\mathrm{err}} \propto \sin((\omega_2 - \omega_1 - \omega_{\mathrm{LO}})t + \phi - \phi_{\mathrm{LO}}) \quad . \tag{B.7}$$

In case both phase and frequency difference of beat note and frequency reference are close to zero, the error signal at short time scales can be approximated by

$$V_{\mathrm{err}} \propto (\omega_2 - \omega_1 - \omega_{\mathrm{LO}})t + \phi - \phi_{\mathrm{LO}} \quad . \tag{B.8}$$

This error signal depends linear on the phase and frequency offset and has a sign that defines the direction of the mismatch. If the phase locked loop is enabled, the error signal is minimized such that both phase and frequency of the beat note frequency follow the frequency reference. Note that the phase difference can be integer multiples of 2π, such that a temporary excursion of the beat note frequency can lead to a phase slip ("cycle slip") of multiples of 2π between the two signals. These cycle slips can be avoided by employing a digital comparator as phase detector, which can record the difference of the number of zero crossings of the two signals and compensate a limited amount of cycle slips [169].

An important quantity for the stabilization loop is the signal-to-noise ratio of the electronic beat note signal. The available signal S is determined by the photocurrent of the beat note signal I_{beat} [167]

$$S = \left\langle I_{\mathrm{beat}}^2 \right\rangle = 2 \cdot \left(\frac{e\eta}{\hbar\omega} \right)^2 \cdot P_1 \cdot P_2 \quad . \tag{B.9}$$

Here, e is the unit charge of an electron, $\hbar\omega$ the photon energy, η the quantum efficiency of the detector and $P_{1,2}$ the optical power contributing to the beat signal according to equation B.6. The noise background on the other hand has different contributions from both optical and electronic noise processes. The noise floor is given by

$$N = \left\langle I_{\mathrm{noise}}^2 \right\rangle = \underbrace{\frac{2e^2\eta f_{\mathrm{bw}}}{\hbar\omega}(P_1 + P_2)}_{\text{laser shot noise}} + \underbrace{2ef_{\mathrm{bw}} \cdot I_{\mathrm{d}}}_{\substack{\text{dark current} \\ \text{shot noise}}} + \underbrace{4Fk_{\mathrm{B}}Tf_{\mathrm{bw}}/R}_{\text{Johnson noise}} \quad , \tag{B.10}$$

within a measurement bandwidth of f_{bw}. The first term originates from the laser shot noise of the laser signals that are not contributing to the beat note (first two terms in equation B.4). The second contribution is induced by the dark current of the photodetector and the last term corresponds to thermal noise of the electrons in a resistor R which depends on the thermal energy $k_{\mathrm{B}}T$. Thus the signal to noise ratio of the beat note detection is given as

$$\frac{S}{N} = \frac{1}{f_{\mathrm{bw}}} \cdot \frac{2 \cdot \left(\frac{e\eta}{\hbar\omega}\right)^2 \cdot P_1 \cdot P_2}{\frac{2e^2\eta}{\hbar\omega}\left(P_1 + P_2\right) + 2e \cdot I_{\mathrm{d}} + 4Fk_{\mathrm{B}}T/R} \quad . \tag{B.11}$$

In case of a laser shot noise limited beat note measurement, the noise is given by (cf. reference [167])

$$\frac{S}{N} = \frac{\eta}{f_{\mathrm{bw}} \cdot \hbar\omega} \frac{P_1 \cdot P_2}{P_1 + P_2} \quad . \tag{B.12}$$

Since the relative power of the laser beams at the photodetector can be adjusted by the polarizer in the setup in figure B.1, we can calculate the angle Θ for an optimized signal-to-noise ratio of the beat note signal. Using $P_1 \propto E_1^2 \cdot \cos^2\Theta$ and $P_2 \propto E_2^2 \cdot \sin^2\Theta$, the best signal to noise ratio can be obtained for Θ_{opt} with

$$\tan^4 \Theta_{\mathrm{opt}} = \frac{P_1}{P_2} \quad . \tag{B.13}$$

B.1   Radio- and microwave frequency mixing

Frequency mixing in the radio frequency and microwave domain can be used to convert two input frequencies into newly generated frequencies. Just like optical frequency mixing, this requires a nonlinear response of the electronic circuit. Most commonly, the nonlinear response originates from Schottky diodes that can be described by [170, 171]

$$I = c_1 \cdot V + c_2 \cdot V^2 + c_3 \cdot V^3 + \ldots \tag{B.14}$$

with the current I, the applied voltage V and diode dependent constants $c_{1,2,3}$. Applying an input $V = V_1 + V_2$ consisting of two harmonic signals $V_1 \propto \mathrm{e}^{i\omega_1 t}$ and $V_2 \propto \mathrm{e}^{i\omega_2 t}$ at frequencies ω_1 and ω_2 leads to the generation of several new frequencies as shown in figure B.2. The two input frequencies are typically referred to as "radio frequency" (RF) and "local oscillator" (LO). The converted frequencies are referred to as "intermediate frequency" (IF).

A special type of electronic mixers are so called "harmonic" or "sub-harmonic" mixers. These mixers are optimized for local oscillator input frequencies at integer fractions of the desired local oscillator frequency close to the RF signal [170]. The nonlinear response of the electronic circuit generates harmonics of the LO-signal and subsequent mixing with the RF-signal generates the low frequency IF signal. Harmonic mixing is typically used for analysis of high frequency microwave signals that are not directly accessible with low phase noise local oscillators. In this thesis, harmonic mixing is used for analysis of the mode spacing beat note of a microresonator-based frequency comb at 85 GHz. Detailed descriptions of harmonic mixing are presented in references [170] and [171].
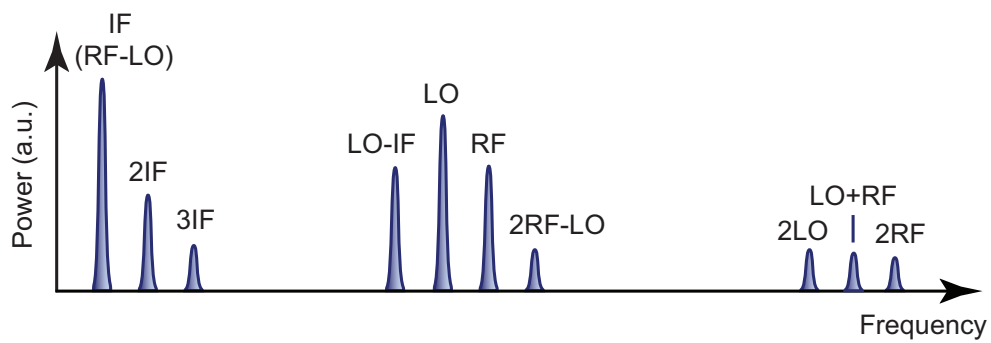
Figure B.2: Different frequency components generated from two input sources (RF and LO) in a radio frequency mixer.

APPENDIX C

Radio frequency counters

Figure C.1: Photo of HP53131A radio frequency counters.

This appendix gives a brief introduction into the working principle of high resolution radio frequency counters (shown in figure C.1), which have been used for equidistance and frequency stabilization measurements in this thesis (chapters 2 and 3). First we have to define the term frequency. Assuming a signal $V(t)$ with

$$V(t) = (V_0 + \epsilon(t)) \cdot \sin(2\pi\nu_0 t + \varphi(t)) \quad , \tag{C.1}$$

with noise terms $\epsilon(t)$ and $\varphi(t)$ [172] and

$$\left| \frac{\epsilon(t)}{V_0} \right| \ll 1 \ , \ \text{and} \quad \left| \frac{\dot{\varphi}(t)}{2\pi\nu_0} \right| \ll 1 \quad , \tag{C.2}$$

we can define the instantaneous phase Φ as

$$\Phi = 2\pi\nu_0 t + \varphi(t) \quad . \tag{C.3}$$

The corresponding frequency of the signal is proportional to the derivative of the phase with respect to the time and given by

$$f(t) = \frac{1}{2\pi} \cdot \frac{\mathrm{d}\Phi}{\mathrm{d}t} = \nu_0 + \frac{1}{2\pi} \cdot \frac{\mathrm{d}\varphi}{\mathrm{d}t} \quad . \tag{C.4}$$

The working principle of radio frequency counters is based on recording certain trigger events and comparing them to the trigger events given by a well defined frequency reference (time base). This principle is illustrated in figure C.2a. Trigger events can be for example the zero crossings of the applied signal. The frequency counter counts the number of trigger events within a certain gate time τ, which can be used to calculate the phase change of the signal to determine the average frequency f_{meas} between the times t_k and $t_k + \tau$ [140]

$$f_{\mathrm{meas}} = \int_{-\infty}^{+\infty} f(t) w_\Pi(t - t_k) \mathrm{d}t = \frac{1}{2\pi\tau} \left(\Phi(t_k + \tau) - \Phi(t_k) \right) \quad , \tag{C.5}$$

with $w_\Pi(t)$ being a rectangular weighting function (Π-type) with $w_\Pi(t) = 1/\tau$ for $0 < t < \tau$ and $w_\Pi(t) = 0$ everywhere else. The adjusted gate time typically starts with a
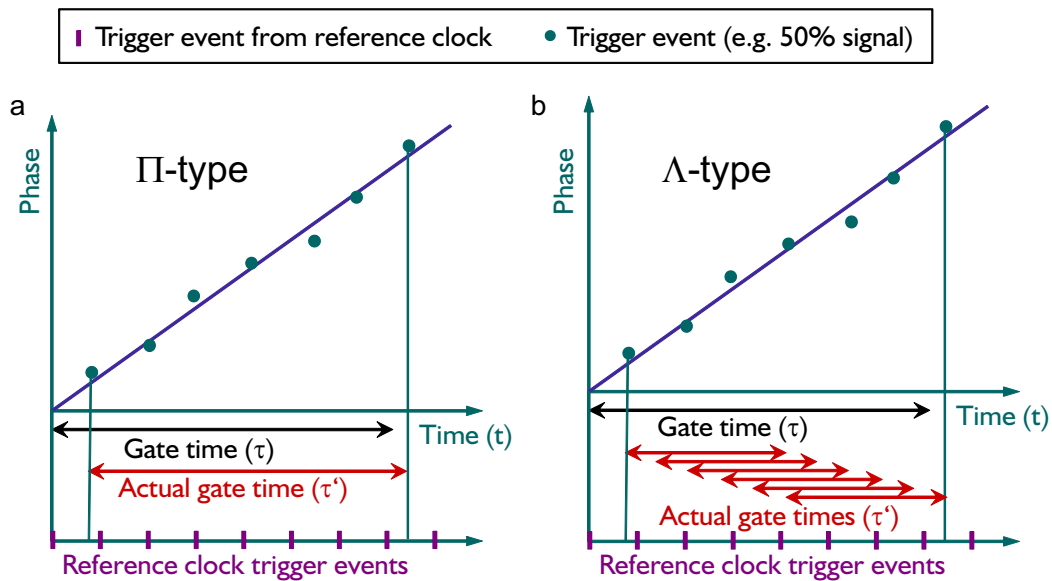
Figure C.2: Working principle of high resolution radio frequency counters. Panel a shows a Π-type counter and panel b the working principle of a Λ-type counter with a Λ-shaped weighting function resulting from splitting up the adjusted gate time τ into several shorter gate times τ'.

trigger event of the applied signal but can also start with a reference clock trigger event, depending on the electronic configuration of the counter. As a result, the actual gate time of the measurement can be different, depending on the applied signal. Higher accuracy of the frequency measurement is achieved by additionally measuring the time-offset between the first and last trigger events of the applied signal and the respective reference clock trigger signals. This time-offset can be measured by quickly charging a capacitor between the trigger events and discharging it with a several hundred times smaller current and measuring the discharging time. Panel a in figure C.2 corresponds to a so-called Π-type counter because of a Π-shaped weighting function as shown in equation C.5. This type of counter uses just the time information of the first and last trigger event during a gate time τ and the exact position of the trigger signals in between does not influence the measurement. Using the additional information of the trigger signals in between can lead to much more precise frequency measurements within the same gate time, which is done by a so-called Λ-type counter shown in figure C.2b. Here, the adjusted gate time is split up into several shorter, overlapping gate times and the displayed frequency measurement is averaged from several shorter measurements. This has the result that trigger signals in the middle of the adjusted gate time contribute more to the result than trigger events at the beginning and end. This leads to a Λ-shaped weighting function for the frequency measurement. Most modern high resolution frequency counters (eg. HP53131A) are Λ-type counters, which influences for example measurements of the Allan-variances as shown by Dawkins et.al. [140]. Most radio frequency counters have several input channels, which allows for example to directly count frequency ratios. In this mode, the frequency counter
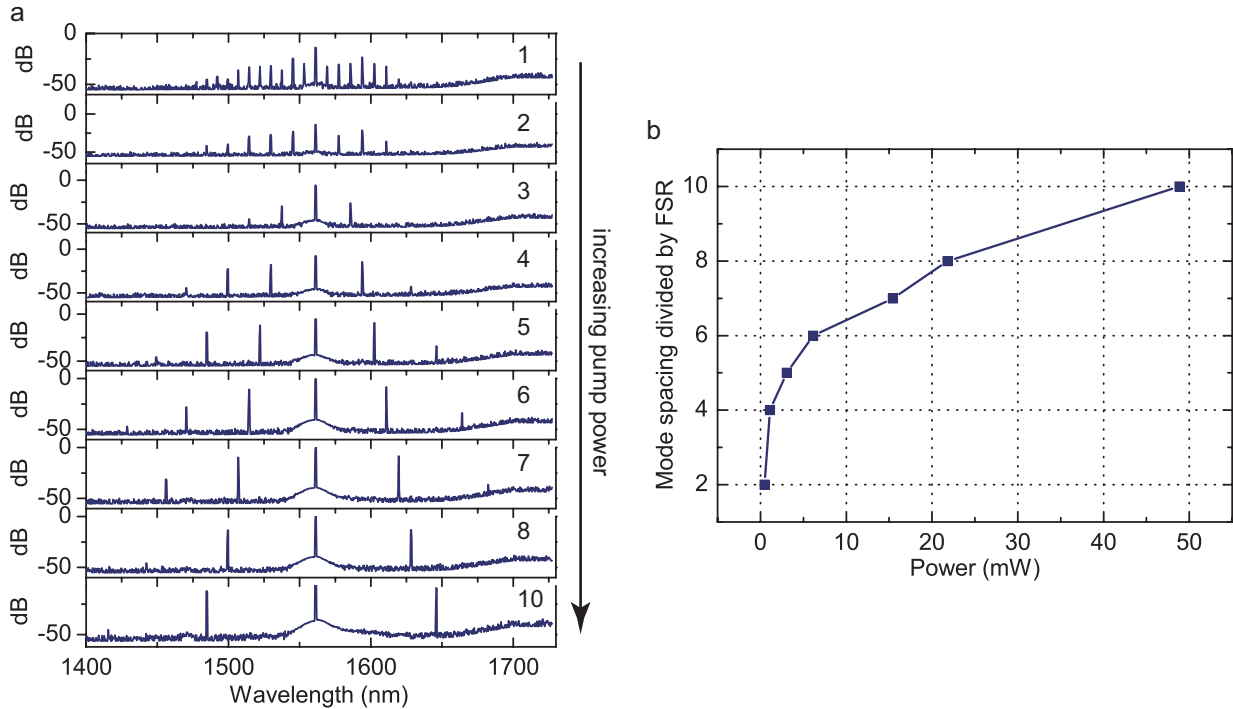
uses one of the applied signals as time base and directly counts the ratio of trigger events within a given gate time. This mechanism is used for equidistance measurements shown in section 2.4.2 of chapter 2.

APPENDIX D

Combs at multiple free spectral ranges

Figure D.1: Comb generation with mode spacings of multiple free spectral ranges. Panel a shows four-wave mixing induced sidebands at different mode spacings in the same microtoroid at different pump power levels. The upper spectrum has a mode spacing of the actual free spectral range of the resonator. The lower panels show combs with integer multiples of the original spacing (the number on the right side of the graphs corresponds to the multiplication factor compared to the fundamental mode spacing). Panel b shows a measurement of the maximum attainable mode spacing multiplication factor as a function of the launched pump power for optimized laser detuning and coupling.

Microresonator-based frequency combs can be generated at mode spacings of integer multiples compared to the cavity's free spectral range [87]. Figure D.1 shows different spectra of four-wave mixing sidebands in a fused silica microtoroid with a fundamental mode spacing of approximately 1 THz. Panel a in figure D.1 shows examples of mode spacing multiplication factors from 1 to 10 at increasing pump powers. This corresponds to mode spacings from 1 THz up to 10 THz. Note that the different mode spacing states mostly change abruptly, however, sometimes intermediate states can be observed with strong modes at higher mode spacings and weaker lines at lower mode spacings in between. In experiments it can be seen that the number of skipped modes is clearly related to the launched pump power, the detuning of the pump laser with respect to the cavity mode and the coupling position (which all influence the intracavity power to some degree). The number of skipped modes depends strongly on the pump laser detuning as well as the coupling condition. Especially for small detunings close to the resonance frequency the fundamental mode spacing can be recovered. This observation is inconsistent with the

observation of generally higher attainable mode spacings at higher powers and indicates that the underlying effect might be related to the cavity dispersion as well as shifts of the maximum four-wave mixing gain at different power levels. Panel b in figure D.1 shows the maximum attainable mode spacing as a function of the launched pump power. "Maximum attainable" means that both the coupling position and laser detuning at a certain pump power is optimized in such a way that the sideband spacing reaches a maximum. A video of the abrupt mode spacing change in a larger resonator with a fundamental free spectral range of approximately 85 GHz can be seen here [173]. The same effect has also been observed in crystalline calcium fluoride resonators as shown by Savchenkov et.al. [89] and a theoretical explanation for this effect in the anomalous dispersion regime is given by Chembo et.al. [76]. A similar explanation could be the shifted parametric gain maximum for different pump power levels as shown in appendix G. Here, the required cavity dispersion $\Delta\omega_k = 2 \cdot \omega_p - \omega_s - \omega_i$ for a maximum parametric gain g scales linear with the pump power P_{in}

$$\Delta\omega_k \propto P_{in} \quad , \tag{D.1}$$

with k being the mode spacing multiplication factor. In case of a negligible third order dispersion in the vicinity of the pump laser, $\Delta\omega_k$ scales with the square of the mode spacing multiplication factor k

$$\Delta\omega_k = k^2 \cdot \Delta\omega_1 \quad , \tag{D.2}$$

with $\Delta\omega_1$ being the detuning parameter for the fundamental mode spacing of the resonator. Thus, it is expected to observe square root dependence between the mode spacing multiplication factor k and the launched power.

$$k \propto \sqrt{P_{in}} \quad , \tag{D.3}$$

However, the data in figure D.1b shows a $k \propto P^\alpha$ with $\alpha = 0.24 \pm 0.01$, which indicates that higher order dispersion terms or other nonlinear interactions of the cavity modes influenced the measurement.

APPENDIX E

Auto- and cross-correlation measurements with microresonator combs

The cavity roundtrip time of a beam of light in a fused silica microtoroid with a radius of 35 μm is $2\pi R \cdot n_{\text{eff}} \cdot \frac{1}{c} \approx 1$ ps. Correspondingly, a pulses generated in this cavity would have a repetition rate in the order of $f_{\text{rep}} = 1$ THz, which exceeds the bandwidth of available photodiodes. The temporal shape of microresonator comb spectra can be investigated by using an autocorrelator setup. The high free spectral range even allows for cross-correlation experiments as a 1-THz-modespacing corresponds to a spacial "pulse" separation of only 300 μm. Periodic and stable waveforms are observed, leading to the conclusion of having a *fixed phase relationship* between the generated microresonator comb modes.

# E.1 Interferometric intensity autocorrelation

An interferometric autocorrelation can be used to measure the length of an optical pulse, in case the pulse shape is known. To measure an interferometric intensity autocorrelation, a signal proportional to the squared intensity of the incident light beams can be used. This is achieved either by using a 2-photon absorption process in a photodiode with a bandgap higher than the energy of one photon, but smaller than the energy of two photons, or by using a nonlinear second harmonic generation (SHG) crystal. The intensity of the second harmonic light is proportional to the total squared intensity of the incident beams inside the SHG crystal. Thus the measured autocorrelation trace is proportional to the interferometric intensity autocorrelation function

$$I_2(\tau) = \int\limits_{-\infty}^{\infty} \left| \left(E\left(t\right) + E\left(t+\tau\right) \right)^2 \right|^2 \mathrm{d}t \tag{E.1}$$

The maximum measured intensity for two overlapping pulses from both interferometer arms ($\tau = 0$) is eight times higher than the measured intensity in case of no pulse overlap. This determines the characteristic contrast ratio of 8:1 for an interferometric autocorrelation measurement.

E.2 Setup for Cross-correlation measurements

The experimental setup for the autocorrelation and cross-correlation measurements is shown in figure E.1, consisting of a Michelson interferometer with a fixed length for one arm and a variable length for the other one. The length of the latter can be changed by a stepper motor controlled translation stage. A 1-mm long periodically poled lithium niobate crystal (PPLN, Thorlabs SHG5-1) is used to generate the second harmonic frequency of the incident light. For higher conversion efficiency the polarization of the beam can be adjusted with half- and quarter-wave-plates and the beam is focused into the PPLN crystal by an achromatic doublet lens. The generated second harmonic light is focused onto a highly sensitive Si Photodiode (New Focus 2151 Si Femtowatt Photoreceiver) after passing a 950 nm short pass filter to block the fundamental wavelength.
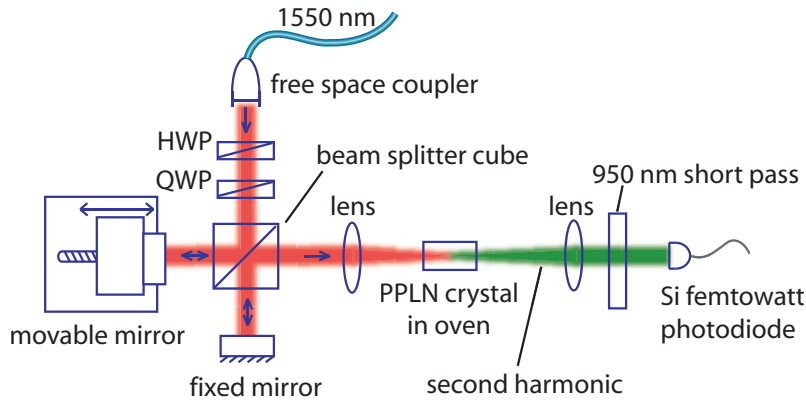
Figure E.1: Autocorrelator Setup. A graded index lens (GRIN lens) is used to couple the light from an optical fiber to a free space Michelson interferometer. Subsequently, the beam is focused into a PPLN crystal to generate the second harmonic of the incident light. Since the conversion efficiency is polarization dependent, a quarter-wave plate (QWP) and a half-wave plate allows to rotate the polarization of the beam. The fundamental wavelength is suppressed with a short pass filter before the autocorrelation measurement with a highly sensitive silicon photodiode.

To record a cross-correlation trace, the stepper motor controlled translation stage is moved with a predefined speed. At the same time the output signal of the photodetector is recorded with an oscilloscope. The recording of one cross-correlation trace typically takes around 1 minute as a result of the low bandwidth of the employed "Femtowatt"-photoreceiver. Later, the time axis of the oscilloscope trace can be calibrated to the length of the variable interferometer arm ℓ, and hence the time delay is $\tau = 2 \cdot \frac{\ell}{c}$ in this arm (where c is the speed of light in air). Figure E.2 shows a photo of the autocorrelator setup.

E.3   Cross-correlation measurements

Owing to the broad bandwidth of the generated combs, dispersion plays an important role in the measurement of the temporal shape of the light leaving the resonator. Since the dispersion of a standard SMF-28 optical fiber is already in the order of 16 $\frac{\text{ps}}{\text{km} \cdot \text{nm}}$ [174], a Fourier limited pulse with an optical bandwidth of 100 nm would spread to 1.6 ps in just 1 m of optical fiber. However, the dispersion of the optical fiber is partly compensated by highly negative dispersion of the optical taper used to couple the light from the microtoroid. These tapered fibers have a group velocity dispersion on the order of $-2000 \frac{\text{ps}}{\text{km} \cdot \text{nm}}$, which has been measured in the group of A. Gaeta [175]. Figure E.3 shows the influence of a tapered optical fiber on the pulse length of a mode locked fiber laser. Experimentally, this dispersion compensation turns out to be difficult for broader wavelengths ranges as a result of higher order dispersion. However, the fact that the measured autocorrelation traces are stable for minutes shows that the parametric sidebands are generated with a *fixed phase relation*. Figure E.4 shows a cross-correlation trace that has been obtained from the output
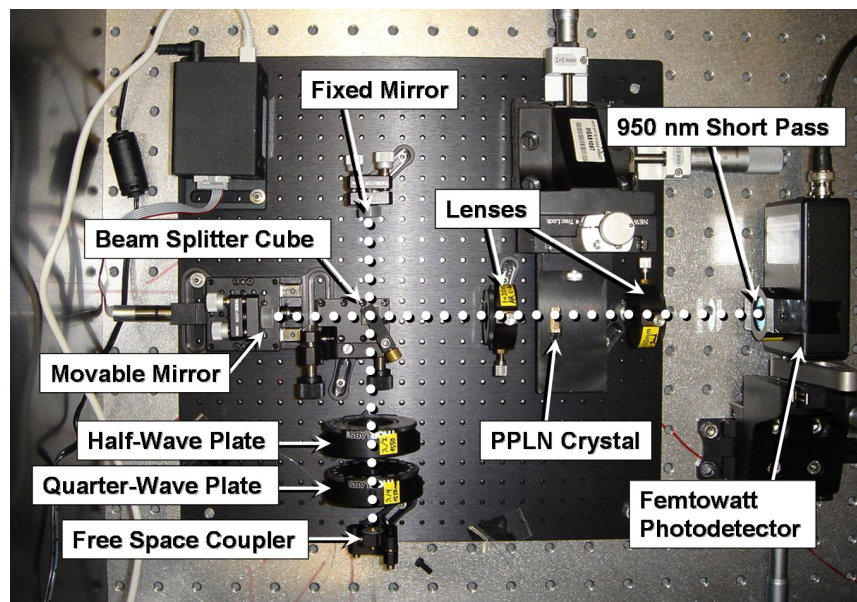
Figure E.2: Photo of the setup that was built to measure the cross-correlation traces. The dotted lines represent the optical path. The configuration of the setup is the same as depicted in figure E.1. PPLN = periodically poled lithium niobate.
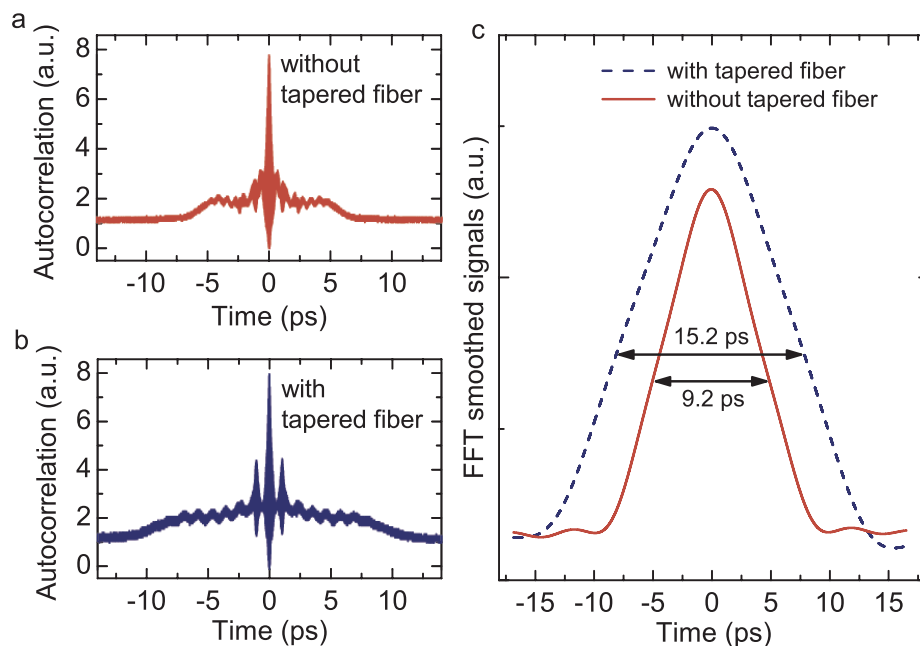
Figure E.3: Dispersive properties of tapered optical fibers. Panel a shows an autocorrelation measurement of a pulse emitted by a mode locked erbium-doped fiber laser. The trace in panel b is the recorded after sending the pulse through a tapered optical fiber (taper region length ≈ 3 cm, minimum diameter ≈ 1 μm). Panel c shows smoothened curves of the data in panel a and b in order to determine the respective pulse lengths.
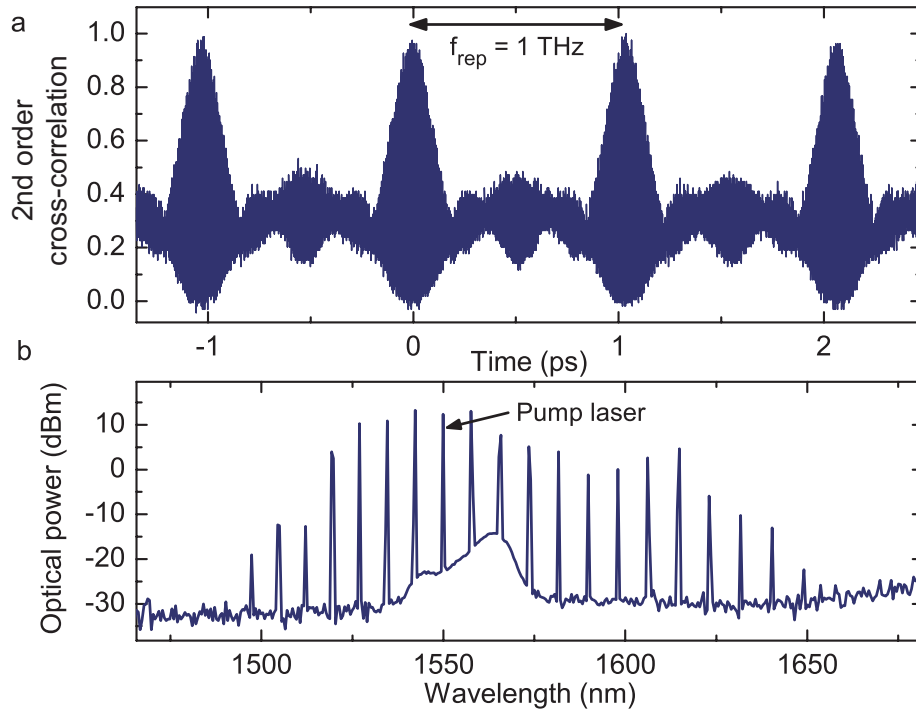
Figure E.4: Interferometric intensity cross-correlation trace and optical spectrum of a microresonator comb with 1 THz mode spacing.

signal of a microtoroid pumped with 70 mW cw power.

The phase matching bandwidth of the employed PPLN crystal for frequency doubling is only in the order of several 10 nm such that only a few comb modes can contribute to the cross-correlation measurement. As a consequence, comparably high pump power is required to generate the second harmonic signal. However, due to the high sensitivity of the used "femtowatt detector" a pump power of approximately 50 mW is already sufficient to generate an observable second harmonic signal. The free spectral range in the spectrum in figure E.4b matches the periodicity of the signal in the autocorrelation trace. Note that a residual pump laser would add a strong background to the cross-correlation measurements. However, pumping the microresonator close to the linecenter of the cavity mode allows to sufficiently suppress the pump laser to a level even below the first sidebands.

Figure E.5 shows a measured cross-correlation trace from a larger microresonator with a free spectral range of approximately 85 GHz. During the measurement, the microresonator comb mode spacing has been doubled by changing the coupling gap (cf. appendix D), corresponding to two circulating "pulses". This change of the optical spectrum is also reflected in the simultaneously measured cross-correlation trace. Note that the measured cross-correlation traces do not exhibit a contrast ratio of 1:8 for well separated pulses as a consequence of the dispersion of the tapered optical fiber and the high repetition rate. Thus, it is not possible to determine a "pulse width" from the cross-correlation measurements. However, also the stabilization measurements in chapter 3 have shown that interference
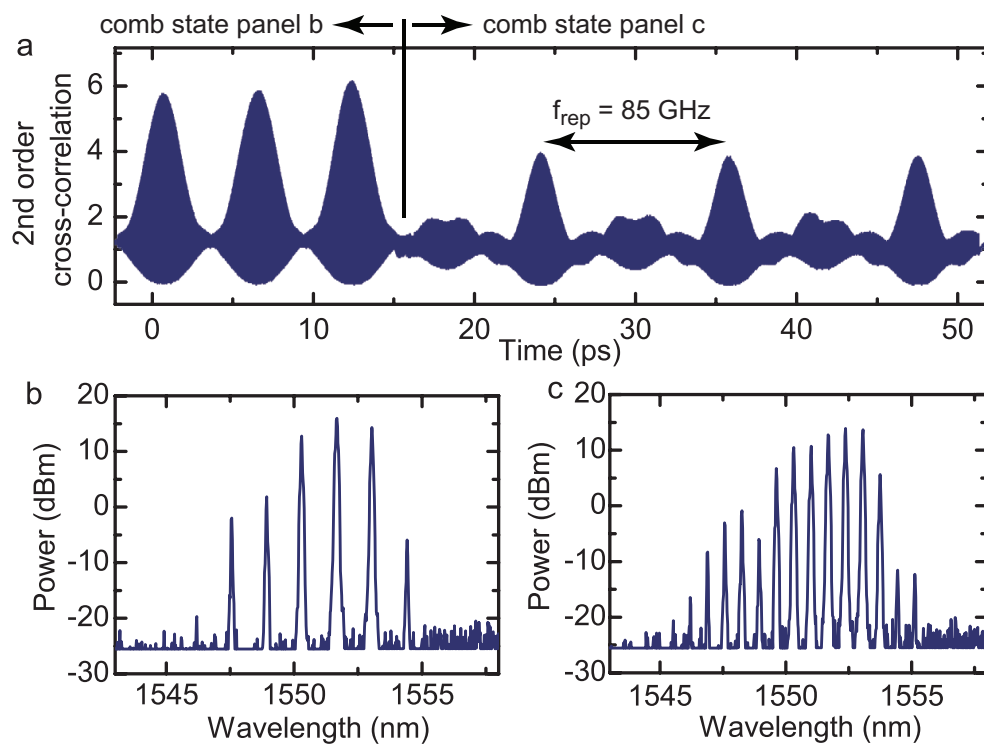
Figure E.5: Interferometric cross-correlation trace and optical spectrum of a microresonator comb with 85 THz free spectral range. The mode spacing of the generated comb has doubled by a coupling change during the measurement (leading to two circulating pulses), which is reflected in the cross-correlation.

of the comb modes leads to a sufficient amplitude modulation in time domain that allows for direct electronic measurement of the mode spacing. Additionally, the cross-correlation traces are stable for long time scales of several minutes (just influenced by pump laser and coupling drifts), which indicates a long term phase coherence of the generated comb modes.
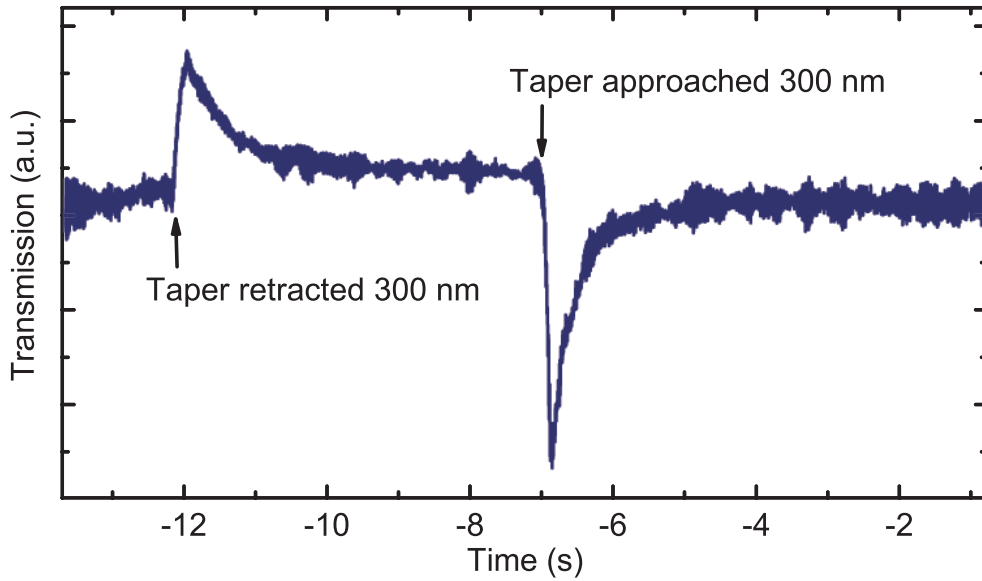
APPENDIX F

Self-stabilized tapered fiber coupling

Figure F.1: Thermal self-stabilization of the tapered optical fiber position. The graph shows the transmission signal of a pump laser (4 W, coupled to a resonator mode) through a tapered optical fiber. Using a piezo translation stage, the tapered fiber is first retracted 300 nm with respect to the resonator and then approached by the same distance. The transmission signal (and thus the intracavity power) automatically returns to its original value after a few seconds.

An interesting effect of thermal self-stabilization of the position of the tapered optical fiber with respect to a fused silica microtoroid is observed at high pump power levels. Figure F.1 shows a graph of this phenomenon. A microtoroid is pumped on resonance (with $P_{in} \approx 4$ W), while simultaneously monitoring the transmission signal through the tapered optical fiber. Now, the tapered optical fiber position is changed by ± 300 nm (first retracted and then approached with respect to the toroid) using a piezo translation stage. The graph in figure F.1 shows that the transmission signal returns to its initial value at a 2 seconds timescale after moving the tapered optical fiber. Since the loss in transmission directly represents the amount of light coupled to the resonator, this effect can be used to automatically stabilize the intracavity power and compensate for coupling gap fluctuation and drifts.

The thermal nature of the stabilization can be inferred from the observation that the tapered fiber (without resonator) moves when changing the pump laser power. If the tapered fiber is approached to a microresonator from a side such that a reduced power in the tapered fiber moves it away form the resonator, the stabilization effect can be explained as follow. In case the tapered fiber moves towards the resonator the power in the tapered fiber is reduced (in the undercoupled regime), which and the taper is thermally retracted back to the original coupling position. In a similar way, a drift of the tapered fiber away from the resonator leads to an increased power in the fiber, inducing a thermal shift towards the resonator. This effect is convenient for long term frequency comb generation at high

pump powers, which is usually limited by drifts of the piezo translation stages. Long term comb generation can also be achieved by having the tapered optical fiber in direct contact with the microresonator (however, good positioning is required in this case in order to not influence the optical quality factor). The thermal effect can also lead to regenerative oscillations of the fiber position in case the fiber is electrostatically sticking to the resonator. In this case the temperature change in the fiber is high enough to pull it away from the resonator and subsequent heating moves it back to the resonator. This effect is shown in the video in reference [176]. Note that the fiber is not actively moved by a piezo controller in this video.

APPENDIX G

Calculation of four-wave mixing gain and threshold

The pump power threshold for four-wave mixing can be calculated based on equation 1.28 in chapter 1. For this calculation, just the first pair of sidebands (signal and idler) are taken into account (cf. references [80, 177]). Moreover it is assumed that the optical power in the pump mode is much higher than in the sidebands. This assumption allows to neglect self-phase modulation effects in the sidebands as well as cross phase modulation in the pump mode. With

$$\Delta\omega = 2\omega_p - \omega_s - \omega_i \quad , \tag{G.1}$$

the coupled mode equations for the photon numbers in pump $|\mathcal{A}_p|^2$, signal $|\mathcal{A}_s|^2$ and idler $|\mathcal{A}_i|^2$ are given as

$$\dot{\mathcal{A}}_p = -\eta_1 \cdot \mathcal{A}_p - i \cdot \eta_2 \cdot |\mathcal{A}_p|^2 \cdot \mathcal{A}_p - 2i \cdot \eta_2 \cdot \mathcal{A}_s \mathcal{A}_p^* \mathcal{A}_i \cdot e^{-i \cdot \Delta\omega \cdot t} \cdot e^{i \cdot \Delta\ell \cdot \varphi} \tag{G.2}$$

$$\dot{\mathcal{A}}_s = -\eta_1 \cdot \mathcal{A}_s - i \cdot \eta_2 \cdot |\mathcal{A}_p|^2 \cdot \mathcal{A}_s - i \cdot \eta_2 \cdot \mathcal{A}_p \mathcal{A}_i^* \mathcal{A}_p \cdot e^{-i \cdot \Delta\omega \cdot t} \cdot e^{i \cdot \Delta\ell \cdot \varphi} \tag{G.3}$$

$$\dot{\mathcal{A}}_i = -\eta_1 \cdot \mathcal{A}_i - i \cdot \eta_2 \cdot |\mathcal{A}_p|^2 \cdot \mathcal{A}_i - i \cdot \eta_2 \cdot \mathcal{A}_p \mathcal{A}_s^* \mathcal{A}_p \cdot e^{-i \cdot \Delta\omega \cdot t} \cdot e^{i \cdot \Delta\ell \cdot \varphi} \quad . \tag{G.4}$$

For further simplification we assume that the generated sidebands are symmetric with respect to the pump laser and resonant in the cavity such that $\Delta\ell = 0$. To calculate the threshold for four-wave mixing it is assumed that the optical power in the pump mode is constant $\dot{\mathcal{A}}_p = 0$. The remaining differential equation system for $\mathcal{A}_s$ and $\mathcal{A}_i$ has time dependent coefficients $e^{-i \cdot \Delta\omega \cdot t}$. In order to obtain time-independent coefficients, we can use the substitution

$$\mathcal{A}_{s,i} = \mathcal{B}_{s,i} \cdot e^{-i \frac{\Delta\omega}{2} \cdot t} \quad . \tag{G.5}$$

This leads to the following linear first order differential equation system with constant coefficients

$$\dot{\mathcal{B}}_s - i \cdot \frac{\Delta\omega}{2} \cdot \mathcal{B}_s = -\eta_1 \cdot \mathcal{B}_s - i \cdot \eta_2 \cdot |\mathcal{A}_p|^2 \cdot \mathcal{B}_s - i \cdot \eta_2 \cdot \mathcal{A}_p^2 \cdot \mathcal{B}_i^* \tag{G.6}$$

$$\dot{\mathcal{B}}_i - i \cdot \frac{\Delta\omega}{2} \cdot \mathcal{B}_i = -\eta_1 \cdot \mathcal{B}_i - i \cdot \eta_2 \cdot |\mathcal{A}_p|^2 \cdot \mathcal{B}_i - i \cdot \eta_2 \cdot \mathcal{A}_p^2 \cdot \mathcal{B}_s^* \quad . \tag{G.7}$$

By complex-conjugating the second equation for the idler mode, the differential equation system can be written in matrix form

$$\begin{pmatrix} \dot{\mathcal{B}}_s \\ \dot{\mathcal{B}}_i^* \end{pmatrix} = \begin{pmatrix} i \cdot \frac{\Delta\omega}{2} - \eta_1 - i \cdot \eta_2 \cdot |\mathcal{A}_p|^2 & -i \cdot \eta_2 \cdot \mathcal{A}_p^2 \\ i \cdot \eta_2 \cdot (\mathcal{A}_p^2)^* & -i \cdot \frac{\Delta\omega}{2} - \eta_1 + i \cdot \eta_2 \cdot |\mathcal{A}_p|^2 \end{pmatrix} \cdot \begin{pmatrix} \mathcal{B}_s \\ \mathcal{B}_i^* \end{pmatrix} \quad . \tag{G.8}$$

In case the coefficient matrix has real eigenvalues $\lambda_{1,2}$, the solutions of the differential equation system are proportional to $e^{\lambda_{1,2} \cdot t}$. Calculation of the eigenvalues yields

$$\lambda_{1,2} = -\eta_1 \pm \sqrt{\eta_2 \cdot \Delta\omega \cdot |\mathcal{A}_p|^2 - \frac{\Delta\omega^2}{4}} \tag{G.9}$$
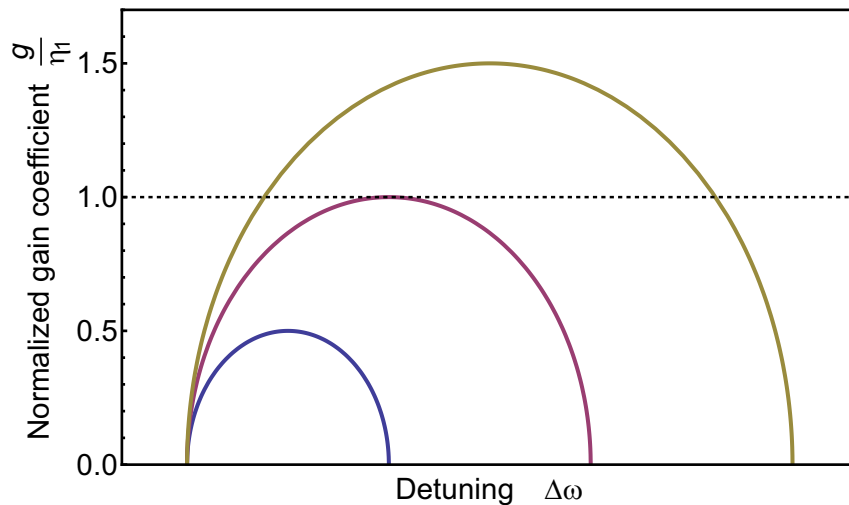
Figure G.1: Normalized parametric gain g/η_1 for three different intracavity powers as function of the detuning $\Delta\omega$. The dashed line indicates the threshold power for parametric frequency conversion. The three curve show the parametric gain below threshold, at threshold and above threshold. Note that the maximum gain scales linear with the optical power in the pump mode.

The temporal evolution of the optical power in the sidebands has two contributions. The first term in the eigenvalues corresponds to the intrinsic cavity loss rate represented by η_1 (note that we assumed a constant η_1 for both sidebands). The second term can be defined as four-wave mixing or parametric gain g and describes the scattering of light from the pump mode into the sidebands. This gain is given by

$$g = \sqrt{\eta_2 \cdot \Delta\omega \cdot |\mathcal{A}_p|^2 - \frac{\Delta\omega^2}{4}} \qquad (G.10)$$

The parametric gain depends on the circulating power in the pump mode and reaches a maximum value for a detuning of $\Delta\omega = 2\eta_2 |\mathcal{A}_p|^2$ as a result of cross-phase modulation and self-phase modulation.

The threshold power for parametric frequency conversion is reached when the eigenvalues $\lambda_{1,2}$ equate to zero (cavity loss equals the parametric gain). Solving for the photon number in the pump mode $\left|\mathcal{A}_p^{\text{thresh}}\right|^2$ yields

$$\left|\mathcal{A}_p^{\text{thresh}}\right|^2 = \frac{\frac{\Delta\omega^2}{4} + \eta_1^2}{\eta_2 \cdot \Delta\omega} \quad . \qquad (G.11)$$

Here, the cavity loss rate is taken into account by η_1, which is related to the optical quality factor Q via

$$\eta_1 = \frac{\pi\nu_L}{Q} \quad . \qquad (G.12)$$

The parametric gain coefficient η_2 in a resonator with refractive index n_0 is determined by

the ratio of nonlinear refractive index n_2 and the mode volume of the resonator V_0

$$\eta_2 = \frac{2\pi \cdot n_2}{n_0^2} \cdot \frac{h\nu_L \cdot c}{V_0} \quad . \tag{G.13}$$

The photon number threshold in equation G.11 can be converted into a seed laser power P_{in} by taking into account the cavity enhancement $\frac{\mathcal{F}}{2\pi}$, the coupling efficiency η_{ext} and the detuning between seed laser ν_L and pump resonance ν_c (cf. equation 1.15 at critical coupling).

$$P_{\text{cav}} = |\mathcal{A}_p|^2 \cdot \frac{h\nu_L \cdot c}{2\pi \cdot R \cdot n_{\text{eff}}} = \underbrace{P_{\text{in}}}_{\substack{\text{launched} \\ \text{power}}} \cdot \underbrace{\eta_{\text{ext}}}_{\substack{\text{coupling} \\ \text{efficiency}}} \cdot \underbrace{\frac{\mathcal{F}}{2\pi}}_{\substack{\text{cavity} \\ \text{enhancement}}} \cdot \underbrace{\frac{1}{1 + 4\left(\frac{\nu_L - \nu_c}{\Delta\nu}\right)^2}}_{\text{Lorentzian lineshape}} \tag{G.14}$$

Here, R is the radius of the microresonator with an effective refractive index n_{eff} and a linewidth of $\Delta\nu$. Using equation G.14 the threshold power $P_{\text{in}}^{\text{thresh}}$ for parametric frequency conversion equates to

$$P_{\text{in}}^{\text{thresh}} = \left[\frac{\Delta\omega^2}{4} + \left(\frac{\pi\nu_L}{Q}\right)^2\right] \cdot \frac{4\pi^2 \cdot n_0^2 \cdot V_0}{\Delta\omega \cdot n_2 \cdot \eta_{\text{ext}} \cdot c \cdot Q} \cdot \left[1 + 4\left(\frac{\nu_L - \nu_c}{\Delta\nu^2}\right)^2\right] \tag{G.15}$$

For a pump laser on resonance ($\nu_L = \nu_c$), this equation can be simplified to

$$P_{\text{in}}^{\text{thresh}} = \left[\frac{\Delta\omega^2}{4} + \left(\frac{\pi\nu_L}{Q}\right)^2\right] \cdot \frac{4\pi^2 \cdot n_0^2 \cdot V_0}{\Delta\omega \cdot n_2 \cdot \eta_{\text{ext}} \cdot c \cdot Q} \tag{G.16}$$

Bibliography

[1] A. Schliesser, P. Del'Haye, N. Nooshi, K. J. Vahala, and T. J. Kippenberg, "Radiation pressure cooling of a micromechanical oscillator using dynamical backaction," *Physical Review Letters* **97**, p. 243905, Dec. 2006.

[2] R. Ma, A. Schliesser, P. Del'Haye, A. Dabirian, G. Anetsberger, and T. J. Kippenberg, "Radiation-pressure-driven vibrational modes in ultrahigh-q silica microspheres," *Optics Letters* **32**, pp. 2200–2202, Aug. 2007.

[3] P. Del'Haye, A. Schliesser, O. Arcizet, T. Wilken, R. Holzwarth, and T. J. Kippenberg, "Optical frequency comb generation from a monolithic microresonator," *Nature* **450**, pp. 1214–1217, Dec. 2007.

[4] P. Del'Haye, O. Arcizet, A. Schliesser, R. Holzwarth, and T. J. Kippenberg, "Full stabilization of a microresonator-based optical frequency comb," *Physical Review Letters* **101**, p. 053903, Aug. 2008.

[5] P. Del'Haye, O. Arcizet, M. L. Gorodetsky, R. Holzwarth, and T. J. Kippenberg, "Frequency comb assisted diode laser spectroscopy for measurement of microcavity dispersion," *Nature Photonics* **3**, pp. 529–533, Sept. 2009.

[6] O. Arcizet, A. Schliesser, P. Del'Haye, R. Holzwarth, and T. J. Kippenberg, *Practical applications of microresonators*, ch. 11. Optical frequency comb generation in monolithic microresonators, pp. 483—506. CRC press, 2009.

[7] P. Del'Haye, T. Herr, E. Gavartin, R. Holzwarth, and T. J. Kippenberg, "Octave spanning frequency comb on a chip." arXiv:0912.4890.

[8] P. Del'Haye, T. J. Kippenberg, and A. Schliesser, "Method and apparatus for optical frequency comb generation using a monolithic microresonator. European (EP 07009067) and US (US 60.916045) patent applications," 2007.

[9] P. Del'Haye, O. Arcizet, and T. J. Kippenberg, "Method and apparatus for frequency comb assisted laser spectroscopy. (US 61/217,220, provisional patent application)," 2009.

[10] L. Rayleigh, "The problem of the whispering gallery," *Scientific Papers* **5**, p. 617, 1912.

[11] R. D. Richtmyer, "Dielectric resonators," *Journal of Applied Physics* **10**, pp. 391–398, June 1939.

[12] V. B. Braginsky, M. L. Gorodetsky, and V. S. Ilchenko, "Quality-factor and nonlinear properties of optical whispering-gallery modes," *Physics Letters A* **137**, pp. 393–397, May 1989.

[13] K. J. Vahala, "Optical microcavities," *Nature* **424**, pp. 839–846, Aug. 2003.

[14] V. S. Ilchenko and A. B. Matsko, "Optical resonators with whispering-gallery modes - part ii: Applications," *IEEE Journal Of Selected Topics In Quantum Electronics* **12**, pp. 15–32, Jan. 2006.

[15] A. B. Matsko and V. S. Ilchenko, "Optical resonators with whispering-gallery modes - part i: Basics," *IEEE Journal Of Selected Topics In Quantum Electronics* **12**, pp. 3–14, Jan. 2006.

[16] T. J. Kippenberg, S. M. Spillane, and K. J. Vahala, "Kerr-nonlinearity optical parametric oscillation in an ultrahigh-Q toroid microcavity," *Physical Review Letters* **93**, p. 083904, Aug. 2004.

[17] A. A. Savchenkov, A. B. Matsko, D. Strekalov, M. Mohageg, V. S. Ilchenko, and L. Maleki, "Low threshold optical oscillations in a whispering gallery mode CaF2 resonator," *Physical Review Letters* **93**, p. 243905, Dec. 2004.

[18] S. M. Spillane, T. J. Kippenberg, and K. J. Vahala, "Ultralow-threshold raman laser using a spherical dielectric microcavity," *Nature* **415**, pp. 621–623, Feb. 2002.

[19] B. K. Min, T. J. Kippenberg, and K. J. Vahala, "Compact, fiber-compatible, cascaded raman laser," *Optics Letters* **28**, pp. 1507–1509, Sept. 2003.

[20] T. J. Kippenberg, S. M. Spillane, D. K. Armani, and K. J. Vahala, "Ultralow-threshold microcavity raman laser on a microelectronic chip," *Optics Letters* **29**, pp. 1224–1226, June 2004.

[21] V. S. Ilchenko, A. A. Savchenkov, A. B. Matsko, and L. Maleki, "Nonlinear optics and crystalline whispering gallery mode cavities," *Physical Review Letters* **92**, p. 043903, Jan. 2004.

[22] A. A. Savchenkov, A. B. Matsko, M. Mohageg, D. V. Strekalov, and L. Maleki, "Parametric oscillations in a whispering gallery resonator," *Optics Letters* **32**, pp. 157–159, Jan. 2007.

[23] I. S. Grudinin and L. Maleki, "Ultralow-threshold raman lasing with CaF2 resonators," *Optics Letters* **32**, pp. 166–168, Jan. 2007.

[24] V. Sandoghdar, F. Treussart, J. Hare, V. LefevreSeguin, J. M. Raimond, and S. Haroche, "Very low threshold whispering-gallery-mode microsphere laser," *Physical Review A* **54**, pp. R1777–R1780, Sept. 1996.

[25] M. Cai, O. Painter, K. J. Vahala, and P. C. Sercel, "Fiber-coupled microsphere laser," *Optics Letters* **25**, pp. 1430–1432, Oct. 2000.

[26] B. K. Min, T. J. Kippenberg, L. Yang, K. J. Vahala, J. Kalkman, and A. Polman, "Erbium-implanted high-Q silica toroidal microcavity laser on a silicon chip," *Physical Review A* **70**, p. 033803, Sept. 2004.

[27] T. J. Kippenberg, J. Kalkman, A. Polman, and K. J. Vahala, "Demonstration of an erbium-doped microdisk laser on a silicon chip," *Physical Review A* **74**, p. 051802, Nov. 2006.

[28] J. Kalkman, A. Polman, T. J. Kippenberg, K. J. Vahala, and M. L. Brongersma, "Erbium-implanted silica microsphere laser," *Nuclear Instruments & Methods In Physics Research Section B-Beam Interactions With Materials And Atoms* **242**, pp. 182–185, Jan. 2006.

[29] D. W. Vernooy, A. Furusawa, N. P. Georgiades, V. S. Ilchenko, and H. J. Kimble, "Cavity qed with high-q whispering gallery modes," *Physical Review A* **57**, pp. R2293–R2296, Apr. 1998.

[30] S. M. Spillane, T. J. Kippenberg, K. J. Vahala, K. W. Goh, E. Wilcut, and H. J. Kimble, "Ultrahigh-Q toroidal microresonators for cavity quantum electrodynamics," *Physical Review A* **71**, p. 013817, Jan. 2005.

[31] T. Aoki, B. Dayan, E. Wilcut, W. P. Bowen, A. S. Parkins, T. J. Kippenberg, K. J. Vahala, and H. J. Kimble, "Observation of strong coupling between one atom and a monolithic microresonator," *Nature* **443**, pp. 671–674, Oct. 2006.

[32] A. M. Armani, R. P. Kulkarni, S. E. Fraser, R. C. Flagan, and K. J. Vahala, "Label-free, single-molecule detection with optical microcavities," *Science* **317**, pp. 783–787, Aug. 2007.

[33] V. B. Braginskii and A. B. Manukin, *Measurement of weak forces in physics experiments*, University of Chicago Press, 1977.

[34] V. B. Braginsky, S. E. Strigin, and S. P. Vyatchanin, "Analysis of parametric oscillatory instability in power recycled ligo interferometer," *Physics Letters A* **305**, pp. 111–124, Dec. 2002.

[35] T. J. Kippenberg, H. Rokhsari, T. Carmon, A. Scherer, and K. J. Vahala, "Analysis of radiation-pressure induced mechanical oscillation of an optical microcavity," *Physical Review Letters* **95**, p. 033901, July 2005.

[36] H. Rokhsari, T. J. Kippenberg, T. Carmon, and K. J. Vahala, "Radiation-pressure-driven micro-mechanical oscillator," *Optics Express* **13**, pp. 5293–5301, July 2005.

[37] H. Rokhsari, T. J. Kippenberg, T. Carmon, and K. J. Vahala, "Theoretical and experimental study of radiation pressure-induced mechanical oscillations (parametric instability) in optical microcavities," *IEEE Journal Of Selected Topics In Quantum Electronics* **12**, pp. 96–107, Jan. 2006.

[38] A. Schliesser, R. Riviere, G. Anetsberger, O. Arcizet, and T. J. Kippenberg, "Resolved-sideband cooling of a micromechanical oscillator," *Nature Physics* **4**, pp. 415–419, May 2008.

[39] A. Schliesser, O. Arcizet, R. Riviere, G. Anetsberger, and T. J. Kippenberg, "Resolved-sideband cooling and position measurement of a micromechanical oscillator close to the heisenberg uncertainty limit," *Nature Physics* **5**, pp. 509–514, July 2009.

[40] R. Riviere, S. Deleglise, S. Weis, E. Gavartin, O. Arcizet, A. Schliesser, and K. T.J., "Optomechanical sideband cooling of a micromechanical oscillator close to the quantum ground state." (in preparation).

[41] T. J. Kippenberg, S. A. Spillane, B. Min, and K. J. Vahala, "Theoretical and experimental study of stimulated and cascaded raman scattering in ultrahigh-Q optical microcavities," *IEEE Journal Of Selected Topics In Quantum Electronics* **10**, pp. 1219–1228, Sept. 2004.

[42] T. Carmon and K. J. Vahala, "Visible continuous emission from a silica microphotonic device by third-harmonic generation," *Nature Physics* **3**, pp. 430–435, June 2007.

[43] D. K. Armani, T. J. Kippenberg, S. M. Spillane, and K. J. Vahala, "Ultra-high-Q toroid microcavity on a chip," *Nature* **421**, pp. 925–928, Feb. 2003.

[44] T. J. Kippenberg, S. M. Spillane, and K. J. Vahala, "Demonstration of ultra-high-Q small mode volume toroid microcavities on a chip," *Applied Physics Letters* **85**, pp. 6113–6115, Dec. 2004.

[45] O. Humbach, H. Fabian, U. Grzesik, U. Haken, and W. Heitmann, "Analysis of oh absorption bands in synthetic silica," *Journal Of Non-Crystalline Solids* **203**, pp. 19–26, Aug. 1996.

[46] B. E. Deal and A. S. Grove, "General relationship for the thermal oxidation of silicon," *Journal of Applied Physics* **36**(12), pp. 3770–3778, 1965.

[47] H. Proksche, G. Nagorsen, and D. Ross, "Insitu measurement of etch velocity of layers on silicon," *Fresenius Journal Of Analytical Chemistry* **341**(1-2), pp. 92–94, 1991.

[48] C. L. Chernick, "Die edelgasverbindungen," *Chemie in unserer Zeit* **1**, p. 33, 2004.

[49] H. F. Winters and J. W. Coburn, "Etching of silicon with XeF2 vapor," *Applied Physics Letters* **34**(1), pp. 70–73, 1979.

[50] K. Sugano and O. Tabata, "Reduction of surface roughness and aperture size effect for etching of Si with XeF2," *Journal Of Micromechanics And Microengineering* **12**, pp. 911–916, Nov. 2002.

[51] E. H. Appelman, "Reaction of xenon difluoride with water and with xenon trioxide," *Inorganic Chemistry* **6**(7), pp. 1305–&, 1967.

[52] P. Del'Haye, "Cascaded parametric frequency conversion in monolithic microresonators," Master's thesis, Ludwig-Maximilians-Universitäet, 2007.

[53] H. A. Haus, *Waves and Fields in Optoelectronics*, Prentice-Hall, 1984.

[54] H. A. Haus, W. P. Huang, S. Kawakami, and N. A. Whitaker, "Coupled-mode theory of optical wave-guides," *Journal of Lightwave Technology* **5**, pp. 16–23, Jan. 1987.

[55] J. C. Knight, G. Cheung, F. Jacques, and T. A. Birks, "Phase-matched excitation of whispering-gallery-mode resonances by a fiber taper," *Optics Letters* **22**, pp. 1129–1131, Aug. 1997.

[56] B. E. Little, J. P. Laine, and H. A. Haus, "Analytic theory of coupling from tapered fibers and half-blocks into microsphere resonators," *Journal Of Lightwave Technology* **17**, pp. 704–715, Apr. 1999.

[57] A. Yariv, "Critical coupling and its control in optical waveguide-ring resonator systems," *IEEE Photonics Technology Letters* **14**, pp. 483–485, Apr. 2002.

[58] J. M. Choi, R. K. Lee, and A. Yariv, "Control of critical coupling in a ring resonator-fiber configuration: application to wavelength-selective switching, modulation, amplification, and oscillation," *Optics Letters* **26**, pp. 1236–1238, Aug. 2001.

[59] A. Yariv, "Universal relations for coupling of optical power between microresonators and dielectric waveguides," *Electronics Letters* **36**, pp. 321–322, Feb. 2000.

[60] M. Cai, O. Painter, and K. J. Vahala, "Observation of critical coupling in a fiber taper to a silica-microsphere whispering-gallery mode system," *Physical Review Letters* **85**, pp. 74–77, July 2000.

[61] T. Carmon, S. Y. T. Wang, E. P. Ostby, and K. J. Vahala, "Wavelength-independent coupler from fiber to an on-chip cavity, demonstrated over an 850nm span," *Optics Express* **15**, pp. 7677–7681, June 2007.

[62] W. A. Pasmooij, P. A. Mandersloot, and M. K. Smit, "Prism-coupling of light into narrow planar optical wave-guides," *Journal Of Lightwave Technology* **7**, pp. 175–180, Jan. 1989.

[63] V. S. Ilchenko, X. S. Yao, and L. Maleki, "Pigtailing the high-q microsphere cavity: a simple fiber coupler for optical whispering-gallery modes," *Optics Letters* **24**, pp. 723–725, June 1999.

[64] M. J. Weber, *Handbook of Optical Materials*, CRC press, 2003.

[65] R. P. Kenny, T. A. Birks, and K. P. Oakley, "Control of optical fiber taper shape," *Electronics Letters* **27**, pp. 1654–1656, Aug. 1991.

[66] T. A. Birks and Y. W. Li, "The shape of fiber tapers," *Journal of Lightwave Technology* **10**, pp. 432–438, Apr. 1992.

[67] S. T. Cundiff and J. Ye, "Colloquium: Femtosecond optical frequency combs," *Reviews of Modern Physics* **75**, pp. 325–342, Jan. 2003.

[68] T. H. Maiman, "Stimulated optical radiation in ruby," *Nature* **187**(4736), pp. 493–494, 1960.

[69] P. A. Franken, G. Weinreich, C. W. Peters, and A. E. Hill, "Generation of optical harmonics," *Physical Review Letters* **7**(4), pp. 118–&, 1961.

[70] Giordmai.JA and R. C. Miller, "Tunable coherent parametric oscillation in LiNbO3 at optical frequencies," *Physical Review Letters* **14**(24), pp. 973–&, 1965.

[71] D. Klyshko, *Photons and Nonlinear Optics*, Gordon and Breach Science Publishers, 1988.

[72] R. H. Stolen and J. E. Bjorkholm, "Parametric amplification and frequency-conversion in optical fibers," *IEEE Journal Of Quantum Electronics* **18**(7), pp. 1062–1072, 1982.

[73] J. Hansryd, P. A. Andrekson, M. Westlund, J. Li, and P. O. Hedekvist, "Fiber-based optical parametric amplifiers and their applications," *IEEE Journal Of Selected Topics In Quantum Electronics* **8**, pp. 506–520, May 2002.

[74] C. W. Thiel, "Four-wave mixing and its applications."

[75] G. Agrawal, *Nonlinear Fiber Optics*, Academic Press, 2006.

[76] Y. K. Chembo and N. Yu, "Modal expansion approach to optical-frequency-comb generation with monolithic whispering-gallery-mode resonators," *Physical Review A* **82**, p. 033801, Sept. 2010.

[77] Y. K. Chembo, D. V. Strekalov, and N. Yu, "Spectrum and dynamics of optical frequency combs generated with monolithic whispering gallery mode resonators," *Physical Review Letters* **104**, p. 103902, Mar. 2010.

[78] Y. K. Chembo and N. Yu, "On the generation of octave-spanning optical frequency combs using monolithic whispering-gallery-mode microresonators," *Optics Letters* **35**, pp. 2696–2698, Aug. 2010.

[79] Y. K. Chembo and N. Yu, "Modeling of optical frequency comb generation in whispering gallery mode resonators and limiting effects," 2010.

[80] A. B. Matsko, A. A. Savchenkov, D. Strekalov, V. S. Ilchenko, and L. Maleki, "Optical hyperparametric oscillations in a whispering-gallery-mode resonator: Threshold and phase diffusion," *Physical Review A* **71**, p. 033804, Mar. 2005.

[81] D. A. Stetser and A. J. Demaria, "Optical spectra of ultrashort optical pulses generated by mode-locked glass - nd lasers - (saturable absorber tau to 2x10-13 sec e)," *Applied Physics Letters* **9**(3), pp. 118–&, 1966.

[82] D. E. Spence, P. N. Kean, and W. Sibbet, "60-fsec pulse generation from a self-mode-locked Ti-sapphire laser," *Optics Letters* **16**, pp. 42–44, Jan. 1991.

[83] H. A. Haus, J. G. Fujimoto, and E. P. Ippen, "Analytic theory of additive pulse and Kerr lens mode-locking," *IEEE Journal Of Quantum Electronics* **28**, pp. 2086–2096, Oct. 1992.

[84] U. Keller, K. J. Weingarten, F. X. Kartner, D. Kopf, B. Braun, I. D. Jung, R. Fluck, C. Honninger, N. Matuschek, and J. A. derAu, "Semiconductor saturable absorber mirrors (SESAM's) for femtosecond to nanosecond pulse generation in solid-state lasers," *IEEE Journal Of Selected Topics In Quantum Electronics* **2**, pp. 435–453, Sept. 1996.

[85] H. A. Haus, J. G. Fujimoto, and E. P. Ippen, "Structures for additive pulse mode-locking," *Journal of the Optical Society of America B-optical Physics* **8**, pp. 2068–2076, Oct. 1991.

[86] H. A. Haus, "Mode-locking of lasers," *Ieee Journal of Selected Topics In Quantum Electronics* **6**, pp. 1173–1185, Nov. 2000.

[87] B. K. Min, L. Yang, and K. Vahala, "Controlled transition between parametric and raman oscillations in ultrahigh-Q silica toroidal microcavities," *Applied Physics Letters* **87**, p. 181109, Oct. 2005.

[88] S. T. Cundiff, "Phase stabilization of ultrashort optical pulses," *Journal Of Physics D-Applied Physics* **35**, pp. R43–R59, Apr. 2002.

[89] A. A. Savchenkov, A. B. Matsko, V. S. Ilchenko, I. Solomatine, D. Seidel, and L. Maleki, "Tunable optical frequency comb with a crystalline whispering gallery mode resonator," *Physical Review Letters* **101**, p. 093902, Aug. 2008.

[90] I. S. Grudinin, N. Yu, and L. Maleki, "Generation of optical frequency combs with a caf2 resonator," *Optics Letters* **34**, pp. 878–880, Apr. 2009.

[91] J. Hofer, "Crystalline resonators for optomechanics and frequency comb generation," Master's thesis, LMU Munich, 2009.

[92] I. S. Grudinin, V. S. Ilchenko, and L. Maleki, "Ultrahigh optical Q factors of crystalline resonators in the linear regime," *Physical Review A* **74**, p. 063806, Dec. 2006.

[93] I. S. Grudinin, A. B. Matsko, A. A. Savchenkov, D. Strekalov, V. S. Ilchenko, and L. Maleki, "Ultra high Q crystalline microcavities," *Optics Communications* **265**, pp. 33–38, Sept. 2006.

[94] V. S. Ilchenko and M. L. Gorodetsky, "Thermal nonlinear effects in optical whispering gallery microresonators," *Laser Physics* **2**, pp. 1004–1009, 1992.

[95] A. E. Fomin, M. L. Gorodetsky, I. S. Grudinin, and V. S. Ilchenko, "Nonstationary nonlinear effects in optical microspheres," *Journal of the Optical Society of America B-optical Physics* **22**, pp. 459–465, Feb. 2005.

[96] D. V. Strekalov and N. Yu, "Generation of optical combs in a whispering gallery mode resonator from a bichromatic pump," *Physical Review A* **79**, p. 041805, Apr. 2009.

[97] T. J. Kippenberg and S. A. Diddams, "Microresonator based optical frequency combs," *Science (in preparation)* , 2010.

[98] L. Razzari, D. Duchesne, M. Ferrera, R. Morandotti, S. Chu, B. E. Little, and D. J. Moss, "Cmos-compatible integrated optical hyper-parametric oscillator," *Nature Photonics* **4**, pp. 41–45, Jan. 2010.

[99] J. S. Levy, A. Gondarenko, M. A. Foster, A. C. Turner-Foster, A. L. Gaeta, and M. Lipson, "Cmos-compatible multiple-wavelength oscillator for on-chip optical interconnects," *Nature Photonics* **4**, pp. 37–40, Jan. 2010.

[100] A. Gondarenko, J. S. Levy, and M. Lipson, "High confinement micron-scale silicon nitride high q ring resonator," *Optics Express* **17**, pp. 11366–11370, July 2009.

[101] D. Milam, M. J. Weber, and A. J. Glass, "Nonlinear refractive-index of fluoride-crystals," *Applied Physics Letters* **31**(12), pp. 822–825, 1977.

[102] I. H. Agha, Y. Okawachi, and A. L. Gaeta, "Theoretical and experimental investigation of broadband cascaded four-wave mixing in high-q microspheres," *Optics Express* **17**, pp. 16209–16215, Aug. 2009.

[103] S. A. Diddams, "The evolving optical frequency comb," *Journal of the Optical Society of America B-optical Physics* **27**, pp. B51–B62, Nov. 2010.

[104] T. M. Fortier, A. Bartels, and S. A. Diddams, "Octave-spanning ti : sapphire laser with a repetition rate ¿ 1 ghz for optical frequency measurements and comparisons," *Optics Letters* **31**, pp. 1011–1013, Apr. 2006.

[105] A. Bartels, D. Heinecke, and S. A. Diddams, "10-ghz self-referenced optical frequency comb," *Science* **326**, pp. 681–681, Oct. 2009.

[106] T. Udem, J. Reichert, R. Holzwarth, and T. W. Hansch, "Accurate measurement of large optical frequency differences with a mode-locked laser," *Optics Letters* **24**, pp. 881–883, July 1999.

[107] T. Udem, J. Reichert, R. Holzwarth, and T. W. Hansch, "Absolute optical frequency measurement of the cesium d-1 line with a mode-locked laser," *Physical Review Letters* **82**, pp. 3568–3571, May 1999.

[108] R. Holzwarth, T. Udem, T. W. Hansch, J. C. Knight, W. J. Wadsworth, and P. S. J. Russell, "Optical frequency synthesizer for precision spectroscopy," *Physical Review Letters* **85**, pp. 2264–2267, Sept. 2000.

[109] S. A. Diddams, D. J. Jones, J. Ye, S. T. Cundiff, J. L. Hall, J. K. Ranka, R. S. Windeler, R. Holzwarth, T. Udem, and T. W. Hansch, "Direct link between microwave and optical frequencies with a 300 THz femtosecond laser comb," *Physical Review Letters* **84**, pp. 5102–5105, May 2000.

[110] T. W. Hansch, "Nobel lecture: Passion for precision," *Reviews of Modern Physics* **78**, pp. 1297–1309, Oct. 2006.

[111] J. Ye and S. T. Cundiff, *Femtosecond Optical Frequency Comb Technology: Principle, Operation and Application*, Springer, 2005.

[112] J. Rauschenberger, T. M. Fortier, D. J. Jones, J. Ye, and S. T. Cundiff, "Control of the frequency comb from a mode-locked erbium-doped fiber laser," *Optics Express* **10**, pp. 1404–1410, Dec. 2002.

[113] P. Kubina, P. Adel, F. Adler, G. Grosche, T. W. Hansch, R. Holzwarth, A. Leitenstorfer, B. Lipphardt, and H. Schnatz, "Long term comparison of two fiber based frequency comb systems," *Optics Express* **13**, pp. 904–909, Feb. 2005.

[114] T. R. Schibli, K. Minoshima, F. L. Hong, H. Inaba, A. Onae, H. Matsumoto, I. Hartl, and M. E. Fermann, "Frequency metrology with a turnkey all-fiber system," *Optics Letters* **29**, pp. 2467–2469, Nov. 2004.

[115] B. R. Washburn, S. A. Diddams, N. R. Newbury, J. W. Nicholson, M. F. Yan, and C. G. Jorgensen, "Phase-locked, erbium-fiber-laser-based frequency comb in the near infrared," *Optics Letters* **29**, pp. 250–252, Feb. 2004.

[116] B. R. Washburn, R. W. Fox, N. R. Newbury, J. W. Nicholson, K. Feder, P. S. Westbrook, and C. G. Jorgensen, "Fiber-laser-based frequency comb with a tunable repetition rate," *Optics Express* **12**, pp. 4999–5004, Oct. 2004.

[117] M. Kourogi, K. Nakagawa, and M. Ohtsu, "Wide-span optical frequency comb generator for accurate optical frequency difference measurement," *IEEE Journal Of Quantum Electronics* **29**, pp. 2693–2701, Oct. 1993.

[118] J. Ye, L. S. Ma, T. Daly, and J. L. Hall, "Highly selective terahertz optical frequency comb generator," *Optics Letters* **22**, pp. 301–303, Mar. 1997.

[119] S. A. Diddams, L. S. Ma, J. Ye, and J. L. Hall, "Broadband optical frequency comb generation with a phase-modulated parametric oscillator," *Optics Letters* **24**, pp. 1747–1749, Dec. 1999.

[120] M. Haelterman, S. Trillo, and S. Wabnitz, "Additive-modulation-instability ring laser in the normal dispersion regime of a fiber," *Optics Letters* **17**, pp. 745–747, May 1992.

[121] M. Haelterman, S. Trillo, and S. Wabnitz, "Dissipative modulation instability in a nonlinear dispersive ring cavity," *Optics Communications* **91**, pp. 401–407, Aug. 1992.

[122] P. Franco, F. Fontana, I. Cristiani, M. Midrio, and M. Romagnoli, "Self-induced modulational-instability laser," *Optics Letters* **20**, pp. 2009–2011, Oct. 1995.

[123] E. Yoshida and M. Nakazawa, "Low-threshold 115-ghz continuous-wave modulational-instability erbium-doped fiber laser," *Optics Letters* **22**, pp. 1409–1411, Sept. 1997.

[124] S. Coen and M. Haelterman, "Modulational instability induced by cavity boundary conditions in a normally dispersive optical fiber," *Physical Review Letters* **79**, pp. 4139–4142, Nov. 1997.

[125] P. Honzatko, P. Peterka, and J. Kanka, "Modulational-instability sigma-resonator fiber laser," *Optics Letters* **26**, pp. 810–812, June 2001.

[126] T. Sylvestre, S. Coen, P. Emplit, and M. Haelterman, "Self-induced modulational instability laser revisited: normal dispersion and dark-pulse train generation," *Optics Letters* **27**, pp. 482–484, Apr. 2002.

[127] C. J. S. de Matos, D. A. Chestnut, and J. R. Taylor, "Low-threshold self-induced modulational instability ring laser in highly nonlinear fiber yielding a continuous-wave 262-ghz soliton train," *Optics Letters* **27**, pp. 915–917, June 2002.

[128] P. Honzatko, P. Peterka, and J. Kanka, "Three- and four-wave model of modulation instability fibre laser," *Journal of Optics A-pure and Applied Optics* **4**, pp. S135–S139, Sept. 2002.

[129] S. M. Zhang, F. Y. Lu, X. Y. Dong, P. Shum, X. F. Yang, X. Q. Zhou, Y. D. Gong, and C. Lu, "Passive mode locking at harmonics of the free spectral range of the intracavity filter in a fiber ring laser," *Optics Letters* **30**, pp. 2852–2854, Nov. 2005.

[130] J. Schroder, S. Coen, F. Vanholsbeeck, and T. Sylvestre, "Passively mode-locked raman fiber laser with 100 ghz repetition rate," *Optics Letters* **31**, pp. 3489–3491, Dec. 2006.

[131] F. Leo, S. Coen, P. Kockaert, S. P. Gorza, P. Emplit, and M. Haelterman, "Temporal cavity solitons in one-dimensional kerr media as bits in an all-optical buffer," *Nature Photonics* **4**, pp. 471–476, July 2010.

[132] M. T. Murphy, T. Udem, R. Holzwarth, A. Sizmann, L. Pasquini, C. Araujo-Hauck, H. Dekker, S. D'Odorico, M. Fischer, T. W. Hansch, and A. Manescau, "High-precision wavelength calibration of astronomical spectrographs with laser frequency combs," *Monthly Notices Of The Royal Astronomical Society* **380**, pp. 839–847, Sept. 2007.

[133] T. Steinmetz, T. Wilken, C. Araujo-Hauck, R. Holzwarth, T. W. Hansch, L. Pasquini, A. Manescau, S. D'Odorico, M. T. Murphy, T. Kentischer, W. Schmidt, and T. Udem, "Laser frequency combs for astronomical observations," *Science* **321**, pp. 1335–1337, Sept. 2008.

[134] F. C. Cruz, "Optical frequency combs generated by four-wave mixing in optical fibers for astrophysical spectrometer calibration and metrology," *Optics Express* **16**, pp. 13267–13275, Aug. 2008.

[135] F. Keilmann, C. Gohle, and R. Holzwarth, "Time-domain mid-infrared frequency-comb spectrometer," *Optics Letters* **29**, pp. 1542–1544, July 2004.

[136] A. Schliesser, M. Brehm, F. Keilmann, and D. W. van der Weide, "Frequency-comb infrared spectrometer for rapid, remote chemical sensing," *Optics Express* **13**, pp. 9029–9038, Oct. 2005.

[137] I. Coddington, W. C. Swann, and N. R. Newbury, "Coherent multiheterodyne spectroscopy using stabilized optical frequency combs," *Physical Review Letters* **100**, p. 013902, Jan. 2008.

[138] J. Mandon, G. Guelachvili, and N. Picque, "Fourier transform spectroscopy with a laser frequency comb," *Nature Photonics* **3**, pp. 99–102, Feb. 2009.

[139] P. Del'Haye, "Video - first evidence for frequency comb generation in a microresonator." http://www.youtube.com/watch?v=omQqSlkKLmc.

[140] S. T. Dawkins, J. J. McFerran, and A. N. Luiten, "Considerations on the measurement of the stability of oscillators with frequency counters," *Ieee Transactions On Ultrasonics Ferroelectrics and Frequency Control* **54**, pp. 918–925, May 2007.

[141] P. Lesage, "Characterization of frequency stability - bias due to the juxtaposition of time-interval measurements," *Ieee Transactions On Instrumentation and Measurement* **32**(1), pp. 204–207, 1983.

[142] T. Carmon, L. Yang, and K. J. Vahala, "Dynamical thermal behavior and thermal self-stability of microcavities," *Optics Express* **12**, pp. 4742–4750, Oct. 2004.

[143] H. Rokhsari, S. M. Spillane, and K. J. Vahala, "Loss characterization in microcavities using the thermal bistability effect," *Applied Physics Letters* **85**, pp. 3029–3031, Oct. 2004.

[144] R. W. Boyd, *Nonlinear Optics*, Academic Press, 1992.

[145] D. W. Allan, "Statistics of atomic frequency standards," *Proceedings of the Institute of Electrical and Electronics Engineers* **54**(2), pp. 221–&, 1966.

[146] D. W. Allan, "Time and frequency (time-domain) characterization, estimation, and prediction of precision clocks and oscillators," *Ieee Transactions On Ultrasonics Ferroelectrics and Frequency Control* **34**, pp. 647–654, Nov. 1987.

[147] C. G. B. Garrett and D. E. McCumber, "Propagation of a gaussian light pulse through an anomalous dispersion medium," *Physical Review A* **1**(2), pp. 305–&, 1970.

[148] L. G. Cohen and C. Lin, "Pulse delay measurements in zero material dispersion wavelength region for optical fibers," *Applied Optics* **16**(12), pp. 3136–3139, 1977.

[149] W. Sellmeier, "Zur Erklärung der abnormen Farbenfolge im Spectrum einiger Substanzen," *Annalen der Physik und Chemie* **219**, pp. 272–282, 1871.

[150] S. Schiller, "Asymptotic-expansion of morphological resonance frequencies in Mie scattering," *Applied Optics* **32**, pp. 2181–2185, Apr. 1993.

[151] M. L. Gorodetsky and A. E. Fomin, "Geometrical theory of whispering-gallery modes," *Ieee Journal Of Selected Topics In Quantum Electronics* **12**, pp. 33–39, Jan. 2006.

[152] M. L. Gorodetsky and A. E. Fomin, "Eigenfrequencies and q factor in the geometrical theory of whispering-gallery modes," *Quantum Electronics* **37**, pp. 167–172, Feb. 2007.

[153] M. Oxborrow, "Traceable 2-d finite-element simulation of the whispering-gallery modes of axisymmetric electromagnetic resonators," *IEEE Transactions On Microwave Theory And Techniques* **55**, pp. 1209–1218, June 2007.

[154] M. Oxborrow, "How to simulate the whispering-gallery-modes of dielectric microresonators in femlab/comsol - art. no. 64520j," *Laser Resonators and Beam Control IX* **6452**, p. 64520J, 2007.

[155] S. A. Diddams, L. Hollberg, and V. Mbele, "Molecular fingerprinting with the resolved modes of a femtosecond laser frequency comb," *Nature* **445**, pp. 627–630, Feb. 2007.

[156] C. Gohle, B. Stein, A. Schliesser, T. Udem, and T. W. Hansch, "Frequency comb vernier spectroscopy for broadband, high-resolution, high-sensitivity absorption and dispersion spectra," *Physical Review Letters* **99**, p. 263902, Dec. 2007.

[157] M. Brehm, A. Schliesser, and F. Keilmann, "Spectroscopic near-field microscopy using frequency combs in the mid-infrared," *Optics Express* **14**, pp. 11222–11233, Nov. 2006.

[158] B. Bernhardt, A. Ozawa, P. Jacquet, M. Jacquey, Y. Kobayashi, T. Udem, R. Holzwarth, G. Guelachvili, T. W. Hansch, and N. Picque, "Cavity-enhanced dual-comb spectroscopy," *Nature Photonics* **4**, pp. 55–57, Jan. 2010.

[159] T. Carmon, H. G. L. Schwefel, L. Yang, M. Oxborrow, A. D. Stone, and K. J. Vahala, "Static envelope patterns in composite resonances generated by level crossing in optical toroidal microcavities," *Physical Review Letters* **100**, p. 103905, Mar. 2008.

[160] Z. Jiang, C. B. Huang, D. E. Leaird, and A. M. Weiner, "Optical arbitrary waveform processing of more than 100 spectral comb lines," *Nature Photonics* **1**, pp. 463–467, Aug. 2007.

[161] M. J. Thorpe, K. D. Moll, R. J. Jones, B. Safdi, and J. Ye, "Broadband cavity ringdown spectroscopy for sensitive and rapid molecular detection," *Science* **311**, pp. 1595–1599, Mar. 2006.

[162] P. Del'Haye, "Video - third harmonic generation in a fused silica microdisk." http://www.youtube.com/watch?v=u6xs0qygA8E.

[163] P. Del'Haye, "Video - cascaded nonlinear interactions in a fused silica microtoroid." http://www.youtube.com/watch?v=f0j2iw6KOfM.

[164] T. J. Kippenberg, S. M. Spillane, and K. J. Vahala, "Modal coupling in traveling-wave resonators," *Optics Letters* **27**, pp. 1669–1671, Oct. 2002.

[165] P. Del'Haye, "Video - coupling between clockwise and counter-clockwise modes in a fused silica microtoroid." http://www.youtube.com/watch?v=QebxATrfCdY.

[166] P. Del'Haye, "Video - third harmonic generation in fused silica microsphere." http://www.youtube.com/watch?v=h08a5blrfLg.

[167] T. Udem, *Phasenkohärente optische Frequenzmessungen am Wasserstoffatom. Bestimmung der Rydberg–Konstanten und der 1S Lamb–Verschiebung.* PhD thesis, Ludwig-Maximilians-Universität München, 1998.

[168] F. Gardner, *Phaselock Techniques*, Wiley-Interscience, 1979.

[169] M. Prevedelli, T. Freegarde, and T. W. Hansch, "Phase-locking of grating-tuned diode-lasers," *Applied Physics B-lasers and Optics* **60**(2-3), pp. S241–S248, 1995.

[170] M. Cohn, J. E. Degenford, and B. A. Newman, "Harmonic mixing with an antiparallel diode pair," *Ieee Transactions On Microwave Theory and Techniques* **23**(8), pp. 667–673, 1975.

[171] L. Devlin, "Mixers." http://www.plextek.com/papers/mixers2.pdf.

[172] J. A. Barnes, A. R. Chi, L. S. Cutler, D. J. Healey, D. B. Leeson, Mcguniga.te, J. A. Mullen, W. L. Smith, R. L. Sydnor, R. F. C. Vessot, and G. M. R. Winkler, "Characterization of frequency stability," *Ieee Transactions On Instrumentation and Measurement* **IM20**(2), pp. 105–&, 1971.

[173] P. Del'Haye, "Video - repetition rate switching in a microresonator-based frequency comb." http://www.youtube.com/watch?v=3gg5kzdAlhE.

[174] *Corning SMF-28 Optical Fiber Product Information.*

[175] M. A. Foster and A. L. Gaeta, "Soliton-effect compression of supercontinuum to few-cycle durations in photonic nanowires," *Optics Express* **13**, pp. 6848–6855, Sept. 2005.

[176] P. Del'Haye, "Video - regenerative oscillations of the tapered fiber position at high power levels.." http://www.youtube.com/watch?v=D-CVVcCOyQo.

[177] T. Kippenberg, *Nonlinear Optics in Ultra-high-Q Whispering-Gallery Optical Microcavities.* PhD thesis, California Institute of Technology, 2004.

Danksagung